DISSERTATION

RHENIUM-OSMIUM GEOCHRONOLOGY AND GEOCHEMISTRY OF THE UPPER JURASSIC MARINE BLACK SHALES, AGARDHFJELLET FORMATION, CENTRAL SPITSBERGEN, SVALBARD AND MERCURY DEGRADATION OF UPPER PERMIAN SHALES, EAST GREENLAND AND MID-NORWEGIAN SHELF

Submitted by

Junhee Park

Department of Geosciences

In partial fulfillment of the requirements

For the Degree of Doctor of Philosophy

Colorado State University

Fort Collins, Colorado

Spring 2024

Doctoral Committee:

Advisor: Judith Hannah

Dennis Harry
Thomas Borch
Svetoslav Georgiev
Øyvind Hammer
Snorre Olaussen

ABSTRACT

RHENIUM-OSMIUM GEOCHRONOLOGY AND GEOCHEMISTRY OF THE UPPER JURASSIC MARINE BLACK SHALES, AGARDHFJELLET FORMATION, CENTRAL SPITSBERGEN, SVALBARD AND MERCURY DEGRADATION OF UPPER PERMIAN SHALES, EAST GREENLAND AND MID-NORWEGIAN SHELF

Every rock has its own story. Rocks are categorized as igneous, metamorphic, and sedimentary types based on their origins and overprinting processes. The human species is confronting the crisis of climate change and some rocks hold a climate story from the past, permitting speculation on the future. On the geological time scale, Earth has experienced both scorching and freezing environments, the latter referred to as Snowball Earth. A critical key to resolving the problems we are facing lies in geology, which deconvolutes environments where specific rocks have formed.

This dissertation addresses Boreal sedimentary sections during the Late Jurassic period by conducting three projects; Project I pinpoints depositional ages for black shales from the Agardhfjellet Formation and discusses Os isotopic ratios in the Boreal ocean during the Late Jurassic. Project II evaluates the depositional environments of the Agardhfjellet Formation, which was deposited during a shelf dysoxic-anoxic event. Project III focuses on Hg degradation incurred during incipient weathering and calls attention to interpreting Hg signals of sedimentary rocks, which have been used as an indicator of ancient volcanism. This dissertation provides new radiometric ages and detailed geochemical discussions of the Late Jurassic Agardhfjellet Formation and cautions the use of Hg concentrations when interpreting from outcrop sections. The findings herein significantly enhance our understanding of shelf dysoxic-anoxic events compared with oceanic anoxic events and Hg behavior during the early stage of weathering.

ACKNOWLEDGEMENTS

I would like to express my heartfelt gratitude to my advisors, Dr. Prof. Holly Stein and Prof. Judith Hannah, for their unwavering support throughout this journey. From the beginning of the program four years ago, they have provided invaluable guidance and nurtured my development as an independent researcher. Together, we navigated through both triumphs and undue challenges during these four years. Furthermore, I want to express my sincere gratitude for their constant support during a challenging period when we faced unjustified expulsion from the department. Their assistance was invaluable in helping me overcome adversities and continue on this academic path. Their contributions have had a profound impact on both my personal growth as a researcher and the overall quality of this dissertation. I firmly believe that without their constant encouragement, I would not have reached this significant milestone in my academic pursuit. I will keep the quote that Holly recommended from the movie "*The Best Exotic Marigold Hotel*": "Everything will be all right in the end. If it's not all right, it is not yet the end."

I am deeply grateful to my esteemed committee members, Prof. Dennis Harry, Prof. Thomas Borch, Dr. Øyvind Hammer, and especially Dr. Snorre Olaussen, for generously giving of their time and expertise to serve on my Ph.D. committee and providing invaluable feedback throughout the process. I would like to extend a special thank you to Dr. Svetoslav Georgiev for his exceptional input and guidance in my research endeavors. I would also like to express my appreciation to AIRIEites, Dr. Gang Yang and Aaron Zimmerman, for their tireless efforts in mentoring me as a budding geochemist, enabling me to advance in this field.

I would like to convey my gratitude to the donors of the McCallum scholarship for their generous support not once but twice during two fiscal years – a contribution that has significantly aided me in pursuing my academic goals.

Last but not least, I express my loving and fervent gratitude to my life partner, Chelsea, who has been a guiding light in the midst of my uncertainties. Your persistent support and love have provided clarity and strength during challenging times and unexpected tribulations. To my parents, I want to say how deeply I love and appreciate you. Your constant presence and unchanging belief in me have been an anchor throughout this journey. I am also grateful to my sister and brother's family for their continuous thoughts of me despite the physical distance that separates us. A special thank you goes out to Fort Collins First Korean Church for their prayers and spiritual support. Your collective faith has been a source of encouragement during both joyful moments and difficult trials. In addition, I am profoundly grateful to Trent and Joan Sauder for their enduring love and prayers. Your steadfast commitment and love have uplifted me in immeasurable ways and made me know what God's love is.

I offer praise to God, who is the Alpha and the Omega. His divine guidance has illuminated my path throughout this journey.

DEDICATION

I would like to dedicate this dissertation to my beloved, Chelsea.

TABLE OF CONTENTS

LIST OF TABLES

LIST OF FIGURES

Chapter 1 Introduction

1.1 Motivation

After water, petroleum (oil) is perhaps the most crucial liquid in human society. The utilization of fossil fuels (coal, oil, and gas) has facilitated labor-intensive tasks. Consequently, climate change is spurred by carbon dioxide emissions from fossil fuel combustion (Lüthi et al., 2008; Manabe and Wetherald 1975). To address this issue, global leaders and scientists have collaborated through entities like the Intergovernmental Panel on Climate Change (IPCC), which asserts that these extraordinary CO_2 levels primarily result from human activities involving fossil fuels (IPCC 2022). Although renewable energy is emerging as a viable alternative, petroleum remains a dominant force globally (Clemente 2015), with predictions showing increasing fossil fuel consumption (Fig. 1.1). Therefore, understanding petroleum systems continues to be vital.

The conventional petroleum system consists of several key elements: source rock, migration, reservoir, seal, and trap (Fig. 1.2). New technology has recently led to unconventional petroleum production, which extracts oil or natural gas directly from the source rock, usually organic-rich black shale. Without source rock, there is no oil and gas. Because not all shales are organic-rich, it is important to identify/evaluate which depositional environments are able to generate potential source rocks. In addition, studies on the depositional settings of organic-rich sediments can shed light on understanding the climate change that the Earth is facing right now. On a larger scale, deposition of organic-rich sediment is a form of carbon capture and storage (CCS) from the atmosphere, hydrosphere, and biosphere into the lithosphere. In particular, the deposition of organic-rich black shales is highly associated with defined Oceanic Anoxic Events (OAEs) through Earth history.

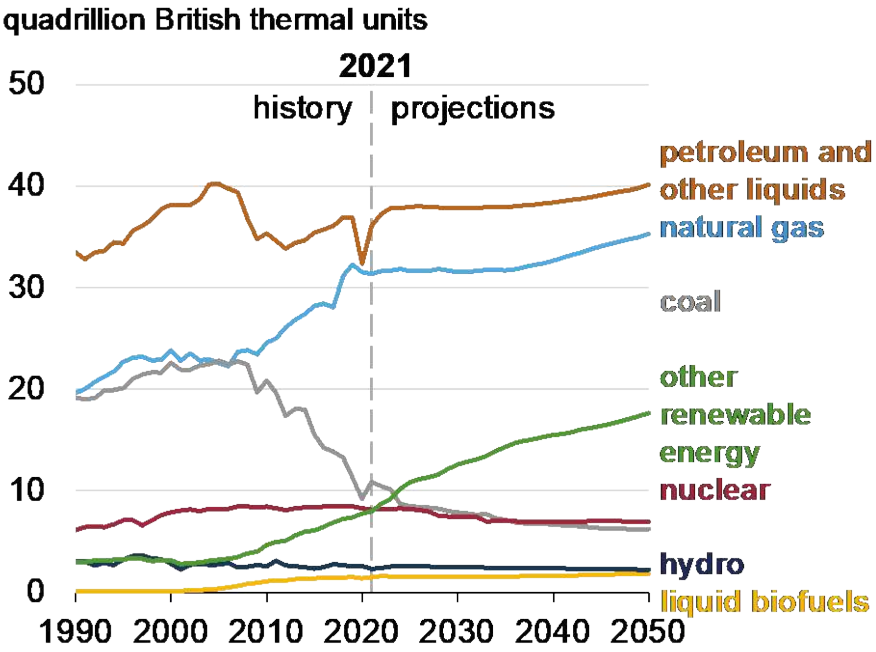

Fig.1.1 Energy consumption by fuel Annual Energy Outlook 2022 by U.S. Energy Information Administration (Nalley and LaRose 2022)

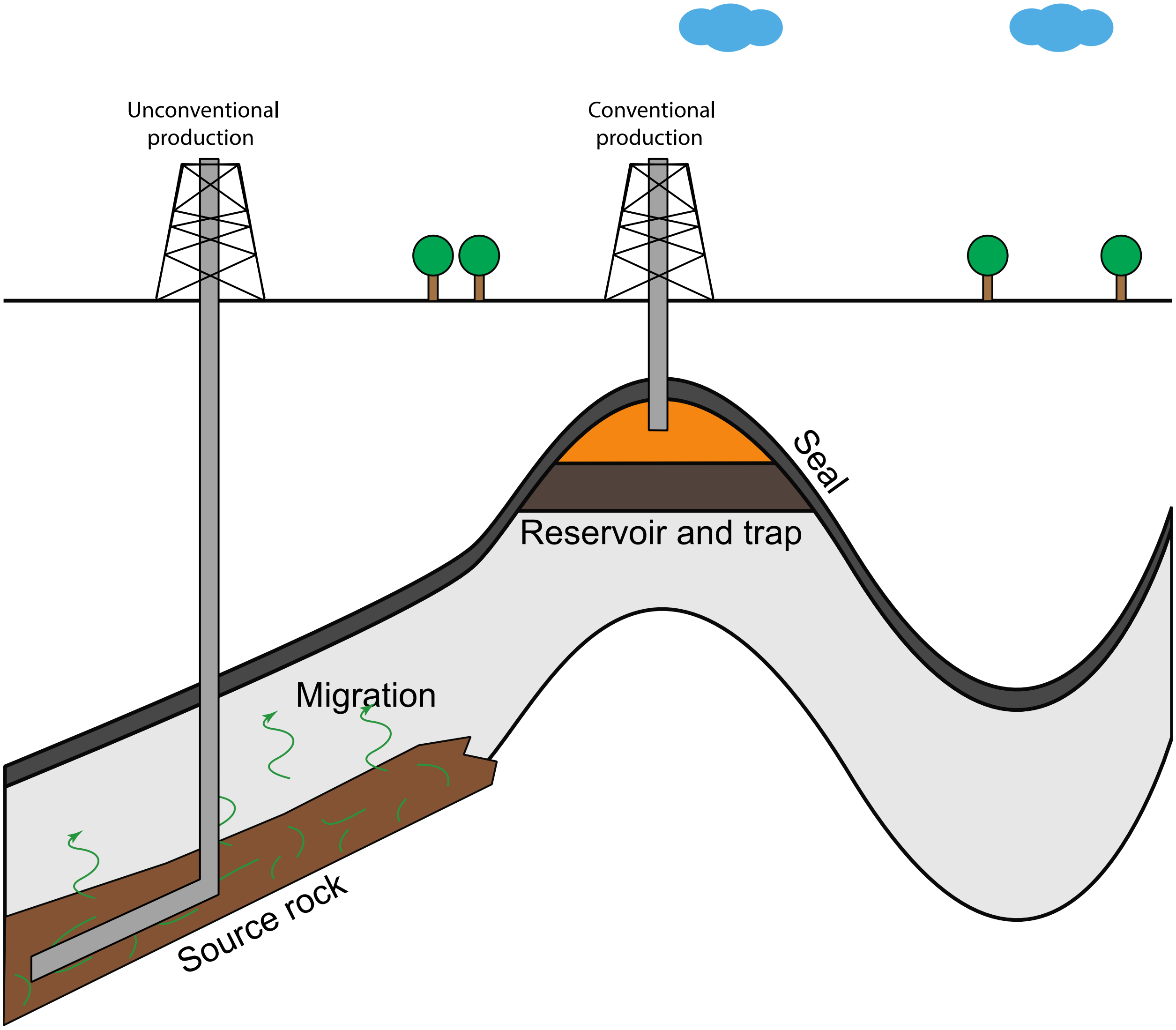

Fig.1.2 Schematic diagram of conventional and unconventional productions from a petroleum system. Five key elements of the petroleum system, source rock, migration, reservoir, trap, and seal, are represented. Source rock is essential in both conventional and unconventional productions of fossil fuel energy.

Since OAE was named and connected with the occurrence of certain black shale horizons (Schlanger and Jenkyns 1976), many causes and effects of OAEs have been proposed. An abrupt temperature rise from increased CO_2 into the atmosphere derived from volcanogenic or methanogenic sources has been considered as the main cause of OAEs (Jenkyns 2010). For example, the Karoo-Ferrar large igneous province (LIP) and the Ontong-Java Plateau are suggested as the triggers of Toarcian OAE and OAE 1a, respectively (Dickson et al. 2021; Turgeon and Creaser, 2008). Furthermore, it is crucial to investigate paleoenvironments associated with OAEs because OAEs are linked to biotic crises and mass extinctions (Reolid et al. (2021); references therein). Geologists postulate anoxic conditions in the circumpolar Arctic during the Late Jurassic - Early Cretaceous based on the widespread presence of prolific black shale layers (e.g., the Upper Jurassic Hekkingen, Draupne, Mandal, or Farsund Formations around the North Sea and Barents Sea). These black shales, not attributed to global OAEs, are distinguished from OAE-associated black by the following: (1) limited to the higher latitudes, rather than a global occurrence of black shale, (2) diachronous onset and termination, (3) up to 20 million years duration compared to OAEs (10 – 100 thousand years), (4) no significant global ^{13}C perturbation, and (5) no remarkable extinction events (Rogov et al. 2020). Since Rogov et al. (2020) proposed a shelf dysoxic-anoxic event (SDAE) to describe Boreal black shales during the Late Jurassic – Early Cretaceous, the causes and effects of SDAE are unclear.

This doctoral study scrutinizes organic-rich black shales from the Agardhfjellet Formation to identify the causes and effects of this Shelf Dysoxic-Anoxic Event (SDAE) and evaluates the depositional paleoenvironments using geochemical and geochronological approaches. At another arctic locality, this doctoral study examines Hg concentrations from outcrop and correlative drill cores concluding that incipient weathering degrades the Hg content held in outcrop exposures.

1.2 Overview

1.2.1 Shelf dysoxic anoxic event (SDAE)

Oceanic Anoxic Events (OAEs) represent periods of global ocean anoxia, often associated with Large Igneous Provinces (LIPs) and/or mass extinctions. LIPs are considered a significant trigger for OAEs, with their extensive carbon emissions disrupting the global carbon cycle. This disruption is often reflected in abnormal carbon isotopic ratios, which serve as a key geochemical indicator of an OAE alongside isotopic ratio excursions of N and O and enrichment of redox-sensitive elements (Jenkyns 2010). The presence of prolific black shale layers such as the Upper Jurassic Hekkingen, Draupne, Mandal, and Farsund Formations in the Boreal realm suggest dysoxic to anoxic ocean environments between Late Jurassic and Early Cretaceous (Georgiev et al., 2017; Tripathy et al., 2018; Georgiev et al., 2019). However, these Formations have not been attributed to an OAE due to their confinement to high-latitude regions and their lack of significant global carbon isotope excursion or correlative volcanisms.

To account for this non-OAE dysoxic-anoxic status during the Middle Jurassic – Early Cretaceous period, Rogov et al. (2020) introduced the concept of Shelf Dysoxic-Anoxic Event (SDAE), representing regional oceanic anoxia as mentioned above (Fig. 1.4). Possible drivers for SDAE could include global climate warming leading to ocean stratification, dysoxic–anoxic conditions, and enhanced productivity (Rogov et al., 2020).

The Volgian Isotopic Carbon Excursion (VOICE), observed in Late Jurassic circumpolar deposits exhibiting a distinctive negative carbon isotopic excursion from the global trend, was followed by a quick restoration at the Jurassic-Cretaceous boundary known as the Weissert Event. Identifying the potential factors that contributed to the unique characteristics of the VOICE in the Boreal realm during the Late Jurassic period could provide significant insights for paleoenvironments at that time. Galloway et al. (2020) proposed a combination of factors such as reduced global sea levels, volcanic activities, or an isolated depositional basin as having a role in shaping the VOICE.

1.2.2 Latest Permian anoxia

The Permian-Triassic boundary marks the Permo-Triassic extinction - Earth's most severe extinction event resulting in the disappearance of ~90% marine life and ~70% terrestrial life forms

(Erwin 1994). This event is also linked with OAE (Algeo et al., 2008), although debates persists whether it is a global or regional event (Heydari et al., 2008). In the late Permian Boreal Ocean euxinia developed persisting untill the earliest Triassic (Bond & Wignall 2010). Rising ocean temperatures & acidity causing oxygen loss have been suggested as possible causes behind subsequent mass extinction (Georgiev et al., 2011). Increasing primary productivity induced by upwelling rather than oceanic stagnation was responsible for maintaining these anoxic conditions (Georgiev et al.,2015).

1.2.3 Geochemical proxies for paleoenvironment

The trace metal (TM) content in organic-rich sediments provides insights into the characteristics of depositional environments, including redox conditions, primary productivity, and water mass restrictions. (Brumsack, 2006; Algeo and Liu, 2020). Trace metal enrichment is generally similar in both upwelling areas and euxinic basins. However, specific TM patterns show variations. Upwelling environments typically exhibit enrichment in Cd and P in sediments while showing depletion in Co and Mn. Conversely, sapropels are often more enriched in Mo, S, Re, As, Cu, Ni, Sb, and Fe due to strong sulfidation within an anoxic water column (Brumsack, 2006). Enrichment factors (EFs) of TMs are utilized to determine TM patterns within sedimentary rocks by normalizing the TM contents against average shale values (Wedepohl 1971). Algeo and Liu (2020) reviewed geochemical datasets for 55 Phanerozoic marine formations ranging from oxic to euxinic by statistical approaches to evaluate which paleoredox proxies are more reliable. The authors concluded that enrichment factors are more effective than TM contents (Algeo and Liu, 2020). However, each proxy has its limitations since a given proxy may be effective in one setting but not another (Tribovillard et al., 2006), necessitating consideration of multiple proxies for evaluating depositional settings.

Among trace metals, particularly, mercury concentrations or Hg/TOC ratio anomalies within sedimentary rocks are frequently interpreted as indicators of massive volcanism – a primary trigger for global environmental disturbances or even mass extinctions (Percival et al., 2018). This stems from volcanic emissions being the largest known source of atmospheric Hg prior to significant anthropogenic contributions. For example, Shen et al. (2019a) compiled 10 intervals of sediments from 10 different sites, including the Permian-Triassic boundary, and concluded that Hg peaks of the sediments were nearly synchronous with the end-Permian extinction horizon, specifically in shallow-water sections, which implies volcanic activity is strongly associated with the mass extinction. Therefore, understanding the behavior of Hg in sedimentary rocks is crucial for interpreting paleoenvironmental conditions and identifying the causes of environmental perturbations in the past.

Stable isotopes of sedimentary rocks have also been used as paleoproxies to provide insights into elemental cycling and changes in the paleoenvironment, such as elemental cycles. Variations in the carbon isotopic composition of marine organic matter have also been used for chemostratigraphic correlations as well as environmental interpretations. For example, Jelby et al. (2020) correlated VOICE in multiple Boreal sedimentary sections with organic carbon isotopic ratio profiles.

Sulfur isotopes from pyrite and carbonate in sedimentary rocks have been used to investigate the sulfur cycles in the ocean during the Earth history. Sulfide is mainly formed by bacterial sulfate reduction (BSR), consuming sulfate and formaldehyde from OM. The fractionation of sulfur isotopes between $\delta^{34}S_{CAS}$, carbonate-associated sulfate (CAS), and $\delta^{34}S_{pyrite}$ occurs during BSR. The $\delta^{34}S_{CAS}$ has been used as a direct indicator of $\delta^{34}S$ of paleoceanic sulfate to reconstruct the marine sulfur cycle under oxic conditions where sulfate is available, but $\delta^{34}S_{pyrite}$

has been alternatively used in silicic clastic sediments under anoxic or euxinic conditions where sulfate is barely available and H_2S can exist. For example, Chen et al. (2022) reported elevated $\delta^{34}S_{pyrite}$ during Toarcian OAE in the Early Jurassic. The authors pointed out that high sedimentation rates, high OM supply, limited pool of sulfate, and anoxia would result in the elevated $\delta^{34}S_{pyrite}$ by providing limited sulfate.

Re and Os are redox-sensitive trace elements, but ^{187}Re decays to ^{187}Os, which makes the isotopic system powerful in the organic-rich sediments as a radiometric dating method. Assuming a closed system after the deposition and constant Os isotope ratio ($^{187}Os/^{188}Os$) in the contemporaneous ocean, the depositional ages of organic-rich sedimentary rocks can be obtained through $^{187}Os/^{188}Os$ - $^{187}Re/^{188}Os$). In addition, the initial Os ratio (Os_i), which is interpreted as the Os isotopic ratio in the contemporaneous ocean, is derived from by the y-intercept on the isochron, which has been used as a proxy to indicate Os sources - radiogenic (continental) versus unradiogenic (mantle-derived).

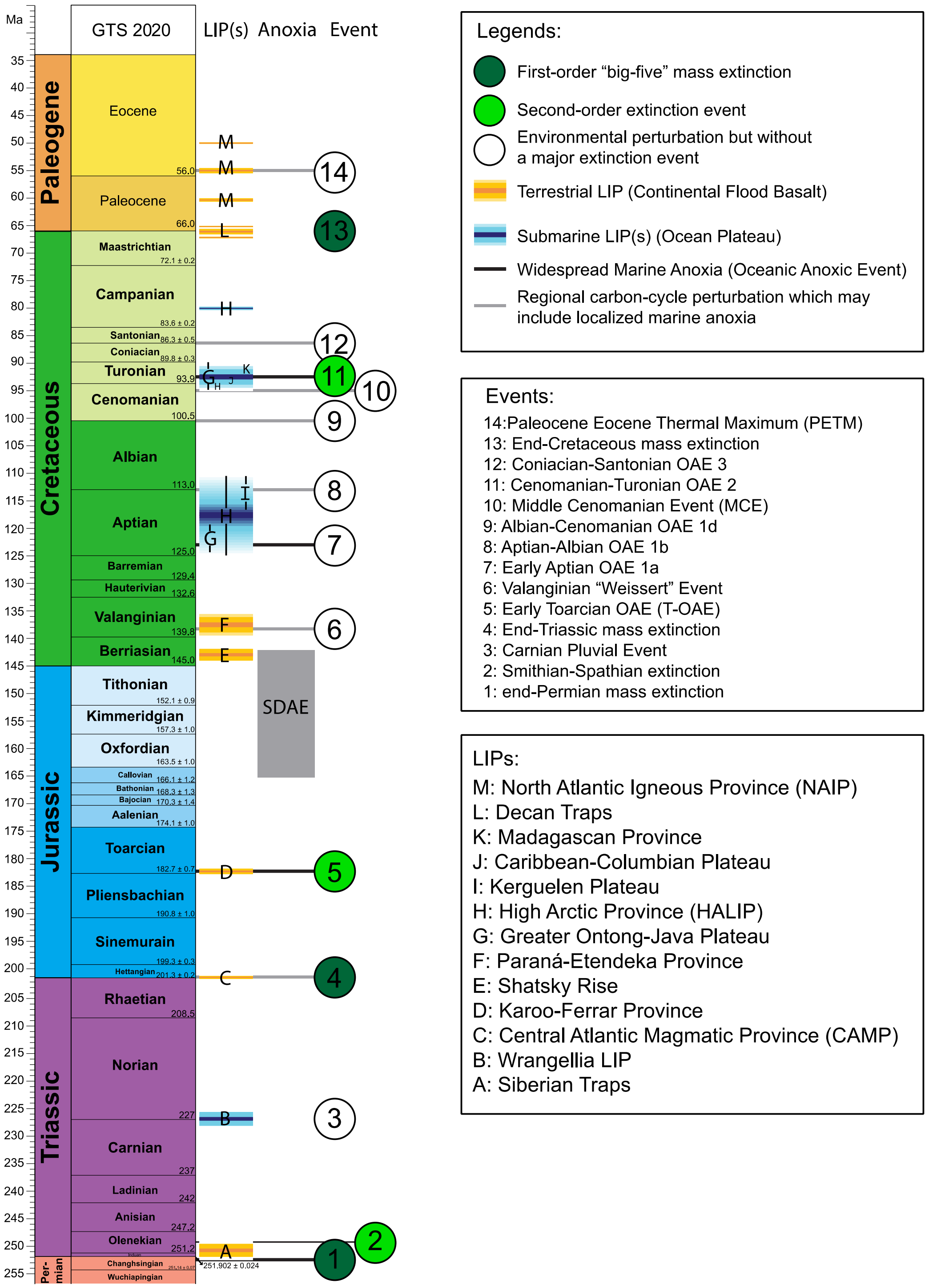

Fig.1.3 Geological time scales with corresponding mass extinction events, ocean anoxic events (OAEs), and volcanic events (LIPs). Shelf dysoxic-anoxic event (SDAE; Rogov et al. 2020) from the Boreal realm is shown by a gray rectangle. Note the much longer duration of the SDAE compared to other anoxic events. Modified from Jenkyns (2010) and Percival et al. (2018).

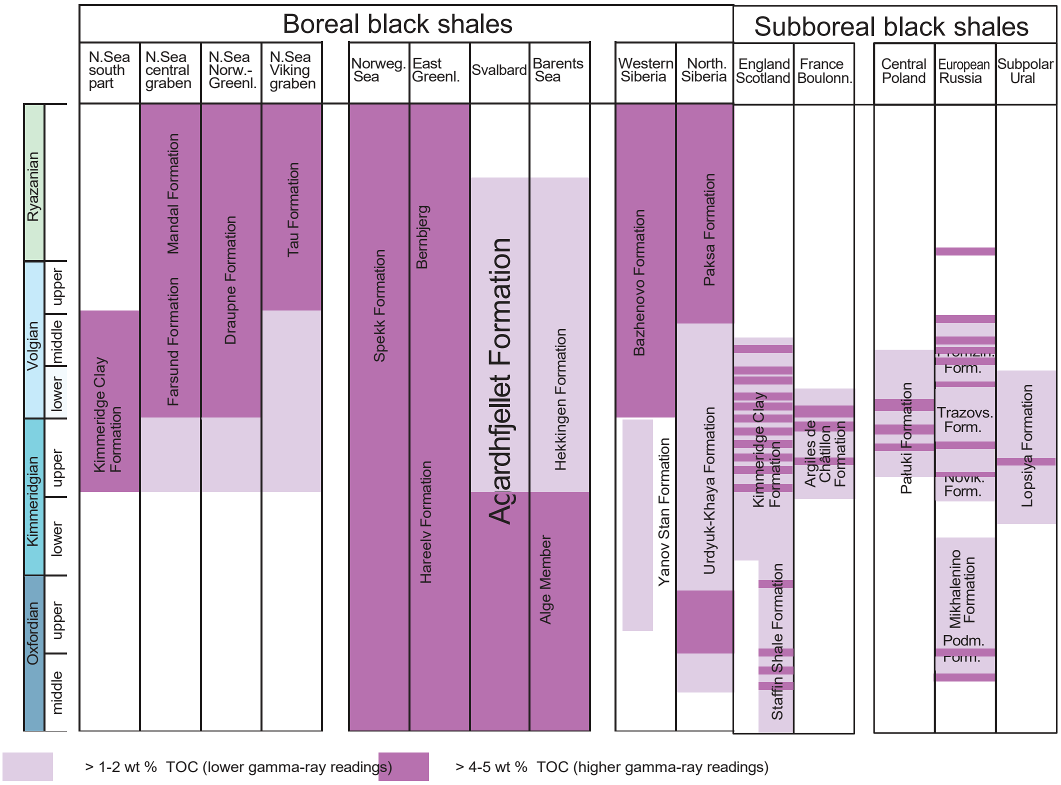

Fig.1.4 Black shale deposition in the Boreal and Subboreal regions during the Late Jurassic to Early Cretaceous. The onset and duration of each location vary. Modified from Rogov et al. (2020).

1.3 Dissertation Objectives and Outlines

This dissertation enhances our understanding of the geological processes that transpired during the Late Jurassic and Late Permian periods. This is achieved by examining black shales from the Agardhfjellet and Ravnefjeld Formations using geochemical analyses and statistical methods. Understanding environments in the past is the key to understanding present-day rapidly changing environments. The dissertation comprises three research projects as follows:

Chapter 2: The first goal of this study is to derive accurate Re-Os radiometric ages for black shales from the Late Jurassic – J/K boundary in the Boreal realm. Accurate and precise radiometric ages are necessary to correlate between the Boreal and Tethyan realms in the geologic past. Through precise Re-Os radiometric dating, we can gain deeper insights into the duration of anoxic events, and the environmental shifts driving those events during the Late Jurassic.

Chapter 3: The second objective of this dissertation is to elucidate the geochemical characteristics of a shelf dysoxic-anoxic event (SDAE) and compare them with those observed in Phanerozoic OAEs. This objective leads to the establishment of mechanisms that fosters SDAE during the Late Jurassic period. By analyzing the geochemical characteristics of SDAE and contrasting them with those of OAE, the differences between these two events can be understood. Additionally, identifying these mechanisms could sheds light on environmental changes during the Late Jurassic by explaining how the Agardhfjellet Formation was deposited during SDAE.

Chapter 4: The third objective of this dissertation is to ascertain how incipient weathering impacts Hg concentrations in black shale, using the Late Permian Ravnefjeld shale as a case study. In addition, new Hg data along with principal component analysis (PCA) was used to assess the effectiveness of Hg/TOC as a geochemical tool for detecting LIP inputs in geological records. By scrutinizing Hg content within black shales, we can comprehend how incipient weathering influences it.

Chapter 5: Here, key findings are highlighted from each chapter, and contributions toward enriching the current knowledge base are outlined; potential avenues for future research are discussed.

Chapter 2 Project I

Re-Os geochronology of the Middle to Upper Jurassic marine black shales, Agardhfjellet Formation, Central Spitsbergen, Svalbard: a cornerstone for global faunal correlation and Ost isotopic change

2.1 Summary

Ammonite provincialism makes it difficult to link the Boreal and Tethyan realms during the Late Jurassic to Early Cretaceous time. Absolute ages through radiometric dating offer new age information that is independent and complementary to relative ages based on biostratigraphy. In this study, we report seven new Re-Os ages for black shales from the Agardhfjellet Formation, Svalbard. We also report pyrolysis results, carbon and sulfur stable isotopic data, and initial $^{187}Os/^{188}Os$ ratios to evaluate the paleoenvironment during organic-rich shale deposition. Re-Os ages are derived from three Boreal ammonite zones: (1) 159.2 and 160.1 Ma from the shale intervals containing *Cadoceras* sp.; (2) 149.6, 149.9, 150.8, and 151.9 Ma from the *Rasenia cymodoce* Zone in the Early Kimmeridgian, which is the equivalent of the *Sutneria platynota* and *Ataxioceras hypselocyclum* zones in the Tethyan realm; (3) 146.8 Ma from an upper Volgian interval above the occurrence of *Laugeites* sp.. Within this 14.5 Myr interval, the initial Os profile shows a gradually increasing trend from 0.335 (one of the lowest shale values throughout the Phanerozoic) to 0.529, consistent with previous initial Os studies and Sr isotopic ratio chemostratigraphic studies. The trend of increasing initial Os ratios indicates an increase in continental runoff relative to unradiogenic Os input from mantle sources, such as seafloor

hydrothermal activity or ultramafic source rocks. We provide new Re-Os geochronological anchors in the Late Jurassic with new Re-Os ages and propose correlations of specific Late Jurassic ammonite zones between the Tethyan and Boreal realms. In turn, the gradual increase in seawater Os isotopic ratios may signal climate change in the Late Jurassic, indicating the increase of radiogenic Os or decrease of unradiogenic Os, induced by high continental runoff or less hydrothermal/volcanic activity.

2.2 Introduction

Correlating the biostratigraphic units between the Boreal and Tethyan realms around the Jurassic – Cretaceous (J/K) boundary using paleontology or magnetostratigraphy has been challenging, partly because the Volgian and Ryazanian chronostratigraphic stages in the Boreal realm are likely mismatched with their corresponding stages, the Tithonian and Berriasian, in the Tethyan realm (Casey, 1963; Kutek and Zeiss, 1975; Baraboshkin, 2004; Zakharov and Rogov, 2008; Rogov, 2014). Several working groups proposed possible global stratotype sections and points (GSSP) for the J/K boundary, but the final choice is still in debate (Wimbledon et al., 2020a, 2020b; Grabowski et al., 2022) While a few studies reported the discovery of Tethyan ammonites in the Boreal realm (Mitta, 2007) and *vice versa* (Dromart et al., 2003), the correlation between the two realms is still only loosely constrained because of the provincialism of ammonites at the time. Although the Norwegian-Greenland Seaway likely connected the Boreal and Tethyan oceans, the link was relatively narrow and shallow before the Eocene, which may have enhanced the ammonite provincialism (Pitman III and Talwani, 1972; Torsvik et al., 2002).

Radiometric ages are a powerful tool to investigate correlations between different locations as they provide absolute ages unaffected by local or regional differences in sediment supply or faunal provincialism. The most accurate and precise method for dating sedimentary successions is usually the U-Pb dating of zircon grains in ash layers within, or bracketing, the sedimentary rocks. However, the paucity of ash layers in the Boreal realm from the Late Jurassic to the J/K boundary requires alternative radiometric approaches. Re-Os isotope chemistry has been widely used to date sedimentary rocks and reconstruct paleoenvironments (Cohen et al., 1999; Creaser et al., 2002; Selby and Creaser, 2003; Cohen, 2004; Selby, 2007; Xu et al., 2009; Georgiev et al., 2011, 2017; Markey et al., 2017). The value of Re-Os ages is now recognized, and along with U-Pb and Ar-Ar ages, they are used as reference radiometric ages in the recent Geologic Time Scale (GTS; Gradstein et al., 2020).

Re-Os isochrons from marine sedimentary sections provide not only age information but also initial $^{187}Os/^{188}Os$ ratios (Os_i), which record the $^{187}Os/^{188}Os$ ratios in contemporaneous seawater during the deposition of the sediment. Where communication with open marine conditions can be affirmed, the Os_i is widely used to place temporal constraints on, for example, atmospheric oxygen evolution, emplacement of large igneous provinces (LIPs), oceanic conditions, climate changes, and extraterrestrial impacts (Hannah et al., 2004; Cohen and Coe, 2007; Ravizza and VonderHaar, 2012; Xu et al., 2014; Georgiev et al., 2020). The temporal variation in seawater $^{187}Os/^{188}Os$ is often compared to the marine $^{87}Sr/^{86}Sr$ curve, as the isotopic ratios are mainly governed by two endmembers of input sources (e.g., Cohen and Coe, 2007; Georgiev et al., 2017) – unradiogenic sources (mantle-derived input or cosmic dust) and radiogenic sources (continental runoff).

The depositional environment in the Boreal realm during the Late Jurassic period may be unique in Earth's history. Rogov et al. (2020) introduced a new concept of anoxia – the shelf dysoxic/anoxic events (SDAEs). Ocean anoxic events (OAEs) are defined as periods of pronounced and widespread oxygen depletion of ocean anoxia that generally lead to the deposition of voluminous organic-rich black shales and are characterized by carbon isotopic excursions in coeval sediments (Schlanger and Jenkyns, 1976; Scholle and Arthur, 1980). In contrast, SDAEs have distinctive characteristics, as they: (1) are mainly restricted to high latitudes, (2) show diachronous onset and termination of SDAE, (3) exhibit prolonged duration (~19 Myr; Georgiev et al., 2017), (4) are not accompanied by carbon isotope excursions spanning the anoxic event, and (5) show no remarkable extinction events (Rogov et al., 2020). Rogov et al. (2020) suggest that the cause of the SDAE may be long-term warming and/or ocean circulation changes.

Here, we report Re-Os ages and Os_i ratios derived from isochrons for black shale intervals in the Agardhfjellet Formation, Svalbard. We include total organic carbon (TOC), pyrolysis results, organic $\delta^{13}C$, and $\delta^{34}S$ in the shales to evaluate the changing depositional conditions with time. The stable isotope and pyrolysis results are in good agreement with previous geochemical, sedimentological, and paleontological studies of the Agardhfjellet Formation (Koevoets et al., 2016, 2018, 2019). Seven new Re-Os ages and Os_i ratios during the Late Jurassic (160.1 Ma – 146.8 Ma) are reported as steppingstones or anchors to correlate ammonite zones between the Boreal and Tethyan realms and refine the geologic time scale (GTS) in the poorly constrained Late Jurassic. The gradual increase in seawater $^{187}Os/^{188}Os$ ratios through the Late Jurassic may imply enhanced continental runoff from radiogenic sources in the Boreal realm.

2.3 Geological setting

The studied area is located near Longyearbyen, Central Spitsbergen, Svalbard archipelago, Arctic Norway, located at approximately 78° 14′ 31″ north and 15° 32′ 04″ east for DH2 and 78° 12′ 00″ north and 15° 49′ 21″ east for DH5R (Fig. 2.1). Svalbard was part of the circumpolar/Boreal realm during the Late Jurassic (*c*. 150 Ma) based on its high paleolatitude (Fig. 2.1a; Torsvik et al., 2002). Drilling the sampled cores was part of a project to test the feasibility of CO_2 storage in Upper Triassic – Middle Jurassic sandstones by the UNIS CO_2 LAB (Braathen et al., 2012; Ogata et al., 2014; Sand et al., 2014). The wells fully sampled the Agardhfjellet Formation, which has an average thickness of about 250 m (Koevoets et al., 2018). This is consistent with exposures of the Agardhfjellet Formation in the Janusfjellet area, about 10 km away from the wells (Dypvik et al., 1991; Hammer et al., 2012).

The Agardhfjellet Formation is situated above the Kapp Toscana Group and is overlain by the Rurikfjellet Formation (Parker, 1967; Smelror et al., 2001). The mudstone-dominated Agardhfjellet Formation is the onshore equivalent of the Fuglen and Hekkingen formations in the southwestern Barents Sea (Dypvik et al., 2002; Worsley, 2008). The organic-rich marine mudstone of the Hekkingen Formation is a prolific source rock for the oil accumulation in the southwestern Barents Sea hydrocarbon province (Henriksen et al., 2011; Abay et al., 2018) The Agardhfjellet Formation consists of four members: Oppdalen, Lardyfjellet, Oppdalssåta, and Slottsmøya in ascending order (Mørk et al., 1999; Hammer et al., 2011; Koevoets et al., 2016, 2018) (Fig. 2.2).

The Oppdalen Member was deposited on a shallow marine shelf during the Bathonian to Oxfordian based on detailed biostratigraphy (Koevoets et al., 2018, 2019). The relatively thin succession, common glauconite, siderite beds, and missing ammonite zones suggest a condensed unit. Well-oxygenated conditions supported vigorous bioturbation (Fig. A1a; Koevoets et al., 2018). In central and western Spitsbergen, the upper Oxfordian to Kimmeridgian Lardyfjellet Member occurs as a well-defined unit coarsening upward from organic-rich offshore marine mudstone (paper shale) without apparent bioturbation (Fig. A1b; Koevoets et al., 2018, 2019) to very fine-grained burrowed distal delta front or lower shoreface deposits representing a prograding clastic wedge sourced from the west. The Upper Kimmeridgian Oppdalssåta Member consists in its lower part of up to medium-grained sandstone sandwiched between organic-rich mudstone. In the upper part and above a regionally correlative glauconite bed, the member shows gradually thinner sandstone beds, suggesting backstepping of a shoreline or delta. The Lower Volgian-Ryazanian Slottsmøya Member represents a return to organic-rich offshore marine mudstone but with a higher silt content than in the mudstone of the Lardyfjellet Member and with occasional occurrence of very fine-grained sandstone. Hammer et al. (2011) found seep carbonates just below and above the Jurassic-Cretaceous boundary (*Craspedites* and *Taimyroceras* ammonites from the Late Jurassic and *Surites* and *Bojarkia* from the Early Ryazanian), indicating seafloor seepage of biogenic or thermogenic hydrocarbons in the Late Volgian to Early Ryazanian.

The Paleogene transpression related to the Cenozoic North Atlantic Sea floor spreading and the Eurekan orogeny (Faleide et al., 2008; Piepjohn, 2016) had the greatest impact on the Mesozoic strata in western and southern Spitsbergen, where contraction from the west resulted in folding, overthrusting, and fracturing (Bergh et al., 1997; Braathen et al., 1999). In the study area, subsequent foreland basin subsidence assigned to the Central Tertiary Basin of more than 3 km (Helland-Hansen, 2010) coupled with a high geothermal gradient (Marshall et al., 2015) caused both mechanical and chemical compaction. Thereby, the Mesozoic sands were transformed to cemented tight sandstones, while the organic matter in the mudstones underwent maturation.

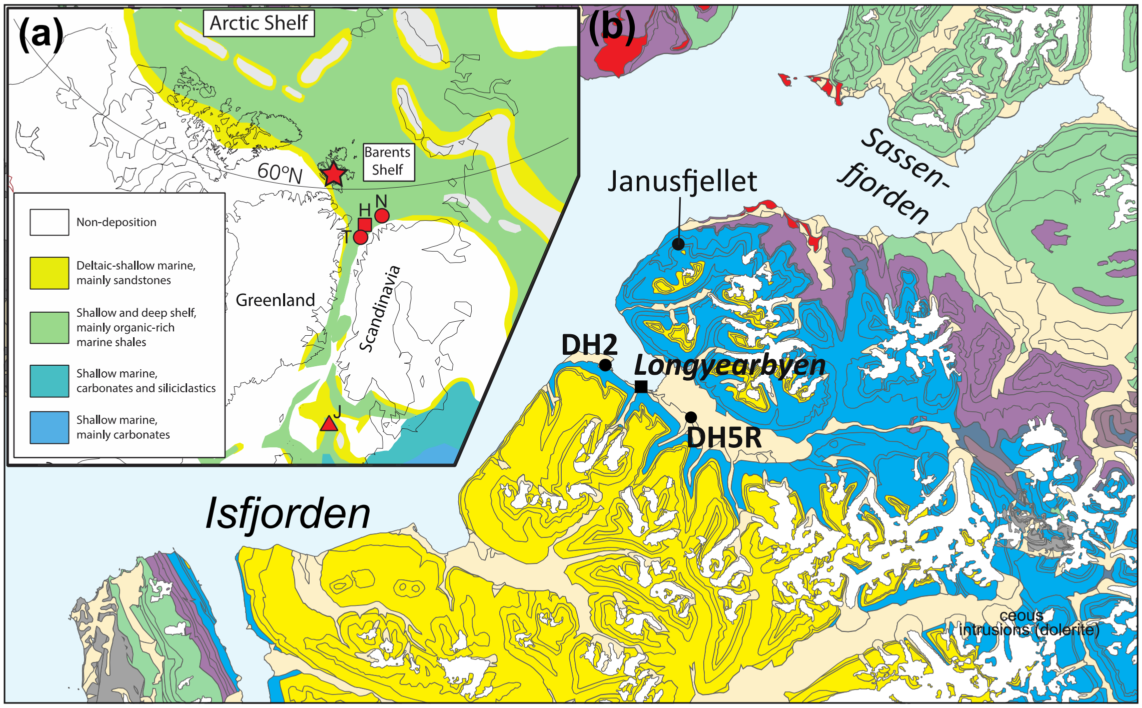

Fig. 2.1 (a) Paleogeographic map of the Boreal realm between Greenland and Norway at ~ 150 Ma (modified from Torsvik et al., 2002). Upper Jurassic black shales from Markey et al. (2017), Georgiev et al. (2017), and Georgiev et al. (2019) are marked by a red square, circles, and triangle (H: Hammerfest; N: Nordkapp; T: Troms III, J: Jæren High). (b) Map of Central Spitsbergen is marked by a red star in (a). Studied samples from drill cores, Dh2 and DH5R, are from the Agardhfjellet Formation, near Longyearbyen, Svalbard (modified from Koevoets et al., 2018, 2019). The outcrop of the Agardhfjellet Formation is located about 10 km north of the drill core sites (Janusfjellet).

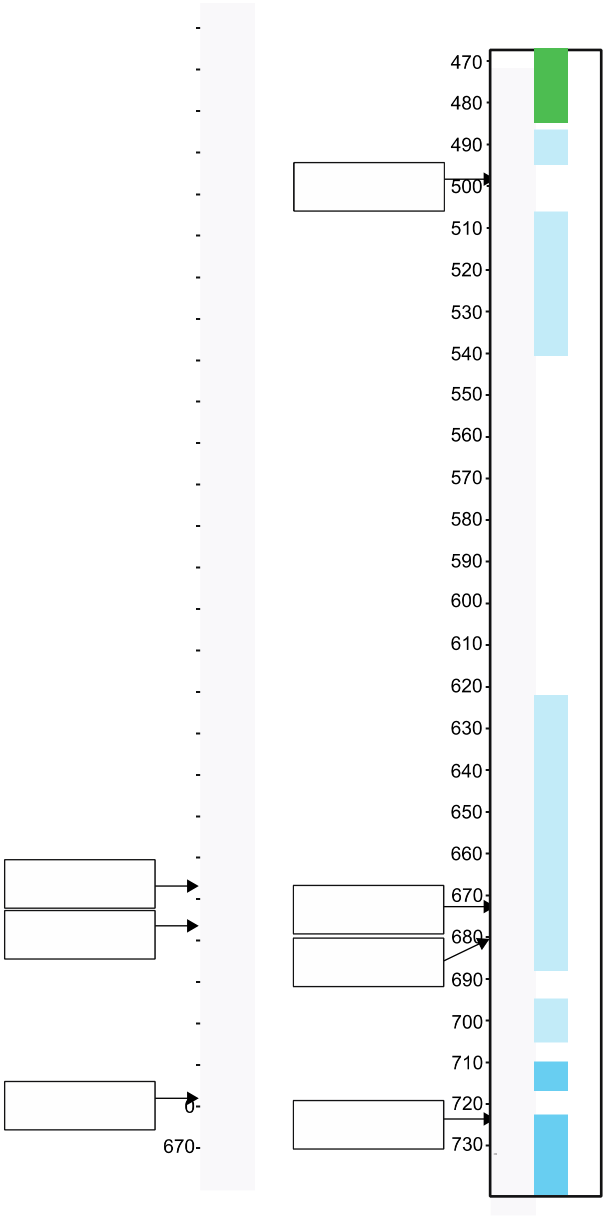

Fig. 2.2 Stratigraphical logs of the drill cores, DH2 and DH5R (modified from Koevoets et al., 2018, 2019) with ages of the stage boundaries from GTS 2020 on the right of the DH2 (Gradstein et al., 2020). Re-Os ages from ~ 10 or 20 cm intervals shown on the left side of each drill hole; arrows mark sampled drill core location. Lithology follows the legend in the upper left. The stage boundaries are derived from biostratigraphy (Koevoets et al., 2019).

2.4 Methods

Twelve black shale intervals from DH2 and DH5R were selected across all members of the Agardhfjellet Formation based on the following criteria: 1) elevated TOC contents, which leads to higher contents of Re and Os; and 2) constrained biostratigraphy, which could be compared with Re-Os radiometric ages, although some of the studied intervals lacked biostratigraphic details. The vertical thickness of the studied black shale intervals ranges from 8 to 20 cm. Black shale samples from these intervals were powdered by micro-drilling of <1 cm intervals for indurated shale or in a corundum mortar and pestle or an agate ball mill for partially shattered intervals (Fig. A1c and d). Each aliquot was treated using the analytic procedures described below.

2.4.1 TOC and HAWK pyrolysis

Source rock properties such as total organic carbon, hydrogen index (HI), oxygen index (OI), and thermal maturity (T_{max}) were acquired based on available hydrocarbon content (S1), remaining hydrocarbon productive potential (S2), and organic carbon dioxide from pyrolysis (S3) by the Hydrocarbon Analyzer with Kinetics (HAWK) system and Leco TOC C230 analyzer at GeoMark Research, Ltd., Humble, Texas, USA. Powder aliquots were treated with HCl to measure the amount of carbonate and eliminate carbonate from the powders.

2.4.2 Carbon and sulfur isotopes

$^{13}C/^{12}C$ of organic carbon and total $^{34}S/^{32}S$ isotopic ratios of the black shale samples were measured using Elemental Analyzer - Isotope Ratio Mass Spectrometry (EA-IRMS) at Iso-Analytical, UK, following their procedure for each element. Powder aliquots for carbon isotopes were decarbonized by 2 M HCl for 2 hours at 60 °C and 24 hours at room temperature. The isotope results are presented with the delta notation (δ) in permil (‰) variations relative to Vienna PeeDee

Belemnite – V-PDB for carbon and to Vienna Canyon Diablo Troilite – V-CDT for sulfur. Two sugar standards for organic C (IA-R005 and IA-R006) and two types of BaSO4 for S (IA-R061 and IAEA-SO-5) were monitored while the samples were measured for quality control. The standard deviations of the four reference materials were 0.05 and 0.09‰ for C (IA-R005 and IA-R006) and 0.12 and 0.11‰ for S (IA-R061 and IAEA-SO-5), respectively. Every fifth sample was measured twice (the average value is reported), with duplicates yielding reproducibility similar to the reference precision. Sulfur isotopes in black shale may represent pyritic sulfur isotopes with some amount of organic-bound sulfur, so we report $\delta^{34}S$ in the samples show $\delta^{34}S_{py}$ hereafter.

2.4.3 Re-Os analyses

The isotope dilution-negative thermal ionization mass spectrometry (N-TIMS) setup at the AIRIE Program at CSU was used for measuring the Re-Os isotopic ratio of powdered shale samples. Weighed shale powders of about 200 – 300 mg were mixed with ^{185}Re and ^{190}Os spikes and digested in CrO_3-H_2SO_4 in sealed Carius tubes in an oven for 48 hours based on the methods from Shirey and Walker (1995) and Selby and Creaser (2003). The following protocols are based on methods from Georgiev et al. (2018, 2019). The osmium from the samples was separated with chloroform and hydrobromic acid (HBr), and Os was micro-distilled with HBr twice for two hours each. The Re-bearing of CrO_3-H_2SO_4 residue was reduced by SO_2 gas. Rhenium in the reduced solutions was purified by anion chromatography following Yang et al. (2020). Analytes of Re and Os were loaded on platinum filaments for analysis by N-TIMS. Rhenium and Os were measured as ReO^{4-} and OsO^{3-} species, respectively. Corrections for isobaric oxygen interferences, instrumental mass fractionation, and analytical blank were conducted after the measurements with in-house Excel sheets. Uncertainties for Re and Os contents and isotopic ratios were determined by numerical error propagation, including weighing and blank correction. Measured Re and Os isotopic ratios were regressed using the Isoplot 4 package (Ludwig, 2012) and drawn by IsoplotR (Vermeesch, 2018).

2.5 Results

Table A1 shows all geochemical data from HAWK and stable isotopes, and Table A2 reports Re-Os results.

2.5.1 HAWK and TOC

Fig. 2.3 shows six key scatter plots with variables from the HAWK pyrolysis to evaluate source rocks. S1, S2, S3, and thermal maturity (T_{max}) were analyzed, and the hydrogen index (HI), oxygen index (OI), and production index (PI) were calculated from S1, S2, and S3. TOC varies from 0.7 wt.% to 11.7 wt.%, showing that the Oppdalen Member has lower TOC values and that the Lardyfjellet Member has higher TOC values than other members (Fig. 2.3 and 2.4). HI from the Lardyfjellet, Oppdalssåta, and Slottsmøya members range from 50 to 135, excluding the lowest value from a sulfide layer (DH5R 607.022 - 607.027 m; S = 20 wt.%). HI of the Oppdalen Member ranges from 19 to 43. OI from the upper three members ranges from 2 to 23, and that from the Oppdalen Member ranges from 6 to 46. T_{max} ranges from 439 to 473 °C. Based on these data, the Lardyfjellet, Oppdalssåta, and Slottsmøya members contain type III kerogens, while the Oppdalen Member contains type IV kerogens (e.g., Fig. 2.3f).

2.5.2 Carbon and sulfur stable isotopes

Fig. 2.4 presents box plots of each member for their C isotopic ratios from organic matter ($\delta^{13}C_{org}$) and sulfur isotopic ratios ($\delta^{34}S$). Studied intervals do not cover the whole section of the Agardhfjellet Formation, so box plots of each member broadly show the changes in the parameters through the formation. Each member shows distinct characteristics. The Lardyfjellet Member shows largest variations in $\delta^{13}C_{org}$ and $\delta^{34}S$, but the Oppdalssåta Member shows little variation because only two samples from this member were analyzed. The average sulfur isotopic composition in the Oppdalen Member is lighter (-36.75‰) than those in the other members (-30.78 – 8.83‰). The Lardyfjellet Member has much more variable $\delta^{34}S$ than the others (−30 to +10 ‰). The carbon isotopic ratios are less variable than the S isotopic ratios from the Oppdalen Member to the Oppdalssåta Member. However, $\delta^{13}C_{org}$ between the Oppdalssåta and Slottsmøya Members decreases by *ca*. 4‰.

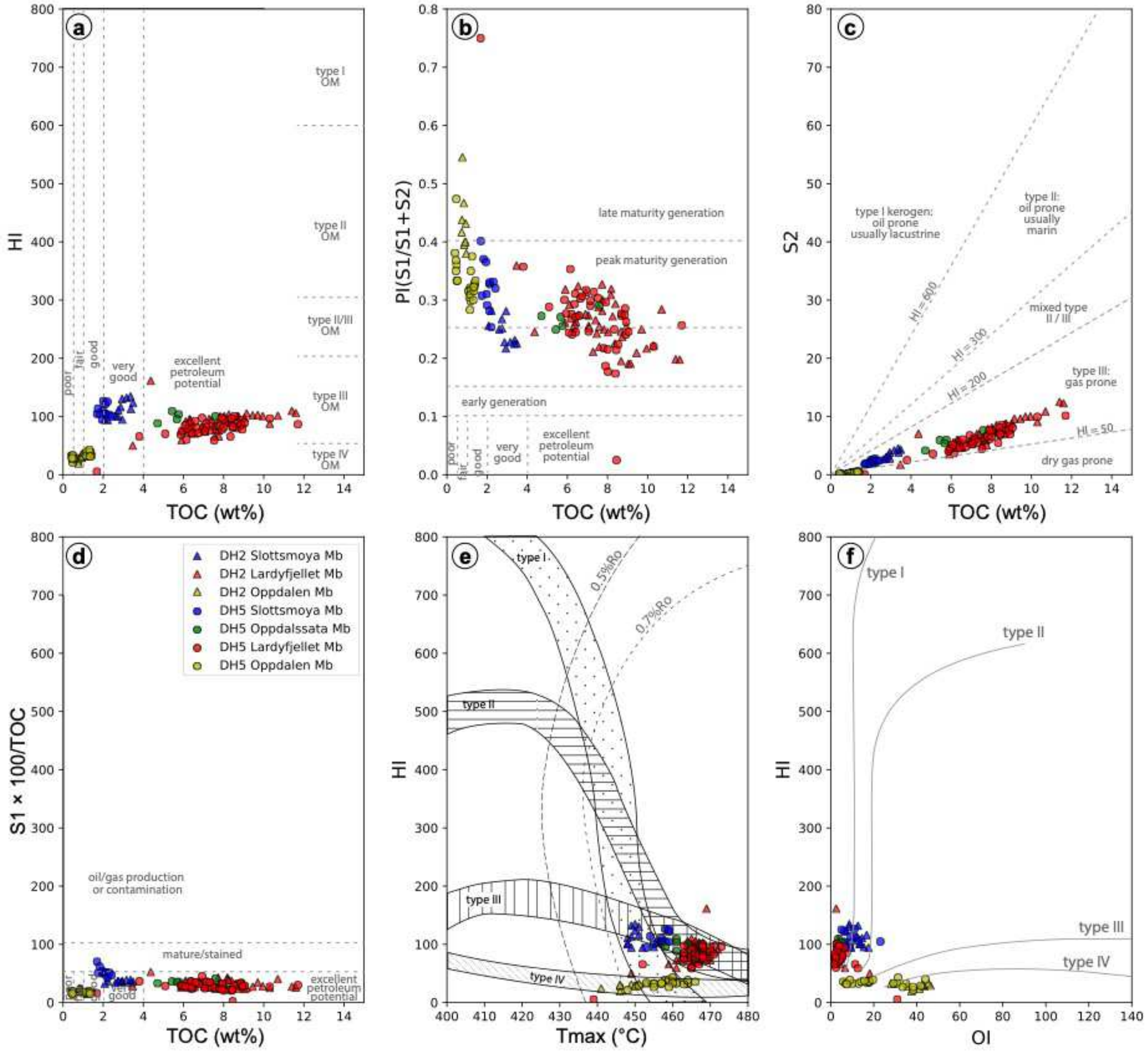

Fig. 2.3 Key x-y plots evaluating source rock and kerogen types in organic-rich black shales from DH2 and DH5R drill cores of the Agardhfjellet Formation. HAWK pyrolysis parameters include S1, S2, S3, T_{max}, and derivative ratios such as hydrogen index (HI, S2/TOC), oxygen index (OI, S3/TOC) production index [PI, S1/(S1+S2)]. Gray lines, dashed lines, and areas that indicate petroleum potential or kerogen types are derived from Georgiev et al. (2019). All members generally showed good source rock potentials with type III kerogen, excluding the Oppdalen Member, the lowermost member of the formation. Thermal maturity indicated by T_{max} in all four members is at the high end of the panel (e).

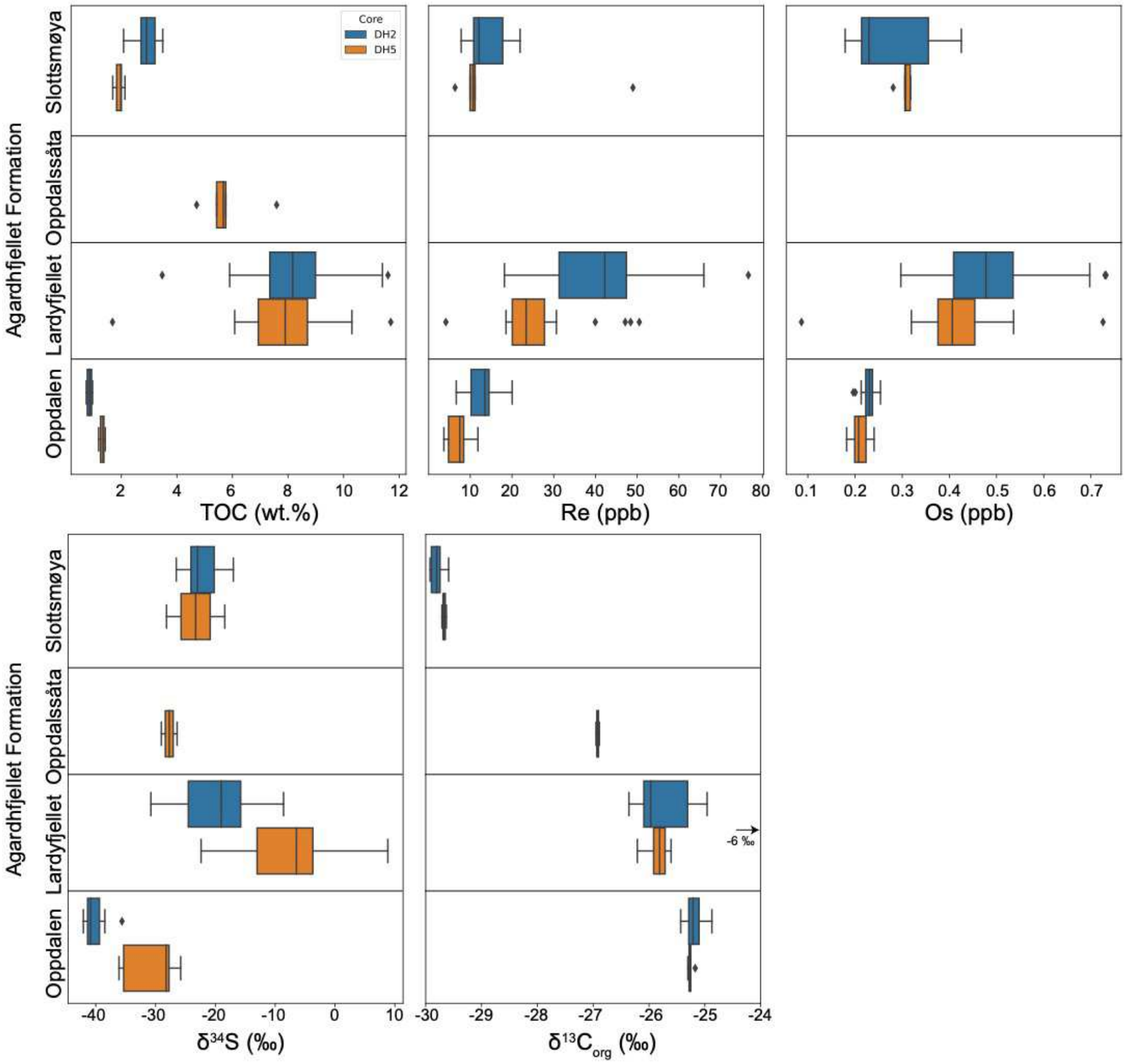

Fig. 2.4 Box plots of TOC, Re, Os, δ^{34}S, and δ^{13}C of each member from DH2 and DH5R drill cores. Outliers are plotted as black diamonds.

2.5.3 Re-Os isochrons

Rhenium and Os concentrations are presented in Fig. 2.4 with box plots for each member, excluding the Oppdalssåta Member. The Oppdalen Member shows relatively low Re and Os concentrations compared to the others, ranging from 3.68 to 20.0 ppb for Re and 0.182 to 0.255 ppb for Os. Rhenium and Os concentrations of the Lardyfjellet and Slottsmøya members range from 7.83 to 76.6 ppb for Re and 0.179 to 0.732 ppb for Os, excluding the lower values from the pyrite band in the interval DH5R 607.022 – 607.027 m (Re = 4.15 ppb and Os = 0.087 ppb).

Three shale intervals in DH5R (DH5R 607, DH5R 613, and DH5R 658 m) yield three isochrons (Fig. 2.5). In the Lardyfjellet Member, 16 cm and 11 cm shale intervals (DH5R 607.007 – 607.171 m, n = 8 and DH5R 613.667 – 613.780 m, n = 18) yield model 1 ages of 151.2 ± 4.3 Ma and 148.8 ± 4.9 Ma with initial Os_i values of 0.511 ± 0.028 and 0.502 ± 0.024, respectively. The DH5R 607 interval is younger than the DH5R 613 interval stratigraphically, but the nominal ages of the two intervals are in reverse order. Given that the ages overlap within their uncertainties, they were treated with Bayesian statistics (Ludwig, 2012) to refine the age information (discussed later). Twenty samples were analyzed from DH5R 613 m, generating a Model 3 age of 140.9 ± 6.7 Ma with an initial Os_i of 0.540 ± 0.034 (not shown here). We, however, excluded a sample and a duplicate of the sample (DH5R 613.695 – 613.705 m) because they had distinctly higher concentrations of trace elements compared with that in other samples in the same interval, possibly due to diagenesis or localized mineralization. An 18 cm interval from the Oppdalen Member (DH5R 658.012 – 658.190 m, n = 8) provided a Model 1 age of 160.3 ± 3.2 Ma with an initial Os_i of 0.3937 ± 0.0082.

Five shale intervals in DH2 (DH2 497, DH2 673, DH2 674, DH2 680, and DH2 724 m) produced four isochrons (Fig. 2.6). Eleven samples from the DH2 497 interval in the Slottsmøya Member, which is the uppermost and youngest interval from this study, provided a Model 1 age of 148.3 ± 7.2 Ma with Os_i of 0.529 ± 0.033. The uncertainty is relatively high, even though the MSWD is close to unity (0.76). This is probably because of the limited ranges of $^{187}Re/^{188}Os$ (203 – 373) and $^{187}Os/^{188}Os$ (1.04 – 1.46).

Three black shale intervals in the Lardyfjellet Member (DH2 673, DH2 674, and DH2 680 m) yield regressions: Model 1 age of 152.6 ± 2.8 Ma with Os_i of 0.458 ± 0.026 from six samples of DH2 673; Model 1 age of 149.1 ± 7.5 Ma with Os_i of 0.502 ± 0.053 from nine samples of DH2 674; and Model 3 age of 152.9 ± 9.0 Ma with Os_i of 0.486 ± 0.096 from 18 samples of DH2 680. The regression from DH2 674 presents a Model 1 age with an MSWD of 1.01, but a relatively limited range of $^{187}Re/^{188}Os$ and $^{187}Os/^{188}Os$ may contribute to high uncertainty. We combined 15 samples from both DH2 673 and 674 to generate a more precise age (Fig. 2.6b) because the two intervals are close (<1 m apart), and samples are in the same unit in terms of lithology (black shale) and chemostratigraphy ($\delta^{13}C_{org}$ and TOC; Koevoets et al., 2018). The combined samples yield a Model 1 age of 150.5 ± 2.4 Ma with Os_i of 0.489 ± 0.018, which is a more precise result that overlaps the regressions from DH2 673 and DH2 674 within uncertainties.

Eighteen samples of DH2 680 reveal two possible regression lines with similar slopes (ages) but different y-intercepts (Os_i; Fig. A2). This may imply rapid variation in seawater $^{187}Os/^{188}Os$ during the deposition of 16 cm of black shale (Xu et al., 2014; Georgiev et al., 2017), the effect of planetary cycles, such as eccentricity, obliquity, and precession (Matsumoto et al., 2021) and/or limited input from the open ocean due to basin restriction (Dickson et al., 2022). Most of the samples (13 out of 18) yielded a more precise Model 1 age of 149.3 ± 3.8 Ma with Os_i of 0.544 ± 0.041; thus, the more precise regression was selected as the representative age of this interval. Twelve samples of DH2 724 provided a Model 1 age of 159.1 ± 2.5 Ma with an initial Os_i of 0.335 ± 0.011, which is similar to the age of a stratigraphically corresponding interval, DH5R 658.

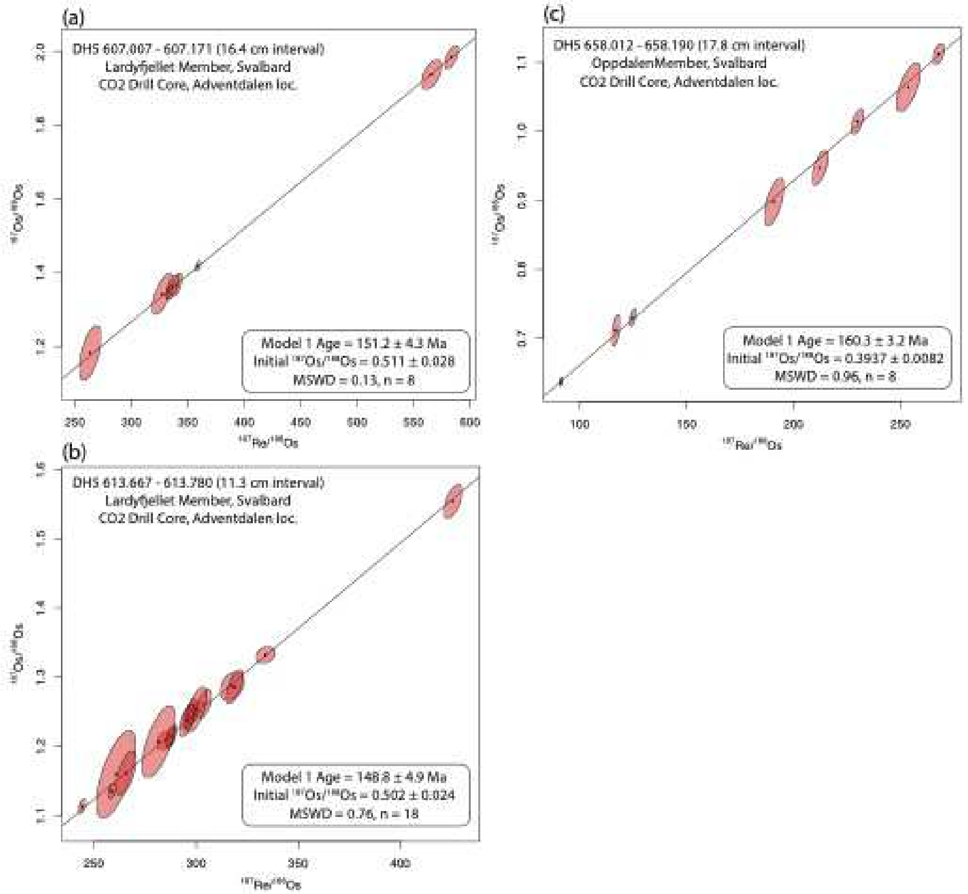

Fig. 2.5 Re-Os isochrons for three intervals from DH5R drill cores. All regression data were calculated by Isoplot 4.15 (Ludwig, 2012) and plotted by online IsoplotR (Vermeesch, 2018). Two regression models are available for the Re-Os method, Model 1 and 3 ages. Model 1 assumes that the data scatter is attributable to analytical uncertainties alone, but model 3 assumes that the scatter exeeds analytical uncertainties, and may be attributed to geologic causes, such as variation in ^{187}Os/^{188}Os of the samples analyzed. Uncertainties of ages and initial Os ratios are 2σ. MSWD is the mean square weighted deviation; generally, model 1 isochrons show MSWD close to unity. Individual points are in black dots, and red ellipses represent the uncertainties of data.

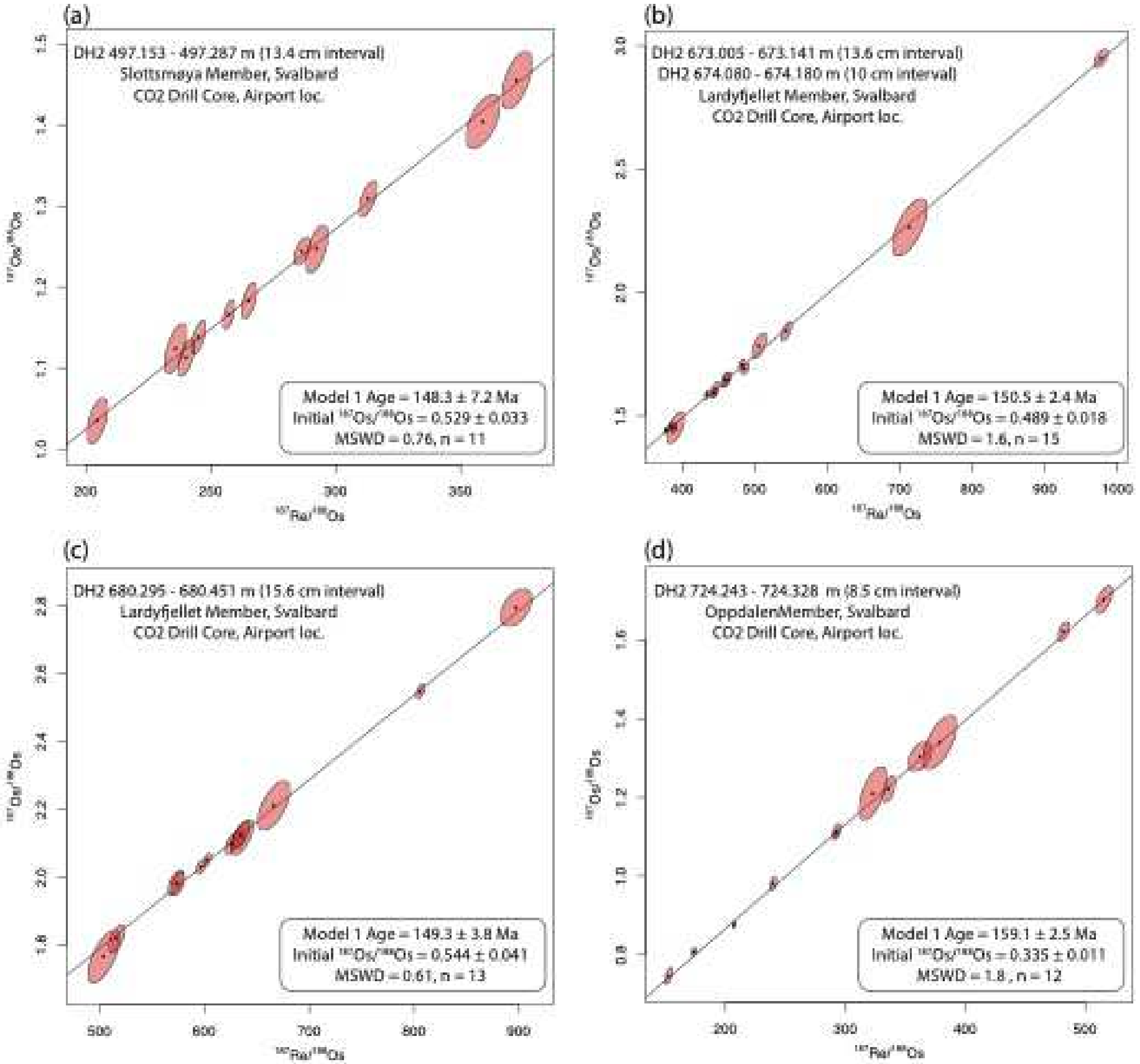

Fig. 2.6 Four Re-Os isochrons for five intervals from DH2 drill cores. Data from DH2 673 and DH2 674 are regressed together in (b) because they are in the same lithology and separated by only ca. 1 m. All descriptions are the same in Fig. 2.5.

2.6 Discussion

2.6.1 Depositional environments through source rock pyrolysis and stable isotope geochemistry

Upper Jurassic – Lower Cretaceous black shales are notably prolific source rocks in the North Atlantic (Norwegian Sea, Barents Sea, and North Sea, e.g., Mutterlose et al., 2003; Georgiev et al., 2017, 2019). While the source-rock formations have different names, such as the Kimmeridge Clay, Farsund and Mandal, Draupne, Tau, Spekk, Hekkingen, Bazhenov, and Agardhfjellet formations, they share key characteristics: elevated TOC contents (> 1 wt.%), deposition at high latitude (sub- and Boreal regions), and long depositional duration. Rogov et al. (2020) proposed a Late Jurassic – earliest Cretaceous shelf dysoxic/anoxic event (SDAE) in high latitudes, distinct from short-duration, ocean anoxic events (OAEs) that are typically synchronous across different basins and associated with carbon isotope excursions and major faunal turnovers (Rogov et al., 2020). Rogov et al. (2020) suggested increasing temperature, limited ocean circulation, enhanced productivity, and reduced salinity as possible causes for SDAEs.

The kerogen in the Lardyfjellet, Oppdalssåta, and Slottsmøya members is currently type III based on HI, S2, and TOC. The high thermal alteration of the Agardhfjellet Formation in Adventdalen (Koevoets et al., 2016; Abay et al., 2017; Ohm et al., 2019) suggests that almost all carbon of Type II kerogen have already been converted to oil and gas. As a result, the remaining kerogen being geochemically analyzed appears as Type III, i.e., black paper shale in the Lardyfjellet and Oppdalssåta members were originally composed of Type II kerogen during deposition. This is also consistent with a few visually analyzed samples from the two wells; the macerals in the siltier parts contain a high percentage of vitrinite-rich type III kerogen, whereas the black paper shales are rich in liptinitic type II (Ohm et al., 2019). A similar trend has also been published recently for the Hekkingen Formation (Cedeño et al., 2021). Geochemical studies of bitumen in the Mesozoic sandstones show that oil has been expelled and migrated from type II or combined II/III kerogen from the Agardhfjellet Formation (Abay et al., 2017).

The Oppdalen Member is dominated by type IV kerogen, different from other members (Fig. 2.4e). Also, low TOC in the Oppdalen Member may indicate well-oxygenated waters or low productivity. TOC in the Lardyfjellet Member is higher than in other members, which may indicate better preservation and/or higher productivity, combined with lower content of silt, which dilutes organic matter in the other members. Samples from the Oppdalen Member plot in the type IV area and are more dispersed than those from other members, but low S2 peaks from the Oppdalen Member may not lend credence to the validity of T_{max} (Peters, 1986).

Vigorous bioturbation and pyrolysis data above of the Oppdalen Member imply enough oxygen to sustain life in the sediment (Fig. A1), where it may have been shallower than the storm wave base, resulting in oxygenated bottom water (Koevoets et al., 2018). On the other hand, the narrow ranges and lower $\delta^{34}S_{py}$ values in the Oppdalen Member (- 42‰ to - 36‰ in DH2 724 and - 36‰ to - 26‰ in DH5R 658) could be the result of a persistent euxinic pool which can precipitate pyrite (Sageman and Lyons, 2003). The main factors controlling $\delta^{34}S_{py}$ are the precipitation of pyrite in the euxinic water column (syngenetic pyrite) and bacterial sulfate reduction (BSR; biogenetic pyrite) in the water column or sediment pore fluids (Lyons et al., 2009). The sulfate-reducing bacteria prefer ^{32}S to ^{34}S when fixing sulfur in pyrite (Jones and Starkey, 1957; Harrison and Thode, 1958). Also, lower $\delta^{34}S_{py}$ values may suggest an adequate connection between the depositional basin and the open ocean, which continuously supplies sulfate with seawater isotopic composition as the local sulfur budget is tapped for pyrite deposition (Lenniger et al., 2014). Therefore, based on low TOC and type IV kerogen, we may assume that the depositional environment was oxygenated and close to the landmass while sediments and OM of the Oppdalen Member were deposited, and its burrows were generated. Then, a euxinic pool developed at the same location, depositing the sediments and OM of the Lardyfjellet Member. In the initial stages of this euxinic pool development, pyrite was precipitated in the existing burrows within the Oppdalen Member (Fig. A1).

In the Lardyfjellet Member, $\delta^{34}S_{py}$ is higher than in the Oppdalen Member. The values of $\delta^{34}S_{py}$ fluctuate not only throughout the members but also within individual sample intervals; in particular, the DH5R 600 and 607 intervals show *ca*. 30‰ variation in $\delta^{34}S_{py}$ (Fig. A3). Fluctuating $\delta^{34}S_{py}$ profiles in the Lardyfjellet Member may indicate that anoxic/euxinic status was not continuously maintained throughout deposition or that BSR was impeded by rapid sediment accumulation (Sageman and Lyons, 2003). As Lenniger et al. (2014) called attention to the positive excursion of $\delta^{34}S_{py}$ at the onset of OAE2, an overall increase in $\delta^{34}S_{py}$ within the Lardyfjellet Member may indicate the beginning of the SDAE. The higher values of $\delta^{34}S_{py}$ from the OAE2 were explained by relatively high sedimentation rates within their studied samples (~ 2 cm/ky), which may have limited the proliferation of sulfate-reducing bacteria (Lenniger et al., 2014). Similarly, episodic high sedimentation rates may have occurred during the deposition of the Lardyfjellet Member. Alternatively, if the depositional basin were restricted, the $\delta^{34}S_{py}$ of syngenetic pyrite could increase. The sulfur isotopic ratios in sediments are affected by numerous controlling factors, such as reservoir properties and prokaryotic reaction pathways (Lyons et al., 2009). Therefore, a more detailed interpretation of the sulfur isotope data should be paired with further studies of the trace metal concentrations or additional isotope data for the Agardhfjellet Formation.

The $\delta^{13}C$ values in the Oppdalen, Lardyfjellet, and Oppdalssåta members are slightly lower (by ~ 2‰), consistent with gradual decreases prior to the Volgian Isotopic Carbon Excursion (VOICE) observed in other sections (Hammer et al., 2012; Jelby et al., 2020). Unfortuantely, finer details for our profile are unavailable because of sampling gaps between the studied intervals. In the Slottsmøya Member, $\delta^{13}C$ is significantly lower than in other members (by *ca*. 4‰), consistent with the observed VOICE. A distinct negative organic carbon isotopic excursion (CIE) was detected from the Volgian organic-rich shale around the circumpolar sites (Galloway et al., 2020, and references therein). Galloway et al. (2020) reviewed VOICE, evaluating possible causes. Volcanism, such as a large igneous province (LIP), is regarded as a common cause of negative CIE even though numerous determining factors affect carbon isotope changes (Kump and Arthur, 1999). Recorded volcanism around the J-K boundary includes the submarine Shatsky Rise in the northwest Pacific Ocean at *ca*. 145 Ma (Mahoney et al., 2005). Rakocinski et al. (2018) reported elevated Hg levels towards the top of the Slottsmøya Member (cf. Hammer et al., 2019), possibly indicating increased volcanism. This could be a cause of C isotopes fluctuations in the Volgian, but the causal link between the Shatsky Rise and the VOICE remains uncertain because of the overall paucity of precise absolute ages around the J/K boundary (Vennari et al., 2014; Lena et al., 2019). Also, initial Os ratios in this study do not record specific volcanic signals (discussed further below). Basaltic magmas of the High Arctic Large Igneous Province, which were likely emplaced during two major pulses at 120 – 130 Ma and 95 – 100 Ma (Kingsbury et al., 2018), are too young to have affected the Volgian global carbon cycle. Galloway et al. (2020) concluded that the VOICE could be interpreted as carbon isotopic signals from an isolated depositional Boreal basin caused by either low global sea level or conventional volcanic disturbance from the Shatsky Rise.

2.6.2 Correlation of the Boreal and Tethyan ammonite zones through the Agardhfjellet Formation

Ammonites are among the most widespread fauna from the Jurassic and are used to define the biostratigraphic zones. Ammonites can be highly provincial, however; in the Middle Jurassic to Early Cretaceous, tens of provinces prevailed (Page, 1999), sharply limiting global correlations. Here, we attempt to connect biozones between the Boreal and Tethyan realms in the Middle to Late Jurassic with radiometric ages.

A constant initial $^{187}Os/^{188}Os$ ratio through an interval of shale selected for dating is fundamental to acquiring precise isochrons and ages (e.g., Stein and Hannah, 2015). Recent studies argue that $^{187}Os/^{188}Os$ in the water column could vary due to astronomical cyclicity or distinctive sediment input into a restricted basin, which may consequently alter the balance between the radiogenic and unradiogenic input to the basin (Matsumoto et al., 2021; Dickson et al., 2022). Matsumoto et al. (2021) point out that initial $^{187}Os/^{188}Os$ ratios within a 2-m interval oscillate cyclically, concluding that the 405 kyr eccentricity cycle may play a critical role in periodic $^{187}Os/^{188}Os$ changes in seawater. Furthermore, $^{187}Os/^{188}Os$ in the Middle to Late Eocene Arctic Ocean varied markedly over a 12-Myr interval, reflecting the strong contrast between hydrothermal input from rifting and limited input from the open ocean (Dickson et al., 2022). The lower precision of the two regression lines from DH2 680 may be the result of similar Os_i variations. Nevertheless, seven intervals from DH2 and DH5R yielded Model 1 ages (Fig. 2.5 and 6). Because the stratigraphic order of the intervals is known, and reversed ages are within uncertainties (DH5R 607 and DH5R 613; DH2 673 + DH2 674 and DH2 680), the ages and uncertainties can be refined by the Bayesian method. To refine the ages of this study further, we added published ages, which show the stratigraphic order by ammonite zones (Fig. 2.7). Details on the application of Bayesian statistics to radiometric ages are found in Ludwig (2012) and Xu et al. (2014). The ages refined by Bayesian statistics will be discussed below (Fig. 2.7 and 2.8).

The Oppdalen Member was deposited during the Early Bathonian to Late Oxfordian over *ca*. 14 Myr based on geochronology, paleontology, and sedimentology studies (Koevoets et al., 2018, 2019). *Cardioceras* sp., representing the Early Oxfordian, and *Cadoceras* sp., representing the late Bathonian to early Callovian, were found in the upper part of the member (DH2 706) and the lower part of the member (DH2 724), respectively (Koevoets et al., 2019). In addition, *Kepplerites (Seymourites) svalbardensis* was found in DH5R 663 m, which is related to *Cadoceras calyx*, corresponding to the Late Bathonian (Koevoets et al., 2019). Our refined age results from the Oppdalen Member are 159.2 + 1.9/- 1.6 Ma from DH5R 658 and 160.1 + 2.0/- 1.7 Ma from DH2 724 (Fig. 2.7), which would fall in the early Oxfordian in GTS 2020 (Hesselbo et al., 2020). These ages are in general agreement with previous Re-Os ages for Oxfordian strata (Georgiev et al., 2017, 157.7 ± 1.39 Ma) and with Kamo and Riccardi (2009), and Briguad et al. (2021) ages from Fig. 2.7 (164.65 ± 0.20 Ma and 163.5 ± 6.0 Ma, respectively). However, biostratigraphy of the DH2 724 and DH5R 663 core depths indicates a Late Bathonian to Early Callovian age for these intervals (Koevoets et al., 2019). However, the latest GTS chart issued in June 2023 reported 161.5 Ma as the Callovian-Oxfordian stage boundary (Cohen et al., 2013; updated), which allows the ages of this study to fall in the late Oxfordian. Considering the uncertainties associated with the two ages from DH5R 658 and DH2 724, these intervals might represent a time frame extending from the late Callovian to early Oxfordian. The newest GTS aligns more closely with the biostratigraphy and radiometric ages than it does with GTS 2020. Nevertheless, there is still a slight disagreement between biostratigraphy and radiometric ages.

Two possible scenarios may explain this inconsistency between the two methods. First, the timing of the system closure may be postponed by specific depositional characteristics, such as a hiatus or low sedimentation rate. The sediment and pore waters must be closed to exchange with the water column in order to activate the Re-Os time clock (Stein and Hannah, 2015). The Oxfordian hiatus was present in the northern hemisphere, but its onset may have been diachronous across different locations (Brikiatis, 2023). The hiatus ended at ~ 160 Ma, which is the top of the *Cordatum* zone or the top of *C. tenuiserratum* zone (Koevoets et al., 2018; Brikiatis, 2023). The ages from DH2 724 (160.1 Ma) and DH5R 658 (159.2 Ma) mark the onset of deposition after the Oxfordian hiatus. As we mentioned earlier, vigorous bioturbation was found by CT scans (Fig. A1a), indicating enough oxygen to support life at some points during or shortly after the deposition These factors may have delayed the Re-Os time clock for some unknown time after deposition.

Alternatively, the *Cadoceras* sp., identified at DH2 724, may have had a longer range than previously assumed, continuing into the Early Oxfordian. Because of the lack of radiometric ages from the Tethyan ammonite zones, we cannot correlate ammonite zones between the Boreal and Tethyan realms one-to-one, but the radiometric ages of this study could be used as steppingstones to a link the two realms in future studies.

Four ages from the Lardyfjellet Member (149.4 + 1.8/- 1.7 Ma, 150.3 + 1.6/- 1.6 Ma, 150.8 + 2.1/- 1.7 Ma, and 151.4 + 2.2/- 2.4 Ma, Fig. 2.7) were identified within the Lower Kimmeridgian. *Amoebites* sp., *Amoebites spathi*, *Amoebites* cf. *pingueforme*, and *Amoebites* cf. *subkitchini* were found at DH2 666 and DH2 679 (Koevoets et al., 2019), all within the *Rasenia cymodoce* zone (Fig. 2.7). Our age results suggest that the ammonite zone by *Rasenia cymodoce* Zone spanned nominally 2.3 Myr but, given uncertainties, may have lasted up to about 5.7 Myr. Selby (2007) provided 154.1 ± 2.2 Ma of the Re-Os ages in the lowermost part of the *Pictonia baylei* zone, which is consistent with our results. Georgiev et al. (2017) reported Re-Os ages of 157.7 ± 1.2 Ma and 150.2 ± 5.01 Ma from the *Aspidoceras hypselum* and *Hybonoticeras beckeri* ammonite zones, respectively. The younger age, 150.2 ± 5.01 Ma, is older than one of the ages from the Lardyfjellet Member of this study, but given the high uncertainty of the age, it could be consistent with other ages.

In the Volgian, Koevoets et al. (2019) found *Laugeites* sp. at the DH2 507 level, which is 10 m below the uppermost interval of this study, DH2 497. The Bayesian-refined age of DH2 497 is 146.8 +0.2/-4.5 Ma, indicating the Late Volgian. Several ammonite zones, including *Epilaugeites vogulicus*, *Craspedites okensis*, *Craspedites taimyrensis*, or *Chaetaites chetae*, are probable, but no ammonite species have been identified yet in or above the interval, DH2 497 (Fig. 2.7). The U-Pb age of *Substeueroceras koeneni* ammonite zone in the Andean realm, which overlaps the *Berriasella jacobi* and *Protacanth. andraeai* zones in the Tethyan realm, was reported as 142.039 ± 0.058 Ma (Lena et al., 2019). We used this U-Pb age as an upper bracket of our Re-Os age in the Volgian because of the nominal ages, but it should be refined further with specific ammonite zones or more precise radiometric ages. Lena et al. (2019) also analyzed ash beds just above the Kimmeridgian-Tithonian boundary in the La Yesera sediment section, Argentina, within the *Virgatosphinctes andesensis* ammonite zone in the Andean realm, which is equivalent to the *Hybonoticeras hybonotum* Zone in the Tethyan (Martínez et al., 2018). The U-Pb zircon age for the ash layer is 147.112 ± 0.078 Ma (Lena et al., 2019).

Considering the substantial uncertainty in the interval DH2 497 from the Slottsmøya Member, excluding limited ranges of ^{187}Re/^{188}Os and ^{187}Os/^{188}Os mentioned above, the possibility of oil seepage needs to be considered. Seep carbonates have been found in the upper parts of the Slottsmøya Member (Hammer et al., 2011), suggesting the presence of migrated hydrocarbon that may have disturbed the Re-Os geochemistry by homogenization of *in situ* organic matter with migrated petroleum (Selby and Creaser, 2005; Lillis and Selby, 2013). However, recent experimental studies have demonstrated that the transfer of Re and Os (and their isotopic ratios) between source rocks and oils is limited, with more than 95% of Re and Os remaining in the source rock (Rooney et al., 2012; Cumming et al., 2014). Moreover, Georgiev et al. (2019) have argued against the significant transfer of Re and Os between source rock and oils based on natural samples from the Brynhild field, Norwegian Barents Sea. Thus, the large uncertainty associated with DH2 497 could be attributed solely to the limited ranges of $^{187}Re/^{188}Os$ and $^{187}Os/^{188}Os$.

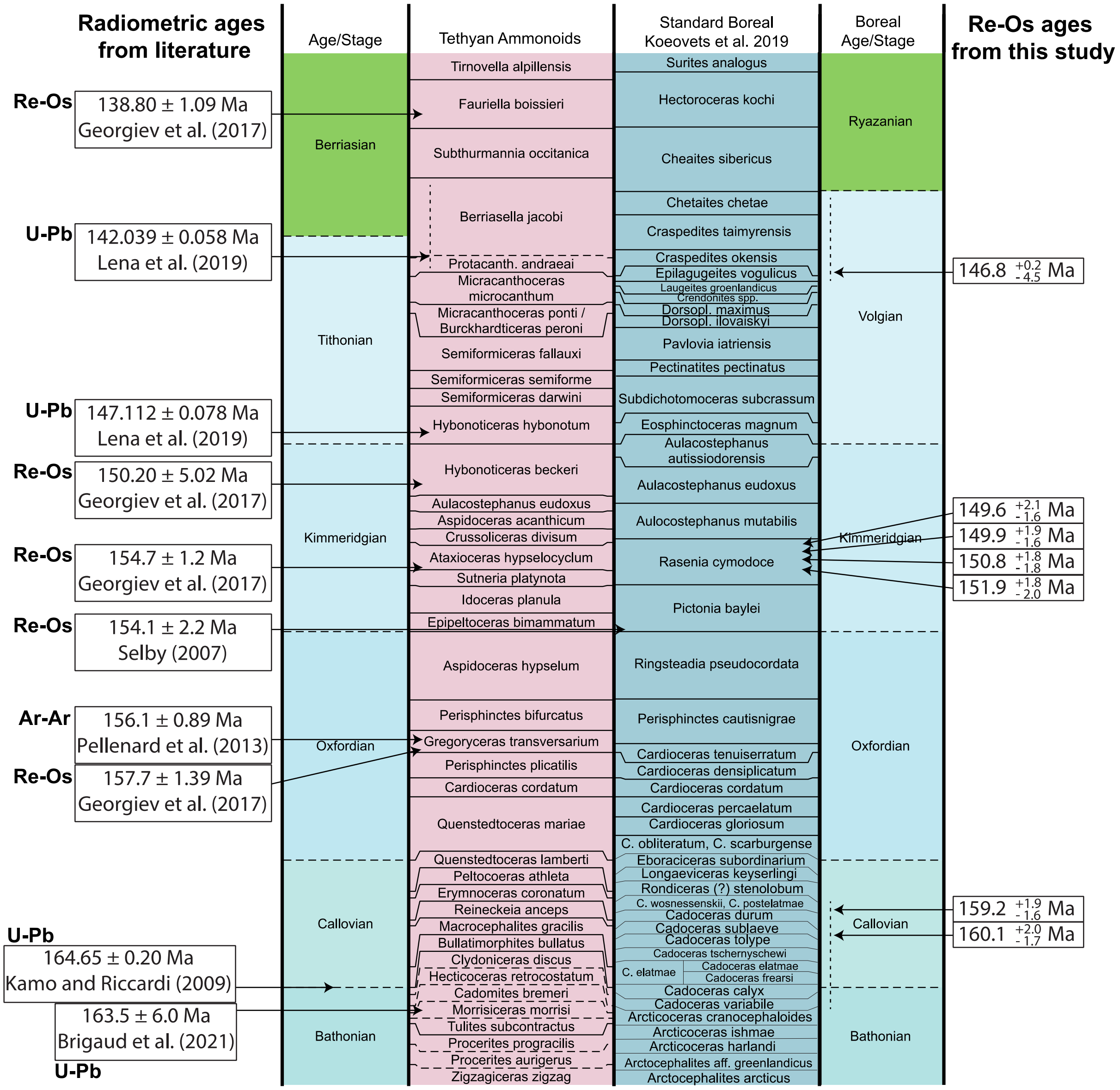

Fig. 2.7 Tethyan and Boreal ammonite biostratigraphy with stages and radiometric ages from literature (left) and this study (right). U-Pb ages (Kamo and Riccardi, 2009; Lena et al., 2019; Brigaud et al., 2021), an Ar-Ar age (Pellenard et al., 2013), and Re-Os ages (Selby, 2007; Georgiev et al. 2017) are presented here. Re-Os ages from this study were refined by Bayesian statistics. Vertical dashed lines indicate possible zones where the dated intervals may come from because specific species have not been determined yet (Koevoets et al., 2019). Ammonite zones and stages are created by TSCreator version 8.0, modified by adding Bathonian and Callovian Boreal ammonite zones from Koevoets et al. (2019).

2.6.3 Os$_i$ and Sr isotope chemostratigraphy

The initial ^{187}Os/^{188}Os ratios, also known as initial Os or Os$_i$ values, of black shales can be determined through Re-Os isochrons. These ratios represent the ^{187}Os/^{188}Os ratios of seawater at the time of sediment deposition (Stein and Hannah, 2015). As such, the initial ^{187}Os/^{188}Os ratio in shales is indicative of global changes in the initial Os isotopic composition of seawater because of the rapid global ocean circulation (thermohaline circulation; 1 kyr) relative to the residence time of Os in the ocean (10-40 kyr). Therefore, chemostratigraphy based on Os isotopic data, like that of Sr isotopic data, is used to correlate sediment records in order to establish the global time scale (Peucker-Ehrenbrink and Ravizza, 2020). Like Sr isotopic ratios, Os isotopic ratios depend on the balance between radiogenic detrital input and unradiogenic (volcanogenic or cosmogenic) input of Os to the ocean. These two endmembers have contrasting Os isotope ratios: ~0.127 for the unradiogenic input from hydrothermal fluids, volcanic input, or cosmic dust, and much higher values (1.26 – 1.4) for radiogenic input from continental detritus or dissolved riverine Os (Peucker-Ehrenbrink and Ravizza, 2000; Cohen, 2004 Stein and Hannah, 2015).

In Fig. 2.8, we integrated our age and Os$_i$ data from the Agardhfjellet Formation with previously published data from the Middle Jurassic to Early Cretaceous Boreal realm sediments (Cohen et al., 1999; Selby, 2007; Georgiev et al., 2017, 2019; Markey et al., 2017; Tripathy et al., 2018), including global Sr isotopic ratio data during the same period (McArthur et al., 2020). Overall, initial Os ratios from this study are consistent with the previous studies, showing a gradual increase in initial Os ratios from a minimum value of 0.335 ± 0.011 at approximately 160 Ma – one of the lowest reported ratios throughout the Phanerozoic – to 0.651 ± 0.059 at *ca.* 139 Ma (Georgiev et al., 2017). Wierzbowski et al. (2017) attributed the lowest ^{87}Sr/^{86}Sr ratio through Phanerozoic time ($\sim$ 0.7068) in the Oxfordian ($\sim$ 160 Ma) to mantle-derived input to the ocean, likely due to increased hydrothermal activity during the breakup of Gondwana. In addition, low temperatures during the Late Callovian to Early Oxfordian (~ 160 Ma) may have reduced continental runoff (Dromart et al., 2003). It is likely that the minimum $^{187}Os/^{188}Os$ around 160 Myr ago, like the minimum Sr isotopic ratio at that time, resulted from increased input from the hydrothermal activity and decreased input from continental weathering.

The lowest reported values of initial Os during the Phanerozoic (0.29 ± 0.03 at 379.0 ± 7.1 Ma; Harris et al., 2013, 0.15 ± 0.12 at 207 ± 12 Ma; Cohen et al., 1999, and 0.33 ± 0.02 at 91.5 ± 8.6 Ma; Selby et al., 2009), are chronologically linked to ocean anoxic events (OAEs), including the Frasnian-Famennian (F-F OAE), Toarcian (T-OAE), and Cenomanian-Turonian OAE2, respectively. Previous studies on the F-F OAE and T-OAE suggest that the minimum Os_i values in the F-F and Toarcian seawater could be attributed to higher input from unradiogenic materials, such as hydrothermal activity and/or ultramafic sources or lower input from continental runoff (Cohen et al., 1999; Harris et al., 2013). On the other hand, the Caribbean LIP is considered the cause of the minimum Os_i value during OAE2 (Selby et al., 2009). Additionally, the minimum initial Os values may also indicate meteorite impacts, although the negative excursions in Os isotopes caused by extraterrestrial material are short-lived (Ravizza and VonderHaar, 2012; Paquay et al., 2014). These events share common characteristics of climatic disturbance, and thus the minimum initial Os_i values may serve as a reliable indicator of such disturbances throughout the Earth's history. The minimum Os_i value observed in this study is associated with the onset of the SDAE, which may have been triggered by high input from unradiogenic sources (hydrothermal activity or weathering of ultramafic rocks) and low continental runoff in the early Late Jurassic, leading to climatic disturbance and the start of the SDAE.

One intriguing feature that sets the SDAE apart from the OAE is its longer duration, lasting approximately 19 Myr compared to less than 1 Myr for OAEs (Rogov et al., 2020). The extended period of black shale deposition observed in the studied section is unique and distinct from other anoxic events during the Mesozoic and Cenozoic. The Paleozoic ferruginous ocean has been proposed to cause longer OAEs lasting approximately 3 million years, including the F-F OAE that started with a minimum low Os ratio (Reershemius and Planavsky, 2021). Ferruginous conditions can enhance benthic phosphorus (P) retention under an anoxic ocean, which can boost primary productivity (Reershemius and Planavsky, 2021). The enhanced P retention under an anoxic ocean may play one of critical roles in the longer period of the SDAE in the Agardhfjellet Formation, while high primary productivity has not been observed. Although the specific environmental factors responsible for prolonging the SDAE are currently unknown, it is hypothesized that enhanced primary productivity in the Boreal realm during the Late Jurassic might have played a role in prolonging the development of anoxic events. Further geochemical investigations of the SDAE may provide more insight into the duration of such events. For example, redox-sensitive trace elements, such as Mo, U, Re, etc., can provide the redox condition or depositional environment (e.g., Tribovillard et al., 2006).

The increasing trend of Os_i during the Late Jurassic could result from higher radiogenic Os input by continental weathering. Accelerated continental weathering may have been caused by a warmer climate during the Toarcian-OAE. The warmer climate, in turn, may have been the result of some combination of methane release from gas hydrate dissociation or terrestrial permafrost thaw, or the introduction of greenhouse gases by magmatism, especially if organic-rich sedimentary sections are intruded. (Hesselbo et al., 2000; Beerling et al., 2002; Cohen et al., 2004; Svensen et al., 2007; DeConto et al., 2012). Cohen et al. (2004) also noted that during a short period (~ hundred thousand years) with a negative carbon isotope excursion, there was an increase in $^{187}Os/^{188}Os$ and $^{87}Sr/^{86}Sr$ due to warmer temperatures, which provoked higher continental weathering (Gaillardet et al., 1999). This abrupt climatic change resulted in mass extinction (Harries and Little, 1999). In contrast, the prolonged climatic change during the SDAE (~ 14 Myr) might have given the biota enough time to adapt to climate change, possibly explaining the absence of a significant mass extinction event during the Late Jurassic (Tennant et al., 2017).

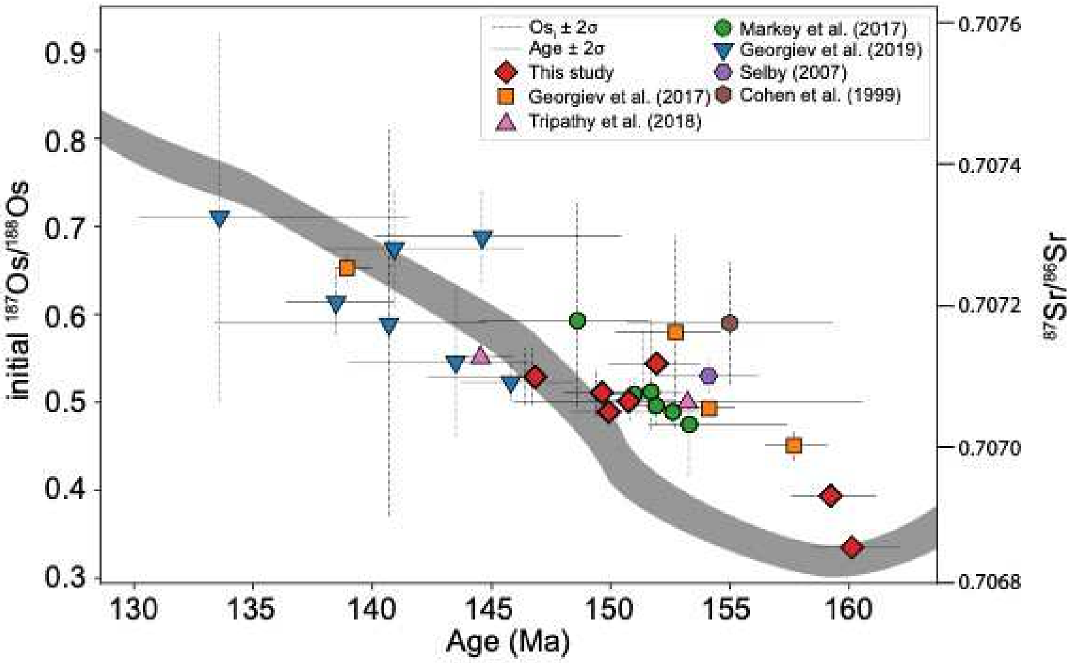

Fig. 2.8 Initial $^{187}Os/^{188}Os$ ratios from this study (red diamonds) and previous studies with the trends of marine $^{87}Sr/^{86}Sr$ in gray line (McArthur et al., 2020). Age uncertainties from Markey et al. (2017), and Georgiev et al. (2017, 2019) were treated by using Bayesian statistics in their studies (black lines). Uncertainties in the initial Os ratio are represented by black dashed lines.

2.7 Conclusion

The decreasing trend of $\delta^{13}C_{org}$ through the Oppdalen, Lardyfjellet, and Oppdalssåta Members, indicating a gradual increase in temperature, and the negative carbon isotope excursion in the Slottsmøya Member, are both consistent with the Volgian Isotopic Carbon Excursion (VOICE) in the Boreal basins. Low TOC and type IV kerogen indicate oxygenated bottom water, but the unchanging light $\delta^{34}S_{py}$ values in the Oppdalen Member support persistent anoxic/euxinic environments. The black shales of the Lardyfjellet Member with fluctuating and higher $\delta^{34}S_{py}$ values represent an unstable anoxic/euxinic condition or rapid sediment accumulation rate. These black shales yielded seven new Re-Os radiometric ages between 160.1 Ma and 146.8 Ma. While the radiometric ages do not perfectly match the Boreal ammonite zones and Tethyan zones, the new geochronology provides a foundation for correlating the Boreal realms with other Upper Jurassic sections. Initial $^{187}Os/^{188}Os$ ratios derived from the isochrons show a gradually increasing trend from a remarkably low value of 0.335 to ca. 0.529 with time; these fit well with trends revealed by previous Re-Os studies in the Boreal realm and the well-established Sr isotopic ratio profile. In addition, the gradual increase of Os_i is likely caused by increased continental runoff or decreased hydrothermal activity during the Late Jurassic. However, further research on the Late Jurassic is necessary to resolve the enigma of the extended duration of black shale deposition throughout the shelf dysoxic/anoxic event (SDAE) in the Boreal realm.

Chapter 3 Project II

Paleoenvironment in the circum-Arctic region during the Middle to Late Jurassic through trace element and stable isotope geochemistry of the Agardhfjellet Formation, Svalbard

3.1 Summary

In the Middle Jurassic to Early Cretaceous period, abundant black shale layers from the Agardhfjellet Formation were deposited in association with shelf dysoxic-anoxic events (SDAEs) recorded predominantly in the circumpolar regions. Generally, oceanic anoxic events (OAEs) throughout Earth's history are linked to the emplacement of large igneous provinces (LIPs); OAEs and LIPs alone or jointly are known to have triggered severe biotic crises in Earth's history. However, the causes of SDAE remain uncertain. This study aims to elucidate the geochemical features of the Upper Jurassic Agardhfjellet Formation using trace element concentrations and stable isotope ratios. The Agardhfjellet Formation formed during ~13 Myr of prolonged anoxic and euxinic conditions, which consists of the Oppdalen, Lardyfjellet, Oppdalssata, and Slottsmoya Members in the ascending order. The onset of oceanic anoxia was between the deposition of its Oppdalen and Lardyfjellet members. The extent of the anoxia varied within the Lardyfjellet Member but likely persisted until the Slottsmøya Member deposition. The depositional basin was highly restricted during anoxic periods, as indicated by Mo/TOC and Mo_{EF}/U_{EF} ratios in the sedimentary rocks. Enhanced continental runoff marked the Oppdalen and Slottsmøya Members, contrasting with the Lardyfjellet Member, which was dominated by authigenic minerals. Compared to other OAEs, such as the Toarcian OAE (184 Ma) or the OAE2 (94 Ma), the Late

Jurassic – Early Cretaceous SDAE, recorded in the Agardhfjellet Formation, is characterized by long-lasting suboxic–anoxic condition, substantial water-mass restriction, and increased continental runoff. The long-lasting SDAE in the Agardhfjellet Formation was predominantly controlled by local hydrographic restriction/isolation rather than widespread ocean anoxia.

3.2 Introduction

Anthropogenic global warming from fossil fuel consumption has contributed to the progressive depletion of oceanic oxygen levels, with climate models projecting increased deoxygenation in the future (Schmidtko et al., 2017; Oschlies et al., 2018). Throughout Earth's geological history, major oceanic deoxygenation instances known as oceanic anoxic events (OAEs), have been associated with substantial input of carbon to the atmosphere and the ocean from volcanic eruptions during emplacement of Large igneous provinces (LIPs) (e.g., Scaife et al., 2017). These events subsequently led to widespread accumulation of organic-rich black shale deposits. The massive input of volcanogenic carbon followed by substantial drawdown of organic carbon in the form of black shales leaves a distinct carbon isotope mark in the geologic record (e.g., Jenkyns, 2010).

OAEs represent significant environmental perturbations linked to abrupt fluctuations in Earth's carbon cycles (e.g., Jenkyns, 2010). Since Schlanger and Jenkyns (1976) first recognized OAEs from global occurrences of coeval organic-rich black shales, it has been proposed that excessive isotopically light carbon emissions from LIPs could potentially trigger OAEs, which are also connected to some of the "big five" mass extinctions (e.g., Percival et al., 2018). The organic-rich rocks deposited during these OAEs often represent major organic-rich source rocks for economic petroleum accumulation. Despite their importance, the initial causes and ultimate consequences of OAEs remain under investigation.

The early Toarcian OAE (T-OAE) around 184 Ma, for example, is characterized by a negative carbon isotopic excursion (CIE), which has been linked to isotopically light carbon emissions from the Karro, Ferrar, and Chon Aike LIP (e.g., Heimdal et al., 2021). Additionally, the Cenomanian – Turonian OAE (OAE2) around 94 Ma, marked by a positive CIE, has been connected to increased primary productivity and subsequent deposition of organic carbon (e.g., Owens et al., 2018). Enriched redox-sensitive trace elements (RSTE), such as Mo and Re, typically found in black shale deposits during OAEs, are easily enriched under reduced conditions. In particular, authigenic Mo enrichment related to total organic carbon (TOC) in sediments has been used as a proxy for basin restriction (e.g., Algeo and Lyons, 2006).

Prolific source rocks for petroleum, such as the Hekkingen and Fuglen Formation in the North Sea and the Barents Sea, respectively, were formed during the Middle Jurassic and Early Cretaceous (Mørk et al., 1999; Lerch et al., 2016; Marín et al., 2020). However, the Middle Jurassic – Early Cretaceous organic-rich black shales are not directly associated with well-known OAEs, and their origins remain a topic of debate. Rogov et al. (2020) recently reviewed the high-latitude organic-rich shale deposits between the Middle Jurassic and Early Cretaceous and described the anoxic event responsible for black shale formation in the Boreal realm as a "Shelf Dysoxic-Anoxic Event (SDAE)" due to its distinct features from other Phanerozoic OAEs. The authors outlined five key SDAE characteristics: (1) concentrated occurrences in the higher latitudes rather than on a global scale; (2) diachronous onset and termination; (3) longer duration (up to 20 million years) in contrast to OAEs (10 – 100 thousand years); (4) absence of significant global ^{13}C perturbation during the events; and (5) lack of notable extinction events (Rogov et al., 2020). Recently, Park et al. (in-review) reported Re-Os ages of the Agardhfjellet Formation from the DH2 and DH5R drill holes by UNIS CO_2 LAB project, including source rock pyrolysis and stable carbon and sulfur isotope, and identified a gradual increase in initial Os ratios, reflecting either enhanced terrestrial runoff or decreasing hydrothermal activity in this time period (Park et al., in-review).

In this study, we discuss new trace elements (including rare earth elements, REEs) and stable isotope data from the DH2 and DH5R intervals to evaluate the depositional environment during the SDAE by pinpointing when the anoxic environment began in the basin and how the source input changed and by comparing the SDAE in the Middle Jurassic – Early Cretaceous with other OAEs during the Phanerozoic.

3.3 Geological settings and samples

The study area is situated in Central Spitsbergen within the Svalbard archipelago, near Longyearbyen, positioned between latitudes 74° – 81° north and longitudes 10° – 35° east like Chapter 2. (Fig. 2.1). Samples were collected from seven new interval of DH2 and DH5R, including samples in Chapter 2. More comprehensive information on the sedimentology, paleontology, and geochronology of the drill cores can be found in Koevoets et al. (2018), Koevoets et al. (2019), and Park et al. (in-review).

3.4 Methods

A set of 151 black shale powder aliquots from 17 core intervals were collected by micro-drilling within less than 1 cm for well-indurated shale intervals from the drill cores. In partially shattered shale intervals, we sampled a layer approximately 1 cm-thick and pulverized shale samples with a corundum mortar and pestle or agate ball mill. Twelve of these 17 intervals were previously analyzed for Re-Os contents and isotopic composition by Park et al. (in review). In this study, present a detailed dataset of new trace elements and nitrogen and oxygen isotope data from

151 black shale samples from all 17 intervals to investigate the paleoenvironmental conditions during the Late Jurassic in the Boreal realm.

3.4.1 Major and trace elements

The major and trace element concentrations of the shale samples were analyzed by Actlabs, Canada using either ICP-OES or ICP-MS, following a four-acid total digestion procedure in-house. To ensure the repeatability of the measurements, the results were cross-checked with standard materials (OREAS) and found to be consistent within a margin of 15%.

Hg analyses were performed using the direct mercury analyzer (Milestone© DMA-80 Evo) in the AIRIE Program at Colorado State University. A nickel boat with approximately 100 to 250 mg of black shale powder was automatically loaded into the DMA combustion chamber to measure the concentration of Hg. SDO-1 and 1632e were used as standard materials, and their standard deviations were measured ±6.09 and ±2.35, respectively. Analytical details for Hg follow the procedure in Park et al. (2022).

3.4.2 Stable isotope data (carbon, nitrogen, oxygen, and sulfur)

The isotopic ratios of $^{13}C/^{12}C$, $^{15}N/^{14}N$, $^{18}O/^{16}O$, and $^{34}S/^{32}S$ of the black shale samples were analyzed using Elemental Analyzer-Isotope Ratio Mass Spectrometry (EA-IRMS) at Iso-Analytical of Cheshire, UK. The details can be found in Georgiev et al. (2015). Standard delta notation was utilized to report isotope ratios relative to V-PDB for $\delta^{13}C_{org}$, $\delta^{13}C_{carb}$, and $\delta^{18}O_{carb}$, V-CDT for $\delta^{34}S$, or air for $\delta^{15}N$. Estimated uncertainties for $\delta^{13}C_{org}$, $\delta^{13}C_{carb}$, $\delta^{15}N$, $\delta^{18}O$, and $\delta^{34}S$ were calculated based on analyses of standard materials and were found to be ±0.06‰, ±0.01‰, ±0.20‰, ± 0.08‰, and ± 0.15‰ in averages, respectively. Each analysis allowed for independent estimates of the organic carbon, nitrogen, and sulfur contents of the samples. Total organic carbon and sulfur contents from the isotope analyses correspond with the results from the trace element and LECO analyses.

3.4.3 Re-Os analyses

To measure the Re-Os isotopic ratio of powdered shale samples, we used the isotope dilution-negative thermal ionization mass spectrometry (N-TIMS) at the AIRIE Program at CSU. First, weighed shale powders (around 200 – 300 mg) were mixed with ^{185}Re and ^{190}Os spikes and digested them in CrO_3-H_2SO_4 in sealed Carius tubes in an oven for 48 hours. Then, the osmium from the samples was separated using chloroform and hydrobromic acid (HBr) and micro-distilled the Os with HBr twice for two hours each. The Re-bearing of CrO_3-H_2SO_4 residue was subsequently reduced by SO_2 gas before rhenium was purified by anion chromatography. Re and Os analytes were loaded on platinum filaments for N-TIMS analysis with ReO_4^- and OsO_3^- species being measured. Uncertainties for Re and Os contents and isotopic ratios were derived by numerical error propagation, taking into account weighing and blank corrections, with corrections for isobaric oxygen interferences, instrumental mass fractionation, and analytical blank conducted after the measurements using in-house Excel sheets. The protocols followed were based on methods from Georgiev et al. (2018, 2019), as well as those from Shirey and Walker (1995) and Selby and Creaser (2003).

3.4.4 Principal component analysis (PCA)

We coded up PCA using Python 3.7 and conducted PCA on different datasets. The PCA run focused on TOC and concentrations of 45 major and trace elements, including Al, Ca, Fe, K, Mg, Na, S, Ti, Ba, Cr, Cu, Li, Mn, Ni, P, Sr, V, Zn, Zr, Ag, As, Be, Bi, Cd, Co, Cs, Ga, Hf, Hg, Mo, Nb, Pb, Rb, Sb, Sc, Se, Sn, Th, Tl, U, Y, Ta, W, Re, and Os. The PCA results of elements and samples were reported. PCA results from trace elements of sedimentary rocks have been used to evaluate dominant phases or detrital sources (Tripathy et al., 2014; Park et al., 2022). A detailed

PCA procedure was followed by Park et al. (2022).

3.5 Results

Table A3 shows all geochemical data, including trace elements and stable isotopes.

3.5.1 Major and trace elements concentrations with REE

In this ternary space, most of the samples from the Lardyfjellet and Oppdalssåta Members are closely located between S/Fe = 0.42 and S/Fe = 1.15 lines with a higher proportion of TOC within the three variables (> 50%) except for three outliers distributed close to the Slottsmøya and Oppdalen Members' area (Fig. 3.1). In contrast, the samples from the Slottsmøya and Oppdalen Members made relatively wider distribution around S/Fe = 0.3 line and S/C = 0.4 line with lower TOC proportion (< 50%) compared to the Lardyfjellet and Oppdalssåta Member

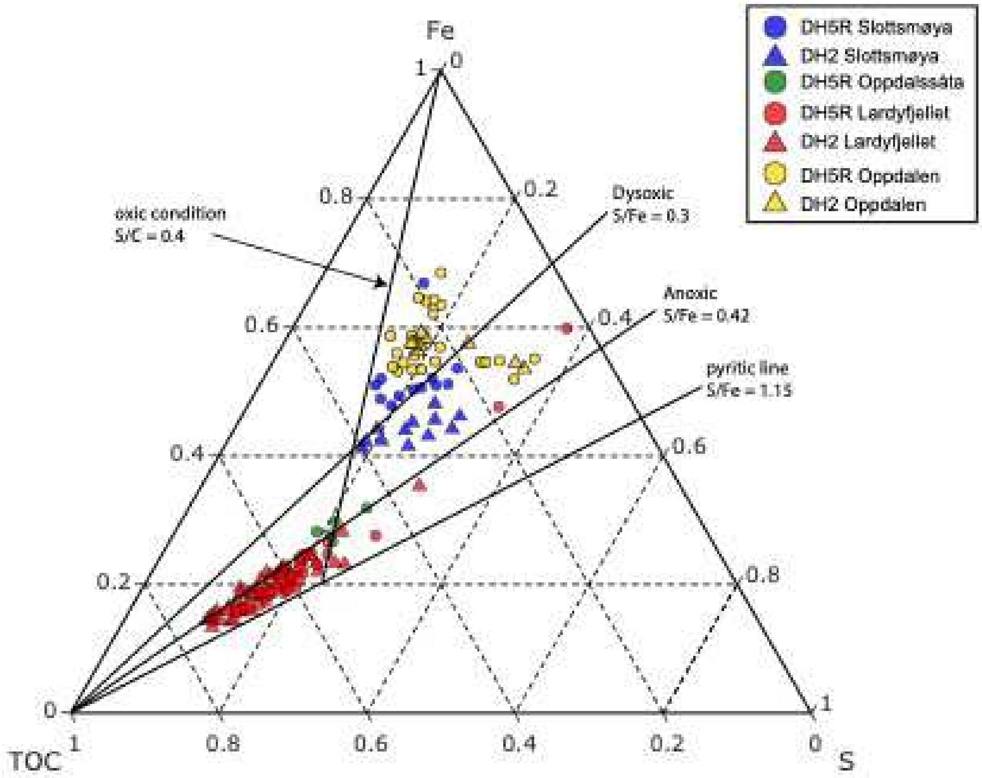

Fig. 3.1 Fe-TOC-S ternary diagram to identify the redox condition of depositional environments (e.g., Hofmann et al., 2000). The ratios between Fe and S determine dysoxic, anoxic, and pyritic (euxinic) conditions on the diagram with certain S/Fe ratios. Oxic condition is determined by an S/C ratio of 0.4, which indicates the ratio of S and C in the modern ocean.

In Fig. 3.2, most of the samples from the Agardhfjellet Formation are located within 0.5 and 1.5 of Mo/TOC ratio lines (dash-dotted lines). The outlier with ~25 ppm of Mo from the Lardyfjellet Member of DH2 has fairly high Ca, Mn, and Zn contents compared to other black shales (9.1% of Ca, 298 ppm of Mn, and 2290 ppm of Zn; DH2 673.031), and the outlier with ~50 ppm of Mo from the Lardyfjellet Member of DH5R is a thick sulfide layer (20% of S; DH5R 607.022). Two intervals of the Oppdalen Member from DH5R 663 and 655, have almost constant and low TOC (< 1.2 wt.%) with variable Mo contents (3 – 11 ppm).

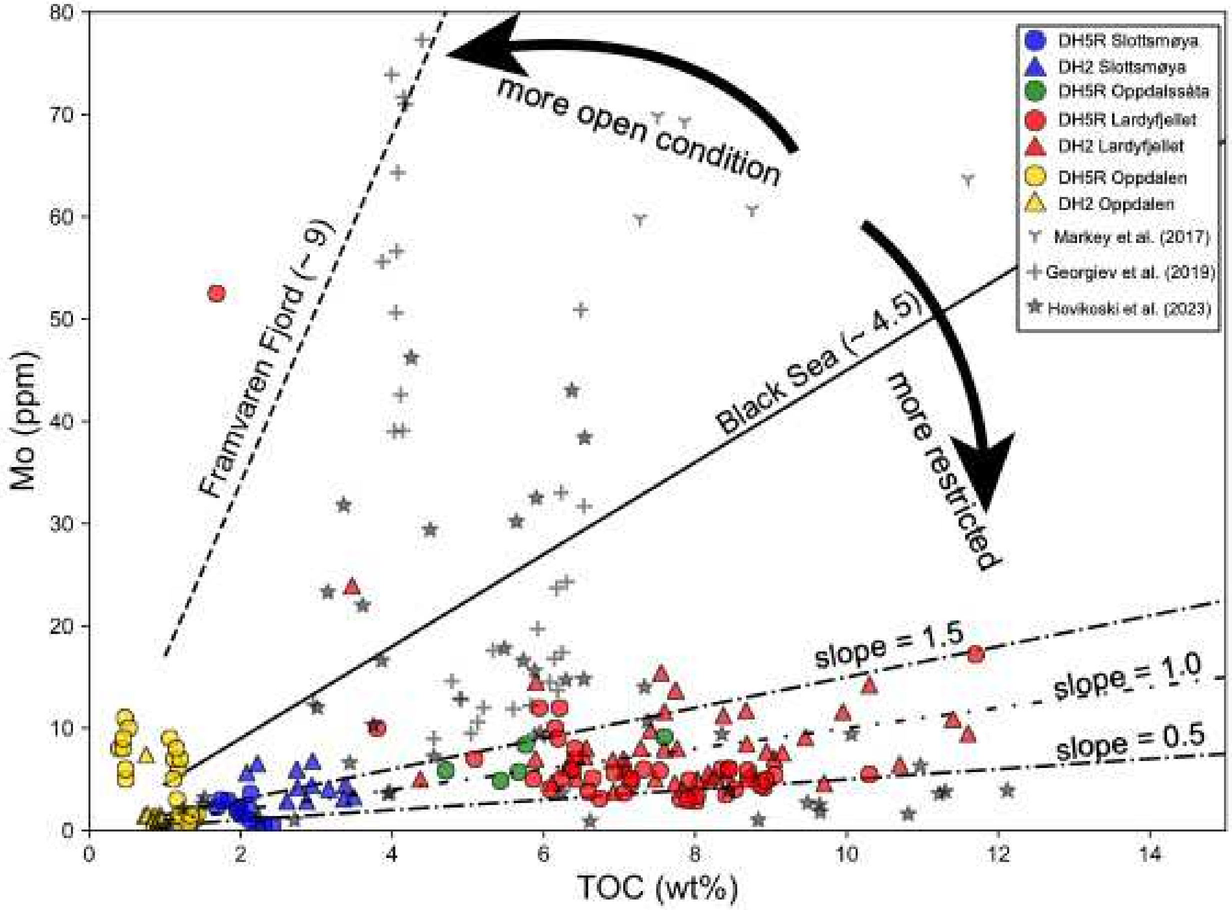

Fig. 3.2 Mo concentrations (ppm) compared to TOC in the Agardhfjellet Formation and published data from the Loppa High, Jæren High, and Wollaston Forland (Markey et al., 2017; Georgiev et al., 2019; Hovikoski et al., 2023). Mo/TOC ratios have been used to identify the degree of basin restriction (Algeo and Lyons, 2006). Mo/TOC ratios of modern anoxic basin examples are shown in a dotted line (the Black Sea) and a solid line (Framvaren Fjord) (Algeo and Lyons, 2006).

Fig. 3.3 shows two biplots with contents of trace elements (Co, Mn, Cd, Mo, Ti, and Zr) with Al contents. Most samples show similar Co×Mn values of 0.1 but various Cd/Mo ratios, ranging from 0.01 to 1 (Fig. 3.3a). Compared to samples from other members, the samples from the Oppdalen Member have lower Cd/Mo values. The contents of Zr relative to Al contents of samples range from 4.91 to 13.4, while six samples of DH2 Lardyfjellet Member have lower Zr/Al_2O_3 than 4 (DH2 673.005, 673.031, 673.070, 674.093, 674.115, and 680.295), and two samples among them have much higher Al_2O_3/TiO_2 over 35 (DH2 673.031 and 673.070; Fig. 3.3b).

The samples from the Oppdalen Member are separated from the main cluster with higher Zr/A_2O_3 values (up to 13.4). When comparing the samples from the Lardyfjellet and the Slottsmøya members, the former samples have lower values of Al_2O_3/TiO_2.

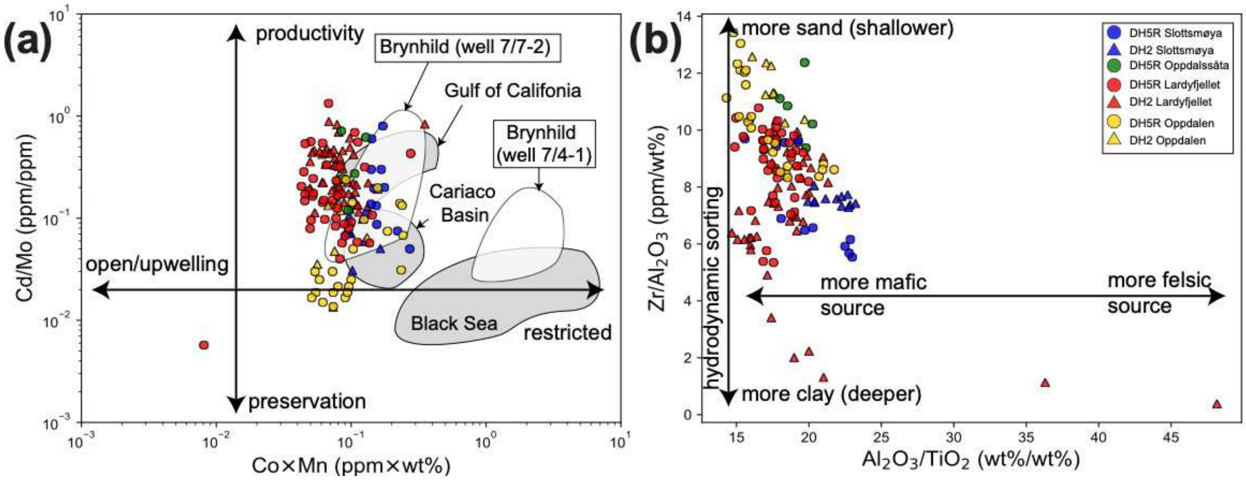

Fig. 3.3 Trace metal constraints for the depositional setting of studied samples. Panel (a) distinguishes between settings of basin restriction and upwelling by values of Co×Mn and dominant processes of organic-rich shale deposition between productivity and preservation by Cd/Mo ratios (fields representing modern-day Black Sea, Cariaco Basin, and Gulf of California from Sweere et al., 2016). Black shales from the Brynhild petroleum system plotted with white areas (Georgiev et al., 2019). Panel (b) shows hydrodynamic sorting characters based on the difference in depositional depth and provenance (e.g., Greber and Dauphas, 2019).

Fig. 3.4 shows Ce, Pr, and Eu anomalies of the samples from the Agardhfjellet Formation. The Oppdalen, Slottsmøya, and Lardyfjellet Members are distinguished by Ce and Pr anomalies (Fig. 3.4a), while the Oppdalssåta Member is intersected with the area of Lardyfjellet Member. Almost half of the samples from the Oppdalen Member are in IIIa and IIb areas, which indicates a positive Ce anomaly. The other half of the samples from the Oppdalen Member and some samples from the Slottsmøya Member show no Ce anomaly (I area). Most of the samples from the Lardyfjellet Member and some from the Slottsmøya Member show negative Ce anomalies (IIa and IIIb areas). There are six outliers apart from the diagonal mainstream of Ce and Pr anomalies with significant negative Pr anomalies from four different intervals (DH2 660, DH5R 489, DH5R 600, and DH5R 613). The REE patterns of the outliers exhibit positive Nd anomalies (Fig. A4), which contribute to the negative Pr anomalies of the samples. The Eu anomalies related to the Ce anomalies did not show any trend.

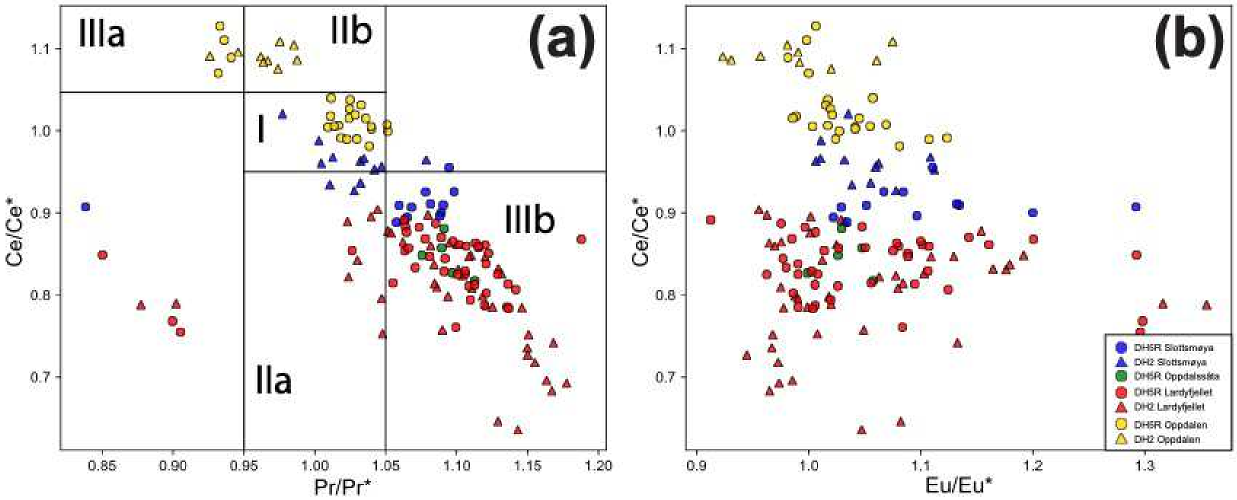

Fig. 3.4 Plots of Ce anomalies with (a) Pr anomalies and (b) Eu anomalies. Anomalies were calculated by normalizing REE concentrations of studied samples with those from the PAAS shale (McLennan, 1989). In panel (a), Field I – no anomaly; Field IIa – positive La anomaly causes apparent negative Ce anomaly; Field IIb – negative La anomaly causes apparent positive Ce anomaly; Field IIIa – real positive Ce anomaly; Field IIIb – real negative Ce anomaly (Shields and Stille, 2001).

3.5.2 C, O, N, and S stable isotope results

Fig. 3.5 shows box plots of TOC, inorganic C, organic C, N, S, and O stable isotope values from 16 studied intervals according to depth when we accept the correlation that the depth of DH2 is 60 m deeper than DH5R (Koevoets et al., 2018). $\delta^{13}C_{inorg}$ fluctuated between -7 and -14‰, while $\delta^{13}C_{org}$ fluctuated between -25 and -27‰ under the Slottsmøya Member (Fig. 3.5b and c). Also, a significant drop of $\delta^{13}C_{org}$ is recorded in the Slottsmøya Member, but the most significant drop of $\delta^{13}C_{inorg}$ is recorded in two intervals, DH2 673 and 674. All N isotope values in the Agardhfjellet Formation showed positive values, with the minimum value of 3.21 in DH2 724 (Fig. 3.5d), showing a moderately increasing trend from bottom to top even though there are fluctuations within both members and intervals. Sulfur isotope values increase from the bottom (~ -50‰) to the middle of the Lardyfjellet Member (~ -10‰) and decrease until ~ -20‰ in the Slottsmøya Member (Fig. 3.5e). The $\delta^{34}S$ variations within each interval are larger in the Lardyfjellet Member compared to other members. In addition, $\delta^{34}S$ shows an overall positive correlation with S concentration (Fig. A6). $\delta^{34}S$ does not show any correlation with TOC, while $\delta^{34}S$ of the Oppdalen Member shows a positive correlation with TOC (Fig. A6). The $\delta^{18}O$ seem to have no general trends with depth or members, but they have a significant correlation with inorganic C isotope values (Fig. A6).

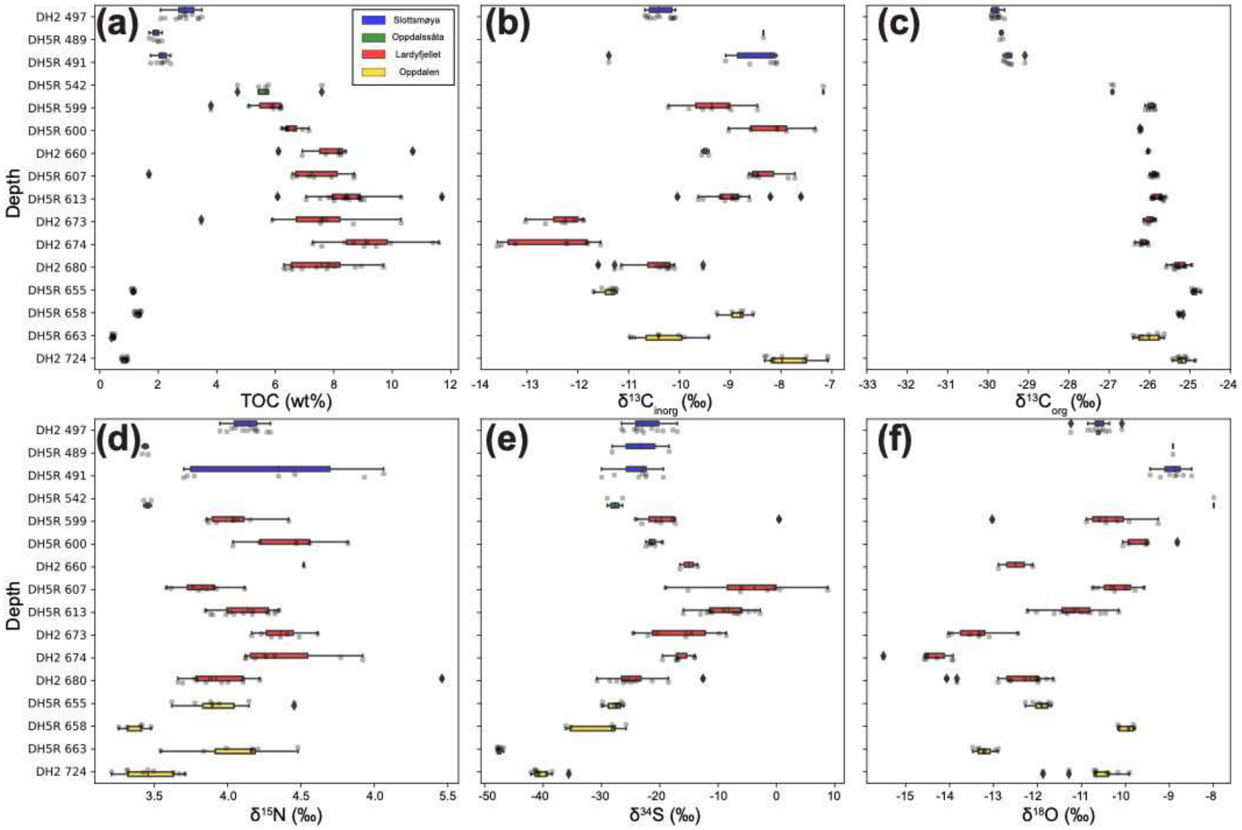

Fig. 3.5 Non-continuous depth profile of TOC (a), inorganic C isotopes (b), organic C isotope (c), N isotope (d), S isotope (e), and O isotope (f).

3.5.3 PCA results

We applied trace element concentrations with TOC into PCA to identify sediment sources from the black shale samples. PCA results are shown in Table 3 and two x-y plots with the first and second principal components (PC1 and PC2) with elements (Fig. 3.6a) and samples (Fig. 3.6b). In general, TOC and redox-sensitive trace metals, such as Re, Os, Mo, V, etc., are loaded with positive PC1, whereas elements associated with terrestrial input, such as Ti, Al, Hf, Zr, etc., are loaded with negative PC2, making two distinct clusters. In terms of PC2, most of the elements are loaded with positive PC2, but Ba, Ni, and Cr are loaded with negative PC2 (-0.6, -0.6, and -0.2, respectively). In Fig. 3.6b, samples from each member are somewhat widely distributed. Samples from the Lardyfjellet, Oppdalssåta, and Slottsmøya Members are distributed horizontally, while samples from the Oppdalen Member are distributed diagonally from the second quadrant to the fourth quadrant. In the Lardyfjellet Member, samples from DH2 are more widely distributed and positive than those from DH5 (red squares vs. red circles).

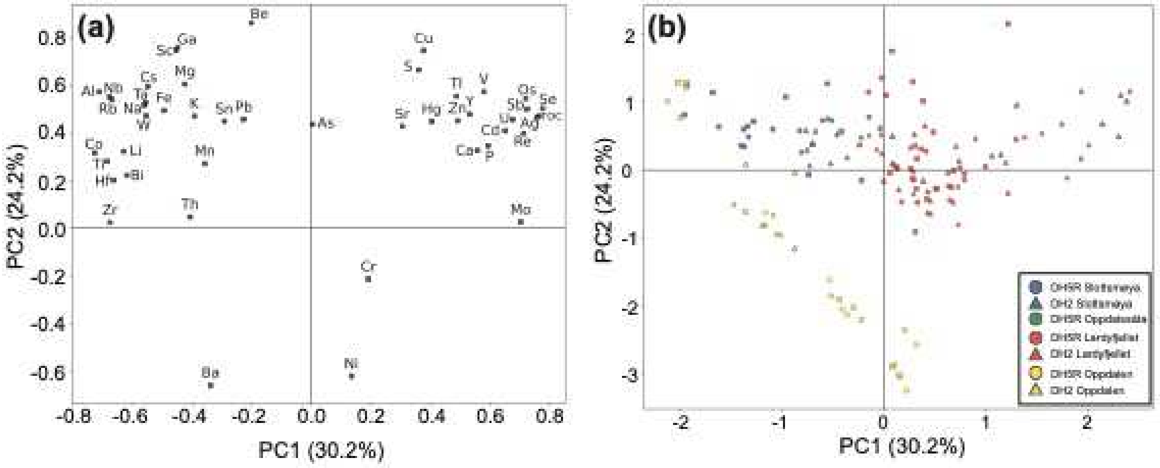

Fig. 3.6 PCA results with shales in the Agardhfjellet Formation. (a) Principal components (PCs) with geochemical values; (b) The distribution of each sample by PC1 and PC2. Arrows indicate dominated tendency of samples based on PCA results in panel (a).

3.6 Discussion

3.6.1 Environmental changes during deposition of the Agardhfjellet Formation

Our new geochemical results are discussed to track the changing paleoredox, detrital input, and basin restriction during the deposition of the Agardhfjellet Formation. Each characteristic will be discussed in detail below.

3.6.1.1 Change in the redox conditions (oxic – anoxic/euxinic – suboxic)

Redox conditions in ancient oceans hold significance for several reasons: 1) association with occurrences of prolific petroleum source rocks (Scholle and Arthur, 1980), 2) influences on life diversification and evolution, including its origin (Lyons et al., 2014), 3) impacts on geochemical cycles, such as N, O, and S, which affect primary productivity (Anbar and Knoll, 2002), and 4) implications for future climate change (Jenkyns, 2010). Paeloredox conditions are evaluated using sedimentary redox-sensitive elements, such as TOC, S, Fe, Mo, U, etc. As each individual proxy has limitations and certain drawback (Tribovillard et al., 2006; Liu and Algeo, 2020), we rely on the combined interpretation of different paleoredox proxies to constrain the redox condition throughout the Agardhfjellet Formation.

The unwavering S/Fe ratios (constant lines from TOC on Fig. 3.1) suggest limited oxygenation and iron-limited depositional environments (Hofmann et al., 2000; Rimmer et al., 2004). Samples from the Lardyfjellet and Oppdalssåta Member fall between the anoxic line (S/Fe = 0.42) and the pyritic line (FeS_2; S/Fe = 1.15), with few outliers, implying relatively steady anoxic/euxinic settings. On the other hand, the samples from the Slottsmøya and Oppdalen members indicate more oxygenated conditions, showing around 0.3 of S/Fe (Fig. 3.1). The Oppdalen Member samples (the oldest and lowermost member) exhibit a scattered distribution with higher Fe proportions instead of forming trends. Samples from the Slottsmøya are distributed similarly to those from the Oppdalen Member, suggesting that while the Lardyfjellet and Oppdalssåta Members were deposited under highly anoxic conditions, sufficient oxygen may have been present in the basin when the Oppdalen and Slottsmøya Members were deposited. Overall, the redox conditions transitioned from an oxic environment in the Bathonian - Oxfordian to an anoxic/euxinic environment during the Kimmeridgian, then returned to a relatively suboxic condition in the Volgian.

PCA results support these findings. A highly positive PC1, loaded with TOC and redox-sensitive trace metals (Mo, Re, U, etc.), indicates anoxic depositional settings (Fig. 3.6a). A negative PC1, loaded with terrestrial input (Zr, Hf, Ti, Al, etc.), suggests enhanced terrestrial runoff (Fig. 3.6a). Although the samples from the Oppdalen Member are widespread in PC1 (-2.2 to +0.4 PC1), the samples from the Lardydjfllet Member are deposited under more anoxic conditions based on higher positive PC1 (Fig. 3.6b). Oxygen levels were likely higher when the Oppdalssåta, Slottsmøya, and Oppdalen members were deposited based on lower and more negative PC1 (Fig. 3.6b). Interestingly, DH2 samples have higher (more positive) PC1 than DH5R samples in the Lardyfjellet Member, which may indicate DH2 samples were deposited under more anoxic/euxinic conditions than DH5R at the same time.

REE patterns of the black shale samples from the Agardhfjellet Formation are flat in PAAS normalized figures with similar values of PAAS (normalized values ~ 1), indicating minimal REE fractionation (Fig. A5). The majority of the samples from the Lardyfjellet Member demonstrate negative Ce anomalies (Ce/Ce* < 1), which serve as a redox indicator since Ce valence is sensitive to the redox state of the ambient environment. In oxic conditions, Ce is enriched in sediments since Ce in water is inactive, whereas Ce in sediments is depleted in the anoxic environment because reduced Ce is released into the water (Wilde et al., 1996). Negative Ce anomalies in rock (Ce/Ce*

< 1) indicate anoxic environments, while positive Ce anomalies (Ce/Ce* > 1) indicate oxic environments. In Fig. 3.4, most samples showed negative Ce anomalies (IIa and IIIb areas), indicating anoxic conditions, while all samples from the Oppdalen Member and a few samples from Slottsmøya Member show no or positive Ce anomalies, indicating suboxic/oxic. Pi et al. (2013) reported that the negative Ce anomaly could enlarge if the OM considerably affects the REE budget, as OM exhibits low Ce/Ce* values (0.3 ~ 0.5). The samples from the Lardyfjellet Member contain the highest TOC levels among all members, resulting in lower Ce/Ce* values and suggesting a higher OM influence on REE content. Six data points with negative Pr anomalies are discussed in the supplementary document.

Barium concentrations between the Oppdalen and Lardyfjellet Members display striking contrasts, revealing significantly lower Ba content in the upper three members (Fig. 3.9). McManus et al. (1998) argued that Ba is an unreliable productivity proxy because it is influenced by suboxic diagenesis. However, should diagenesis be limited, Ba contents could serve as a productivity proxy (Falkner et al., 1993; Liguori et al., 2016). Barite ($BaSO_4$) is the predominant sedimentary Ba host, existing in both oxic and anoxic environments (Falkner et al., 1993). Elevated barite or Ba levels in the Oppdalen Member suggest oxic depositional conditions, while the decreased Ba content in upper members indicates anoxic depositional environments (Liguori et al., 2016).

3.6.1.2 Change in detrital source input

PCA has been used to identify the dominant source of the sediments (e.g., Tripathy et al., 2014; Park et al., 2022). Positive PC1 is associated with enriched redox-sensitive trace elements (RSTE), indicating higher authigenic minerals in sedimentary samples. In contrast, negative PC1 is linked with detrital elements (Al, Th, Zr, etc., Fig. 3.6a). Samples from the Lardyfjellet, Oppdalssåta, and Slottsmøya are horizontally spread (Fig. 3.6b), not only showing limited effect of PC2 but also implying changes in influence of detrital input during the Late Jurassic. Notably, Lardyfjellet Member samples predominantly exhibit positive PC1 values, suggesting an authigenic mineral abundance, whereas all Oppdalssåta and Slottsmøya Member samples and most Oppdalen Member samples display negative PC1, implying considerable continental input (Fig. 3.6b). Dramatic elemental input shifts might have occurred before and after the Lardyfjellet Member, which probably resulted from sea-level fluctuations, tectonic events, and variations in weathering runoff rates (Koevoets et al., 2018; Hovikoski et al., 2023). Fu et al. (2017) also documented that enhanced continental runoff enforces basin stratification, which is consistent with the redox conditions described above.

In contrast to other members, samples from the Oppdalen Member are distributed diagonally in Fig. 3.6b, which is primarily attributable to negative PC2, featuring Ba, Ni, and Cr enrichment and depleted RSTE and/or terrestrial elements in DH5R 655 and 663. Elevated Cr and Ni concentrations likely originate from ultramafic sources (Garver et al., 1996; Amorosi, 2012), while high concentrations of Ba would be influenced by the oxic environment as discussed above (Liguori et al., 2016). Although Cr and Ni have been used as paleoredox proxies, enrichments of Cr and Ni in the Oppdalen Member have been affected by other factors, such as sources, based on the oxic condition during the deposition of the Oppdalen Member. Nickel and Cr concentrations have been used as source indicators of sedimentary rocks, particularly in the ultramafic source rock context (Garver et al., 1996). Garver et al. (1996) proposed that sediments exhibiting elevated Cr and Ni concentrations (Cr > 150 ppm and Ni > 100 ppm), with a Cr/Ni ratio around 1.6, which corresponds to ultramafic rock Cr/Ni ratios, could be considered to have ultramafic source rocks. In addition, Holocene sediments in Italy, derived from ultramafic-rich sources, show ~ 1.2 Cr/Ni ratios with 143 ppm of Cr and 84 ppm of Ni (Amorosi, 2012), as opposed to UCC's ~ 2.0 of Cr/Ni ratio with 92 ppm of Cr and 47 ppm of Ni (Rudnick and Gao, 2003). Consequently, the high contents of Cr and Ni found in all samples from DH5R 655 and 663, combined with ~ 1.5 of Cr/Ni ratio, indicate an ultramafic-rich source. New isochrons from those intervals showed decent nominal ages (167 Ma and 165 Ma) with extremely high uncertainties (MSWDs = 78 and 31) (Fig. A7). The large uncertainties may have stemmed from ultramafic sources with various $^{187}Os/^{188}Os$ ratios when the samples were deposited. The oxic environment and/or ultramafic-rich source may have contributed to distinct elemental variation within the Oppdalen Member.

The relationships between $\delta^{34}S$ and TOC underwent a significant change between the Oppdalen and Lardyfjellet Members (Fig. A6b). The Oppdalen Member samples exhibit a strong correlation between these two values ($R^2 = 0.8$), while the other samples show a weaker correlation ($R^2 = 0.1$). High correlations between $\delta^{34}S_{py}$ and TOC in Toarcian black shales suggest an abundance of bioavailable OM played an important role in sulfur fractionation under the water through cell-specific sulfate reduction rates (csSRR) (Chen et al., 2022). The kerogen type of the Oppdalen Member is terrestrial, whereas the kerogen type of the other members is marine (Park et al., in-review). Consequently, it can be inferred that terrestrial organic matter may have played a role in influencing sulfur isotope fractionation via csSRR.

The chemistry of Zr, Al, and Ti can reveal the water depth and sources of fine-grained terrestrial sediments since these elements are refractory in the ocean, preserving their source characteristics (Greber and Dauphas, 2019; Georgiev et al., 2020). Sediments from the Oppdalen Member contain higher sand content compared to others, suggesting a shallower depositional setting (Fig. 3.3b) (Koevoets et al., 2018). Samples from the Lardyfjellet and Slottsmøya Members show lower values of Zr/Al_2O_3, indicative of deeper depositional settings. In particular, the

Zr/Al_2O_3 values of six samples from DH2 (DH2 673.005, 673.031, 673.070, 674.093, 674.115, and 680.295) are exceptionally lower than those of other samples. Two of these six samples (DH2 673.031 and DH2 673.070) also showed extremely higher Al_2O_3/TiO_2, indicating a more felsic source, while most of the samples have a more mafic source. However, the two samples (DH2 673.031 and DH2 673.070) have substantially higher carbonate content (33 wt.% and 17 wt.%, respectively), rendering the source evaluation based on Zr, Al, and Ti inapplicable for these samples (Greber and Dauphas, 2019). Nevertheless, the depositional settings when the two samples were deposited would have been favorable for carbonate deposition, differing from the other environment during the Late Jurassic when the deposition of clastic material was favorable.

Hafnium is regarded as a geochemical twin of Zr because neither is easily fractionated through geological processes. The concentrations of Zr and Hf from 134 shale and mudstone samples collected by the EarthChem database show a trend of Zr/Hf values, approximately 35, similar to those found in the upper continental crust (UCC) (Fig. A8). The Agardhfjellet Formation, however, follows a distinct trend line with Zr/Hf ~ 25 (Fig. 3.7). Fractionation processes between Zr and Hf in sedimentary rocks have been reported in two scenarios: 1) impact of Zr- and Hf-rich grains from the peraluminous granite (Bucholz and Spencer, 2019) and/or 2) formation of salt minerals and evaporites (Censi et al., 2017). Even though Zr and Hf have similar partition coefficients during factional crystallization in most types of magmas, Hf has a higher partition coefficient than Zr when peraluminous magmas are involved ($Al_2O_3 > Na_2O + K_2O + CaO$; Linnen and Keppler, 2002). Additionally, Censi et al. (2017) observed lower Zr/Hf ratios in evaporites, attributed to different behavior during halite crystallization. As no evaporite records have been found in the Boreal basin during the Late Jurassic, the lower Zr/Hf values from the Agardhfjellet Formation may be explained by intermittent felsic source effects, particularly peraluminous granite

(Bucholz and Spencer, 2019).

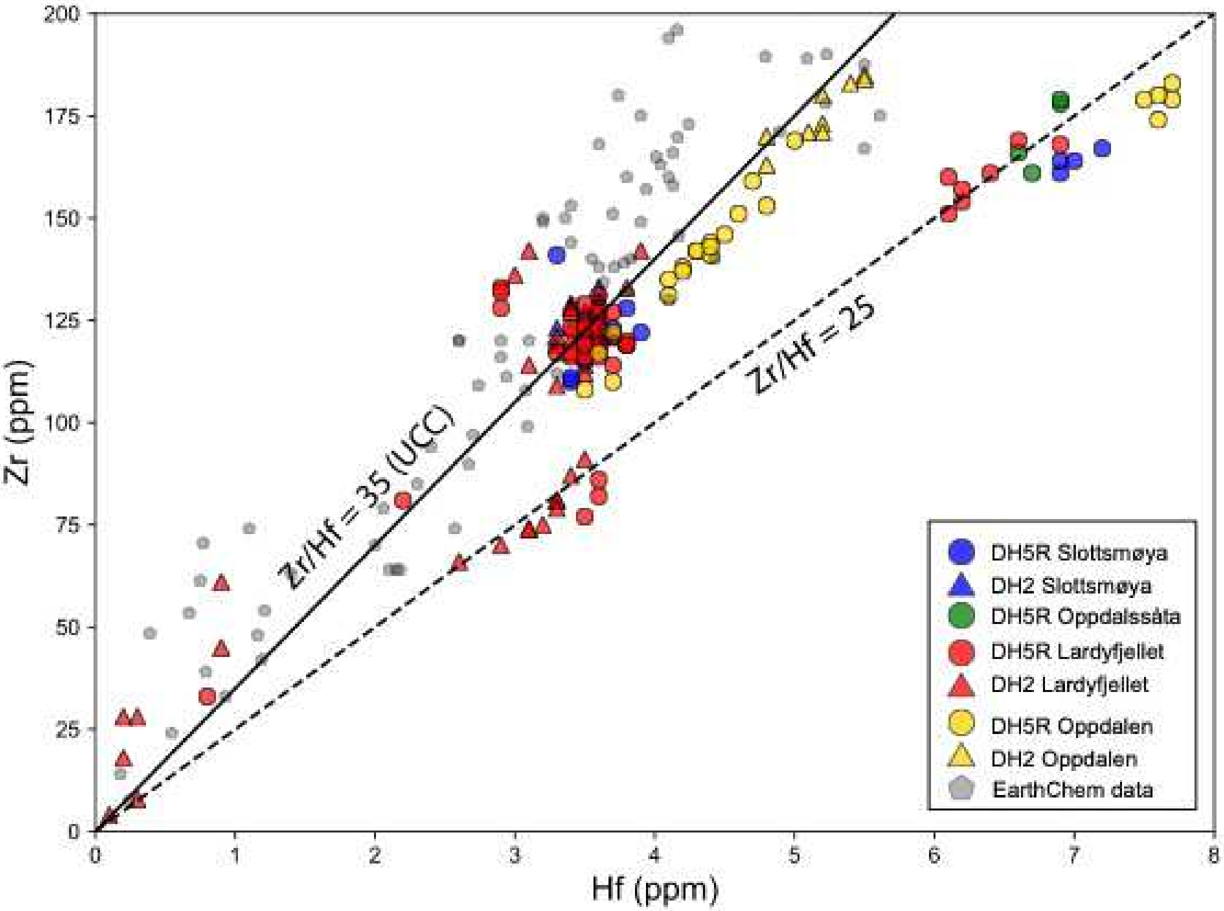

Fig. 3.7 Zr and Hf concentrations of the Agardhfjellet formation shale in ppm. Grey hexagons represent black shales from the EarthChem database (~ 130 samples). A black solid line and dotted line represent Zr/Hf = 35, which is the upper continental crust value (Rudnick and Gao, 2003), and Zr/Hf = 25, respectively.

Al_2O_3/TiO_2 and Zr/Hf derived-source evaluations seem contradictory when considering samples with lower Zr/Hf ratios as being from a felsic source. High Al_2O_3/TiO_2 values are derived from enriched Al content over Ti content by dominant felsic sources, while low Al_2O_3/TiO_2 values are derived from enriched Ti content over Al content by dominant mafic sources. Al and Ti exhibit similar behavior during sedimentary processes, such as mineral sorting (Greber and Dauphas, 2019). However, refractory minerals in sedimentary rocks, like ilmenite and titanite, contain the majority of Zr and Hf input into sediment (Bingen et al., 2001), with Zr and Hf displaying positive correlations with Ti (Fig. A9). Therefore, determining the source differences based solely on Al_2O_3/TiO_2 is challenging. When considering Zr/Hf ratios, it can be inferred that some samples were predominantly influenced by felsic source rocks.

3.6.1.3 Changes in the basin restriction and productivity

Assessing the degree of restriction in a depositional basin is essential for accurately evaluating the basin environment. Molybdenum can reveal valuable information about both paleoredox and paleohydrographic conditions (Algeo and Lyons, 2006). The concentration of Mo can reflect changes in the Mo burial flux, with a decrease in Mo/TOC ratios potentially indicating a reduction in aqueous Mo concentrations due to the absence or scarcity of deep water renewal caused by hydrographic restriction (Algeo and Lyons, 2006). Algeo and Lyons (2006) provided Mo/TOC ratios of various modern basins based on the degree of restriction (Fig. 3.2). When comparing data from the Agardhfjellet Formation to these modern basins, the depositional environment of the Agardhfjellet Formation was extremely restricted throughout the Late Jurassic (Mo/TOC ~ 0.46 except for two outliers), similar to some extremely restricted basins in T-OAE, such as the Cleveland Basin, Yorkshire, United Kingdom (McArthur et al., 2008). Two outliers with higher Mo/TOC were discovered in a sulfide layer (DH5R 607.022) and a sample with high Ca contents (DH2 673.031). Intriguingly, in the Oppdalen Member, two intervals out of four (DH5R 655 and DH5R 663) and one sample from DH2 724 show higher Mo contents compared with similarly low TOC with the other two intervals (DH5R 658 and DH2 724). We argue that Mo was replenished from time to time around the Oxfordian, but seawater Mo burial into sediment was limited by the relatively oxygenated water column.

The enrichment factors (EF) of redox-sensitive trace elements provide not only redox states but also specific environments, such as the degree of restriction (Algeo and Tribovillard, 2009; Tripathy et al., 2018). The EF is defined by the following equation:

$$x_{EF} = \left[\left(\frac{x}{Al}\right)_{sample} \middle/ \left(\frac{x}{Al}\right)_{UCC} \right]$$

In this equation, x_{sample} represents the concentration of element x and Al_{sample} represents the Al concentrations of target samples, while x_{UCC} and Al_{UCC} represent concentrations of x and Al of upper continental crust (UCC) from Rudnick and Gao (2003). According to Algeo and Tribovillard (2009), the relationship between Mo_{EF} and U_{EF} helps indicate water mass chemistry evolution, which is associated with the degree of restriction (Fig. 3.8). Molybdenum and U behave differently during their transfer from water to sediment. While Mo transfers through a particulate Mn-Fe-oxyhydroxide shuttle, U uptake occurs at the boundary of Fe(II) and Fe(III), which is earlier than Mo uptake (Algeo and Tribovillard, 2009). In Fig. 3.8, the Agardhfjellet Formation samples follow the strongly restricted basin array. The degree of basin restriction changed significantly during the Late Jurassic, with the Lardyfjellet Member experiencing the strongest isolation from the open sea. An outlier from the Lardyfjellet Member in DH5R is from a sulfide layer (DH5R 607.020), which may also indicate sporadic occurrences of highly euxinic environment during the restricted period. The more restricted nature of the DH2 location compared to DH5R around 152 Ma is evidenced by the highly restricted cluster of samples exclusive to DH2.

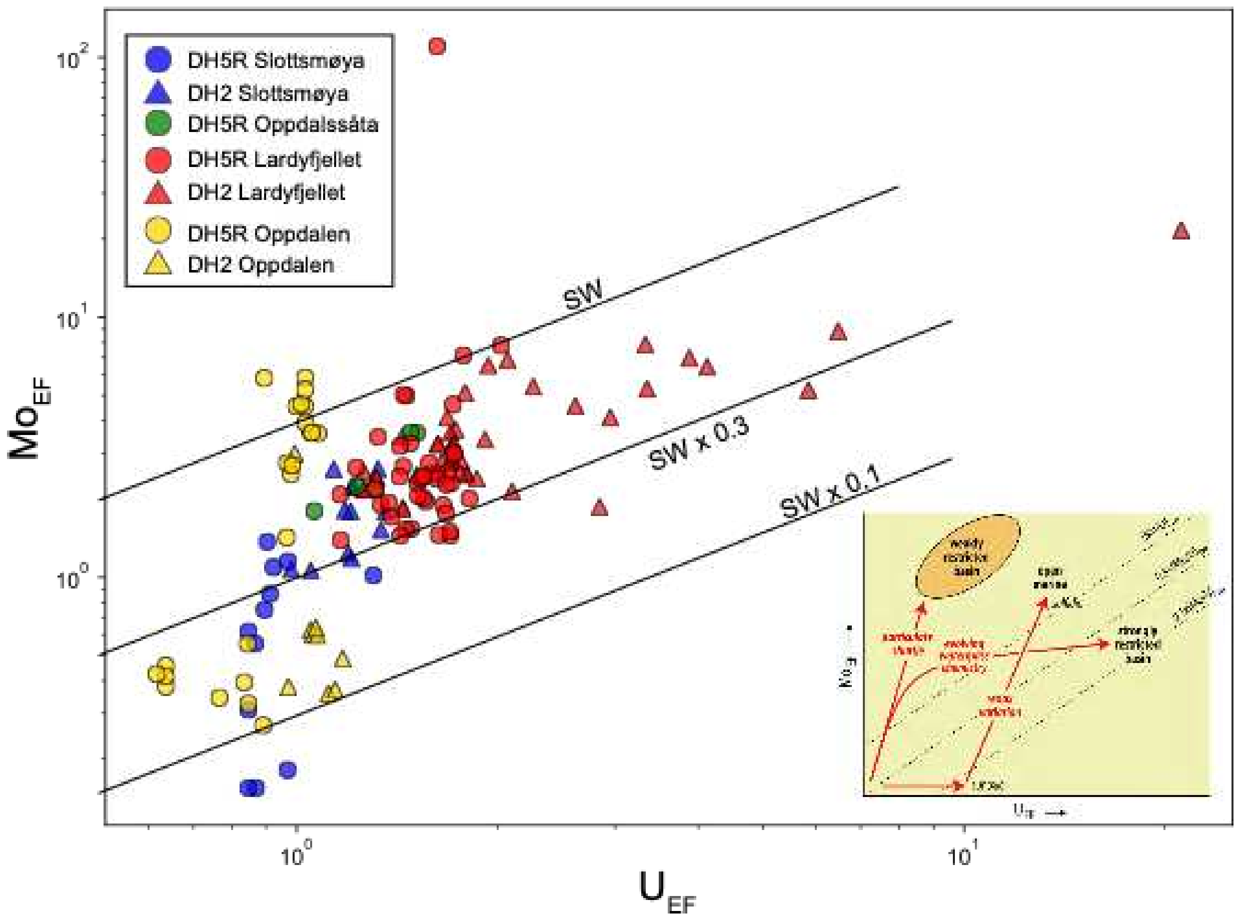

Fig. 3.8 Uranium EFs and Mo EFs for the Agardhfjellet Formation shale. The seawater line (SW) is calculated with molar ratios between Mo and U. Two lines below the seawater line are multiplied by 0.3 and 0.1. A guide figure in the lower right corner is from Algeo and Tribovillard (2009).

As discussed above, the correlation between $\delta^{34}S$ and TOC dramatically changed between the Oppdalen Member and Lardyfjellet Member. Assuming that the $\delta^{34}S$ values of the black shales primarily originated from sulfide, lower $\delta^{34}S$ values would suggest sulfate replenishment from well-connected open oceans. Thus, following the deposition of Oppdalen Member, it can be inferred that connectivity between the Boreal basin and open oceans became restricted. This observation aligns with results derived from trace elements and enrichment factors, further substantiating this conclusion.

Four trace elements, Cd, Mo, Co, and Mn, behave variably under different redox conditions, affecting their pathways to sediment; for example, Mn exhibits increased solubility under reducing conditions, whereas Co, Cd, and Mo are more effectively removed to sediment (Sweere et al., 2016). Sweere et al. (2016) suggested a Cd/Mo vs. Co×Mn diagram with modern organic-rich deposit settings, including the Black Sea and Arabian Sea to evaluate relative restriction vs. open/upwelling and productivity vs. preservation (Fig. 3.3a). Although all samples from the Agardhfjellet Formation fell within a relatively similar area, the Oppdalen Member exhibited lower productivity than others. Interestingly, samples from the Agardhfjellet Formation were clustered in the area that was less restricted than the Black Sea or Arabian Sea, unlike the results from Mo-TOC and Mo_{EF}-U_{EF} diagrams. The primary source of Co and Mn would be riverine input (Sweere et al., 2016), but the riverine input into the Boreal basin during the Late Jurassic might have been insufficient in Co and Mn. In this case, the value of Co×Mn could be lower than the expected values even if the degree of restriction is much higher than that of the modern seas.

Nitrogen isotopes can act as valuable paleoenvironmental proxies by reflecting whether a given environment is characterized more by restriction or by upwelling dominance. This inference is based on the premise that living organisms primarily contribute nitrogen, which subsequently becomes part of sedimentary organic matter (Quan et al., 2013). For instance, low $\delta^{15}N$ (+2.5 to +4.2‰) identified in the Late Permian Hovea-3 black shales indicate a more restricted depositional basin (Georgiev et al., 2020). In contrast, elevated $\delta^{15}N$ (~ +10‰) associated with the Late Permian Greenland black shales suggest an environment predominantly governed by upwelling processes (Georgiev et al., 2015). The relatively limited variation in $\delta^{15}N$ measurements for black shale samples from the Agardhfjellet Formation – ranging only from 3.21 to 5.46 with an average value of around 4.03 – may point towards a restricted depositional basin generated significantly by cyanobacterial nitrogen fixation activities (Georgiev et al., 2020).

3.6.2 Depositional model for the Agardhfjellet Formation during SDAE

Consistent geochemical proxy results from each member enable us to propose potential environmental scenarios for three stages of the Agardhfjellet Formation deposition, although continuous chemostratigraphy is not available because of discontinuous sample collection.

Stage I (the Oppdalen Member) (Fig. 3.9a): The Oppdalen Member was likely deposited under the oxic condition based on the Fe-S-TOC diagram and positive or no Ce anomaly. The Oppdalen Member was the beginning of the deposit after a hiatus between the Middle and Late Jurassic periods (Brikiatis, 2023), and the coldest time around the Middle and Late Jurassic based on the strong Boreal ammonites' invasion into the Tethyan realm (Dromart et al., 2003). Accordingly, the sea level when the Oppdalen Member was deposited might be lowest during the Late Jurassic. Lower values of sulfur isotope from the Oppdalen Member indicate continuous supplies of sulfate ions from the open ocean. Although Mo/TOC values from the Oppdalen Member are low, seawater's oxic nature may have prevented Mo deposition. The sediments of the Oppdalen Member consist of high Ti, Al, Th, and Zr concentrations, indicative of a predominantly terrestrial input rather than authigenic input. In addition, high contents of Cr and Ni in the intervals DH5R 655 and 663 from the Oppdalen Member suggest intermittent contributions of ultramafic sources. Thus, we suggest that a combination of felsic and ultramafic sources may have strongly affected the depositional environment at this time.

Stage II (the Lardyfjellet Member) (Fig. 3.9b): The samples from the Lardyfjellet Member from the Fe-S-TOC diagram are aligned well between the anoxic and pyritic lines, which indicates the anoxic/euxinic depositional conditions. Gradual increases in Sr isotopic and initial Os isotopic ratios denote enhanced radiogenic input from continents (McArthur et al., 2020; Park et al., in-review). The samples from the Lardyfjellet Member have higher authigenic components based on

PCA results (positive or higher PC1 of the Lardyfjellet Member) (Fig. 3.6b), indicating continental runoff affected the depositional environment less. Nevertheless, the fact that $^{187}Os/^{188}Os$ and $^{87}Sr/^{86}Sr$ in the seawater gradually increased shows the increase in the influence of radiogenic sources in spite of low continental input. Extremely low values of Mo/TOC and higher values of U_{EF} compared to Mo_{EF} from the Lardyfjellet Member show the restricted depositional environment. In particular, DH2 samples, deposited in a deeper part of the basin, have higher U enrichment, indicating a high degree of restriction (Algeo and Tribovillard, 2009). The highly restricted basin may have hindered the oxic water replenishment from open oceans.

Stage III (the Slottsmøya Member) (Fig. 3.9c): The samples from the Slottsmøya Member show a somewhat similar distribution with samples from the Oppdalen Member in the Fe-S-TOC diagram but have a lower iron proportion, which indicates a less oxygenated condition than that of the Oppdalen Member. Ce anomalies from the Slottsmøya Member plot between the samples from the Oppdalen and Lardyfjellet members. Thus, the redox condition of the Slottsmøya might be suboxic. The highest values of the initial Os ratio and Sr isotopic ratio indicate the enhanced influence of radiogenic Os and Sr sources compared to the past, which was possibly induced by increased temperature. Additionally, lower values of $\delta^{13}C$ in the Slottsmøya Member are consistent with the occurrence of the Volgian isotopic carbon excursion (VOICE) (Galloway et al., 2020), which may be the result of hydrocarbon seep (Hammer et al., 2011) which could have intensified global warming. In terms of sources, PCA results show that the samples from the Slottsmøya Member are loaded with negative PC1 and positive PC2 between the clusters of the Oppdalen and Lardyfjellet members, indicating a higher proportion of riverine input compared to the Lardyfjellet Member.

(c) Slottsmøya (~ 147Ma)

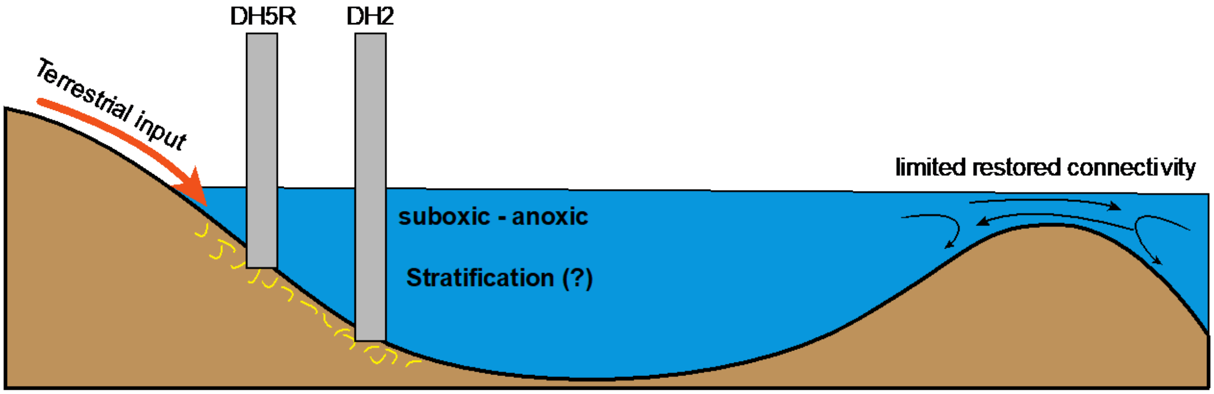

(b) Lardyfjellet (~152 Ma)

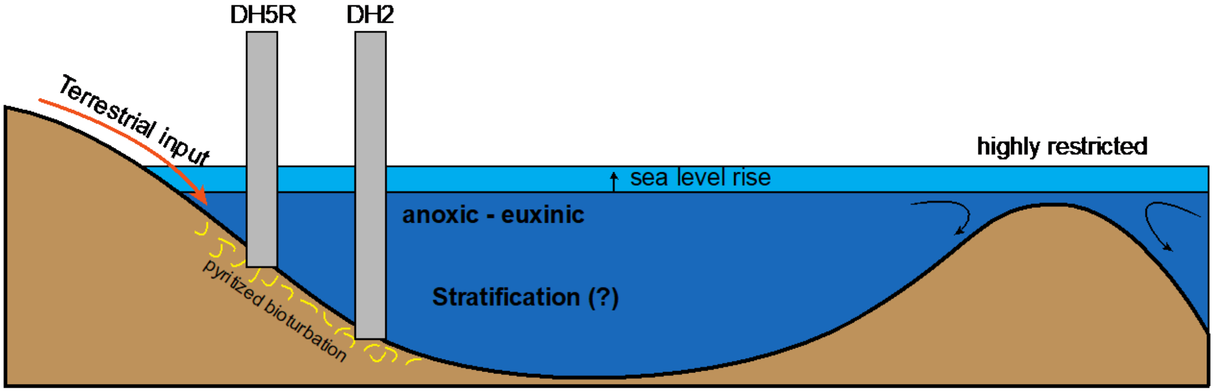

(a) Oppdalen (~160 Ma)

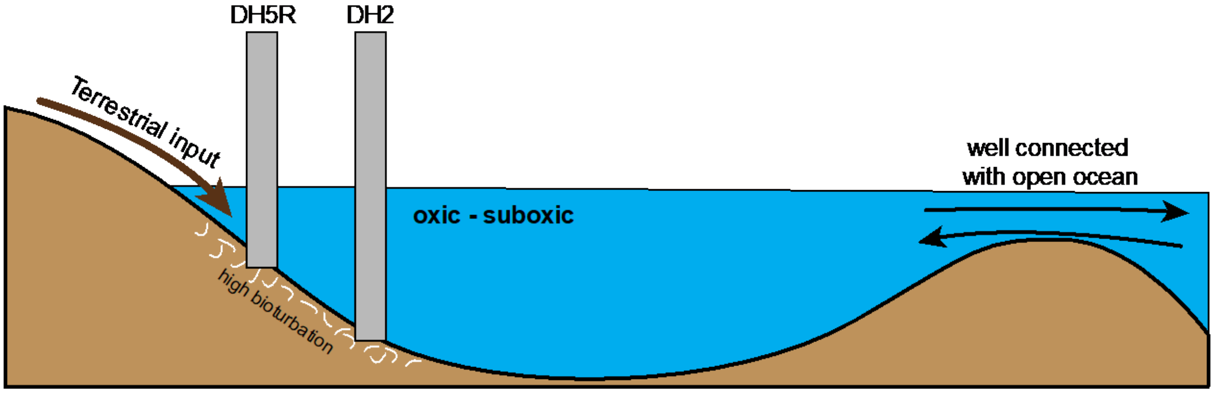

Fig. 3.9 Scenarios of environmental evolution during the deposition of the Agardhfjellet Formation. (a) Oxic conditions prevailed during the deposition of the Oppdalen Member, with terrestrial inputs influencing sediment composition mainly. Sea levels were possibly at their lowest in the Late Jurassic, with lower sulfur isotope values indicating sulfate ion supplies from the open ocean. (b) Anoxic/euxinic conditions characterized the Lardyfjellet Member, with PCA results suggesting a reduced impact of continental runoff on the depositional environment. Extremely low Mo/TOC values and higher U_{EF} compared to Mo_{EF} indicate a restricted depositional environment, potentially hindering the replenishment of oxic water from open oceans. (c) The Slottsmøya Member is associated with suboxic conditions, with Ce anomalies highlighting a suboxic redox environment. This period likely experienced the enhanced influence of radiogenic Os and Sr sources, with lower $\delta^{13}C$ values correlating with the VOICE event. Sea levels during this stage may have been at their highest due to increased methane content. The detailed descriptions are in the main text.

3.6.3 Paleoenvironmental characteristics during the Late Jurassic in the Boreal realm

3.6.3.1 Paleogeography, Paleoceanography, and Paleo-atmospheric circulation

Disturbed ocean circulation and restriction from the open ocean have been raised as contributing factors to distinct depositional settings of the Boreal (Bjerrum et al., 2001; Korte et al., 2015; Hovikoski et al., 2023). A modeling study of the Early Jurassic paleoceanography suggests a southward ocean current through the Viking corridor, which connected the Boreal Ocean and Tethys (Fig. 2.1a; Bjerrum et al., 2001). However, an ammonite ecological study of the Middle Jurassic proposes a northward-flowing current (Callomon, 2003). Although definitive evidence for a Late Jurassic ocean around the Boreal realm currents remains elusive, the contemporary paleoclimate may have been influenced by paleoceanographic characteristics that impacted the climate (Korte et al., 2015). Hovikoski et al. (2023) reported the restricted condition of the Viking corridor during the Late Jurassic to Early Cretaceous. Prolonged rifting potentially influenced oceanographic circulation and seafloor deoxygenation in the Boreal realm (Bjerrum et al., 2001; Hovikoski et al., 2023), and the rifting-driven topography facilitated spatially distinct distributions of anoxic and oxygenated pockets (Hovikoski et al., 2023).

Armstrong et al. (2016) simulated the Hadley circulation during the Late Jurassic period based on paleogeography (155.5 Ma) since this atmospheric circulation, with its ascending and descending air movements, potentially determines dry, subtropical climate conditions in paleoclimates through precipitation proxies. The Late Jurassic Hadley circulation seemed to be in high latitudes, indicating a subtropical climate (warm and wet) in 30°N – 40°N where the Kimmeridgian Clay Formation occurred, suggesting a warmer climate in the Boreal realm than the present-day Boreal realm (Armstrong et al., 2016).

Although the depositional condition of the Late Jurassic Boreal realm is still debating, the geochemical features of the Agardhfjellet Formation may indicate similar conditions described above. The exceptionally low δ^{34}S values in the Oppdalen Member indicate the influence of sulfate, implying substantial connectivity with the open ocean, but the higher δ^{34}S values observed in the Lardyfjellet Member suggest that sulfate replenishment from the open ocean ceased (Fig. 3.4e). Thus, it can be inferred that during deposition of the Lardyfjellet Member, any oceanic currents linking the Boreal basin and open ocean were likely severely restricted (Fig. 3.9b).

3.6.3.2 Warming World

One of the critical climatic disturbances during the Late Jurassic would have been global warming (Price and Rogov, 2009; Dera et al., 2011; Nozaki et al., 2013). Analyzing δ^{18}O in well-preserved Oxfordian–Volgian belemnites from the Russian Platform, Price and Rogov (2009) reported steadily negative oxygen isotope, indicating a prolonged episode of gradual warming. Compiled oxygen isotope data from belemnite and bivalve fossils with a statistical approach revealed low temperature in the Callovian, followed by a gradual increase during the Late Jurassic (Dera et al., 2011). Similarly, the initial osmium isotope ratios from Late Jurassic organic-rich black shales show a gradually increasing trend (Markey et al., 2017; Georgiev et al., 2019; Park et al., in-review). Initial Os isotope ratios represent contemporaneous Os isotopes of seawater, which depend on how the input material differs between unradiogenic and radiogenic sources (mantle-derived vs. continental runoff) (Stein and Hannah, 2015). Os isotope in the seawater of the Boreal basin during the Late Jurassic gradually increased from ~160 Ma to ~147 Ma, signifying enhanced continental runoff (radiogenic Os), possibly due to increasing temperature (Markey et al., 2017; Georgiev et al., 2019; Park et al., in-review).

The causes of global warming during the Late Jurassic remain uncertain; however, several potential contributing factors have been proposed. Nozaki et al. (2013) reported notably low $^{187}Os/^{188}Os$ ratios (as low as 0.10) in sulfide deposits from southwest Japan, which was part of the open ocean of the Panthalassa around 150 Ma. They argued that intense hydrothermal activity may have instigated global warming. On the other hand, the studied Boreal black shales do not show a remarkably low unradiogenic Os isotope ratio (Markey et al., 2017; Georgiev et al., 2019; Park et al., in-review), suggesting considerable restriction during the Late Jurassic, which could have isolated the Boreal realm from open oceans like Panthalassa. Greenhouse gases, including methane or carbon dioxide, have been associated with global warming and OAEs (e.g., Jenkyns, 2003). Methane release from gas hydrate during the Oxfordian has been inferred based on negative carbon isotope excursion (CIE) in carbonate successions (Padden et al., 2001; Louis-Schmid et al., 2007). During the Volgian, seep carbonate bodies were discovered, with carbon isotope data from both carbonate and organic matter exhibiting negative CIEs (Hammer et al., 2011, 2012); this phenomenon is also referred to as the VOICE event (e.g., Galloway et al., 2020). Furthermore, regarding prolonged anoxic conditions during the Late Jurassic, anaerobic decay could be one of the major effects on the water columns. The major decay of OM Is bifurcated between methanogenesis and sulfate reduction, depending on the available electron acceptor. If sulfate acts as the main electron acceptor, sulfate reduction can be dominated, and if carbon compounds, such as carbon dioxide, act as the main electron acceptors, methanogenesis can be dominated during the decay of OM (Oremland and Polcin, 1982). When an anoxic/euxinic condition has been initiated in the studied basin, sulfate seemed available for sulfate reduction during the anaerobic decay of OM. However, the development of water mass restriction and subsequent limitation of sulfate replenishment might have led to a shift in anaerobic decay dominance from sulfate reduction to methanogenesis. In addition, the methanogenic anaerobic decay of OM could have been boosted by the increase in temperature (Maltby et al., 2018).

The geochemical findings from black shales of the Agardhfjellet Formation are not explicitly associated with temperature changes, even though $\delta^{18}O$ from fossils or carbonates has been used as a paleoproxy for temperature (e.g., O'Connor et al., 2019). $\delta^{18}O$ values range from -16‰ to -8‰ (Fig. 3.5f), which may result from diagenesis or fluid metasomatism (Kaufmann and Knoll, 1995). Nevertheless, Hermoso et al. (2013) argued that lower $\delta^{18}O_{carb}$ up to -7‰ in the Early Toarcian black shale from the southern Paris basin could be associated with enhanced riverine input. Since $\delta^{18}O$ against $\delta^{13}C_{inorg}$ shows a significant positive correlation ($R^2 = 0.6$) (Fig. A6c), meteoric fluid could have influenced $\delta^{18}O$ in carbonates (Algeo et al., 1992). Still, it is difficult to correlate lower $\delta^{18}O$ from the Agardhfjellet Formation with enhanced continental input due to the possibility of diagenesis.

3.6.4 Comparison between SDAE and OAEs

The Late Jurassic SDAE and typical Phanerozoic OAEs share several characteristics, such as massive organic-rich black shale deposit, positive $\delta^{34}S$, and considerable drops and rebound of the initial Os isotope ratio. Also, the transition between bioturbated and laminated layers observed in black shales from OAEs is also observed here in the SDAE (Koevoets et al., 2018, 2019).

Contrary to the general Phanerozoic OAEs, carbon isotope negative excursion generally associated with the onset of OAEs has not been observed during the SDAE, although the VOICE is observed in the late stage of the event (Jelby et al., 2020). There is no record of large igneous provinces (LIPs) around the onset of the SDAE, which may have caused the anoxia event.

In particular, the hydrographic restriction of depositional basins during the Mesozoic OAEs has been investigated in common with Mo/TOC ratios (Tribovillard et al., 2012; Fernández-Martínez et al., 2023). Fernández-Martínez et al. (2023) reviewed debates over the low Mo concentrations in Lower Toarcian black shales, introducing both the "local restriction model" and the "global drawdown model." The former highlights the vital role of restricted basins in limiting Mo replenishment from the open ocean, also referred to as the "basin reservoir effect" (Algeo and Lyons, 2006), while the latter proposes that global Mo drawdown may occur to some extent.

Fernández-Martínez et al. (2023) reported Mo/TOC ratios of T-OAE sections from the Western and Eastern Tethys, Northern and Southern Panthalassa, noting patterns of low Mo/TOC ratios during T-OAE (below the ratio of the Black Sea, ~ 4.5) and higher Mo/TOC ratios before/after the event. The authors concluded that the T-OAE resulted from global carbon distribution, likely triggered by the Karoo-Ferrar-Chon Aike LIP eruption, which influenced global Mo drawdown. However, regional and local factors such as basin restriction and hydrological cycles were probably superimposed (Fernández-Martínez et al., 2023). On the other hand, Mo/TOC ratios of OAE2 sections from the Western Tethys and North Atlantic reported comparable ratios (average Mo/TOC of four sections ~ 4.9 except for extremely high ratios by samples with < 1% of TOC) to those of the Black Sea (Westermann et al., 2014).

Mo/TOC ratios of SDAE from our study show an extremely low ratio trend in Fig. 3.2 except for the samples from the Oppdalen Member (Mo/TOC ~ 1). The Lardyfjellet, Oppdalssåta, and Slottsmøya Members were deposited under a highly restricted basin compared to T-OAE and OAE2 described above. Other organic-rich black shale sections from the Jæren High within the North Sea and Loppa High within the Barents Sea around the J/K boundary were plotted in Fig. 3.2 and show relatively higher Mo/TOC ratios (Markey et al., 2017; Georgiev et al., 2019). The Mo/TOC of many samples are distributed between 4.5 and 9, but some samples of well 7/7-2 from the Jæren High are clustered below Mo/TOC ~ 4.5. Georgiev et al. (2019) mentioned that shales from well 7/7-2 were deposited under less euxinic conditions than other shale and higher thermal maturity of shales from well 7/7-2 than others. Thermal maturity may impact Mo speciation in organic-rich black shale, which may redistribute Mo in the sedimentary rocks (Ardakani et al., 2016). Some of the Wollaston Forland results showed extremely low Mo/TOC ratios (Hovikoski et al., 2023). Hovikoski et al. (2023) proposed that tectonic evolution may have strongly influenced paleoenvironmental conditions, including hydrographic restriction. Nevertheless, the shales from the Agardhfjellet Formation during the SDAE indicate that local/regional basin restriction played a crucial role in prolonging the anoxic event beyond the duration of general Phanerozoic anoxic events.

Therefore, the Late Jurassic SDAE featured by the Agardhfjellet Formation shares several commonalities with typical Phanerozoic OAEs, including the deposit of massive organic-rich black shale, positive $\delta^{34}S$ shifts, and substantial fluctuations in the initial Os isotope ratios. However, it distinguishes itself through a lack of carbon isotope excursion at its onset and an absence of associated LIPs. The Mo/TOC ratios indicate that the Agardhfjellet Formation during the SDAE was deposited under highly restricted basin conditions compared to T-OAE and OAE2. While global factors like LIP eruptions may trigger events like T-OAE and influence global MO drawdown, our study emphasizes that local/regional factors such as basin restriction play a pivotal role in shaping the SDAE uniquely. This may disentangle the complexity of the SDAE as a first step.

3.7 Conclusion

The Late Jurassic – Early Cretaceous shelf dysoxic-anoxic event (SDAE), which potentially influenced the deposition of the Agardhfjellet Formation, is not yet completely understood. This study presents the distinct geochemical characteristics of the Agardhfjellet Formation, which was deposited during the SDAE. Trace element concentrations, including rare earth elements in the lowermost Oppdalen Member reveal a relatively oxic basin well-connected to the open ocean, which facilitated the replenishment of chemical components within the water mass. Continental inputs during the deposition of the Oppdalen Member may have ranged from ultramafic to felsic sources. With the onset of the Lardyfjellet Formation, the basin environment transitioned to anoxic-euxinic conditions, possibly due to nearly closed connectivity with the open ocean. Authigenic minerals prevailed the sediments during this time. In the Slottsmøya Member, negative carbon isotope values consistent with the VOICE event were observed. Subsequently, the degree of basin restriction reverted to a similar level as in the Oppdalen Member, and the redox conditions transitioned back to suboxic. SDAE shares similarities with the Phanerozoic OAEs such as black shale deposition and/or basin restriction. However, differences also exist, including a more prolonged duration and distinct spatial scales. The causative factors underlying the SDAE remain undetermined, but hydrographic restriction may have played a significant role in massive black shale deposition for ~ 15 Myr in the Agardhfjellet Formation based on extremely low Mo/TOC and U_{EF} enrichment over Mo_{EF}.

Chapter 4 Project III

Degradation of Hg signals on incipient weathering: Core versus outcrop geochemistry of Upper Permian shales, East Greenland and Mid-Norwegian Shelf

4.1 Summary

Mercury (Hg) enrichment and elevated ratios of Hg to total organic carbon (Hg/TOC) in sedimentary rocks have often been linked to volcanism from large igneous provinces (LIPs). Primary Hg and TOC contents of sediments can be altered by secondary processes like extreme weathering. These effects must be evaluated before tying Hg anomalies in weathered rocks directly to LIP events. However, the effects of *incipient* weathering on Hg contents and Hg/TOC ratios are not known. In this study, we elucidate the behavior of Hg during incipient weathering by investigating visually pristine black shales from outcrops of the Ravnefjeld Formation in East Greenland (GRL) and comparing them to drill core equivalent intervals acquired from the same outcrop area and correlative shales from the mid-Norwegian shelf (MNS). By using geochemical investigations and principal component analysis, we characterize the main host phases of Hg and relate the different Hg contents of pristine samples from GRL and MNS to different Hg inputs during shale deposition. Compared with pristine drill core samples, incipiently weathered outcrop shales have up to 77% lower Hg contents and up to 64% lower Hg/TOC ratios. Incipient weathering causes the early degradation of Hg signals, which masks the primary Hg and Hg/TOC signals in sedimentary rocks. Therefore, we suggest that the presence and effects of weathering in sedimentary rock should be evaluated before discussing Hg signals.

4.2 Introduction

Large igneous provinces (LIPs) have been regarded as the main trigger of global environmental perturbations or even mass extinctions (e.g., Percival et al. 2015; Shen et al. 2019b). Because volcanic emissions are the largest known source of atmospheric Hg prior to significant anthropogenic inputs, mercury (Hg) concentration or Hg/TOC ratio anomalies in sedimentary rocks are commonly interpreted as tracers of massive volcanism (e.g., Percival et al. 2018; Clapham and Renne 2019).

Characterization of the input sources of Hg is important for interpreting Hg contents. The size and type of volcanoes and proximity to landmass have been identified as the main factors to affect Hg contents in sedimentary rocks (Percival et al. 2018; Them II et al. 2019). Recognition of true anomalies in Hg input requires that Hg concentrations be normalized to total organic carbon (TOC), reported as Hg/TOC ratios because organic matter (OM) is the acclaimed primary host of Hg in sedimentary rocks (e.g., Fitzgerald and Lyons 1973; Gehrke et al. 2009. Sulfide and clay minerals, however, may also contain significant amounts of Hg. For example, Shen et al. (2020) show that sulfide can be the primary host phase of Hg in sedimentary rocks deposited under strongly euxinic conditions, and Kongchum et al. (2011) report a substantial relationship between Hg contents and the amount of clay minerals in modern sediments. Therefore, understanding depositional settings and the host of Hg in sedimentary rocks are essential for geochemical interpretations.

Measured Hg contents and Hg/TOC ratios in sediments are affected by the post-depositional history of the rock as well as the depositional setting. Charbonnier et al. (2020) investigated the impact of intense weathering on Hg/TOC anomalies compared to relatively pristine samples. Total organic carbon was almost completely removed from their weathered samples and, as a result, Hg/TOC appeared anomalously high. This exaggerated Hg/TOC signal can be mistakenly interpreted as an indicator of LIP activity if the oxidation of sedimentary rocks is not considered. Such misinterpretation should be easily avoidable, as extreme weathering can be identified with the naked eye, for example by the color-change in weathered samples (Charbonnier et al. 2020).

The mobility of Hg during incipient weathering has not yet been studied. Unlike extreme weathering, incipient weathering of shale is harder to identify visually, especially in black organic-rich shales (Marynowski et al. 2011; Georgiev et al. 2012; Tuttle et al. 2014; Marynowski et al. 2017) and is usually defined by chemical means. Peng et al. (2004) define "incipient" weathering as oxidation of sulfide, but limited oxidation of OM. It is well-known that sulfide is oxidized rapidly and earlier than the oxidation of OM (Petsch et al. 2000; Wildman et al. 2004). Incipient weathering is known to alter primary elemental contents significantly (e.g., S, Pb, Sc), the oxygen content of OM (oxygen index; OI), and Re-Os isotopic ratios in shale (Georgiev et al. 2012). Significant reductions in TOC, S, Mo, and changes in stable isotope compositions have been reported in partially weathered black shales (e.g., Marynowski et al. 2017). Similarly, any differential mobility of Hg and TOC during incipient weathering has the potential to alter primary Hg/TOC ratios in sedimentary rocks, which may lead to misinterpreted signals. It is essential, therefore, to evaluate Hg behavior during incipient weathering so that the geologic significance of Hg signals and Hg/TOC ratios can be accurately interpreted.

In this study, we report the effects of incipient weathering on Hg contents and Hg/TOC ratios in incipiently weathered organic-rich shale from East Greenland (GRL) outcrops, adjacent correlative pristine drill core, and coeval pristine shale from the mid-Norwegian shelf (MNS) drill core. We discuss the main host phases of Hg and the fate of Hg during and after incipient weathering by using principal component analysis (PCA) and newly acquired Hg concentration data. We suggest incipient weathering plays a pivotal role in the early degradation of Hg contents in sedimentary rocks.

4.3 Geological settings and samples

The shales of the Upper Permian Ravnefjeld Formation of East Greenland reflect anoxic-euxinic conditions immediately preceding the Permian-Triassic (P-Tr) extinction, marked by high organic matter and sulfur contents, and absence of bioturbation (Piasecki and Stemmerik 1991; Georgiev et al. 2011). We sampled eleven 1-cm-thick vertical drill core intervals (core GGU303102, drilled onshore on a plateau above the valley cut by Triaselv ("Triassic River") of East Greenland, 20 m total depth). The studied samples belong to two organic-rich shale units recognized within shallow drill core, known as the upper and lower laminated intervals of the Ravnefjeld Formation, respectively (GRL-UL and GRL-LL; Fig. 4.1). Correlative samples from the Ravnefjeld Formation in GRL were collected from an outcrop in the Triaselv valley on the east side of Schuchert Dal, East Greenland, 6.7 km northwest of the drill core location (Fig. 4.1). The 29 collected outcrop samples were subdivided into four groups based on their stratigraphic position within the outcrop: GRL-O1-a, GRL-O1-b, GRL-O2-a, and GRL-O2-b. The Lower Turbidite Unit from offshore drill core 6611/09-U-01 in MNS, which penetrates a sandstone- and siltstone-rich turbidite sequence, is considered a stratigraphic equivalent of the Ravnefjeld Formation in GRL in terms of geochemistry and palynology (Bugge et al. 2002; Hochuli et al. 2010). The GRL and MNS depositional localities were close to each other before the opening of the North Atlantic during the Permian-Triassic (Müller et al. 2005). Twenty-four samples from four vertical intervals from the MNS core were studied. From top to bottom, these are the laminated intervals (MNS- UL1, MNS-UL2, and MNS-LL), and the Bottom Shale interval (MNS-

BS; Fig. 4.1). Additional details on the geological setting and samples are provided in Georgiev et al. (2012).

Re-Os dating of GRL and MNS shales using drill core samples yield precise latest Permian ages (253–252 Ma), and Re-Os and other trace element concentration data were used to argue for simultaneous anoxia, temperature increase, and rising acidity (Georgiev et al. 2011). In stark contrast, incipiently weathered black shale from the Ravnefjeld Formation in GRL outcrop showed poor isochroneity (Georgiev et al. 2012). Further geochemical study of the pristine samples using Cd and N isotopes and trace metal data suggests that the Greenland-Norway seaway, in which GRL and MNS samples were deposited, had strong upwelling and high nutrient utilization (Georgiev et al. 2015).

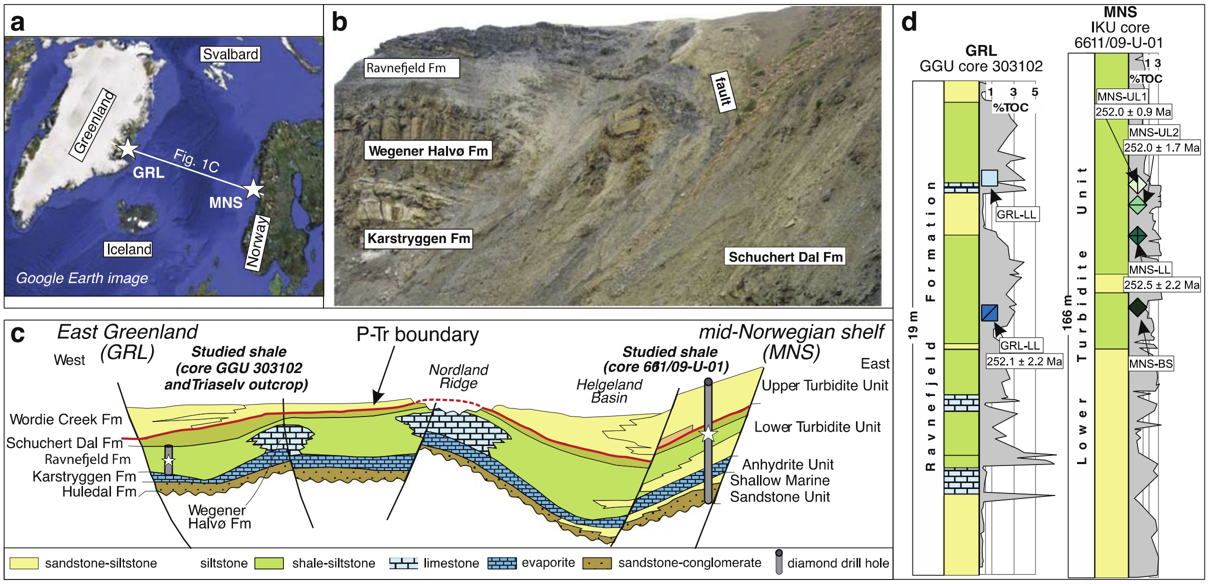

Fig. 4.1 (a) Locations of the two sections, East Greenland (GRL) and mid-Norwegian shelf (MNS); (b) View of GRL Ravnefjeld Formation shales (upper left); (c) Lithostratigraphic cross-section between GRL and MNS from Upper Permian to Lower Triassic formations. White stars indicate shale sections in this study. (d) Detailed lithostratigraphy and chemostratigraphy of TOC for the Ravnefjeld Formation in GRL and Lower Turbidite Unit in MNS. The six sampled shale intervals are marked with different symbols and abbreviations on their locations with Re-Os ages. Modified from Georgiev et al. (2012).

4.4 Methods

Shale powders were prepared as part of previous studies (Georgiev et al. 2012). Mercury contents were obtained using the direct mercury analyzer (Milestone© DMA-80 Evo) in the AIRIE Program labs at Colorado State University. About 100 to 250 mg of black shale powder is weighed and transferred into a nickel boat which is autonomously loaded into the DMA combustion chamber. The sample undergoes combustion, catalyzation (conversion to native mercury), amalgamation, and spectrophotometry.

Measured mercury intensity is compared to a calibration curve derived from systematic measurements of serial dilutions of a liquid mercury standard (SCP Science AA Standard). Instrument and Ni boat backgrounds are monitored during each run and geological reference materials (SDO-1 and NIST 1632e) are routinely analyzed to track instrument accuracy and precision. The average Hg value of SDO-1 measured here is 7% higher than the expected reference value, which is within the reported uncertainties (Kane 1993). All measurements are within 10% variance of the average.

The average Hg value of NIST 1632e measured here is 4% higher than the expected reference, and all measurements are within 10% variance of the average, excluding a single measurement showing 12% higher Hg content than the average. Table 2-1 shows the detailed results of standards monitored during measurements. All samples except two with limited powder were measured twice in two duplicate runs; we used the average value of the two duplicate runs as representative Hg contents of these samples (Table 2-2). Most duplicate runs reproduced within 10%. Duplicates of two samples in MNS-UL1, 241.12–241.14 and 241.19–241.20 are reproducible within 14% and 11%, respectively. Mercury concentration data are discussed together with published geochemical datasets for the same GRL and MNS samples (Georgiev et al. 2011, 2012).

Principal component analysis, also known as empirical orthogonal functions or factor analysis, is a statistical method that reduces the dimensionality of data through use of a new coordinate system. PCA chooses an eigenvector having the highest eigenvalue as the first coordinate, called the first principal component (PC 1). PC 1 explains the greatest variance of the dataset among all the eigenvectors. Then, among all other eigenvectors that are orthogonal to PC 1, the second principal component (PC 2) explains the second most variance of the dataset, and the total number of principal components is determined by the dimensionality of the dataset (Jolliffe 2002).

Other geochemical studies show that PCA is a valuable tool when numerous data must be dealt with simultaneously. For example, Dypvik and Harris (2001) extracted the principal components from 33 elemental contents and ratios of 244 rock samples from Svalbard and the Barents Sea; they related Factor 1 (PC 1) – explaining 42% of the elemental distribution in the samples – to organic carbon, and Factor 2 (PC 2) – explaining 16% of the variance – to carbonates. Tripathy et al. (2014) utilized PCA to elucidate the main source of elements for black shales from the Cambrian-Ordovician boundary and to evaluate the paleo-redox conditions.

We coded up PCA using Python 3.7 and conducted PCA on two different datasets. The first PCA run focused on drill core samples with 23 chemical variables (Re, Os, Hg, V, Mo, TOC, Ca, Sr, Cu, Cr, Ni, Mn, Zn, Co, S, Sc, Fe, Mg, Al, Rb, Th, P, and Cd contents; Table 4.2) to identify the difference in sediment inputs. The second PCA run focused on both GRL outcrop and GRL drill core samples with five variables (Hg, S, Sc, Hydrogen Index – HI, and Oxygen Index – OI; Table 4.4), which are all likely affected by weathering, to verify the behavior of Hg during incipient weathering.

Table 4.1 Hg values of standard materials, SDO-1 and NIST 1632e, measured as quality control

No.	SDO-1 (ppb)	1632e (ppb)
1	206	141
2	202	135
3	195	138
4	208	141
5	202	145
6	184	132
7	205	134
8	203	151
9	209	147
10	208	158
11	205	141
12	189	136
13	209	145
14	210	144
15	223	130
16	-	139
17	-	140
18	-	141
19	-	132
20	-	138
20	-	139
Mean	204	141
Reference	*190	**135
Difference	7%	4%

*Kane (1993)
**Cao et al. (2021)

4.5 Results

All data in this study are available in the supplementary data file (Tables 4.2, 4.3, and 4.5). Mercury contents for the GRL and MNS samples vary between 10 and 144 ppb (Fig. 4.2a and b), and ratios of Hg/TOC for GRL and MNS samples vary between 10 and 59 (Fig. 4.2c and d). In MNS shales, Hg contents systematically increase up-section from MNS-BS to MNS-UL1 (15 ppb to 81 ppb on average). In GRL shales, Hg contents are notably higher than for MNS shales, reaching mean values of 110 ppb Hg for GRL drill core samples and 75 ppb Hg for GRL outcrop samples. The Hg/TOC ratios vary similarly to Hg contents, with two distinctions: (1) Hg/TOC ratios in the MNS-BS are higher than Hg/TOC ratios in the remaining, organic-rich MNS-BS units, and (2) the difference between Hg/TOC ratios of GRL core and GRL outcrop samples decreases. Hg contents of MNS core and GRL core samples plotted against TOC, S, Ca, and Al, as proxies for OM, sulfide, carbonate, and clay minerals, respectively, reveal several important features (Fig. 4.3). The suboxic MNS-BS samples deviate from the trends defined by most other anoxic samples from MNS and GRL, suggesting that the presence of dissolved oxygen in the water column affects Hg speciation. When the MNS-BS samples are excluded, Hg concentrations in all remaining anoxic and euxinic shales show the strongest positive correlation with Ca ($p < 0.01$ and $r = 0.83$, $n = 27$; Fig. 4.3a), followed by a relatively good positive correlation with TOC ($p < 0.01$ and $r = 0.59$, $n = 24$; Fig. 4.3b; note that the three GRL-UL samples are excluded from these statistics, as discussed below). Interestingly, the MNS data generally form curvilinear arrays in Fig. 4.3, unlike GRL samples that define relatively tight, high Hg clusters.

Results from the first PCA for MNS and GRL core samples are shown in Fig. 4.4a and b. Most of the elements are bisected by the first principal component (PC 1), which can explain 53% of the elemental distribution (Fig. 4.4a). PC 1 is ascribed to a contrast between two different element groups: Re, Mo, S, Os, V, and TOC have strong positive signals (>0.5 for PC 1), whereas Al, Rb, Fe, and Th show strong negative signals (<−0.5 for PC 1). The second component, PC 2, explains 21% of the elemental distribution and includes Ca, Mn, and Cr as positive PC 2 and TOC, S, and Fe as negative PC 2. When individual groups of samples are plotted in this two-component space (PC 1 vs. PC 2), GRL and MNS sample groups are clearly separated (Fig. 4.4b). Outcrop samples from GRL were compared with their equivalent core samples to directly examine weathering effects on Hg concentrations in black shale by the second PCA (Fig. 4.4c and d). Here, PC 1 explained 72% of the elemental distribution and isolated OI from other variables (Fig. 4.4c). Outcrop and core shales have distinct PC 1 (Fig. 4.4d). Only Hg shows a highly negative PC 2 value (−0.75).

4.6 Discussion

4.6.1 Weathered outcrop and pristine black shale samples

GRL outcrop samples all show poor Re-Os isochroneity, whereas the GRL-LL core produced a precise Re-Os isochron (Georgiev et al. 2011, 2012). Importantly, the GRL outcrop samples do not have significant weathered features such as a yellowish-reddish color; rather, the disturbed Re-Os isotope systematics, the lower S contents compared to correlative GRL core samples, and the higher oxygen indices from Rock-Eval analyses found in GRL outcrop samples mark their state of incipient weathering (Georgiev et al. 2012). The uppermost studied core interval from GRL, GRL-UL, also exhibits geochemical signals indicative of more subtle weathering and produced a disturbed Re-Os isochron (Georgiev et al. 2012). These authors suggested that a notably shallower depth for GRL-UL (~4.5 m) might have put these shales in contact with oxidizing surface water or groundwater, whereas GRL-LL (~10 m depth) was below the reach of oxidizing water. Thus, GRL outcrop shales, and, to a lesser degree, the GRL-UL drill core interval have been affected by oxidation.

The lowermost shale interval in MNS, the MNS-BS, plots away from other drill core shale samples (Fig. 4.3, Fig. 4.4b). Low concentrations of redox-sensitive trace elements (RSTE: U, V, Se, Re, Os, and Mo) and sulfide-bound trace elements (SBTE: Ni, Zn, Cu, As, Co, and Cd) and low Mo/TOC ratio for MNS-BS shales suggest deposition under more oxygenated conditions, which is also reflected in the larger scatter of the Re-Os isochron data for this interval (MSWD = 14; Georgiev et al. 2011). Here, we focus on estimating Hg behavior in organic-rich black shale during incipient weathering by comparing pristine organic-rich shales with their weathered counterparts (weathered GRL and pristine GRL). As the MNS-BS has no weathered analogue among the studied samples, MNS-BS data are not used to evaluate the effects of weathering. However, all pristine samples, including MNS-BS, are used to evaluate the depositional environment and the hosts of Hg within the GRL-MNS shales.

Table 4.2 Principal component loadings for the first PCA with drill core samples from GRL and MNS.

Sample	PC1	PC2
ORG-454	6.29E-01	1.54E+00
ORG-455	5.47E-01	1.33E+00
ORG-456	5.51E-01	1.33E+00
ORG-428	1.80E+00	2.89E-01
ORG-429	1.54E+00	1.98E-01
ORG-430	1.39E+00	1.29E-01
ORG-431	1.53E+00	5.92E-01
ORG-432	1.25E+00	4.62E-01
ORG-452	1.04E+00	9.05E-01
ORG-433	1.34E+00	6.56E-01
ORG-453	1.57E+00	6.40E-01
ORG-405	-2.95E-01	-8.25E-01
ORG-475	1.52E-01	-8.28E-01
ORG-407	5.96E-01	-9.47E-01
ORG-476	-6.16E-01	-4.83E-01
ORG-477	1.85E-01	-5.23E-01
ORG-478	-4.94E-02	-8.31E-01
ORG-321	-2.11E-01	-7.84E-01
ORG-322	-1.75E-01	-9.13E-01
ORG-323	5.28E-01	-9.96E-01
ORG-324	-1.38E-02	-1.03E+00
ORG-344	-1.58E-01	-1.15E+00
ORG-345	-1.22E-01	-8.87E-01
ORG-363	-7.75E-01	-6.70E-01
ORG-364	-9.60E-01	-8.05E-01
ORG-365	-8.47E-01	-1.30E+00
ORG-366	-6.35E-01	-9.53E-01
ORG-367	-5.16E-01	-1.18E+00
ORG-368	-5.81E-01	-1.12E+00

Elements	PC 1 (52.5%)	PC 2(19.9%)
Re	0.88	-0.16
Os	0.91	-0.07
Hg	0.84	0.21
V	0.86	0.23
Mo	0.83	-0.43
TOC	0.72	-0.62
Ca	0.05	0.90
Sr	-0.82	0.20
Cu	0.33	-0.31
Cr	0.21	0.71
Ni	0.89	0.03
Mn	-0.30	0.61
Zn	0.90	0.27
Co	0.05	0.04
S	0.45	-0.80
Sc	-0.75	-0.20
Fe	-0.67	-0.57
Mg	-0.80	0.37
Al	-0.88	0.27
Rb	-0.84	-0.04
Th	-0.62	-0.76
P	-0.82	-0.44
Cd	0.95	0.11

Table 4.3 Principal component loadings for the second PCA with drill core and outcrop samples from GRL.

Sample	PC1	PC2
ORG-210	4.38E-01	-1.46E+00
ORG-169	-1.63E-01	-5.12E-01
ORG-170	1.24E-01	-1.12E+00
ORG-171	1.15E-01	-1.60E+00
ORG-172	3.49E-01	-9.72E-01
ORG-173	8.32E-02	-4.46E-01
ORG-207	1.30E-01	-2.62E-01
ORG-208	2.67E-01	-4.34E-01
ORG-209	-6.94E-01	-1.72E+00
ORG-212	7.94E-01	1.16E+00
ORG-310	6.88E-01	4.54E-01
ORG-309	7.87E-01	2.51E-01
ORG-308	9.45E-01	5.51E-01
ORG-307	9.68E-01	1.54E+00
ORG-311	8.98E-01	8.92E-01
ORG-312	8.24E-01	9.04E-01
ORG-400	2.52E-01	-3.25E-01
ORG-401	9.53E-01	-4.95E-01
ORG-402	2.72E-01	-1.54E-01
ORG-403	-2.26E-01	3.35E-01
ORG-300	1.48E+00	7.79E-01
ORG-301	9.37E-01	9.32E-01
ORG-302	1.53E+00	1.08E+00
ORG-305	9.70E-01	1.57E+00
ORG-285	1.78E-01	-2.68E-01
ORG-286	6.76E-02	-8.30E-01
ORG-287	3.18E-01	-5.18E-01
ORG-288	1.35E-01	-1.19E+00
ORG-289	2.14E-01	-3.01E+00
ORG-454	-6.87E-01	-2.44E+00
ORG-455	-5.52E-01	-2.42E+00
ORG-456	-9.05E-01	-2.38E+00
ORG-428	-1.70E+00	7.96E-01
ORG-429	-1.85E+00	5.88E-01
ORG-430	-1.80E+00	5.96E-01
ORG-431	-1.56E+00	1.02E+00
ORG-432	-1.74E+00	6.93E-01
ORG-452	-1.53E+00	6.27E-01
ORG-433	-1.77E+00	3.48E-01
ORG-453	-1.68E+00	2.09E-01

Elements	PC 1 (72%)	PC 2(13%)
Hg	-6.6E-01	-7.5E-01
S	-9.4E-01	2.3E-01
Sc	-8.9E-01	1.9E-01
HI	-8.1E-01	1.1E-02
OI	9.2E-01	-1.1E-01

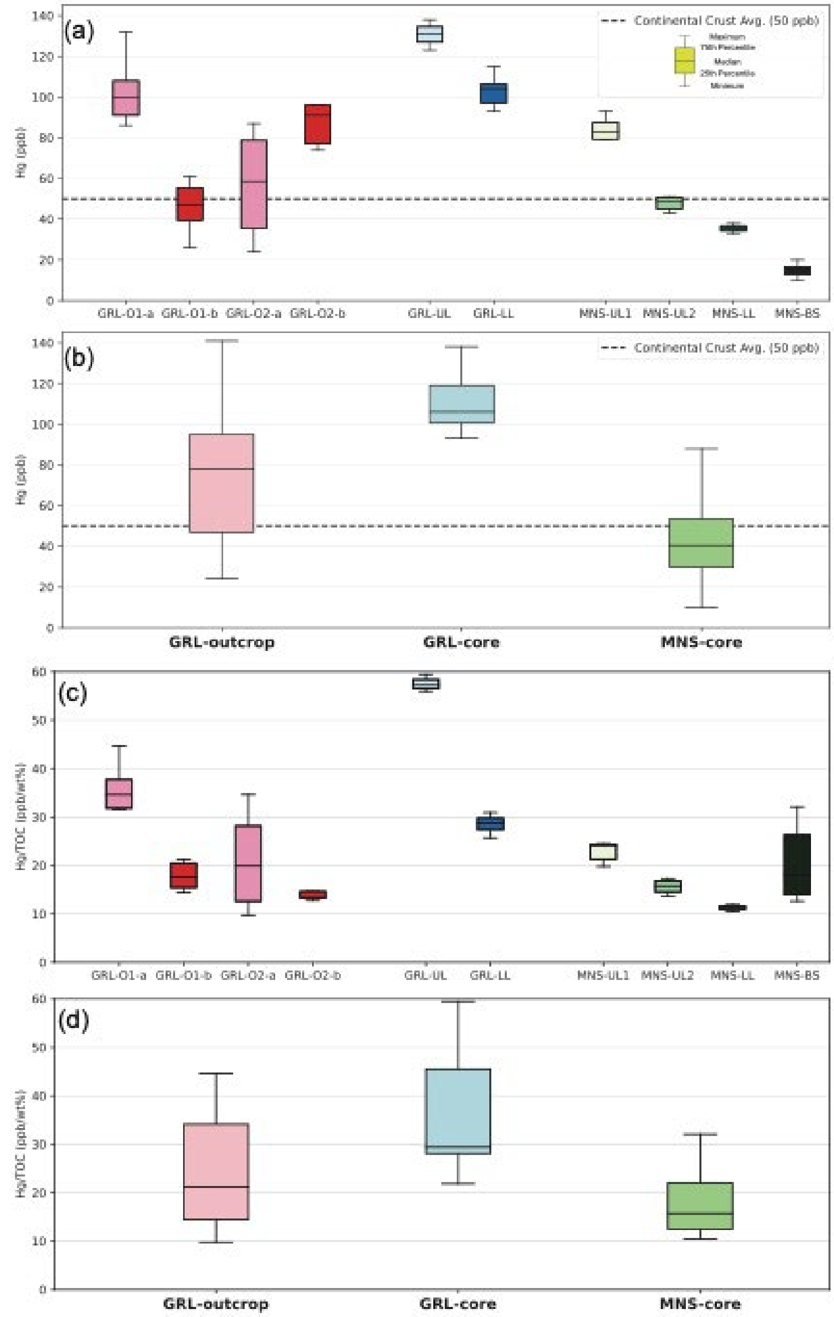

Fig. 4.2 Box plots of Hg contents from different groups in GRL and MNS. (a) Box plot of all groups in GRL outcrop, GRL core, and MNS core. The GRL samples have higher Hg contents than the MNS samples. MNS-BS has a much lower Hg concentration compared to other groups. Outcrop samples show the highest variability in Hg concentrations. (b) Merged box plot of GRL outcrop, GRL core, and MNS core. Mercury contents of the three groups are statistically different in each group at 95% confidence ($p < 0.01$). The average Hg value of the continental crust of 50 ppb is from Rudnick et al. (2003). (c) and (d) Normalizing Hg to TOC reduces the spread among sample groups; in particular, MNS-BS overlaps all other MNS groups.

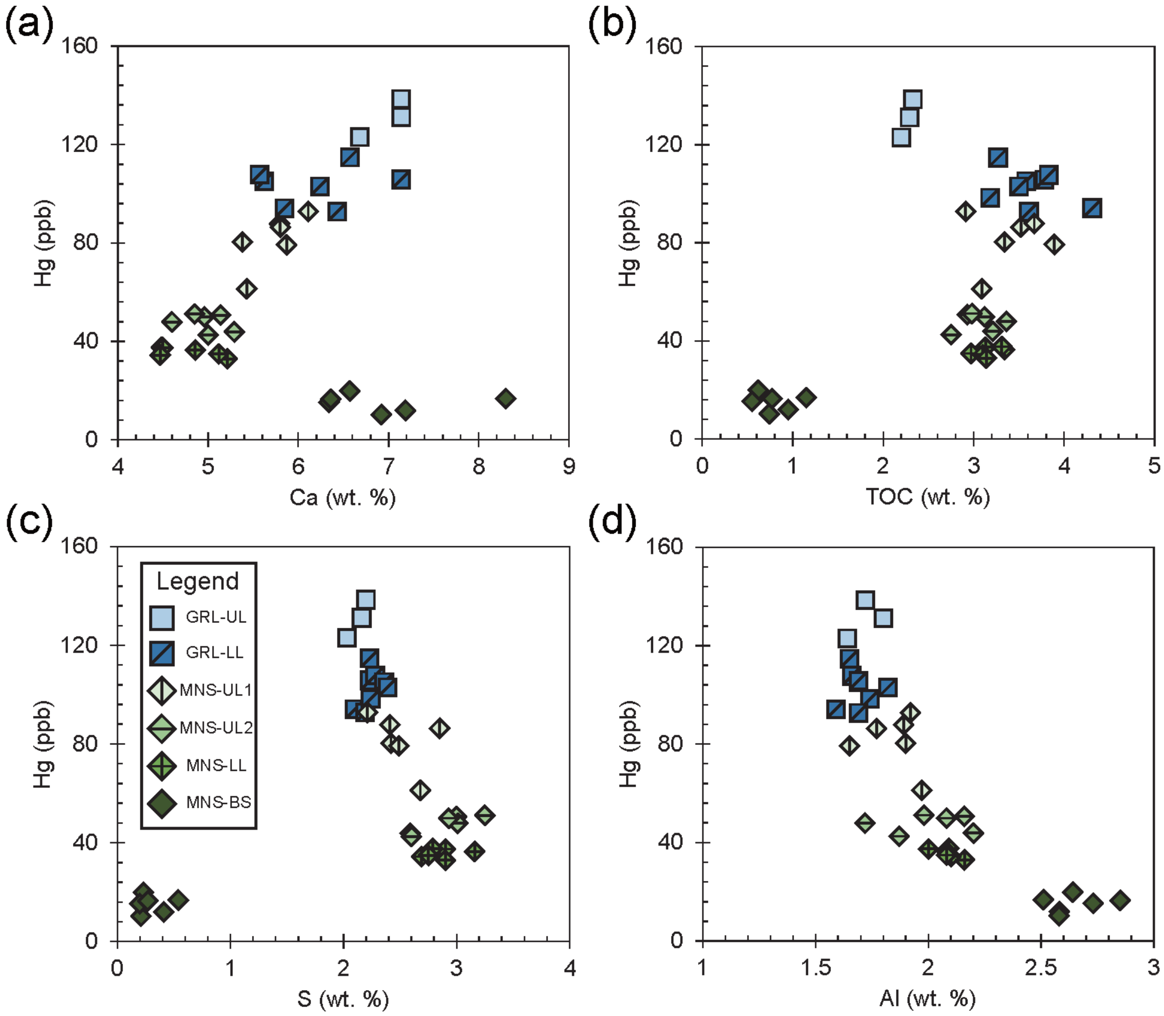

Fig. 4.3 X-Y plots of Hg versus selected elemental proxies for possible hosts in GRL and MNS core samples – (a) Ca for carbonate, (b) TOC for organic matter, (c) S for sulfide, and (d) Al for clay. Note that MNS-BS is a suboxic shale deposited prior to the overlying anoxic MNS and GRL shales that are characterized by high contents of redox-sensitive metals like Mo, Re, Cd, and Se (Georgiev et al. 2011, 2015).

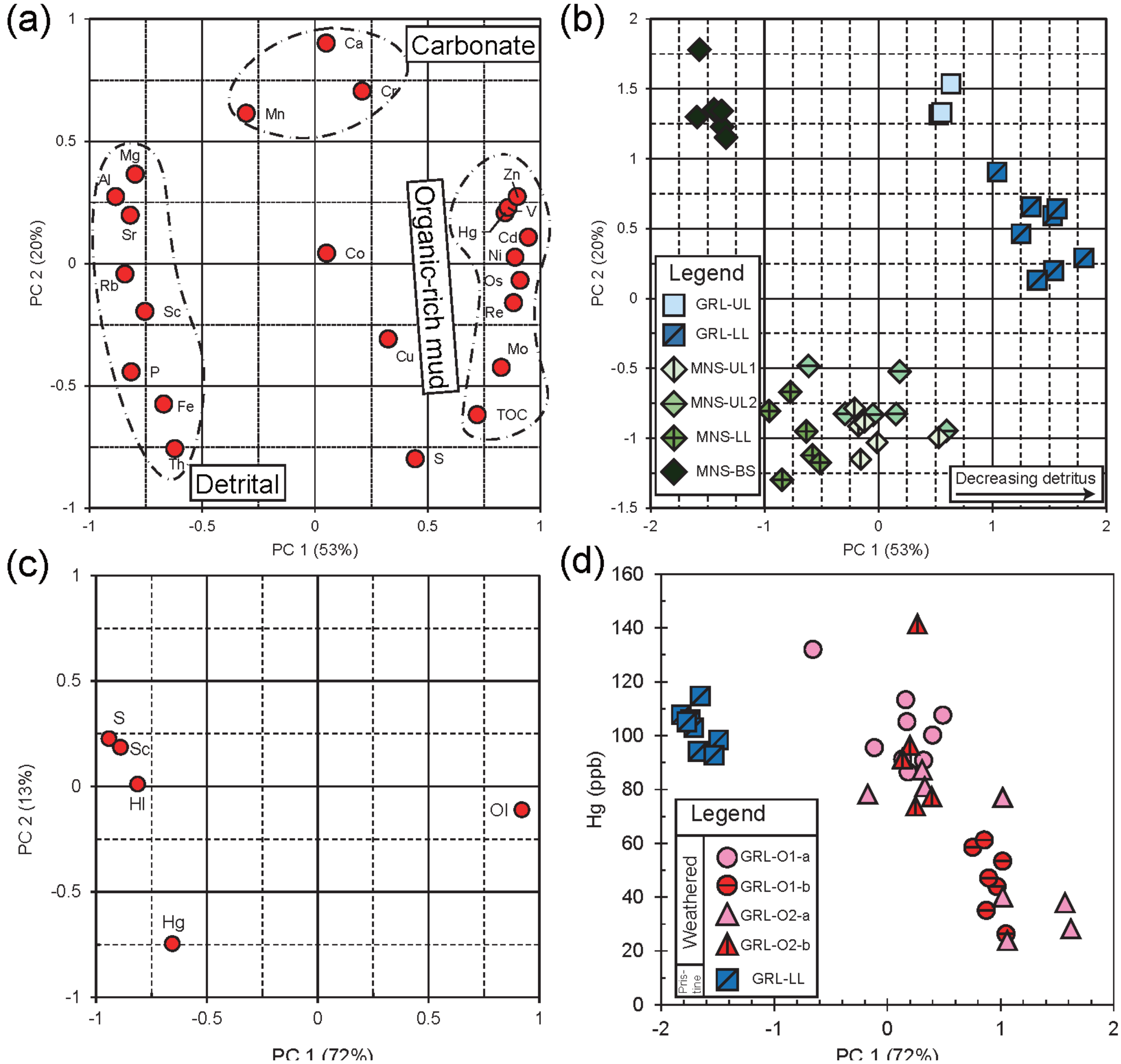

Fig. 4.4 The results of the first PCA with pristine GRL and MNS drill core samples (a, b) and the second PCA with pristine GRL samples and incipiently weathered GRL outcrop samples (c, d); (a) Principal components (PCs) with major and trace elements; (b) The distribution of core samples by PC 1 and PC 2. GRL and MNS shales are grouped by PC 1 and PC 2, indicating different depositional environments; (c) PC 1 and PC 2 of the second PCA with variables vulnerable to incipient weathering (Note that HI is hydrogen index and OI is oxygen index from Rock-Eval analyses); (d) Hg contents vs. PC 1 of the second PCA, indicating the degree of the weathering. The good correlation between Hg contents and PC 1 indicates that Hg is vulnerable to incipient weathering. Note that GRL-UL unit shows chemical evidence for incipient weathering, whereas all remaining units in GRL core samples are considered pristine and unaffected by weathering (Georgiev et al. 2012).

4.6.2 Depositional environments and hosts for Hg

GRL drill core shales have twice the average Hg content of MNS drill core shales (Fig. 4.2, Fig. 4.3), even though shales at both localities are time equivalent, deposited at 252 Ma near each other prior to the opening of the North Atlantic Ocean (Georgiev et al. 2012). When PCA was performed with pristine black shales only (GRL-UL, MNS-UL1, MNS-UL2, MNS-LL, and MNS-BS; Fig. 4.4a and b), Fig. 4.4a shows that the majority of the elemental variations (51%) are explained by PC 1 representing authigenic (positive PC 1) and detrital minerals (negative PC 1). Although GRL and MNS Upper Permian shales both reflect anoxic conditions (Georgiev et al. 2012), pristine MNS shales show more detrital input (PC 1 between −1 and + 1) than pristine GRL with PC 1 > 1 (Fig. 4.4b). The difference in the detrital vs. authigenic phases apparently exerts a primary control of Hg contents in GRL and MNS. This observation is consistent with the interpretation from heavier C isotopes in MNS black shales, suggesting a higher proportion of terrigenous OM compared to GRL black shales (Bugge et al. 2002). Sanei and Goodarzi (2006) pointed out that terrigenous OM is too refractory to concentrate Hg in its structure chemically. Thus, the differences in Hg concentrations between MNS and GRL could be attributable to the changing balance between two distinct sources: the supply of terrigenous materials and the formation of authigenic phases.

The MNS data are aligned along a curvilinear line towards the tight cluster of GRL samples (Fig. 4.3), suggesting that the depositional environment in MNS gradually evolved towards an environment similar to GRL. Of all MNS samples, the MNS-UL1 shales are most similar to GRL-LL samples in Hg contents (Fig. 4.2, Fig. 4.3). Our first PCA results show that detrital inputs decrease (PC 1 increases) from MNS-LL towards MNS-UL1 and MNS-UL2 (Fig. 4.4b), which again suggests that the balance between detrital supply and authigenic precipitation is the major control on Hg content of these shales. Georgiev et al. (2015) argued that the strength of upwelling in MNS was steadily developed from MNS-BS to MNS-LL and MNS-UL, and the upwelling in GRL is stronger than in MNS. Thus, linear arrays of MNS data towards GRL data in Fig. 4.3 may also reflect this gradual increase of the upwelling strength in MNS.

The main potential hosts for Hg in shale are OM, sulfide, and clay minerals (e.g., Shen et al. 2020), with carbonate minerals representing an additional possibility in modern sediments (Orecchio and Polizzotto 2013). The inverse relationship between Hg and Al in all studied shales clearly shows that the detrital influx (marked by high Al contents) into the anoxic-euxinic depositional basin dilutes Hg contents (Fig. 4.3d). Interestingly, Ca contents display the best positive correlation with Hg ($p < 0.01$ and $r = 0.83$; Fig. 4.3a), suggesting that carbonates may host significant Hg in shales. To assess whether carbonate in MNS shales holds Hg or not, we analyzed the solutions and shale residues following HCl treatment of selected MNS shales. Black shale powders were soaked in 1 mol/L HCl until all CO2 was degassed. Residual shale was separated from the acidic solution, rinsed with Milli-Q water, and dried. Precipitates of the acidic solution may contain any Hg held by carbonates unless lost during the experiment. We analyzed both the precipitates (to evaluate is Hg was released during carbonate dissolution) and the residual shales (to confirm the extent of Hg removal during carbonate dissolution). The similar contents of original powders and de-carbonized powders (the residual shale after being treated by HCl) show that carbonate does not hold Hg in MNS shale (Fig. 4.5 and Table 4.4). Therefore, we exclude clay and carbonate minerals as a significant host for Hg, noting that further research is needed to identify the relationship between Hg and Ca in other settings.

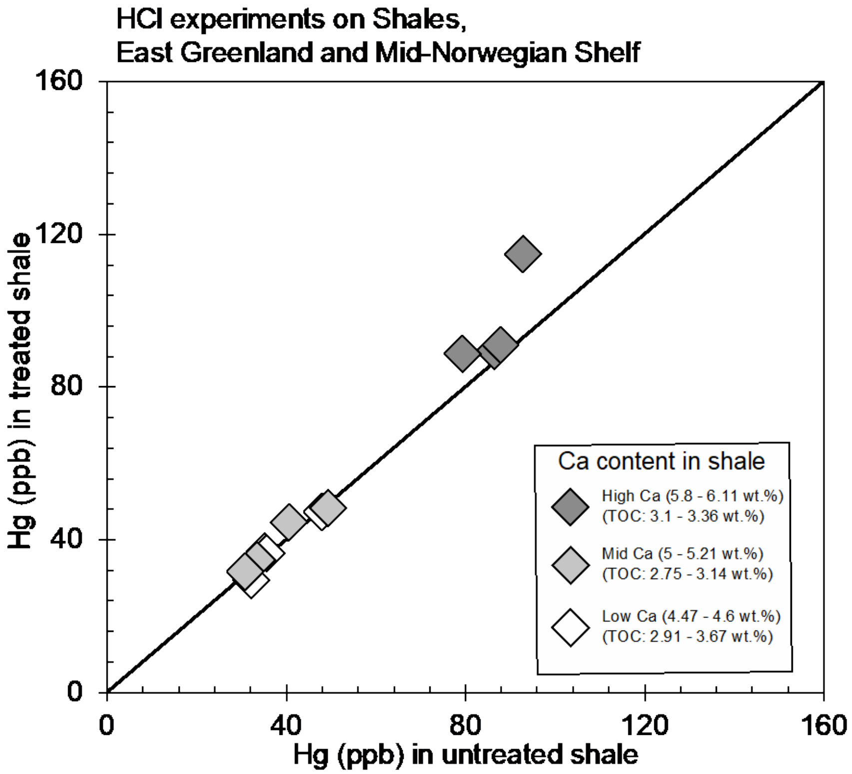

Fig. 4.5 Hg contents before (x-axis) and after (y-axis) the HCl treatment of shale powders. De-carbonized shales after the HCl treatment have similar contents to the original untreated powders, indicating that carbonate is not a significant host of mercury.

Like Al, S contents also show an inverse correlation with Hg, indicating that sulfide minerals are not the main host of Hg in shale (Fig. 4.3c), although Shen et al. (2019a) argued that syngenetic pyrite would take in Hg under intensely reduced/euxinic conditions. In contrast, TOC has a positive correlation with Hg in studied shales (Fig. 4.3b). The coefficient of determination – r value – of the Hg vs. TOC regression (r = 0.59) seems too low to firmly establish that OM is the principal host for Hg. However, the correlation is significant based on the p-value ($p < 0.01$). Also, other possible hosts such as clay, carbonate, and sulfide were excluded as significant Hg hosts, as shown above. Collectively, these observations suggest that OM is the significant host of Hg in the studied samples.

Table 4.4 Hg contents in shales before and after the HCl treatment.

Low Ca (4.47 - 4.6 wt%)	ORG#	original Hg	after the HCl treatment	Hg in carbonates	mass balance
#1	ORG-323	48	54	4	47
#2	ORG-366	32	31	7	29
#3	ORG-367	35	40	4	37
#4	ORG-368	36	41	4	36
Mid Ca (5 - 5.21 wt%)					
#5	ORG-324	49	53	5	48
#6	ORG-345	41	51	2	45
#7	ORG-363	33	38	5	35
#8	ORG-364	31	33	7	32
High Ca (5.8 - 6.11 wt%)					
#9	ORG-475	86	102	7	89
#10	ORG-407	79	104	4	89
#11	ORG-476	93	130	8	115
#12	ORG-477	88	107	1	91

The Mo/TOC ratio in shales is often used to estimate the degree of basin restriction during shale deposition, where low ratios imply a more restricted basin, and high ratios imply a less restricted basin (e.g., Algeo and Lyons 2006). Studied shales in GRL and MNS were deposited in a less restricted basin based on their relatively high Mo/TOC ratio (~16.7) compared with the Black Sea (~4.5). However, the GRL-MNS basin was more restricted than the present-day Saanich Inlet (Mo/TOC of 45), indicating moderate water restriction for GRL-MNS (Georgiev et al. 2011). Also, the high TOC contents of studied organic-rich shales resulted from a high paleoproductivity caused by intense upwelling (Georgiev et al. 2015). The high correlation between TOC and Hg contents, high paleoproductivity by upwelling, and moderate restriction with limited dissolved oxygen supplies might cause OM to be the principal host of Hg in the Late Permian MNS-GRL basins.

Shen et al. (2020) proposed a cross-plot between S and TOC to classify OM-hosted and sulfide-hosted Hg (Fig. 4.6), noting that the diagram needs further work and development. Our study suggests that this plot has limited applications. Mercury in the studied shales is hosted mainly by OM (Fig. 4.3b in the manuscript), and sulfide does not show any positive correlations with Hg (Fig. 4.3c in the manuscript), but our shales plot in a tight cluster in the sulfide-hosted area. Clearly, the TOC-S plot does not well distinguish the Hg host. Between the 1:1 and 1:0.35 lines a large number of sulfide-hosted and OM-hosted data overlap (Fig. 4.6). As a starting point to examine the utility of this TOC-S plot, the sedimentary rocks in this band of overlap should be revisited in detail to more quantitatively identify the main host for Hg.

4.6.3 Effects of incipient weathering on Hg contents

In the second PCA, based on weathered and unweathered GRL samples only (Fig. 4.4c and d), negative values of PC 1 are related to higher HI and S, Sc, and Hg contents, which collectively indicate weaker weathering or no weathering. In contrast, positive values of PC 1 related to higher OI indicate stronger weathering (Fig. 4.4c). Hydrogen index is a proxy of the hydrogen content of kerogen, and OI is for the oxygen content (Peters 1986). These results are consistent with the conclusions of previous studies that show HI decreases and OI increases in black shales during post-depositional processes such as oxidation or maturation (Vandenbroucke and Largeau 2007; Georgiev et al. 2012; Marynowski et al. 2017; Charbonnier et al. 2020). As a result, PC 1 in the second PCA can be used as a reliable indicator for the degree of weathering in outcrop-derived shale samples (Fig. 4.4d). Of the five key parameters defining PC 1, only Hg shows a notable (negative) relation to PC 2, which is mainly determined by various Hg contents from GRL samples. PC 2 accounts for only 13% of the elemental distribution, which is much less significant than PC 1 (72%).

The weathering indicator PC 1 shows a significant correlation with Hg in weathered shales ($r = 0.81$, $p < 0.01$). The average TOC content in weathered GRL shales is 9% lower than in pristine GRL (3.28 wt% vs. 3.63 wt%, respectively). However, outcrop shales lost up to 77% of Hg during

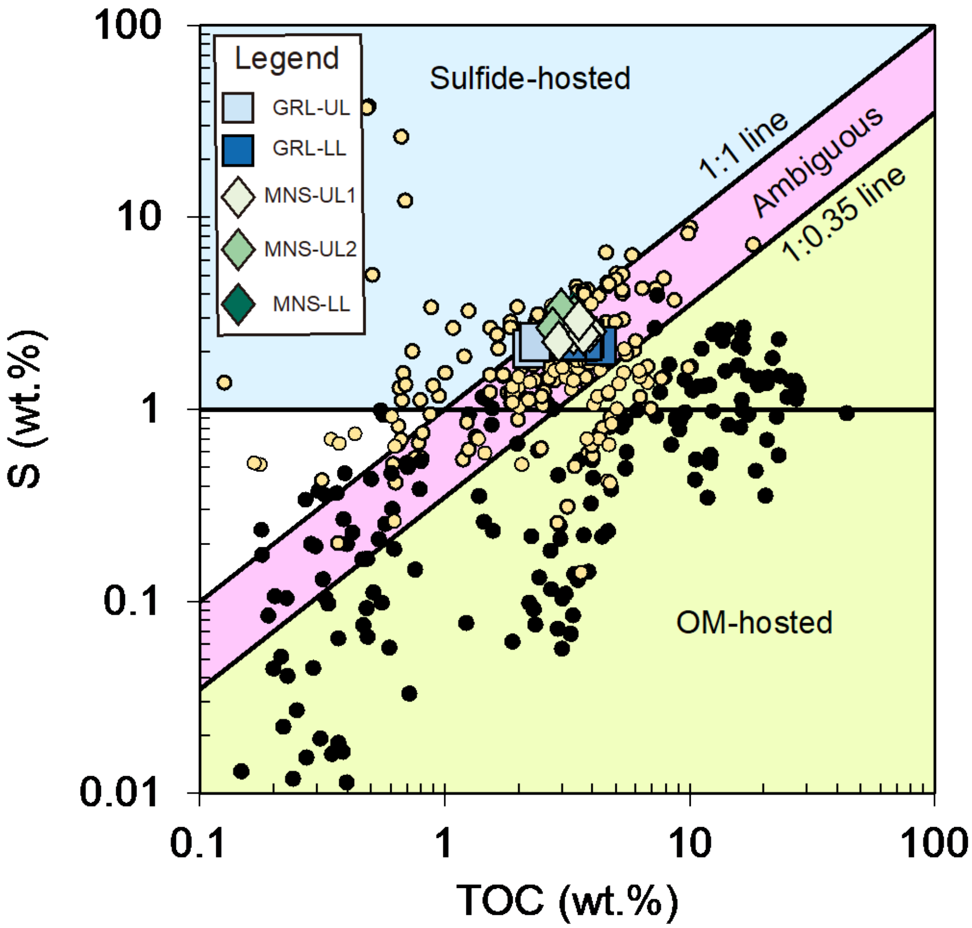

Fig. 4.6 Modified TOC-S plot to identify the main host for Hg as suggested by Shen et al. (2020). Yellow and black dots represent sulfide-hosted Hg and OM-hosted Hg sediments (excluding modern day), respectively (Shen et al. 2020; Them II et al. 2019; Zheng et al. 2018; Shen et al. 2019a). Shen et al. (2020) suggested the 1:0.35 line could be a threshold between OM-hosted and sulfide-hosted sediments, but the studied shales here are all located above this threshold. The area between the 1:0.35 and 1:1 lines, as designated here (pink), includes sediments with both sulfide-hosted and OM-hosted Hg. Notably, the shales in our study, whether pyrite-bearing or not, plot closely together, in a space that is perhaps more appropriately labeled "ambiguous." In sum, use of a TOC versus S plot does not well describe the host association for Hg.

incipient weathering from an average of 103 ppb Hg in the pristine samples down to a low of 24 ppb Hg in weathered samples (Fig. 4.4d). The ratios of Hg/TOC in outcrop shales also show up to 64% lower values compared to pristine samples (from 28 down to 10; Fig. S3a). Similar decreasing trends are shown in variations of other weathering vulnerable elements (Mo and Re) with PC 1 of the second PCA (Fig. 4.6).

Three possible processes might explain the OM-hosted Hg loss during incipient weathering. First, partial degradation of OM, which causes minimal to small TOC loss, could play a critical role in Hg retention during incipient weathering if Hg-rich entities are degraded. Mercury data on modern sediment from eutrophic lakes indicate that soluble organic matter (SOM; the easily degradable lipid fraction) concentrates Hg and other OM-related metals, even as SOM accounts for 2.5 wt% of the whole rock on average (Sanei and Goodarzi 2006). In addition, transformations of the kerogen and SOM structure by the oxidation process may release Hg hosted by OM. Low molecular weight organic compounds like methylnaphthalenes, dibenzofuran, or dibenzothiophene are susceptible even during incipient weathering (Marynowski et al. 2011), and some of these may account for part of the Hg loss. Loss of Mo and altered Mo stable isotope ratios were also reported from partially weathered black shales (Marynowski et al. 2017). In addition, destruction of specific components in kerogen that may preferentially hold Hg may play the main role in releasing Hg. Preferential destruction of aliphatic kerogen compared to carbonyl and aromatic components during weathering has been reported, although the degree of weathering of the studied samples was higher than incipient weathering (Petsch et al. 2001). Thus, Hg loss in samples during incipient weathering could be caused by partial degradation or transformations of OM. In our study, sulfide oxidation is unlikely to be the main reduction process for Hg in the studied shales because sulfide is not a primary host of Hg in pristine samples (Fig. 4.2c). In sedimentary rocks with sulfide-hosted Hg, the Hg concentrations will be more vulnerable to incipient weathering because oxidation of sulfide is faster and occurs earlier than that of OM (Petsch et al. 2000; Wildman et al. 2004; Georgiev et al. 2012; Marynowski et al. 2017).

Our results show that incipient weathering may dampen and conceal originally higher Hg and Hg/TOC ratios in sedimentary rocks (Fig. 4.4d and S2a). Peaks of Hg signals in sediments have been highlighted as a LIP tracer for decades, but concealed Hg signals in sedimentary sections came to be highlighted recently. For example, the Toarcian Oceanic Anoxic Event (T-OAE; 183 Ma) is a well-studied anoxic event that was probably caused by eruptions of the Karoo-Ferrar LIP (e.g., Percival et al. 2015). Elevated Hg contents and Hg/TOC ratios would be expected in Toarcian sediments, but some T-OAE sections do not show Hg anomalies (Them II et al. 2019). The authors ruled out the possibility of diagenesis (including weathering) to explain the lack of Hg/TOC signals because they assumed that Hg is mainly hosted by OM (Them II et al. 2019). Nonetheless, results in this study, in which TOC (representing OM) and Hg are impacted at different stages of weathering, suggest that dampened Hg/TOC signals may be caused by incipient weathering. Also, the magnitude of Hg/TOC peaks in some ancient organic-rich shales may depend on how euxinic the depositional environment is (Shen et al. 2020). Under strongly euxinic conditions, sulfide is a more prominent host for Hg, and incipient weathering may indeed affect sulfide-hosted Hg concentrations more profoundly than our samples, in which Hg is mainly hosted by OM.

Overall, we suggest a schematic diagram of Hg, S, TOC, and Hg/TOC changes with the degree of weathering (Fig. 4.7). The ratio is established at a certain point when the rock is pristine. During incipient weathering, TOC and Hg content decrease with different slopes while S content decreases severely. As a result, the Hg/TOC ratio decreases, even though TOC content remains relatively constant. During extreme weathering, loss of TOC is dramatic, and the Hg/TOC ratio may increase sharply as TOC contents decrease to 1% or less (Charbonnier et al. 2020). Thus, incipient weathering may release Hg, masking possible positive Hg anomalies even as TOC contents remain constant. Extreme weathering, in contrast, can degrade organic matter, resulting in loss of TOC and an increase in Hg/TOC, potentially misinterpreted as a positive Hg anomaly. Given these results, caution is necessary for the interpretation of Hg concentrations and Hg/TOC ratios, particularly when positive anomalies are expected, but not observed, even if the shales look fresh and TOC values do not seem to be strongly reduced by weathering.

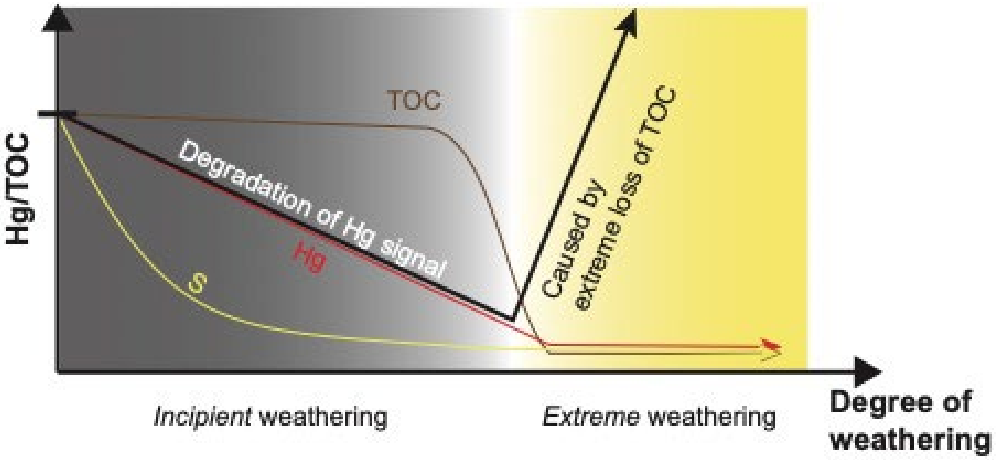

Fig. 4.7 Schematic illustration of Hg/TOC ratio, TOC, Hg, and S changes in organic-rich shales during weathering. Degradation of Hg signals occurs even with incipient and invisible weathering, while degradation of OM is limited as shown in this study. This lowers the Hg/TOC ratio, a parameter in use to characterize paleo-environments. In contrast, loss of organic matter during extreme weathering dramatically increases Hg/TOC ratios (Charbonnier et al. 2020). The loss of S proceeds OM loss (Petsch et al. 2000; Georgiev et al. 2012).

4.7 Conclusion

Detailed analysis of mercury contents using statistical tools and an expanded geochemical dataset from previous studies of GRL and MNS Upper Permian shales clarify the effect of incipient weathering on shale Hg contents. Mercury contents from the GRL and MNS drill cores average 110 ppb and 55 ppb, respectively; the difference between the two sites is attributed to the degree of detrital influx, including kerogen types (OM sources). A detailed comparison between Hg and possible host elements demonstrates that organic matter is the main Hg host in Upper Permian shales from GRL and MNS drill cores. Those shales were deposited in a setting with a high paleoproductivity by upwelling and moderate basin restriction. Up to 77% Hg loss and up to 64% lower Hg/TOC ratios were observed in incipiently weathered GRL outcrop shales that appear visually fresh (based on Re-Os isotopic characteristics and other chemical criteria). Destruction of soluble organic matter or specific kerogen entities and transformation of kerogen components are the likely causes of lower Hg contents of partly weathered samples, although further research is needed to constrain the exact cause. The observed Hg loss upon incipient weathering calls for prudent interpretations of Hg data in outcrop shales. Identification of weathering is an essential prerequisite that needs to be applied prior to interpretations of paleoenvironmental conditions based on the Hg geochemistry of outcrop samples.

Chapter 5 Conclusions and Future Work

These studies explored the Middle-Late Jurassic black shales through the Re-Os radiometric dating method in loosely constrained Boreal sections and assessed depositional environments using geochemical parameters. One study examined Hg degradation during incipient weathering by examining both weathered and pristine drill cores from latest Permian black shales. Chapter 2 presents seven new Re-Os ages from the Agardhfjellet Formation and discussed the source of initial Os in the ocean during the Late Jurassic. Chapter 3 provides a detailed examination of the geochemical characteristics of organic-rich shale from the Agardhfjellet Formation, including C, S, O, and N stable isotopes, to reveal basin environment evolution from 160 Ma to 147 Ma. Chapter 4 specifically scrutinizes mercury (Hg) in organic-rich black shale concerning how weathering impacts Hg signals in sedimentary rocks widely used as a volcanic proxy.

In Chapter 2, we dated the Agardhfjellet formation—one of the most hydrocarbon-prolific source rocks—using Re-Os ages due to the limitation of the biostratigraphy by prevalent provincialism among ammonite species hindering realm connections. The Re-Os radiometric method offers benefits for dating the depositional ages of organic-rich shales—major hosts for Re and Os—and estimating paleocean geochemistry with initial Os ratios.

Key findings included:

1. Seven new Re-Os ages derived from Late Jurassic black shale samples ranging between 160.1 Ma and 146.8 Ma.
2. These new ages serve as cornerstones for correlating Boreal sections with other realms such as Tethyan or Andean regions.
3. The rise in initial Os ratios during the studied period suggests increased terrestrial runoff or reduced unradiogenic Os input from mantle-derived sources.

Chapter 3 conducted comprehensive geochemical investigations on Agardhfjellet Formation, evaluating depositional setting evolution during the shelf anoxic-dysoxic event based on major/trace elements and stable isotopes; principal component analysis distinguished sediment sources.

Key findings included:

1. SDAE recorded in the Agardhfjellet Formation mainly initiated Oxfordian between Oppdalen Member and Lardyfjellet Member.
2. Terrestrial sediment source decreased at the boundary between Oppdalen & Lardyfjellet Members, favoring hydrogenous (authigenic) sources.
3. Basin restriction degree based on Mo/TOC and Mo_{EF} related to U_{EF} was significantly high during Lardyfjellet Member deposition compared to other members.
4. Compared to other Phanerozoic OAEs such as Toarcian OAE & OAE2, organic-rich black shale from the Agardhfjellet Formation may have been deposited under more restricted conditions where local/regional isolation played a critical role rather than global deposition.

Chapter 4 examined Hg degradation within well-studied Upper Permian black shale section from the East Greenland/Mid-Norwegian Shelf, identifying early-stage weathering—incipient weathering—impact on Hg concentration loss; principal component analysis quantified weathering degree based on vulnerable geochemical values with Hg contents such as HI, OI, TOC, S, and Sc.

Key findings included:

1. Despite similar location/age of lower turbidite black shale from the Mid-Norwegian Shelf (MNS) & black shale from the Ravnefjeld Formation in East Greenland (GRL), PCA results revealed greater terrestrial input impact on MNS black shale.

2. Mercury in both GRL & MNS pristine samples is primarily hosted by organic matter rather than sulfide or clay minerals.

3. Incipient weathering recorded by sulfide loss but not organic matter (TOC) loss affects Hg concentrations in sedimentary rocks based on PCA results. This necessitates caution when investigating Hg signals of sediments as a volcanic activity proxy, even if rocks appear visually pristine.

The International Commission on Stratigraphy (ICS) has regularly updated radiometric ages for Stages, Periods, or Eras in its *INTERNATIONAL CHRONOSTRATIGRAPHIC CHART* since 2013 (Cohen et al., 2013), also known as GTS (Geologic Time Scale). However, the Late Jurassic to Early Cretaceous remains complex in terms of defining precise ages due to the absence of global boundary stratotype sections and points (GSSP) that determine stage boundaries as international standards (Cohen et al., 2013).

Most radiometric ages have been derived from U-Pb and Ar-Ar dating methods; however, these methods are often limited due to a lack of ash layers containing mineral grains for the specific radiometric methods. This dissertation, for some stratigraphic intervals, has contributed accurate and precise Late Jurassic ages to better constrain the GTS. In particular, the Oxfordian stage was updated in the latest International Chronostratigraphic Chart from 163.5 - 157.3 Ma to 161.5 - 154.8 Ma, which is consistent with the Re-Os ages results in Chapter 2. Furthermore, this dissertation has taken initial steps towards characterizing geochemical features during a Shelf Dysoxic-Anoxic Event (SDAE), a relatively new concept (Rogov et al., 2020) related to ocean anoxia but crucial for understanding one of the most prolific petroleum source rocks deposited during the Middle Jurassic – Early Cretaceous. The study also highlights the need for extreme caution when interpreting Hg signals derived from samples of outcropping sedimentary rocks that may appear fresh and pristine, but in fact are incipiently altered; thus this work provides a contribution valuable for working groups using Hg signals as paleoproxies.

Despite progress made through this dissertation, many questions remain about how large amounts of organic matter could have been deposited during the Middle Jurassic – Early Cretaceous. Future research plans include refining Re-Os ages around the J/K boundary with more data from upper intervals of the Agardhfjellet Formation. Additionally, collaboration with researchers working on biomarkers for ancient methane release is needed as volcanic activities may not fully explain warming and environmental disturbances during this enigmatic period.

Furthermore, I plan to develop a numerical model study for reconstructing atmospheric/oceanic circulation patterns that might have affected depositional environments but remained unstudied until now. Such modeling will validate geochemical interpretations through sedimentary rocks by controlling environmental factors like temperature or carbon/sulfur cycles.

Lastly, I aim to explore additional aspects concerning Hg geochemistry, including Hg isotopes, which can provide unique insights into Hg deposition within highly restricted basins predominantly influenced by terrestrial runoff—most previous literature on Hg or Hg isotopes is associated with volcanic activities. The proposed research may unravel secrets behind massive organic matter deposition during the Late Jurassic by evaluating changes in photic zone euxinia and Hg sources via Hg isotope analyses—ultimately contributing to paleoclimate and geochemistry communities by providing new insights for interpreting Hg signals as indicators of paleoenvironment.

References

Abay, T. B., Karlsen, D. A., Lerch, B., Olaussen, S., Pedersen, J. H., & Backer-Owe, K. (2017). Migrated petroleum in outcropping Mesozoic sedimentary rocks in Spitsbergen: Organic geochemical characterization and implications for regional exploration. *Journal of Petroleum Geology*, *40*(1), 5-36.

Abay, T. B., Karlsen, D. A., Pedersen, J. H., Olaussen, S., & Backer-Owe, K. (2018). Thermal maturity, hydrocarbon potential and kerogen type of some Triassic–Lower Cretaceous sediments from the SW Barents Sea and Svalbard. *Petroleum Geoscience*, *24*(3), 349-373.

Algeo, T. J., & Liu, J. (2020). A re-assessment of elemental proxies for paleoredox analysis. *Chemical Geology*, *540*, 119549.

Algeo, T. J., & Lyons, T. W. (2006). Mo–total organic carbon covariation in modern anoxic marine environments: Implications for analysis of paleoredox and paleohydrographic conditions. *Paleoceanography*, *21*(1).

Algeo, T. J., & Tribovillard, N. (2009). Environmental analysis of paleoceanographic systems based on molybdenum–uranium covariation. *Chemical Geology*, *268*(3-4), 211-225.

Algeo, T. J., Wilkinson, B. H., & Lohmann, K. C. (1992). Meteoric-burial diagenesis of Middle Pennsylvanian limestones in the Orogrande Basin, New Mexico; water/rock interactions and basin geothermics. *Journal of Sedimentary Research*, *62*(4), 652-670.

Amorosi, A. (2012). Chromium and nickel as indicators of source-to-sink sediment transfer in a Holocene alluvial and coastal system (Po Plain, Italy). *Sedimentary Geology*, *280*, 260-269.

Anbar, A. D., & Knoll, A. H. (2002). Proterozoic ocean chemistry and evolution: a bioinorganic bridge?. *Science*, *297*(5584), 1137-1142.

Ardakani, O. H., Chappaz, A., Sanei, H., & Mayer, B. (2016). Effect of thermal maturity on remobilization of molybdenum in black shales. *Earth and Planetary Science Letters*, 449, 311-320.

Armstrong, H. A., Wagner, T., Herringshaw, L. G., Farnsworth, A. J., Lunt, D. J., Harland, M. M., Imber, J., Loptson, C., & Atar, E. F. (2016). Hadley circulation and precipitation changes controlling black shale deposition in the Late Jurassic Boreal Seaway. *Paleoceanography*, *31*(8), 1041-1053.

Baraboshkin, E. Y. (2004). Boreal-Tethyan correlation of Lower Cretaceous ammonite scales. *Moscow University Geology Bulletin*, 59(6), 9-20.

Beerling, D. J., Lomas, M. R., & Gröcke, D. R. (2002). On the nature of methane gas-hydrate dissociation during the Toarcian and Aptian oceanic anoxic events. *American Journal of Science*, *302*(1), 28–49.

Bennett, W. W., & Canfield, D. E. (2020). Redox-sensitive trace metals as paleoredox proxies: a review and analysis of data from modern sediments. *Earth-Science Reviews*, 204, 103175.

Bergh, S. G., Braathen, A., & Andresen, A., (1997). Interaction of basement-involved and thin-skinned tectonism in the Tertiary Fold-Thrust belt of central Spitsbergen, Svalbard. *American Association of Petroleum Geologists Bulletin*, 81, 637–661.

Bingen, B., Austrheim, H., & Whitehouse, M. (2001). Ilmenite as a source for zirconium during high-grade metamorphism? Textural evidence from the Caledonides of Western Norway and implications for zircon geochronology. *Journal of Petrology*, *42*(2), 355-375.

Bjerrum, C. J., Surlyk, F., Callomon, J. H., & Slingerland, R. L. (2001). Numerical paleoceanographic study of the Early Jurassic transcontinental Laurasian Seaway. *Paleoceanography*, *16*(4), 390-404.

Bond, D. P., & Wignall, P. B. (2010). Pyrite framboid study of marine Permian–Triassic boundary sections: a complex anoxic event and its relationship to contemporaneous mass extinction. *GSA Bulletin*, *122*(7-8), 1265-1279.

Braathen, A., Bergh, S.G., & Maher, H.D. Jr. (1999). Application of a critical wedge taper model to the Tertiary transpressional foldthrust belt on Spitsbergen. *Geological Society of America Bulletin 111*, 1468−1485.

Braathen, A., Bælum, K., Christiansen, H.H., Dahl, T., Eiken, O., Elvebakk, H., Hansen, F., Hanssen, T.H., Jochmann, M., Johansen, T.A., Johnsen, H., Larsen, L., Lie, T., Mertes, J., Mørk, A., Mørk, M. B., Nemec, W., Olaussen, S., Oye, V., Rød, K., Titlestad, G. O., Tveranger, J., & Vagle, K. (2012). The Longyearbyen CO 2 Lab of Svalbard, Norway—initial assessment of the geological conditions for CO 2 sequestration. *Norwegian Journal of Geology/Norsk Geologisk Forening*, *92*(4).

Brigaud, B., Andrieu, S., Blaise, T., Haurine, F., & Barbarand, J. (2021). Calcite uranium–lead geochronology applied to hardground lithification and sequence boundary dating. Sedimentology, 68(1), 168-195.

Brikiatis, L. (2023). A major orbito-hyetal event at the middle-to-late Oxfordian transition (Late Jurassic). *Marine and Petroleum Geology*, *148*, 106064.

Brumsack, H. J. (2006). The trace metal content of recent organic carbon-rich sediments: Implications for Cretaceous black shale formation. *Palaeogeography, Palaeoclimatology, Palaeoecology*, 232(2–4), 344–361. https://doi.org/10.1016/j.palaeo.2005.05.011

Bucholz, C. E., & Spencer, C. J. (2019). Strongly peraluminous granites across the Archean–Proterozoic transition. *Journal of Petrology*, *60*(7), 1299-1348.

Bugge, T., Ringas, J. E., Leith, D. A., Mangerud, G., Weiss, H. M., & Leith, T. L. (2002). Upper Permian as a new play model on the mid-Norwegian continental shelf: Investigated by shallow stratigraphic drilling. *AAPG Bulletin*, 86(1), 107–127.

Callomon, J. H. (2003). The Middle Jurassic of western and northern Europe: its subdivisions, geochronology and correlations. *GEUS Bulletin*, *1*, 61-73.

Casey, R. (1963). *The dawn of the Cretaceous period in Britain*. South-Eastern Union of Scientific Societies.

Cedeno, A., Ohm, S., Escalona, A., Marín, D., Olaussen, S., & Demchuk, T. (2021). Upper Jurassic to Lower Cretaceous source rocks in the Norwegian Barents Sea, part I: Organic geochemical, petrographic, and paleogeographic investigations. *Marine and Petroleum Geology*, *134*, 105342.

Censi, P., Inguaggiato, C., Chiavetta, S., Schembri, C., Sposito, F., Censi, V., & Zuddas, P. (2017). The behaviour of zirconium, hafnium and rare earth elements during the crystallisation of halite and other salt minerals. *Chemical Geology*, *453*, 80-91.

Charbonnier, G., Adatte, T., Föllmi, K. B., & Suan, G. (2020). Effect of intense weathering and postdepositional degradation of organic matter on Hg/TOC proxy in organic-rich sediments and its implications for deep-time investigations. *Geochemistry, Geophysics, Geosystems*, 21(2).

Chen, W., Kemp, D. B., Newton, R. J., He, T., Huang, C., Cho, T., & Izumi, K. (2022). Major sulfur cycle perturbations in the Panthalassic Ocean across the Pliensbachian-Toarcian boundary and the Toarcian Oceanic Anoxic Event. *Global and Planetary Change*, *215*, 103884.

Clapham, M. E., & Renne, P. R. (2019). Flood Basalts and Mass Extinctions. *Annual Review of Earth and Planetary Sciences*, 47(1), 275–303.

Clemente, J. (2015). Three Reasons Oil Will Continue to Run the World. *Forbes. April*, *20*.

Cohen, A. S. (2004). The rhenium–osmium isotope system: applications to geochronological and palaeoenvironmental problems. *Journal of the Geological Society*, 161(4), 729–734.

Cohen, A. S., & Coe, A. L. (2007). The impact of the central Atlantic magmatic province on climate and on the Sr -and Os-isotope evolution of seawater. *Palaeogeography, Palaeoclimatology, Palaeoecology*, 244(1-4), 374–390.

Cohen, A. S., Coe, A. L., Bartlett, J. M., & Hawkesworth, C. J. (1999). Precise re–os ages of organic-rich mudrocks and the Os isotope composition of Jurassic seawater. *Earth and Planetary Science Letters*, 167(3-4), 159–173.

Cohen, A. S., Coe, A. L., Harding, S. M., & Schwark, L. (2004). Osmium isotope evidence for the regulation of atmospheric CO_2 by continental weathering. *Geology*, *32*(2), 157–160.

Cohen, K.M., Finney, S.C., Gibbard, P.L. & Fan, J.-X. (2013; updated) The ICS International Chronostratigraphic Chart. Episodes 36: 199-204.

Creaser, R. A., Sannigrahi, P., Chacko, T., & Selby, D. (2002). Further evaluation of the Re-Os geochronometer in organic-rich sedimentary rocks: A test of hydrocarbon maturation effects in the Exshaw Formation, Western Canada Sedimentary Basin. *Geochimica et Cosmochimica Acta*, 66(19), 3441-3452.

Cumming, V. M., Selby, D., Lillis, P. G., & Lewan, M. D. (2014). Re–Os geochronology and Os isotope fingerprinting of petroleum sourced from a Type I lacustrine kerogen: Insights from the natural Green River petroleum system in the Uinta Basin and hydrous pyrolysis experiments. *Geochimica et Cosmochimica Acta*, 138, 32-56.

Dean, W. E. (1974). Determination of carbonate and organic matter in calcareous sediments and sedimentary rocks by loss on ignition; comparison with other methods. *Journal of Sedimentary Research*, 44 (1), 242–248.

Dean, W. E., & Arthur, M. A. (1989). Iron-sulfur-carbon relationships in organic-carbon-rich sequences; I, Cretaceous Western Interior Seaway. *American Journal of Science*, *289*(6), 708-743.

DeConto, R. M., Galeotti, S., Pagani, M., Tracy, D., Schaefer, K., Zhang, T., Pollard, D., & Beerling, D. J. (2012). Past extreme warming events linked to massive carbon release from thawing permafrost. *Nature*, *484*(7392), 87–91.

Dera, G., Brigaud, B., Monna, F., Laffont, R., Pucéat, E., Deconinck, J. F., Pellenard, P., Joachimski, M. M., & Durlet, C. (2011). Climatic ups and downs in a disturbed Jurassic world. *Geology*, *39*(3), 215-218.

Dickson, A. J., Cohen, A. S., & Davies, M. (2021). The osmium isotope signature of Phanerozoic large igneous provinces. *Large Igneous Provinces: A Driver of Global Environmental and Biotic Changes*, 229-246.

Dickson, A. J., Davies, M., Bagard, M.-L., & Cohen, A.S. (2022) Quantifying seawater exchange rates in the Eocene Arctic Basin using osmium isotopes. *Geochemical Perspectives Letter,* 24, 7–11.

Dromart, G., Garcia, J. P., Picard, S., Atrops, F., Lécuyer, C., & Sheppard, S. M. F. (2003). Ice age at the Middle–Late Jurassic transition?. *Earth and Planetary Science Letters*, *213*(3-4), 205-220.

Dypvik, H., Eikeland, T., Backer-Owe, K., Andresen, A., Johanen, H., Elverhøi, A., Nagy, J., Haremo, P., & Biærke, T. (1991). The Janusfjellet subgroup (Bathonian to Hauterivian) on central Spitsbergen: a revised lithostratigraphy. *Polar Research*, 9(1), 21–44.

Dypvik, H., & Harris, N. B. (2001). Geochemical facies analysis of fine-grained siliciclastics using Th/U, Zr/Rb and (Zr + Rb)/Sr ratios. *Chemical Geology*, 181(1–4), 131–146.

Dypvik, H., Håkansson, E., & Heinberg, C. (2002). Jurassic and Cretaceous palaeogeography and stratigraphic comparisons in the north Greenland-Svalbard region. *Polar Research*, *21*(1), 91–108.

Erwin, D. H. (1994). The Permo–Triassic extinction. *Nature*, *367*(6460), 231-236.

Faleide, J. I., Tsikalas, F., Breivik, A. J., Mjelde, R., Ritzmann, O., Engen, Ø., Wilson, J., & Eldholm, O. (2008). Structure and evolution of the continental margin off Norway and the Barents Sea. *Episodes Journal of International Geoscience*, *31*(1), 82-91.

Falkner, K. K., Bowers, T. S., Todd, J. F., Lewis, B. L., Landing, W. M., & Edmond, J. M. (1993). The behavior of barium in anoxic marine waters. *Geochimica et Cosmochimica Acta*, *57*(3), 537-554.

Fernández-Martínez, J., Ruíz, F. M., Rodríguez-Tovar, F. J., Piñuela, L., García-Ramos, J. C., & Algeo, T. J. (2023). Euxinia and hydrographic restriction in the Tethys Ocean: Reassessing global oceanic anoxia during the early Toarcian. *Global and Planetary Change*, 104026.

Fitzgerald, W., Lyons, W. (1973). Organic mercury compounds in coastal waters. *Nature* 242, 452–453.

Fu, X., Wang, J., Zeng, S., Feng, X., Wang, D., & Song, C. (2017). Continental weathering and palaeoclimatic changes through the onset of the Early Toarcian oceanic anoxic event in the Qiangtang Basin, eastern Tethys. *Palaeogeography, Palaeoclimatology,* *Palaeoecology*, 487, 241-250.

Gaillardet, J., Dupré, B., Louvat, P., & Allegre, C. J. (1999). Global silicate weathering and CO_2 consumption rates deduced from the chemistry of large rivers. *Chemical Geology*, *159*(1-4), 3–30.

Galloway, J. M., Vickers, M. L., Price, G. D., Poulton, T., Grasby, S. E., Hadlari, T., Beauchamp, B., & Sulphur, K. (2020). Finding the VOICE: organic carbon isotope chemostratigraphy of late Jurassic–early Cretaceous Arctic Canada. *Geological Magazine*, *157*(10), 1643–1657.

Garver, J. I., Royce, P. R., & Smick, T. A. (1996). Chromium and nickel in shale of the Taconic foreland; a case study for the provenance of fine-grained sediments with an ultramafic source. *Journal of Sedimentary Research*, *66*(1), 100-106.

Geologic TimeScale Foundation (J.G. Ogg, executive director) (2022). TimeScale Creator (version 8.0), [Java software].

Gehrke, G. E., Blum, J. D., & Meyers, P. A. (2009). The geochemical behavior and isotopic composition of Hg in a mid-Pleistocene western Mediterranean sapropel. *Geochimica et Cosmochimica Acta*, 73(6), 1651-1665.

Georgiev, S., Stein, H. J., Hannah, J. L., Bingen, B., Weiss, H. M., & Piasecki, S. (2011). Hot acidic late Permian seas stifle life in record time. *Earth and Planetary Science Letters*, 310(3-4), 389–400.

Georgiev, S. V., Stein, H. J., Hannah, J. L., Henderson, C. M., & Algeo, T. J. (2015). Enhanced recycling of organic matter and Os-isotopic evidence for multiple magmatic or meteoritic inputs to the Late Permian Panthalassic Ocean, Opal Creek, Canada. *Geochimica et Cosmochimica Acta*, *150*, 192-210.

Georgiev, S. V., Stein, H. J., Hannah, J. L., Xu, G., Bingen, B., & Weiss, H. M. (2017). Timing, duration, and causes for Late Jurassic–Early Cretaceous anoxia in the Barents Sea. *Earth and Planetary Science Letters*, 461, 151–162.

Georgiev, S. V., Stein, H. J., Hannah, J. L., Yang, G., Markey, R. J., Dons, C. E., Pedersen, J. H., & Di Primio, R. (2019). Comprehensive evolution of a petroleum system in absolute time: the example of Brynhild, Norwegian North Sea. *Chemical Geology*, *522*, 260–282.

Georgiev, S. V., Stein, H. J., Yang, G., Hannah, J. L., Böttcher, M. E., Grice, K., Holman, A. I., Turgeon, S., Simonsen, S., & Cloquet, C. (2020). Late Permian–early Triassic environmental changes recorded by multi-isotope (Re-Os-N-Hg) data and trace metal distribution from the Hovea-3 section, western Australia. *Gondwana Research*, *88*, 353–372.

Georgiev, S. V., Zimmerman, A., Yang, G., Goswami, V., Hurtig, N. C., Hannah, J.L., & Stein, H.J. (2018). Comparison of chemical procedures for Re-isotopic measurements by N-TIMS. *Chemical Geology*, *483*, 151-161.

Grabowski, J., Aguirre-Urreta, B., Deconinck, J.-F., Erba, E., Frau, C., Li, G., Martinez, M., Matsuoka, A., Michalik, J., Mutterlose, J., Price, G., Reháková, D., Schmitz, M. D., Schnabl, P., Szives, O., Wierzbowski, A., 2022. Where should the Jurassic System end? In: Pálfy, J., Főzy, I. (Eds.), *11th International Congress on the Jurassic System 29*, p.70. Program, abstracts, and field trip guide.

Gradstein, F. M., Ogg, J. G., Schmitz, M. D., & Ogg, G. M. (Eds.). (2020). Geologic Time Scale 2020. Elsevier.

Grasby, S. E., Beauchamp, B., Bond, D. P. G., Wignall, P. B., & Sanei, H. (2016). Mercury anomalies associated with three extinction events (Capitanian Crisis, Latest Permian

Extinction and the Smithian/Spathian Extinction) in NW Pangea. *Geological Magazine*, 153(2), 285–297.

Greber, N. D., & Dauphas, N. (2019). The chemistry of fine-grained terrigenous sediments reveals a chemically evolved Paleoarchean emerged crust. *Geochimica et Cosmochimica Acta*, *255*, 247-264.

Hammer, Ø., Collignon, M., & Nakrem, H. A. (2012). Organic carbon isotope chemostratigraphy and cyclostratigraphy in the Volgian of Svalbard. *Norwegian Journal of Geology/Norsk Geologisk Forening*, 92.

Hammer, Ø., Nakrem, H. A., Little, C. T., Hryniewicz, K., Sandy, M. R., Hurum, J. H., Druckenmiller, P., Knutsen, E. M., & Høyberget, M. (2011). Hydrocarbon seeps from close to the Jurassic–Cretaceous boundary, Svalbard. *Palaeogeography, Palaeoclimatology, Palaeoecology*, *306*(1-2), 15–26.

Hannah, J. L., Bekker, A., Stein, H. J., Markey, R. J., & Holland, H. D. (2004). Primitive Os and 2316 Ma age for marine shale: implications for Paleoproterozoic glacial events and the rise of atmospheric oxygen. *Earth and Planetary Science Letters*, 225(1-2), 43–52.

Harries, P. J., & Little, C. T. (1999). The early Toarcian (Early Jurassic) and the Cenomanian–Turonian (Late Cretaceous) mass extinctions: similarities and contrasts. *Palaeogeography, Palaeoclimatology, Palaeoecology*, *154*(1-2), 39–66.

Harris, N. B., Mnich, C. A., Selby, D., & Korn, D. (2013). Minor and trace element and Re-Os chemistry of the Upper Devonian Woodford Shale, Permian Basin, west Texas: Insights into metal abundance and basin processes. *Chemical Geology*, *356*, 76–93.

Harrison, A. G., & Thode, H. G. (1958). Mechanism of the bacterial reduction of sulphate from isotope fractionation studies. *Transactions of the Faraday Society*, *54*, 84–92.

Heimdal, T. H., Goddéris, Y., Jones, M. T., & Svensen, H. H. (2021). Assessing the importance of thermogenic degassing from the Karoo Large Igneous Province (LIP) in driving Toarcian carbon cycle perturbations. *Nature Communications*, *12*(1), 6221.

Heydari, E., Arzani, N., & Hassanzadeh, J. (2008). Mantle plume: the invisible serial killer—application to the Permian–Triassic boundary mass extinction. *Palaeogeography, Palaeoclimatology, Palaeoecology*, *264*(1-2), 147-162.

Helland-Hansen, W. (2010). Facies and stacking patterns of shelf deltas within the Palaeogene Battfjellet Formation, Nordenskiold Land, Svalbard: implications for subsurface reservoir prediction. *Sedimentology 57*, 190–208.

Henriksen, E., Bjørnseth, H., Hals, T., Heide, T., Kiryukhina, T., Kløvjan, O., Larssen, G. B., Ryseth, A., Rønning, K., Sollid, K., & Stoupakova, A. (2011). Uplift and erosion of the greater Barents Sea: impact on prospectivity and petroleum systems. *Geological Society, London, Memoirs*, *35*(1), 271–281.

Hermoso, M., Minoletti, F., & Pellenard, P. (2013) Black shale deposition during Toarcian super-greenhouse driven by sea level. *Climate of the Past*, 9, 2703–2712.

Hesselbo, S., Ogg, J., Ruhl, M., Hinnov, L., & Huang, C. (2020). The Jurassic Period. In *Geologic Time Scale 2020*, pages 955–1021.

Hesselbo, S. P., Gröcke, D. R., Jenkyns, H. C., Bjerrum, C. J., Farrimond, P., Morgans Bell, H. S., & Green, O. R. (2000). Massive dissociation of gas hydrate during a Jurassic oceanic anoxic event. *Nature*, 406(6794), 392-395.

Hochuli, P. A., Vigran, J. O., Hermann, E., & Bucher, H. (2010). Multiple climatic changes around the Permian-Triassic boundary event revealed by an expanded palynological record from mid-Norway. *Bulletin of the Geological Society of America*, 122(5–6), 884–

896.

Hofmann, P., Ricken, W., Schwark, L., & Leythaeuser, D. (2000). Carbon–sulfur–iron relationships and δ13C of organic matter for late Albian sedimentary rocks from the North Atlantic Ocean: paleoceanographic implications. *Palaeogeography, Palaeoclimatology, Palaeoecology*, *163*(3-4), 97-113.

Hovikoski, J., Olivarius, M., Bojesen-Koefoed, J. A., Piasecki, S., Alsen, P., Fyhn, M. B. W., Sharp, I., Bjerager, M., Vosgerau, H., Lindström, S., Bjerrum, C., & Ineson, J. (2023). Late Jurassic–Early Cretaceous marine deoxygenation in NE Greenland. *Journal of the Geological Society*, *180*(3).

IPCC (2022) *Climate Change 2022: Mitigation of Climate Change Working Group III Contribution to the IPCC Sixth Assessment Report*. Cambridge University Press.

Jelby, M. E., Śliwińska, K. K., Koevoets, M. J., Alsen, P., Vickers, M. L., Olaussen, S., & Stemmerik, L. (2020). Arctic reappraisal of global carbon-cycle dynamics across the Jurassic–Cretaceous boundary and Valanginian Weissert Event. *Palaeogeography, Palaeoclimatology, Palaeoecology*, *555*, 109847.

Jenkyns, H. C. (2003). Evidence for rapid climate change in the Mesozoic–Palaeogene greenhouse world. *Philosophical Transactions of the Royal Society of London. Series A: Mathematical, Physical and Engineering Sciences*, *361*(1810), 1885-1916.

Jenkyns, H. C. (2010). Geochemistry of oceanic anoxic events. *Geochemistry, Geophysics, Geosystems*, *11*(3).

Jolliffe, I. T. (2002). *Principal component analysis for special types of data* (pp. 338-372). Springer New York.

Jones, G. E., & Starkey, R. L. (1957). Fractionation of stable isotopes of sulfur by microorganisms and their role in deposition of native sulfur. *Applied Microbiology*, *5*(2), 111-118.

Kamo, S. L., & Riccardi, A. C. (2009). A new U–Pb zircon age for an ash layer at the Bathonian–Callovian boundary, Argentina. *GFF*, 131(1-2), 177-182.

Kane, J. S. (1993). USGS reference sample Devonian Ohio Shale SDO-1. *U.S. Geological Survey*.

Kingsbury, C. G., Kamo, S. L., Ernst, R. E., Söderlund, U., & Cousens, B. L. (2018). U-Pb geochronology of the plumbing system associated with the Late Cretaceous Strand Fiord Formation, Axel Heiberg Island, Canada: part of the 130-90 Ma High Arctic large igneous province. *Journal of Geodynamics*, 118, 106-117.

Koevoets, M. J., Abay, T., Hammer, Ø., & Olaussen, S. (2016). High-resolution organic carbon–isotope stratigraphy of the Middle Jurassic–Lower Cretaceous Agardhfjellet Formation of central Spitsbergen, Svalbard. *Palaeogeography, Palaeoclimatology, Palaeoecology*, *449*, 266-274.

Koevoets, M. J., Hammer, Ø., & Little, C. T. (2019). Palaeoecology and palaeoenvironments of the Middle Jurassic to lowermost Cretaceous Agardhfjellet Formation (Bathonian-Ryazanian), Spitsbergen, Svalbard. *Norwegian Journal of Geology*, *99*(1).

Koevoets, M. J., Hammer, Ø., Olaussen, S., Senger, K., & Smelror, M. (2018). Integrating subsurface and outcrop data of the Middle Jurassic to Lower Cretaceous Agardhfjellet Formation in central Spitsbergen. *Norwegian Journal of Geology*, *98*(4).

Korte, C., Hesselbo, S. P., Ullmann, C. V., Dietl, G., Ruhl, M., Schweigert, G., & Thibault, N. (2015). Jurassic climate mode governed by ocean gateway. *Nature communications*, *6*(1), 10015.

Kump, L. R., & Arthur, M. A. (1999). Interpreting carbon-isotope excursions: carbonates and organic matter. *Chemical Geology*, 161(1-3), 181–198.

Kutek, J., & Zeiss, A. (1975). A contribution to the correlation of the Tithonian and Volgian stages: the ammonite fauna from Brzostówka near Tomaszów Mazowiecki, Central Poland. In *Mém. Bur. Rech. Géol. Min., 86 (Colloque sur la limite JurassiqueCrétacé, Lyon, Neuchâtel, 1973)* 123, 128.

Large, R. R., Halpin, J. A., Danyushevsky, L. V., Maslennikov, V. V., Bull, S. W., Long, J. A., ... & Calver, C. R. (2014). Trace element content of sedimentary pyrite as a new proxy for deep-time ocean–atmosphere evolution. *Earth and Planetary Science Letters*, 389, 209-220.

Lena, L., López-Martínez, R., Lescano, M., Aguire-Urreta, B., Concheyro, A., Vennari, V., Naipauer, M., Samankassou, E., Pimentel, M., Ramos, V. A., & Schaltegger, U. (2019). High-precision U–Pb ages in the early Tithonian to early Berriasian and implications for the numerical age of the Jurassic–Cretaceous boundary. *Solid Earth*, 10(1), 1–14.

Lenniger, M., Nøhr-Hansen, H., Hills, L. V., & Bjerrum, C. J. (2014). Arctic black shale formation during Cretaceous Oceanic Anoxic Event 2. *Geology*, *42*(9), 799-802.

Lerch, B., Karlsen, D. A., Matapour, Z., Seland, R., & Backer-Owe, K. (2016). Organic geochemistry of Barents Sea petroleum: thermal maturity and alteration and mixing processes in oils and condensates. *Journal of Petroleum Geology*, *39*(2), 125-148.

Liguori, B. T., ALMEIDA, M. G., & REZENDE, C. E. (2016). Barium and its Importance as an Indicator of (Paleo) Productivity. *Anais da Academia Brasileira de Ciências*, *88*, 2093-2103.

Lillis, P. G., & Selby, D. (2013). Evaluation of the rhenium–osmium geochronometer in the

Phosphoria petroleum system, Bighorn Basin of Wyoming and Montana, USA. *Geochimica et Cosmochimica Acta*, 118, 312-330.

Linnen, R. L., & Keppler, H. (2002). Melt composition control of Zr/Hf fractionation in magmatic processes. *Geochimica et Cosmochimica Acta*, *66*(18), 3293-3301.

Liu, J., & Algeo, T. J. (2020). Beyond redox: Control of trace-metal enrichment in anoxic marine facies by watermass chemistry and sedimentation rate. *Geochimica et Cosmochimica Acta*, *287*, 296-317.

Louis-Schmid, B., Rais, P., Logvinovich, D., Bernasconi, S. M., & Weissert, H. (2007). Impact of methane seeps on the local carbon-isotope record: a case study from a Late Jurassic hemipelagic section. *Terra Nova*, *19*(4), 259-265.

Ludwig, K. (2012). User's manual for isoplot version 3.75–4.15: A geochronological toolkit for Microsoft excel. 5. *Berkley Geochronological Centre, Special Publication*.

Lüthi, D., Le Floch, M., Bereiter, B., Blunier, T., Barnola, J. M., Siegenthaler, U., Raynaud, D., Jouzel, J., Fischer, H., Kawamura, K., & Stocker, T. F. (2008). High-resolution carbon dioxide concentration record 650,000–800,000 years before present. *Nature*, *453*(7193), 379-382.

Lyons, T. W., Anbar, A. D., Severmann, S., Scott, C., & Gill, B. C. (2009). Tracking euxinia in the ancient ocean: a multiproxy perspective and Proterozoic case study. *Annual Review of Earth and Planetary Sciences*, *37*(1), 507-534.

Lyons, T. W., Reinhard, C. T., & Planavsky, N. J. (2014). The rise of oxygen in Earth's early ocean and atmosphere. *Nature*, *506*(7488), 307-315.

Mahoney, J. J., Duncan, R. A., Tejada, M. L. G., Sager, W. W., & Bralower, T. J. (2005). Jurassic-Cretaceous boundary age and mid-ocean-ridge–type mantle source for Shatsky

Rise. *Geology*, 33(3), 185-188.

Maltby, J., Steinle, L., Löscher, C. R., Bange, H. W., Fischer, M. A., Schmidt, M., & Treude, T. (2018). Microbial methanogenesis in the sulfate-reducing zone of sediments in the Eckernförde Bay, SW Baltic Sea. *Biogeosciences*, *15*(1), 137-157.

Manabe, S., & Wetherald, R. T. (1975). The effects of doubling the CO_2 concentration on the climate of a general circulation model. *Journal of Atmospheric Sciences*, *32*(1), 3-15.

Marín, D., Helleren, S., Escalona, A., Olaussen, S., Cedeño, A., Nøhr-Hansen, H., & Ohm, S. (2020). The Middle Jurassic to lowermost Cretaceous in the SW Barents Sea: Interplay between tectonics, coarse-grained sediment supply and organic matter preservation. *Basin Research*, *33*(2), 1033-1055.

Markey, R., Stein, H., Hannah, J., Georgiev, S., Pedersen, J., & Dons, C. (2017). Re-Os identification of glide faulting and precise ages for correlation from the Upper Jurassic Heikkingen Formation, southwestern Barents Sea. *Palaeogeography, Palaeoclimatology, Palaeoecology*, 466, 209–220.

Marshall, C., Uguna, J., Large, D. J., Meredith, W., Jochmann, M., Friis, B., Vane, C., Spiro, B. F., Snape, C. E., & Orheim, A. 2015. Geochemistry and petrology of Palaeocene coals from Spitzbergen—Part 2: maturity variations and implications for local and regional burial models. *International Journal of Coal Geology*, 143, 1-10.

Martínez, M. K., Kietzmann, D. A., Llanos, M. I., Leanza, H. A., & Luppo, T. (2018). Magnetostratigraphy and cyclostratigraphy of the Tithonian interval from the Vaca Muerta Formation, southern Neuquén Basin, Argentina. *Journal of South American Earth Sciences*, *85*, 209–228.

Marynowski, L., Kurkiewicz, S., Rakociński, M., & Simoneit, B. R. (2011). Effects of weathering on organic matter: I. Changes in molecular composition of extractable organic compounds caused by paleoweathering of a Lower Carboniferous (Tournaisian) marine black shale. *Chemical Geology*, 285(1-4), 144-156.

Marynowski, L., Pisarzowska, A., Derkowski, A., Rakociński, M., Szaniawski, R., Środoń, J., & Cohen, A. S. (2017). Influence of palaeoweathering on trace metal concentrations and environmental proxies in black shales. *Palaeogeography, Palaeoclimatology, Palaeoecology*, 472, 177-191.

Matsumoto, H., Coccioni, R., Frontalini, F., Shirai, K., & Kuroda, J. (2021). Osmium isotopic evidence for eccentricity-paced increases in continental weathering during the latest Hauterivian, Early Cretaceous. *Geochemistry, Geophysics, Geosystems*, *22*(12).

McArthur, J. M., Algeo, T. J., Van de Schootbrugge, B., Li, Q., & Howarth, R. J. (2008). Basinal restriction, black shales, Re-Os dating, and the Early Toarcian (Jurassic) oceanic anoxic event. *Paleoceanography*, *23*(4).

McArthur, J., Howarth, R., Shields, G., & Zhou, Y. (2020). Strontium isotope stratigraphy. In *Geologic Time Scale 2020*, 211–238.

McManus, J., Berelson, W. M., Klinkhammer, G. P., Johnson, K. S., Coale, K. H., Anderson, R. F., Kumar, N., Burdige, D. J., Hammond, D. E., Brumsack, H.J., McCorkle, D.C., & Rushdi, A. (1998). Geochemistry of barium in marine sediments: Implications for its use as a paleoproxy. *Geochimica et Cosmochimica Acta*, *62*(21-22), 3453-3473.

Mitta, V. (2007). Ammonite assemblages from basal layers of the Ryazanian stage (Lower Cretaceous) of central Russia. *Stratigraphy and Geological Correlation*, 15(2), 193–205.

Mørk, A., Dallmann, W. K., Dypvik, H., Johannessen, E.P., Larssen, G.B., Nagy, J., Nøttvedt, A., Olaussen, S., Pchelina, T.M., & Worsley, D. (1999) Mesozoic lithostratigraphy. In

Dallmann, W.K.(Ed) Lithostratigraphic Lexicon of Svalbard. Upper Palaeozoic to Quaternary bedrock. Review and recommendations for nomenclature use. Committee on the Stratigraphy of Svalbard. *Norwegian Polar Institute*, 127-214.

Mutterlose, J., Brumsack, H., Flögel, S., Hay, W., Klein, C., Langrock, U., Lipinski, M., Ricken, W., Söding, E., Stein, R., & Swientek, O. (2003). The Greenland-Norwegian seaway: A key area for understanding Late Jurassic to Early Cretaceous paleoenvironments. *Paleoceanography*, 18(1).

Müller, R., Nystuen, P. J., Eide, F., & Lie, H. (2005). Late Permian to Triassic basin infill history and palaeogeography of the Mid-Norwegian shelf-East Greenland region. *Norwegian Petroleum Society Special Publications*, 12(C), 165–189.

Nalley, S., & LaRose, A. (2022). Annual energy outlook 2022 (AEO2022). *Energy Information Agency*, *23*.

Nielsen, J. K., & Shen, Y. (2004). Evidence for sulfidic deep water during the Late Permian in the East Greenland Basin. *Geology*, 32(12), 1037–1040.

Nozaki, T., Kato, Y., & Suzuki, K. (2013). Late Jurassic ocean anoxic event: Evidence from voluminous sulphide deposition and preservation in the Panthalassa. *Scientific Reports*, *3*(1), 1889.

O'Connor, L. K., Robinson, S. A., Naafs, B. D. A., Jenkyns, H. C., Henson, S., Clarke, M., & Pancost, R. D. (2019). Late Cretaceous temperature evolution of the southern high latitudes: A TEX86 perspective. *Paleoceanography and Paleoclimatology*, *34*(4), 436-454.

Ogata, K., Senger, K., Braathen, A., Tveranger, J., & Olaussen, S. (2014). The importance of natural fractures in a tight reservoir for potential CO2 storage: a case study of the Upper

Triassic–Middle Jurassic Kapp Toscana group (Spitsbergen, Arctic Norway). *Geological Society, London, Special Publications*, *374*(1), 395–415.

Ohm, S. E., Larsen, L., Olaussen, S., Senger, K., Birchall, T., Demchuk, T., Hodson, A., Johansen, I., Titlestad, G. O., Karlsen, D. A., & Braathen, A. (2019). Discovery of shale gas in organic-rich Jurassic successions, Adventdalen, Central Spitsbergen, Norway. *Norwegian Journal of Geology* 99, 343–370.

Orecchio, S., & Polizzotto, G. (2013). Fractionation of mercury in sediments during draining of Augusta (Italy) coastal area by modified Tessier method. *Microchemical Journal*, 110, 452-457.

Oremland, R. S., & Polcin, S. (1982). Methanogenesis and sulfate reduction: competitive and noncompetitive substrates in estuarine sediments. *Applied and Environmental Microbiology*, *44*(6), 1270-1276.

Oschlies, A., Brandt, P., Stramma, L., & Schmidtko, S. (2018). Drivers and mechanisms of ocean deoxygenation. *Nature Geoscience*, *11*(7), 467-473.

Owens, J. D., Lyons, T. W., & Lowery, C. M. (2018). Quantifying the missing sink for global organic carbon burial during a Cretaceous oceanic anoxic event. *Earth and Planetary Science Letters*, *499*, 83-94.

Padden, M., Weissert, H., & de Rafelis, M. (2001). Evidence for Late Jurassic release of methane from gas hydrate. *Geology*, *29*(3), 223-226.

Page, K. N. (1996). *Mesozoic ammonoids in space and time*. In Ammonoid paleobiology (pp. 755-794). Boston, MA: Springer US.

Park, J., Stein, H. J., Georgiev, S. V., & Hannah, J. L. (2022). Degradation of Hg signals on incipient weathering: Core versus outcrop geochemistry of Upper Permian shales, East

Greenland and Mid-Norwegian Shelf. *Chemical Geology*, *608*, 121030.

Park, J., Stein, H. J., Hannah, J. L., Georgiev, S. V., Hammer, Ø., & Olaussen, S. (in-review). Re-Os geochronology of the Middle to Upper Jurassic marine black shales, Agardhfjellet Formation, Central Spitsbergen, Svalbard: a cornerstone for global faunal correlation and Os isotopic change. *Palaeogeography, Palaeoclimatology, Palaeoecology*

Parker, J. R. (1967). The Jurassic and Cretaceous sequence in Spitsbergen. *Geological Magazine*, 104(5), 487–505.

Paquay, F. S., Ravizza, G., & Coccioni, R. (2014). The influence of extraterrestrial material on the late Eocene marine Os isotope record. *Geochimica et Cosmochimica Acta*, *144*, 238–257.

Pellenard, P., Nomade, S., Martire, L., Ramalho, F. D. O., Monna, F., & Guillou, H. (2013). The first ^{40}Ar–^{39}Ar date from Oxfordian ammonite-calibrated volcanic layers (bentonites) as a tie-point for the Late Jurassic. *Geological Magazine*, 150(6):1136–1142.

Peng, B., Song, Z., Tu, X., Xiao, M., Wu, F., & Lv, H. (2004). Release of heavy metals during weathering of the Lower Cambrian Black Shales in western Hunan, China. *Environmental Geology*, 45(8), 1137–1147.

Percival, L. M., Jenkyns, H. C., Mather, T. A., Dickson, A. J., Batenburg, S. J., Ruhl, M., Hesselbo, S. P., Barclay, R., Jarvis, I., Robinson, S. A., & Woelders, L., (2018). Does large igneous province volcanism always perturb the mercury cycle? Comparing the records of Oceanic Anoxic Event 2 and the end-Cretaceous to other Mesozoic events. *American Journal of Science*, *318*(8), 799-860.

Percival, L. M. E., Witt, M. L. I., Mather, T. A., Hermoso, M., Jenkyns, H. C., Hesselbo, S. P., Al-Suwaidi, A. H., Storm, M. S., Xu, W., & Ruhl, M. (2015). Globally enhanced mercury deposition during the end-Pliensbachian extinction and Toarcian OAE: A link to the Karoo-Ferrar Large Igneous Province. *Earth and Planetary Science Letters*, 428, 267–280.

Peters, K. E. (1986). Guidelines for evaluating petroleum source rock using programmed pyrolysis. *AAPG bulletin*, 70(3), 318-329.

Petsch, S. T., Berner, R. A., & Eglinton, T. I. (2000). A field study of the chemical weathering of ancient sedimentary organic matter. *Organic Geochemistry*, 31(5), 475-487.

Petsch, S. T., Smernik, R. J., Eglinton, T. I., Oades, J. M. (2001). A solid state 13C-NMR study of kerogen degradation during black shale weathering, *Geochimica et Cosmochimica Acta*, 65 (12), 1867-1882.

Peucker-Ehrenbrink, B., & Ravizza, G. (2000). The marine osmium isotope record. *Terra Nova*, 12(5), 205-219.

Peucker-Ehrenbrink, B., & Ravizza, G. (2020). Osmium isotope stratigraphy. In *Geologic Time Scale 2020*, 239–257.

Pi, D. H., Liu, C. Q., Shields-Zhou, G. A., & Jiang, S. Y. (2013). Trace and rare earth element geochemistry of black shale and kerogen in the early Cambrian Niutitang Formation in Guizhou province, South China: Constraints for redox environments and origin of metal enrichments. *Precambrian Research*, *225*, 218-229.

Piasecki, S., & Stemmerik, L. (1991). Late Permian anoxia in central East Greenland. *Geological Society Special Publication*, 58(58), 275–290.

Piepjohn, K., von Gosen, W., & Tessensohn, F. (2016). The Eurekan deformation in the Arctic: an outline. *Journal of the Geological Society, London*, 173, 1007–1024.

Pitman III, W. C., & Talwani, M. (1972). Sea-floor spreading in the North Atlantic. *Geological*

Society of America Bulletin, 83(3), 619-646.

Price, G. D., & Rogov, M. A. (2009). An isotopic appraisal of the Late Jurassic greenhouse phase in the Russian Platform. *Palaeogeography, Palaeoclimatology, Palaeoecology*, *273*(1-2), 41-49.

Rakocinski, M., Zaton, M., Marynowski, L., Gedl, P., & Lehmann, J. (2018). Redox conditions, productivity, and volcanic input during deposition of uppermost Jurassic and Lower Cretaceous organic-rich siltstones in Spitsbergen, Norway. *Cretaceous Research*, 89, 126–147.

Ravizza, G., & VonderHaar, D. (2012). A geochemical clock in earliest Paleogene pelagic carbonates based on the impact-induced Os isotope excursion at the Cretaceous-Paleogene boundary. *Paleoceanography*, *27*(3).

Reershemius, T., & Planavsky, N. J. (2021). What controls the duration and intensity of ocean anoxic events in the Paleozoic and the Mesozoic? *Earth-Science Reviews*, 221, 103787.

Reolid, M., Mattioli, E., Duarte, L. V., & Ruebsam, W. (2021). The Toarcian Oceanic Anoxic Event: where do we stand?. *Special Publications*, *514*(1), 1-11.

Rimmer, S. M., Thompson, J. A., Goodnight, S. A., & Robl, T. L. (2004). Multiple controls on the preservation of organic matter in Devonian–Mississippian marine black shales: geochemical and petrographic evidence. *Palaeogeography, Palaeoclimatology, Palaeoecology*, *215*(1-2), 125-154.

Rogov, M. (2014). Infrazonal subdivision of the Volgian Stage in its type area using ammonites and correlation of the Volgian and Tithonian Stages. In *STRATI 2013: First International Congress on Stratigraphy At the Cutting Edge of Stratigraphy*, 577-580.

Rogov, M. A., Shchepetova, E. V., & Zakharov, V. A. (2020). Late Jurassic–earliest Cretaceous prolonged shelf dysoxic–anoxic event and its possible causes. *Geological Magazine*, *157*(10), 1622-1642.

Rooney, A. D., Selby, D., Lewan, M. D., Lillis, P. G., & Houzay, J. P. (2012). Evaluating Re–Os systematics in organic-rich sedimentary rocks in response to petroleum generation using hydrous pyrolysis experiments. *Geochimica et Cosmochimica Acta*, 77, 275-291.

Rudnick, R. L., & Gao, S. (2003). Composition of the continental crust. *The crust*, 3, 1-64.

Sageman, B. B., & Lyons, T. W. (2003). 7.06 – Geochemistry of Fine-grained Sediments and Sedimentary Rocks. In H. D. Holland., & K. K. Turekian (Eds.). *Treatise on Geochemistry* (pp. 115-158). Oxford, United Kingdom: Pergamon.

Sand, G., Braathen, A., & Olaussen, S. (2014). Longyearbyen CO_2 Lab – tales of research and education. *Norwegian Journal of Geology*, *94*, 77-82.

Sanei, H., & Goodarzi, F. (2006). Relationship between organic matter and mercury in recent lake sediment: The physical-geochemical aspects. *Applied Geochemistry*, 21(11), 1900–1912.

Scaife, J. D., Ruhl, M., Dickson, A. J., Mather, T. A., Jenkyns, H. C., Percival, L. M. E., Hesselbo, S. P., Cartwright, J., Eldrett, J. S., Bergman, S. C., & Minisini, D. (2017). Sedimentary mercury enrichments as a marker for submarine large igneous province volcanism? Evidence from the Mid-Cenomanian event and Oceanic Anoxic Event 2 (Late Cretaceous). *Geochemistry, Geophysics, Geosystems*, 18(12), 4253-4275.

Schlanger, S. O., & Jenkyns, H. C. (1976). Cretaceous oceanic anoxic events: causes and consequences. *Geologie en mijnbouw*, *55*(3-4).

Schmidtko, S., Stramma, L., & Visbeck, M. (2017). Decline in global oceanic oxygen content during the past five decades. *Nature*, *542*(7641), 335-339.

Scholle, P. A., & Arthur, M. A. (1980). Carbon isotope fluctuations in Cretaceous pelagic limestones: potential stratigraphic and petroleum exploration tool. *AAPG Bulletin*, *64*(1), 67-87.

Selby, D. (2007). Direct Rhenium-Osmium age of the Oxfordian-Kimmeridgian boundary, Staffin Bay, Isle of Skye, UK, and the Late Jurassic time scale. *Norwegian Journal of Geology*, 87(3), 291-299.

Selby, D., & Creaser, R. A. (2003). Re-Os geochronology of organic rich sediments: an evaluation of organic matter analysis methods. *Chemical Geology*, *200*(3-4), 225-240.

Selby, D., & Creaser, R. A. (2005). Direct radiometric dating of hydrocarbon deposits using rhenium - osmium isotopes. *Science*, 308(5726), 1293-1295.

Selby, D., Mutterlose, J., & Condon, D. J. (2009). U–Pb and Re-Os geochronology of the Aptian/Albian and Cenomanian/Turonian stage boundaries: implications for timescale calibration, osmium isotope seawater composition and Re-Os systematics in organic-rich sediments. *Chemical Geology*, *265*(3-4), 394-409.

Shen, J., Chen, J., Algeo, T. J., Yuan, S., Feng, Q., Yu, J., Zhou, L., O'Connell, B., & Planavsky, N. J. (2019a). Evidence for a prolonged Permian–Triassic extinction interval from global marine mercury records. *Nature Communications*, 10(1), 1–9.

Shen, J., Algeo, T. J., Chen, J., Planavsky, N. J., Feng, Q., Yu, J., & Liu, J. (2019b). Mercury in marine Ordovician/Silurian boundary sections of South China is sulfide-hosted and non-volcanic in origin. *Earth and Planetary Science Letters*, 511, 130–140.

Shen, J., Feng, Q., Algeo, T. J., Liu, J., Zhou, C., Wei, W., Liu, J., Them, T. R., Gill, B. C., & Chen, J. (2020). Sedimentary host phases of mercury (Hg) and implications for use of Hg as a volcanic proxy. *Earth and Planetary Science Letters*, 543.

Shields, G., & Stille, P. (2001). Diagenetic constraints on the use of cerium anomalies as palaeoseawater redox proxies: an isotopic and REE study of Cambrian phosphorites. *Chemical Geology*, *175*(1-2), 29-48.

Shirey, S. B., & Walker, R. J. (1995). Carius tube digestion for low-blank rhenium-osmium analysis. *Analytical Chemistry*, *67*(13), 2136-2141.

Smelror, M., Mørk, A., Mørk, M. B. E., Weiss, H. M., & Løseth, H. (2001). Middle Jurassic-Lower Cretaceous transgressive-regressive sequences and facies distribution off northern Nordland and Troms, Norway. *Norwegian Petroleum Society Special Publications*, *10*, 211-232.

Stein, H., & Hannah, J. (2015). Rhenium-Osmium geochronology – sulfides, shales, oils, and mantle, In J. Rink., & J. Thompson (Eds.). *Earth Sciences Series, Encyclopedia of Scientific Dating Methods* (pp. 1-25), New York, USA: Springer

Surlyk, F., Hurst, J. M., Piasecki, S., Rolle, F., Scholle, P. A., Stemmerik, L., & Thomsen, E. (1986). The Permian of the western margin of the Greenland Sea – a future exploration target, *in* Halbouty, M.T., ed., *Future petroleum provinces of the world: American Association of Petroleum Geologists Memoir 40*, p. 629-659.

Svensen, H., Planke, S., Chevallier, L., Malthe-Sørenssen, A., Corfu, F., & Jamtveit, B. (2007). Hydrothermal venting of greenhouse gases triggering Early Jurassic global warming. *Earth and Planetary Science Letters*, 256(3-4), 554-566.

Sweere, T., van den Boorn, S., Dickson, A. J., & Reichart, G. J. (2016). Definition of new trace-metal proxies for the controls on organic matter enrichment in marine sediments based on Mn, Co, Mo and Cd concentrations. *Chemical Geology*, *441*, 235-245.

Tennant, J. P., Mannion, P. D., Upchurch, P., Sutton, M. D., & Price, G. D. (2017). Biotic and environmental dynamics through the Late Jurassic–Early Cretaceous transition: evidence for protracted faunal and ecological turnover. *Biological Reviews*, *92*(2), 776-814.

Them, T. R., Jagoe, C. H., Caruthers, A. H., Gill, B. C., Grasby, S. E., Gröcke, D. R., Yin, R., & Owens, J. D. (2019). Terrestrial sources as the primary delivery mechanism of mercury to the oceans across the Toarcian Oceanic Anoxic Event (Early Jurassic). *Earth and Planetary Science Letters*, 507, 62–72.

Torsvik, T. H., Carlos, D., Mosar, J., Cocks, L. R. M., & Malme, T. (2002). Global reconstructions and North Atlantic paleogeography 440 Ma to recent. *BATLAS–Mid Norway plate reconstruction atlas with global and Atlantic perspectives. Geological Survey of Norway, Trondheim*, *18*, 39.

Tribovillard, N., Algeo, T. J., Baudin, F., & Riboulleau, A. J. C. G. (2012). Analysis of marine environmental conditions based on molybdenum–uranium covariation—Applications to Mesozoic paleoceanography. *Chemical Geology*, *324*, 46-58.

Tribovillard, N., Algeo, T. J., Lyons, T., & Riboulleau, A. (2006). Trace metals as paleoredox and paleoproductivity proxies: an update. *Chemical Geology*, *232*(1-2), 12-32.

Tripathy, G. R., Hannah, J. L., & Stein, H. J. (2018). Refining the Jurassic-Cretaceous boundary: Re-Os geochronology and depositional environment of Upper Jurassic shales from the Norwegian Sea. *Palaeogeography, Palaeoclimatology, Palaeoecology*, *503*, 13-25.

Tripathy, G. R., Hannah, J. L., Stein, H. J., & Yang, G. (2014). Re-Os age and depositional environment for black shales from the Cambrian-Ordovician boundary, Green Point, western Newfoundland. *Geochemistry, Geophysics, Geosystems*, *15*(4), 1021-1037.

Tripathy, G. R., Singh, S. K., & Ramaswamy, V. (2014). Major and trace element geochemistry of Bay of Bengal sediments: Implications to provenances and their controlling factors.

Palaeogeography, Palaeoclimatology, Palaeoecology, 397, 20–30.

Turgeon, S. C., & Creaser, R. A. (2008). Cretaceous oceanic anoxic event 2 triggered by a massive magmatic episode. *Nature*, 454(7202), 323-326.

Tuttle, M. L. W., Fahy, J. W., Elliott, J. G., Grauch, R. I., & Stillings, L. L. (2014). Contaminants from Cretaceous black shale: I. Natural weathering processes controlling contaminant cycling in Mancos Shale, southwestern United States, with emphasis on salinity and selenium. *Applied Geochemistry*, 46, 57–71.

Vandenbroucke, M., & Largeau, C. (2007). Kerogen origin, evolution and structure. *Organic Geochemistry*, 38(5), 719-833.

Vennari, V. V., Lescano, M., Naipauer, M., Aguirre-Urreta, B., Concheyro, A., Schaltegger, U., Armstrong, R., Pimentel, M., & Ramos, V. A. (2014). New constraints on the Jurassic–Cretaceous boundary in the High Andes using high-precision U–Pb data. *Gondwana Research*, *26*(1), 374–385.

Vermeesch, P. (2018). IsoplotR: A free and open toolbox for geochronology. *Geoscience Frontiers*, 9(5), 1479–1493.

Vine, J. D., & Tourtel, E. B. (1970). Geochemistry of black shale deposits - A summary report. *Economic Geology*, 65(3), 253–272.

Wedepohl, K. H. (1971). Environmental influences on the chemical composition of shales and clays. *Physics and Chemistry of the Earth*, *8*, 307-333.

Westermann, S., Vance, D., Cameron, V., Archer, C., & Robinson, S. A. (2014). Heterogeneous oxygenation states in the Atlantic and Tethys oceans during Oceanic Anoxic Event 2. *Earth and Planetary Science Letters*, *404*, 178-189.

Wierzbowski, H., Anczkiewicz, R., Pawlak, J., Rogov, M. A., & Kuznetsov, A. B. (2017).

Revised Middle–Upper Jurassic strontium isotope stratigraphy. *Chemical Geology*, 466, 239–255.

Wilde, P., Quinby-Hunt, M. S., & Erdtmann, B. D. (1996). The whole-rock cerium anomaly: a potential indicator of eustatic sea-level changes in shales of the anoxic facies. *Sedimentary Geology*, *101*(1-2), 43-53.

Wildman, R. A., Berner, R. A., Petsch, S. T., Bolton, E. W., Eckert, J. O., Mok, U., & Evans, J. B. (2004). The weathering of sedimentary organic matter as a control on atmospheric O2: I. Analysis of a black shale. *American Journal of Science*, 304(3), 234–249.

Wimbledon, W.A., Rehakova, D.,Svobodova, A.,Schnabl, P., Pruner, P., Elbra, T., Šifnerová, K., Kdýr, Š.I., Frau, C., Schnyder, J., Galbrun, B., 2020a. Fixing a J/K boundary: a comparative account of key Tithonian-Berriasian profiles in the departments of Drômeand Hautes-Alpes, France. *Geologica Carpathica 71*, 2446.

Wimbledon, W., Reháková, D., Svobodová, A., Elbra, T., Schnabl, P., Pruner, P., Šifnerová, K., Kdýr, Š., Frau, C., Schnyder, J., Galbrun, B., Vaňková, L., Dzyuba, O., Copestake, P., Hunt, C., Riccardi, A., Poulton, T., Bulot, L., DeLena, L.,2020b. The proposal of a GSSP for the Berriasian Stage (Cretaceous System): Part2. *Volumina Jurassica XVIII* (2), 119–158.

Worsley, D. (2008). The post-Caledonian development of Svalbard and the western Barents Sea. *Polar research*, *27*(3), 298-317.

Xu, G., Hannah, J. L., Stein, H. J., Bingen, B., Yang, G., Zimmerman, A., Weitschat, W., Mørk, A., & Weiss, H. M. (2009). Re–Os geochronology of arctic black shales to evaluate the Anisian–Ladinian boundary and global faunal correlations. *Earth and Planetary Science Letters*, 288(3-4), 581–587.

Xu, G., Hannah, J. L., Stein, H. J., Mørk, A., Vigran, J. O., Bingen, B., Schutt, D. L., & Lundschien, B. A. (2014). Cause of Upper Triassic climate crisis revealed by Re–Os geochemistry of Boreal black shales. *Palaeogeography, Palaeoclimatology, Palaeoecology*, 395, 222–232.

Yang, G., Zimmerman, A., Hurtig, N.C., Georgiev, S.V., Goswami, V., Hannah, J.L., & Stein, H.J., 2020. Chemical procedures for rhenium extraction from geological samples: Optimising the anion resin bead clean-up step. *Geostandards and Geoanalytical Research*, 44(2), pp.231-242.

Zakharov, V., & Rogov, M. (2008). Let the Volgian stage stay in the Jurassic. *Russian Geology and Geophysics*, 49(6), 408–412.

Ziegs, V., Horsfield, B., Skeie, J. E., & Rinna, J. (2017). Petroleum retention in the Mandal formation, central graben, Norway. *Marine and Petroleum Geology*, 83, 195–214.

Appendix

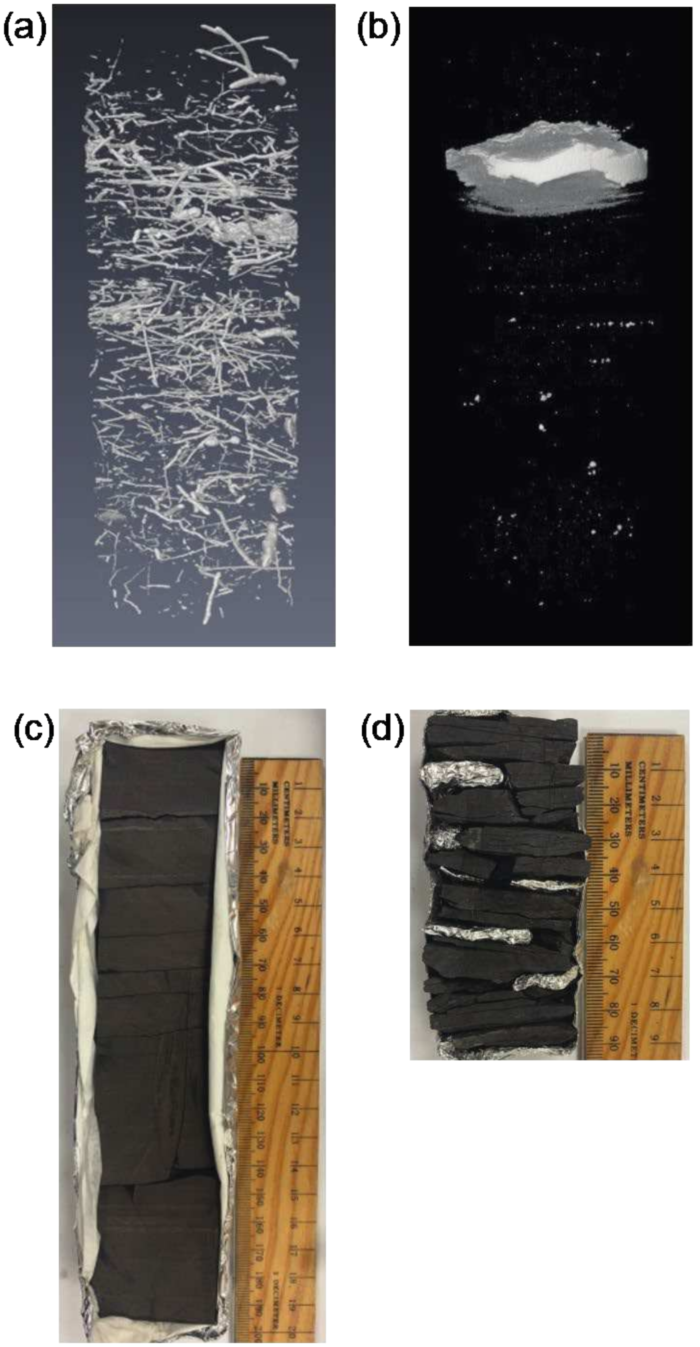

Fig. A1 CT scan images for intervals, DH2 724.24 – 724.34 m (a) (Koevoets et al., 2019) and DH5 607.00– 607.10 m (b) and images of intervals, DH2 680.28 – 680.47 (c) and DH5 658.00 – 658.10 m (d). The CT scan images are in black and white, showing brighter color for denser material. In black shale samples, brighter parts generally indicate sulfide minerals, especially pyrite. In (a), cylindrical pyritized burrows penetrate the black shale drill core vertically and horizontally. Pyritization occurred after the conditions were sufficiently reducing. The vigorous bioturbation here implies oxygenated bottom water. On the other hand, there is no bioturbation in (b), but a horizontal pyrite band in the upper part of the interval. No bioturbation and the occurrence of the pyrite band imply anoxic–euxinic conditions.

(c) is an example of indurated intervals, and (d) is an example of shattered intervals.

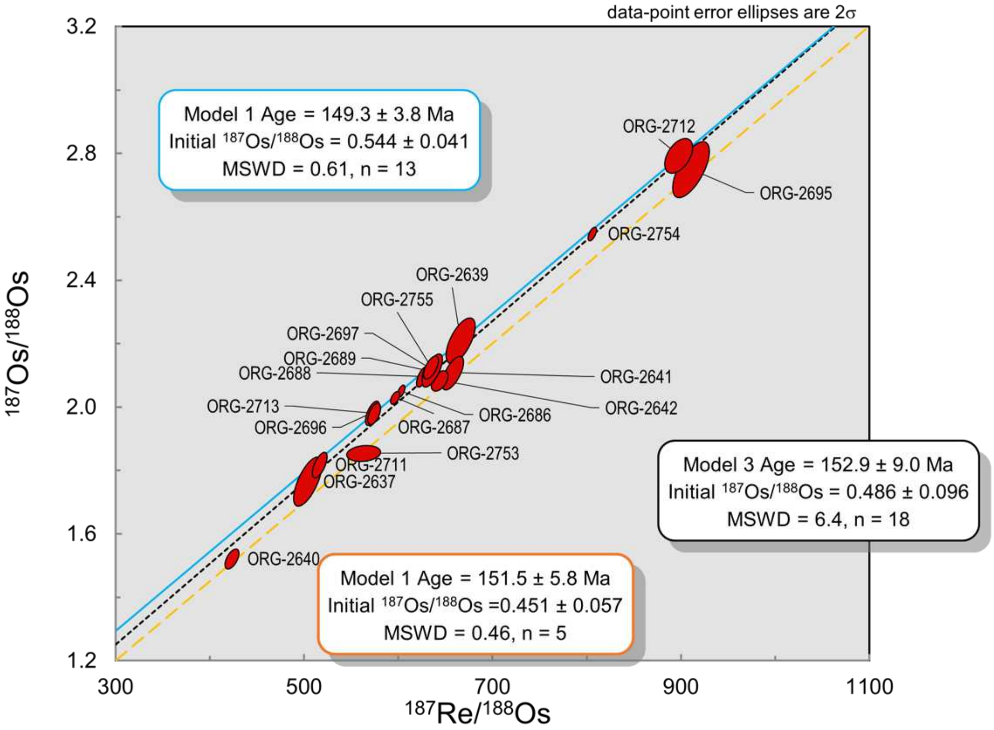

Fig. A2 An isochron of 18 samples of DH2 680 m. The regression line of all data (black dotted) shows the model 3 age with 152.9 ± 9.0 Ma with 0.486 ± 0.096 of initial Os ratio. The measured 187Re/188Os and 187Os/188Os seemingly have two starting points (initial Os ratios) at the same time within their age uncertainty. The orange dashed line is the regression from ORG-2640, 2641, 2642, 2695, and 2753, and the cyan solid line is the regression from the remaining 13 samples. The regression results of each are included in the orange and cyan boxes, respectively. The rapid variation of initial Os during the deposition is one of the main reasons why the Re-Os clock may be disturbed (Stein et al., 2015). The variation of initial Os ratios might be affected by cyclicity or limited input from the open ocean by basin restriction (Matsumoto et al., 2022; Dickson et al., 2022).

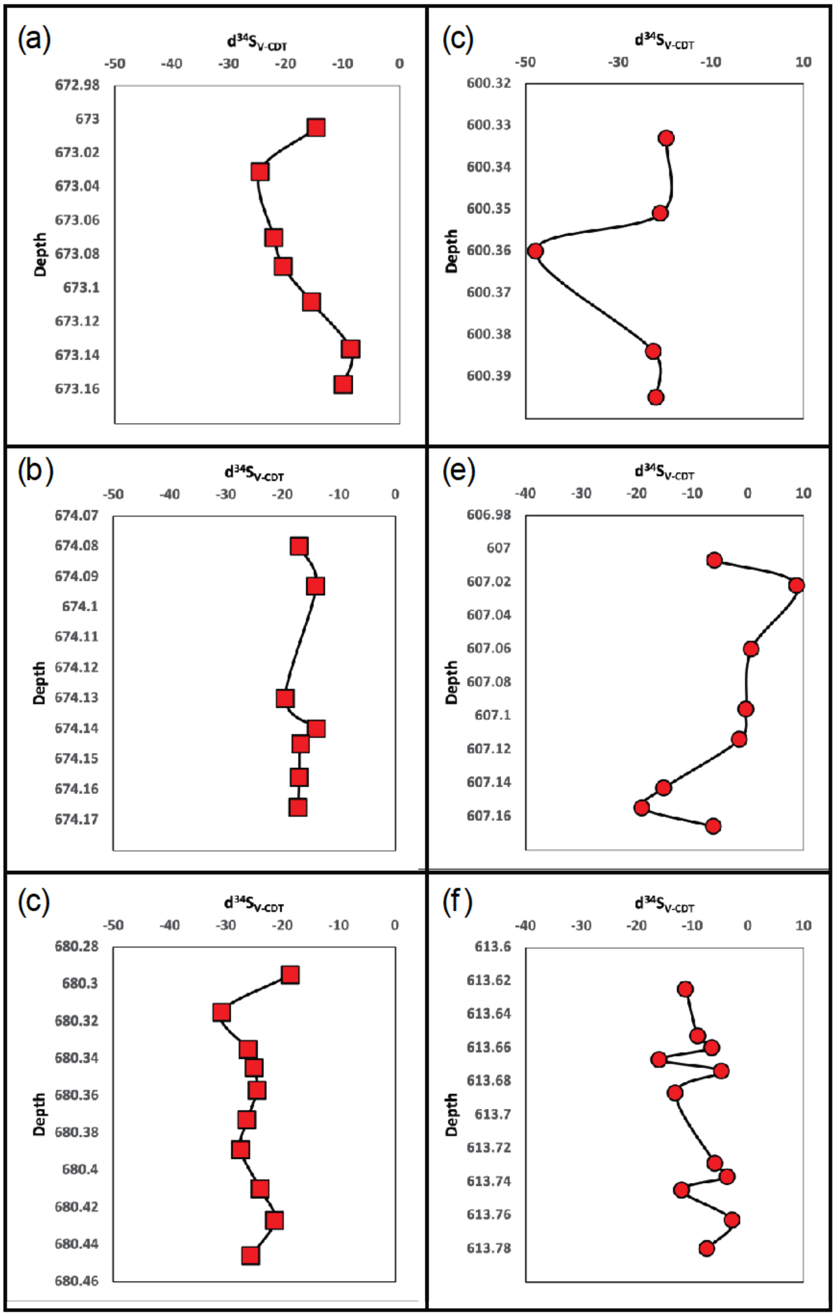

Fig. A3 $\delta^{34}S_{py}$ profiles from the Lardyfjellet Member in DH2 (a, b, and c) and DH5R (d, e, and f). The S isotopic ratios of pyrite in the Lardyfjellet Member are lighter than that in the Oppdalen Member. In particular, DH5R 600 and 607 show c. 30‰ of fractionation in each interval (~ 10 cm and ~ 15 cm, respectively).

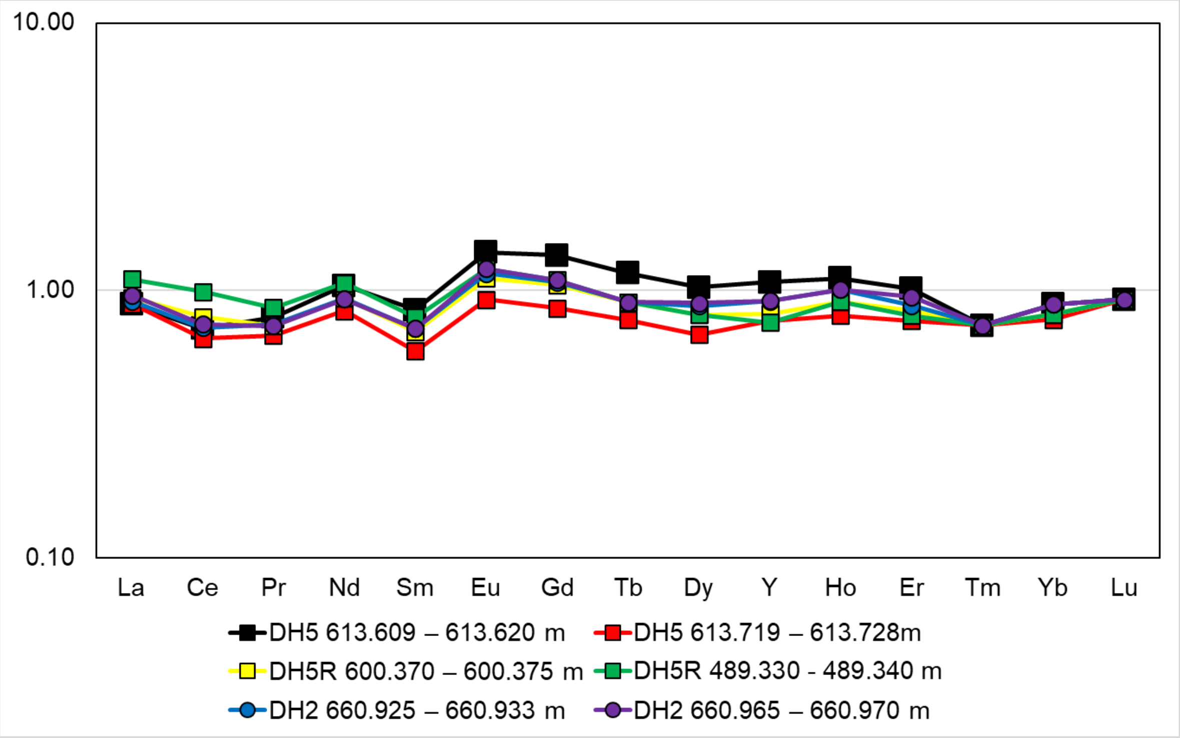

Fig. A4 Six samples of negative Pr anomalies. All samples exhibit positive Nd anomalies.

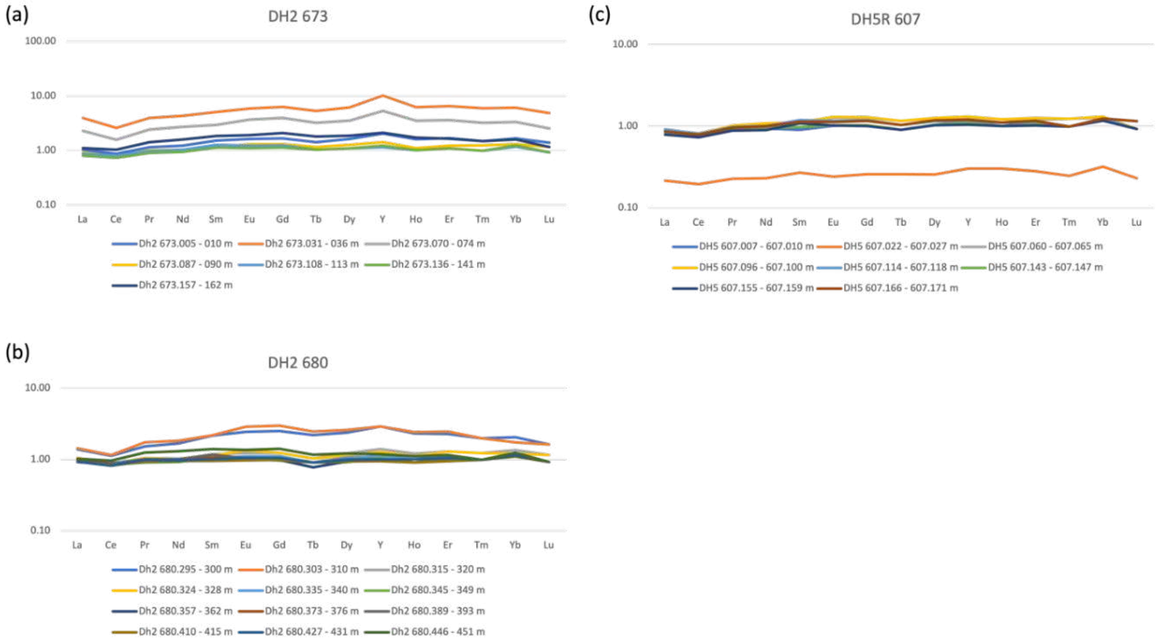

Fig. A5 REE patterns normalized to PAAS of three intervals (DH2 673, DH2 680, and DH5R 607), which include some outliers.

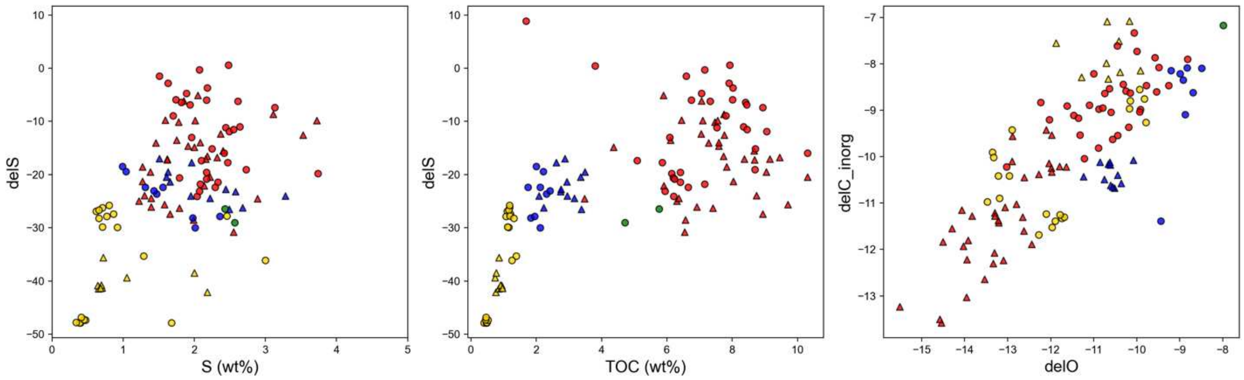

Fig. A6 The scatter plots of sulfur isotopes with sulfur contents (a), TOC (b), and inorganic carbon isotope and oxygen isotope (c).

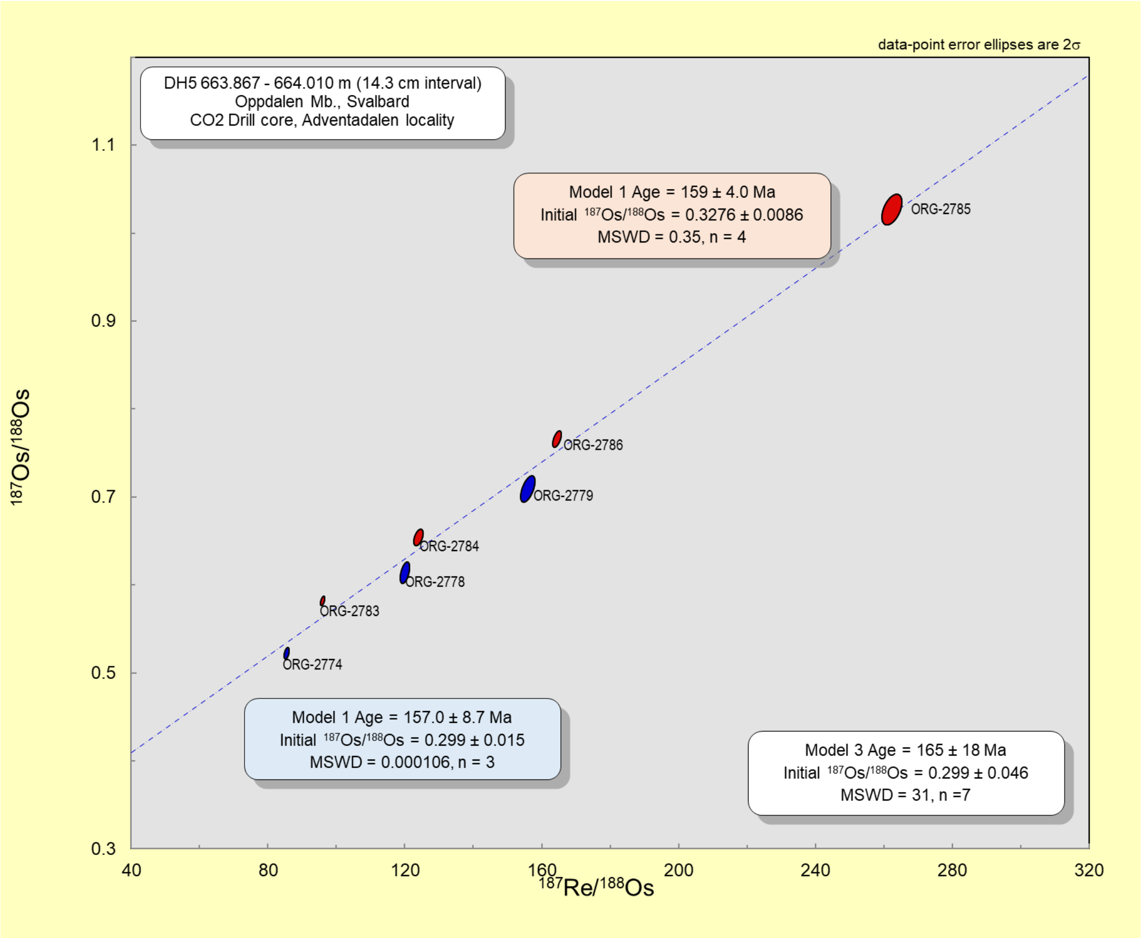

Fig. A7a Re-Os isochron of DH5R 633. Seven points yield 165 ± 18 Ma with 31 of MSWD. When samples were separated by two groups (red and blue), they yielded more plausible ages and uncertainties.

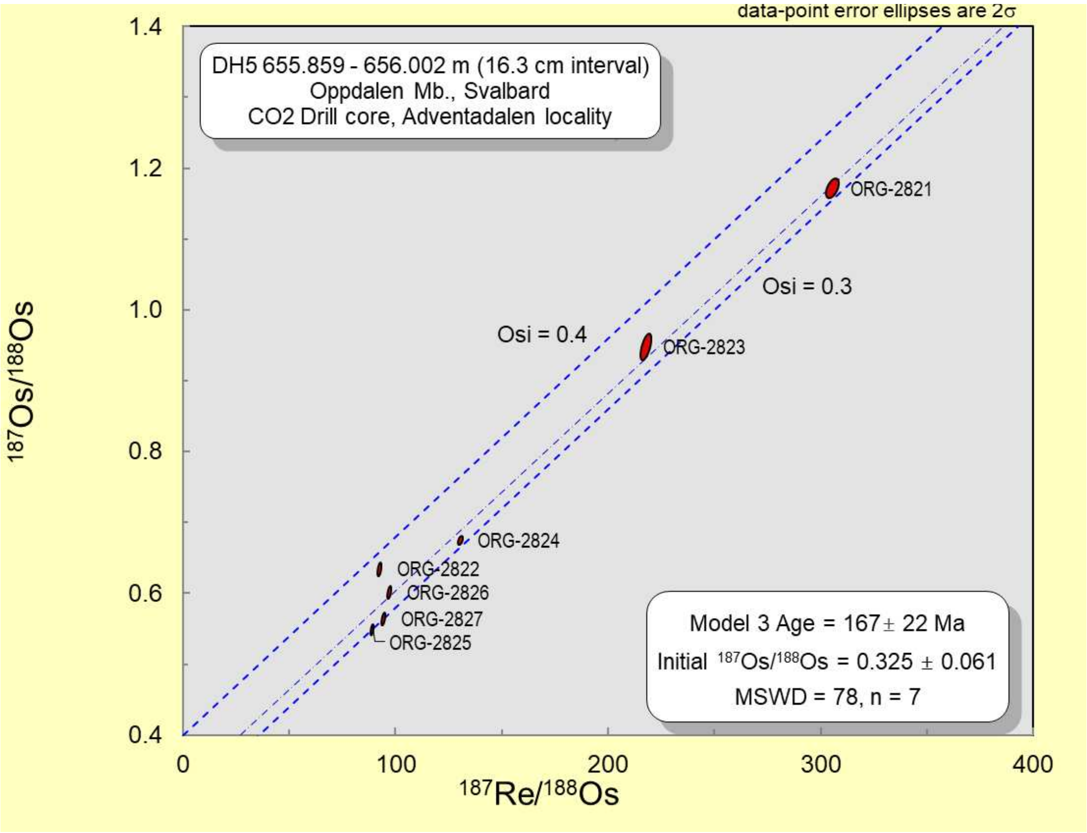

Fig. A7b Re-Os isochron of DH5R 655. Seven points yield 167 ± 22 Ma with 78 of MSWD. Thick dotted lines represent initial Os ratios of 0.4 and 0.3.

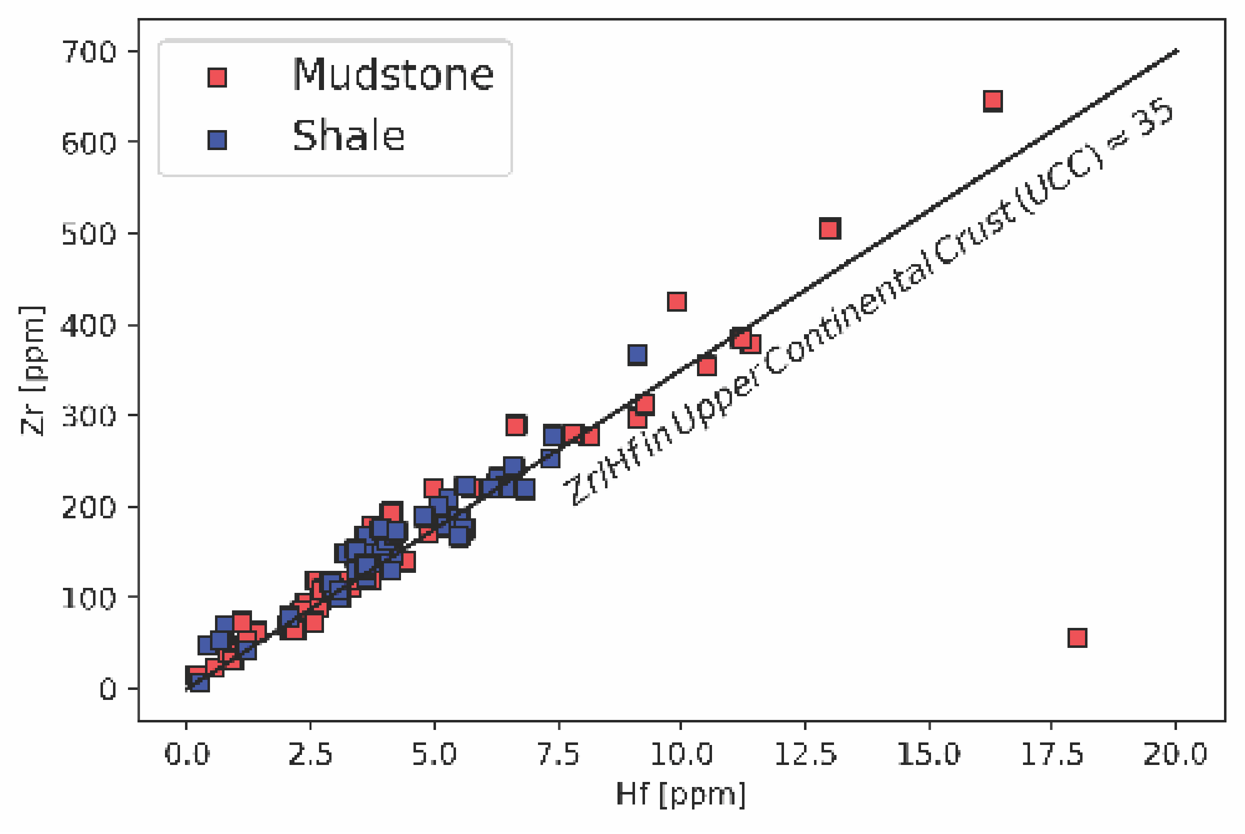

Fig. A8 Zr and Hf concentrations of 134 shale and mudstone samples from EarthChem database. Mudstone versus shale designation is specified in the references.

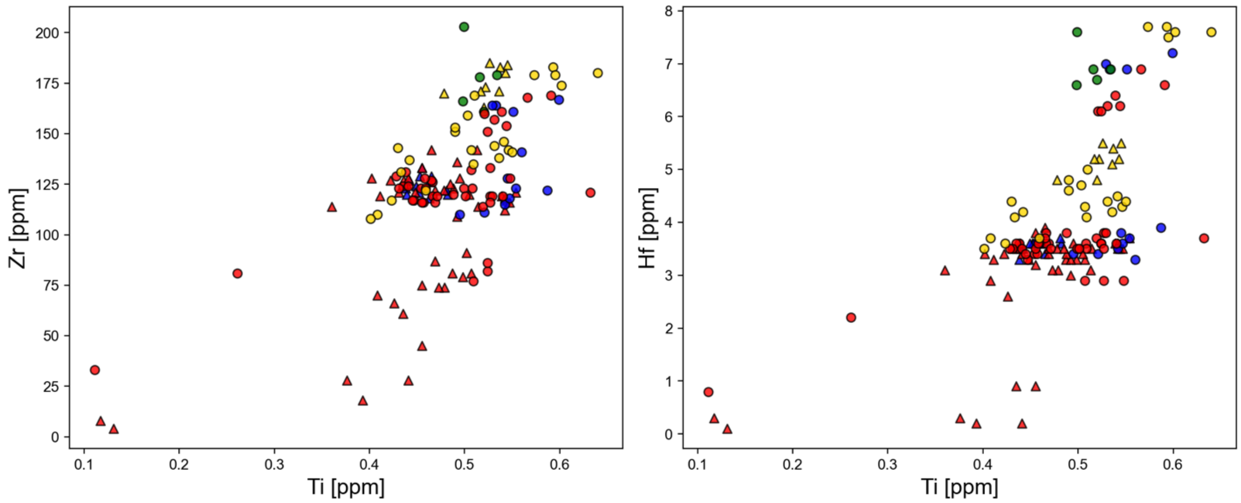

Fig. A9 The biplots between Zr and Ti (a) and Hf and Ti (b).

Table A1 TOC, HAWK pyrolysis, and δ13C and δ34S stable isotope results

DH2 drill core													
Slottsmøya Member	**TOC (wt.%)**	**S1 (mg HC/g)**	**S2 (mg HC/g)**	**S3 (mg CO_2/g)**	**Tmax (°C)**	**S2/S3**	**HI (S2 x 100/TOC)**	**OI (S3 x 100/TOC)**	**PI (S1/(S1+S2))**	**PP (S1+S2)**	**Percent Carbonate (wt.%)**	**$\delta^{13}C_{org,\ V\text{-}PDB}$**	**$\delta^{34}S_{V\text{-}CDT}$**
DH2 497.153 - 157 m*	2.22	0.82	2.09	0.39	452	5	94	18	0.28	2.91	7.42	-29.74	-26.23
DH2 497.170 - 173 m	2.08	0.68	1.98	0.32	455	6	95	15	0.26	2.66	6.87	-29.69	-23.99
DH2 497.180 - 185 m$^{\$}$	2.74	1	2.74	0.38	448	7	100	14	0.27	3.74	4.61	-29.80	-23.19
DH2 497.192 - 195 m$^{\$}$	2.94	1.06	3.83	0.25	451	15	130	9	0.22	4.89	7.63	-29.91	-21.35
DH2 497.200 - 205 m	2.95	1.09	2.79	0.28	449	10	95	9	0.28	3.88	5.22	-29.83	-23.97
DH2 497.215 - 220 m	3.49	1.25	4.3	0.25	450	17	123	7	0.23	5.55	4.83	-29.89	-19.47
DH2 497.228 - 233 m$^{\$}$	3.38	1.15	3.82	0.41	449	9	113	12	0.23	4.97	8.77	-29.91	-26.54
DH2 497.235 - 240 m	3.16	1.23	4.17	0.4	449	10	132	13	0.23	5.4	5.47	-29.92	-24.42
DH2 497.247 - 252 m*	3.36	1.31	4.52	0.29	450	16	135	9	0.22	5.83	5.76	-29.81	-20.44
DH2 497.260 - 265 m$^{\$}$	2.87	0.98	3.33	0.48	451	7	116	17	0.23	4.31	6.79	-29.74	-17.00
DH2 497.283 - 287 m	2.75	1.02	3.04	0.4	448	8	111	15	0.25	4.06	5.57	-29.75	-22.77
DH2 497.290 - 295 m	2.61	0.88	2.64	0.35	448	8	101	13	0.25	3.52	6.07	-29.59	-17.74
Lardyfjellet Member													
DH2 660.820 - 830 m	6.11	2.3	5.57	0.28	467	20	91	5	0.29	7.87	6.96	-26.01	-13.53
DH2 660.850 - 860 m	8.4	3.13	7.54	0.24	467	31	90	3	0.29	10.67	6.14	-	-
DH2 660.880 - 890 m	6.92	2.5	5.47	0.25	468	22	79	4	0.31	7.97	5.44	-	-
DH2 660.925 – 933 m	8.19	3.49	7.45	0.39	472	19	91	5	0.32	10.94	4.88	-	-
DH2 660.953 – 960 m	8.17	3.26	7.31	0.36	466	20	89	4	0.31	10.57	4.59	-	-
DH2 660.965 – 970 m	7.73	3.3	6.79	0.35	471	19	88	5	0.33	10.09	5.04	-26.06	-16.53
DH2 660.982 – 990 m	10.7	4.3	10.84	0.37	465	29	101	3	0.28	15.14	3.77	-	-
DH2 661.010 – 015 m	8.26	3.19	8.54	0.32	467	27	103	4	0.27	11.73	3.50	-	-
DH2 673.005 - 010 m	7.59	2.02	5.92	0.34	463	17	78	4	0.25	7.94	6.86	-25.94	-14.61
DH2 673.031 - 036 m	3.47	0.97	1.73	0.63	449	3	50	18	0.36	2.7	33.24	-26.14	-24.54
DH2 673.070 - 074 m*	5.9	1.63	3.49	0.39	461	9	59	7	0.32	5.12	17.34	-25.99	-22.05
DH2 673.087 - 090 m$^{\$}$	10.3	2.58	9.04	0.3	464	30	88	3	0.22	11.62	5.50	-25.85	-20.46
DH2 673.108 - 113 m	8.67	2.36	7.23	0.43	464	17	83	5	0.25	9.59	4.41	-25.88	-15.52
DH2 673.136 - 141 m	7.74	2.29	5.86	0.36	462	16	76	5	0.28	8.15	6.34	-26.03	-8.61
DH2 673.157 - 162 m	7.55	2	4.96	0.33	459	15	66	4	0.29	6.96	7.45	-26.11	-9.85
DH2 674.080 - 090 m	8.37	2.18	7.49	0.34	466	22	89	4	0.23	9.67	10.50	-26.36	-17.03
DH2 674.093 - 098 m*	7.28	1.87	6.99	0.49	466	14	96	7	0.21	8.86	10.30	-26.21	-14.07
DH2 674.105 - 110 m	9.95	2.77	10.02	0.34	466	29	101	3	0.22	12.79	9.78	-	-
DH2 674.115 - 120 m	11.4	3.09	12.5	0.4	465	31	110	4	0.20	15.59	7.50	-	-
DH2 674.130 -133 m	9.04	2.08	8.84	0.38	466	23	98	4	0.19	10.92	8.62	-26.17	-19.52
DH2 674.140 - 144 m	7.59	1.81	6.44	0.38	464	17	85	5	0.22	8.25	5.88	-26.05	-13.98
DH2 674.145 - 150 m	9.45	2.55	9.63	0.34	467	28	102	4	0.21	12.18	3.60	-26.24	-16.73
DH2 674.156 - 160 m$^{\$}$	9.15	2.27	9.63	0.35	464	28	105	4	0.19	11.9	5.09	-26.10	-17.04
DH2 674.166 - 170 m	8.68	2.1	8.67	0.37	464	23	100	4	0.19	10.77	4.88	-26.03	-17.24
DH2 674.175 - 180 m	11.6	3.02	12.27	0.44	466	28	106	4	0.20	15.29	6.60	-	-
DH2 680.295 - 300 m*	7.83	2.61	7.85	0.28	468	28	100	4	0.25	10.46	6.57	-25.31	-18.53
DH2 680.303 - 310 m	7.76	2.20	5.13	0.16	465	32	66	2	0.30	7.33	6.1	-25.58	-12.58
DH2 680.315 - 320 m$^{\$}$	6.54	2.28	4.76	0.21	461	23	73	3	0.32	7.04	5.85	-25.43	-30.78
DH2 680.324 - 328 m	6.56	1.76	4.65	0.16	467	29	71	2	0.27	6.41	6.8	-25.40	-28.54
DH2 680.335 - 340 m	6.91	2.18	5.73	0.29	465	20	83	4	0.28	7.91	6.19	-25.37	-26.05
DH2 680.345 - 349 m	6.3	2.03	6.02	0.32	466	19	96	5	0.25	8.05	5.90	-25.31	-24.99
DH2 680.357 - 362 m	6.36	2.08	5.96	0.34	466	18	94	5	0.26	8.04	5.68	-25.26	-24.47
DH2 680.373 - 376 m*	7.41	2.53	7	0.5	466	14	94	7	0.27	9.53	7.87	-25.26	-26.26
DH2 680.389 - 393 m$^{\$}$	8.94	2.71	7.92	0.32	466	25	89	4	0.25	10.63	4.77	-25.13	-27.39
DH2 680.410 - 415 m	8.74	2.72	8.77	0.35	468	25	100	4	0.24	11.49	5.24	-25.11	-23.91
DH2 680.427 - 431 m	8.03	2.62	8.09	0.44	468	18	101	5	0.24	10.71	3.02	-25.13	-21.30
DH2 680.446 - 451 m	9.7	3.32	9.96	0.46	468	22	103	5	0.25	13.28	2.59	-24.96	-25.60
Oppdalen Member													
DH2 724.243 - 247 m*	0.753	0.14	0.18	0.31	441	1	24	41	0.44	0.32	5.73	-24.87	-42.07
DH2 724.255 - 258 m$^{\$}$	0.737	0.15	0.21	0.32	446	1	28	43	0.42	0.36	4.19	-25.43	-39.38
DH2 724.263 - 267 m$^{\$}$	0.773	0.18	0.15	0.29	446	1	19	38	0.55	0.33	6.31	-25.21	-38.49
DH2 724.275 - 279 m	0.86	0.17	0.26	0.37	446	1	30	43	0.40	0.43	5.13	-25.06	-35.62
DH2 724.282 - 285 m	0.843	0.21	0.24	0.3	450	1	28	36	0.47	0.45	5.72	-25.10	-41.45
DH2 724.294 - 298 m	0.937	0.22	0.29	0.4	449	1	31	43	0.43	0.51	6.07	-25.12	-40.86
DH2 724.306 - 310 m	0.928	0.18	0.27	0.43	450	1	29	46	0.40	0.45	5.56	-25.29	-41.30
DH2 724.315 - 319 m*	0.905	0.2	0.3	0.41	453	1	33	45	0.40	0.5	5.73	-25.26	-40.76
DH2 724.324 - 328 m	0.963	0.19	0.31	0.27	451	1	32	28	0.38	0.5	5.32	-25.34	-41.36

Continued to Table A1

DH5R drill core													
Slottsmøya Member													
DH5R 489.330 - 340 m	1.69	1.187	1.77	0.39	457	5	105	23	0.40	2.96	7.52	-	-
DH5R 489.340 - 345 m	1.98	0.99	2.2	0.23	457	10	111	12	0.31	3.19	4.01	-29.63	-18.43
DH5R 489.358 - 365 m	2	1.04	2.53	0.22	458	12	127	11	0.29	3.57	1.18	-29.71	-28.17
DH5R 489.440 - 450 m	1.83	1.13	1.92	0.24	458	8	105	13	0.37	3.05	3.74	-	-
DH5R-489.485 - 490 m	2.13	1.08	2.22	0.2	459	11	104	9	0.33	3.3	1.57	-	-
Oppdalssåta Member													
DH5R 542.205 – 210 m	4.71	1.56	4.16	0.18	461	23	88	4	0.27	5.72	0.47	-26.89	-29.03
DH5R 542.267 – 273 m	7.59	3.13	7.62	0.2	464	38	100	3	0.29	10.75	0.28	-	-
DH5R 542.305 – 310 m	5.43	1.97	5.93	0.19	461	31	109	3	0.25	7.9	1.23	-	-
DH5R 542.375 – 380 m	5.76	2.05	5.97	0.29	461	21	104	5	0.26	8.02	3.28	-26.95	-26.40
DH5R 542.445 – 450 m	5.67	2.01	5.41	0.27	458	20	95	5	0.27	7.42	0.29	-	-
Lardyfjellet Member													
DH5R 600.320 – 327 m	6.36	2.31	5.57	0.21	468	27	88	3	0.29	7.88	3.3	-	-
DH5R 600.333 - 336 m[*]	6.41	1.50	4.63	0.25	469.00	19	72	4	0.24	6.13	5.1	-26.24	-19.55
DH5R 600.342 – 350 m	6.39	2.3	5.1	0.27	465	19	80	4	0.31	7.4	3.6	-	-
DH5R 600.351 - 356 m	6.23	1.56	4.91	0.15	470	33	79	2	0.24	6.47	4.6	-26.21	-20.84
DH5R 600.360 - 365 m	6.41	1.69	4.55	0.14	463	33	71	2	0.27	6.24	5.5	-26.22	-21.42
DH5R 600.370 – 375 m	6.93	3.14	6.76	0.25	463	27	98	4	0.32	9.9	5.0	-	-
DH5R 600.384 – 390 m	6.65	2.35	5.41	0.32	466	17	81	5	0.30	7.76	4.1	-26.21	-22.39
DH5R 600.395 – 400 m	7.15	2.57	6.29	0.33	465	19	88	5	0.29	8.86	3.9	-6.44	-21.79
DH5R 607.007 - 010 m[$]	6.74	2.13	4.82	0.28	464	17	72	4	0.31	6.95	6.5	-25.92	-5.96
DH5R 607.022 - 027 m[$]	1.68	0.27	0.09	0.52	439	0	5	31	0.75	0.36	19.0	-26.00	8.83
DH5R 607.060 - 065 m[$]	7.92	2.58	6.13	0.42	464	15	77	5	0.30	8.71	5.7	-25.93	0.62
DH5R 607.096 - 100 m[*]	7.15	2.5	5.86	0.3	463	20	82	4	0.30	8.36	6.2	-25.86	-0.31
DH5R 607.114 - 118 m	6.59	2.28	6.07	0.25	465	24	92	4	0.27	8.35	6.5	-25.79	-1.51
DH5R 607.143 - 147 m[$]	8.7	2.84	7.56	0.27	464	28	87	3	0.27	10.4	5.4	-25.95	-15.15
DH5R 607.155 - 159 m	8.69	2.65	6.92	0.35	463	20	80	4	0.28	9.57	6.1	-25.86	-19.04
DH5R 607.166 - 171 m	7.32	2.54	5.55	0.31	463	18	76	4	0.31	8.09	5.7	-25.81	-6.18
DH5R 613.540 – 545 m	8.91	2.66	8.4	0.27	468	31	94	3	0.24	11.06	1.13	-	-
DH5R 613.555 – 565 m	8.53	2.47	8.58	0.24	468	36	101	3	0.22	11.05	1.98	-	-
DH5R 613.609 – 620 m	8.88	3.01	7.53	0.38	463	20	85	4	0.29	10.54	3.81	-	-
DH5R 613.625 - 629 m[*]	7.53	1.93	4.43	0.95	465	5	59	13	0.30	6.36	3.6	-25.66	-11.17
DH5R 613.640 - 645 m	8.34	1.82	5.47	0.15	467	36	66	2	0.25	7.29	4.7	-25.91	-11.00
DH5R 613.653 - 657 m	7.81	1.82	6.56	0.32	467	21	84	4	0.22	8.38	4.8	-25.71	-8.96
DH5R 613.660 - 664 m	8.4	1.71	8.13	0.36	471	23	97	4	0.17	9.84	4.5	-25.65	-6.45
DH5R 613.667 – 674 m	10.3	2.81	9.95	0.39	473	26	97	4	0.22	12.76	1.7	-25.81	-15.95
DH5R 613.674 - 678 m	7.06	1.72	5.27	0.31	466	17	75	4	0.25	6.99	4.9	-25.72	-4.74
DH5R 613.687 - 690 m[$]	6.08	1.67	5.17	0.45	466	11	85	7	0.24	6.84	19.8	-25.74	-13.03
DH5R 613.695 – 705 m	11.7	3.5	10.14	0.35	469	29	87	3	0.26	13.64	2.0	-	-
DH5R 613.705 - 708 m	8.44	1.86	6.83	0.16	467	43	81	2	0.21	8.69	4.7	-25.92	-6.88
DH5R 613.719 – 728m	8.86	2.9	7.67	0.42	470	18	87	5	0.27	10.57	3.7	-	-
DH5R 613.729 - 733 m[$]	8.01	1.79	6.52	0.43	468	15	81	5	0.22	8.31	4.4	-25.60	-5.87
DH5R 613.737 - 742 m	8.02	1.64	7.62	0.5	470	15	95	6	0.18	9.26	7.6	-25.69	-3.71
DH5R 613.745 – 755 m	9.05	2.63	8.07	0.25	470	32	89	3	0.25	10.7	1.9	-25.96	-11.91
DH5R 613.750 - 755 m[*]	8.45	0.18	7	0.12	471	58	83	1	0.03	7.18	4.5	-25.93	-11.53
DH5R 613.763 - 767 m[*]	7.9	1.77	7.7	0.32	468	24	97	4	0.19	9.47	5.6	-25.73	-2.78
DH5R 613.78 m	8.93	2.47	6.94	0.21	468	33	78	2	0.26	9.41	1.8	-25.91	-7.37
Oppdalen Member													
DH5R 658.012 – 016 m	1.37	0.24	0.49	0.08	466	6	36	6	0.33	0.73	4.96	-	-
DH5R 658.028 - 035 m[*]	1.38	0.26	0.54	0.27	458	2	39	20	0.33	0.8	5.72	-25.17	-35.33
DH5R 658.040 - 045 m	1.25	0.24	0.4	0.37	455	1	32	30	0.38	0.64	5.40	-25.30	-36.11
DH5R 658.054 – 059 m	1.42	0.23	0.46	0.1	464	5	32	7	0.33	0.69	2.37	-	-
DH5R 658.085 – 090 m	1.18	0.21	0.47	0.52	459	1	40	44	0.31	0.68	5.16	-25.25	-25.81
DH5R 658.105 – 110 m	1.19	0.21	0.39	0.12	461	3	33	10	0.35	0.6	2.03	-25.26	-27.76
DH5R 658.150 – 160 m	1.35	0.24	0.52	0.12	464	4	39	9	0.32	0.76	3.02	-	-
DH5R 658.163 – 170 m[*$]	1.31	0.24	0.56	0.41	460	1	43	31	0.30	0.8	5.51	-25.28	-28.23
DH5R 658.185 - 190 m	1.34	0.2	0.42	0.1	463	4	31	7	0.32	0.62	2.80	-	-

[*] means the averaged value by duplicate of carbon isotopes

[$] means the averaged values by duplicate of sulfur isotopes

Table A2 Re-Os measurement results

DH2 drill core **Slottsmoya Member**	**ORG run #**	**Re**	**Error**	**Os**	**Error**	**^{187}Re/^{188}Os**	**Error**	**^{187}Os/^{188}Os**	**Error**	**rho**	**Re%**	**Os%**
DH2 497.153 – 157 m	ORG-2699	21.9	0.13	0.343	0.002	359	5	1.40	0.03	0.5794	0.9%	0.3%
DH2 497.170 – 173 m	ORG-2700	11.1	0.07	0.292	0.002	205	3	1.03	0.02	0.5528	1.9%	0.3%
DH2 497.180 – 185 m	ORG-2721	12.5	0.05	0.214	0.001	323	3	1.28	0.02	0.5101	1.1%	0.6%
DH2 497.192 – 195 m	ORG-2701	19.3	0.04	0.399	0.002	265	3	1.18	0.02	0.5670	1.1%	0.2%
DH2 497.200 – 205 m	ORG-2630	8.77	0.03	0.202	0.002	236	4	1.12	0.03	0.6109	1.3%	0.5%
DH2 497.215 – 220 m	ORG-2631	15.7	0.05	0.238	0.002	373	5	1.46	0.03	0.5773	0.8%	0.5%
DH2 497.228 – 233 m	ORG-2702	19.1	0.04	0.425	0.002	245	2	1.14	0.02	0.6324	1.1%	0.5%
DH2 497.235 – 240 m	ORG-2632	11.7	0.04	0.221	0.001	292	4	1.25	0.02	0.5742	1.2%	0.5%
DH2 497.247 – 252 m	ORG-2633	11.4	0.05	0.221	0.001	287	3	1.24	0.01	0.5430	1.3%	0.5%
DH2 497.260 – 265 m	ORG-2634	10.0	0.01	0.213	0.001	257	2	1.17	0.02	0.5676	1.3%	0.5%
DH2 497.283 – 287 m	ORG-2703	17.3	0.02	0.392	0.002	240	3	1.11	0.02	0.6376	1.2%	0.2%
Lardyfjellet Member												
DH2 673.005 – 010 m	ORG-2644	44.7	0.08	0.485	0.003	544	6	1.84	0.03	0.6544	0.6%	0.3%
DH2 673.031 – 036 m	ORG-2645	76.6	0.22	0.517	0.002	977	8	2.95	0.03	0.6115	0.3%	0.3%
DH2 673.070 – 074 m	ORG-2646	61.9	0.12	0.534	0.009	714	20	2.26	0.09	0.6563	0.4%	0.3%
DH2 673.087 – 090 m	ORG-2647	61.2	0.28	0.730	0.003	487	5	1.69	0.02	0.5371	0.4%	0.2%
DH2 673.108 – 113 m	ORG-2648	42.2	0.30	0.610	0.008	391	10	1.45	0.05	0.6332	0.6%	0.2%
DH2 673.136 – 141 m	ORG-2649	36.6	0.11	0.533	0.002	389	4	1.45	0.02	0.5815	0.7%	0.3%
DH2 673.157 – 162 m	ORG-2650	42.4	0.15	0.536	0.034	455	54	1.61	0.27	0.6965	0.7%	0.3%
DH2 674.080 – 090 m	ORG-1707	42.4	0.12	0.491	0.004	506	8	1.78	0.04	0.6427	0.5%	0.1%
DH2 674.093 – 098 m	ORG-2715	26.5	0.08	0.445	0.002	330	3	1.28	0.02	0.6339	1.1%	0.4%
DH2 674.105 – 110 m	ORG-1708	46.5	0.12	0.600	0.004	446	5	1.61	0.03	0.6336	0.4%	0.1%
DH2 674.115 – 120 m	ORG-1709	55.5	0.13	0.698	0.004	460	5	1.65	0.03	0.6566	0.4%	0.1%
DH2 674.130 –133 m	ORG-2716	31.0	0.04	0.517	0.002	348	3	1.71	0.02	0.6512	0.9%	0.4%
DH2 674.140 – 144 m	ORG-2717	29.7	0.05	0.438	0.002	383	3	1.46	0.02	0.5928	1.0%	0.4%
DH2 674.145 – 150 m	ORG-1710	48.9	0.20	0.590	0.002	482	4	1.71	0.02	0.4975	0.4%	0.1%
DH2 674.156 – 160 m	ORG-2718	44.1	0.05	0.570	0.002	444	3	1.59	0.02	0.6424	0.6%	0.3%
DH2 674.166 – 170 m	ORG-2719	34.4	0.04	0.515	0.002	377	2	1.44	0.01	0.6461	0.9%	0.4%
DH2 674.175 – 180 m	ORG-1711	55.5	0.14	0.732	0.003	435	3	1.59	0.02	0.5789	0.4%	0.1%
DH2 680.295 – 300 m	ORG-2637	32.3	0.06	0.375	0.005	504	12	1.77	0.06	0.6732	0.5%	0.2%
DH2 680.295 – 300 m dup.	ORG-2711	31.6	0.08	0.361	0.003	516	6	1.82	0.03	0.6380	1.1%	0.5%
DH2 680.285 – 290 m$^{\$}$	ORG-2753	31.9	0.59	0.335	0.001	563	15	1.86	0.02	0.1685	0.8%	0.3%
DH2 680.303 – 310 m	ORG-2754	50.2	0.06	0.395	0.001	806	4	2.55	0.02	0.5952	0.6%	0.3%
DH2 680.315 – 320 m$^{\$}$	ORG-2695	66.6	0.13	0.473	0.005	911	16	2.75	0.07	0.6546	0.3%	0.2%
DH2 680.315 – 320 m dup.	ORG-2712	66.0	0.43	0.478	0.003	897	12	2.79	0.05	0.4751	0.5%	0.4%
DH2 680.324 – 328 m	ORG-2755	41.5	0.12	0.397	0.002	635	6	2.13	0.03	0.6100	0.7%	0.3%
DH2 680.335 – 340 m	ORG-2639	46.4	0.22	0.427	0.005	666	13	2.21	0.06	0.6356	0.4%	0.2%
DH2 680.345 – 349 m	ORG-2686	38.2	0.06	0.382	0.001	603	3	2.05	0.02	0.5874	0.8%	0.3%
DH2 680.357 – 362 m$^{\$}$	ORG-2640	36.5	0.22	0.491	0.003	423	6	1.52	0.03	0.5648	0.5%	0.2%
DH2 680.357 – 362 m dup.	ORG-2696	36.3	0.08	0.379	0.002	572	6	1.98	0.03	0.6196	0.5%	0.3%
DH2 680.357 – 362 m trip.	ORG-2713	35.5	0.11	0.370	0.002	574	5	1.98	0.03	0.5376	0.9%	0.5%
DH2 680.373 – 376 m$^{\$}$	ORG-2641	50.0	0.12	0.461	0.004	658	9	2.11	0.04	0.6565	0.3%	0.2%
DH2 680.389 – 393 m$^{\$}$	ORG-2642	46.8	0.26	0.440	0.002	644	7	2.09	0.03	0.4858	0.4%	0.2%
DH2 680.410 – 415 m	ORG-2687	47.4	0.14	0.478	0.002	597	4	2.03	0.02	0.5126	0.6%	0.2%
DH2 680.427 – 431 m	ORG-2688	39.9	0.06	0.386	0.002	626	5	2.10	0.03	0.6177	0.6%	0.2%
DH2 680.446 – 451 m	ORG-2689	46.0	0.14	0.441	0.002	632	6	2.11	0.03	0.5552	0.6%	0.2%
DH2 680.446 – 451 m dup.	ORG-2697	46.1	0.05	0.440	0.004	636	9	2.12	0.04	0.6725	0.4%	0.2%
Oppdalen Member												
DH2 724.243 – 247 m	ORG-2652	6.78	0.03	0.231	0.002	153	3	0.75	0.02	0.6070	3.8%	0.4%
DH2 724.255 – 258 m	ORG-2653	6.65	0.04	0.201	0.001	174	2	0.81	0.01	0.3720	3.9%	0.4%
DH2 724.263 – 267 m	ORG-2654	10.6	0.04	0.236	0.001	240	3	0.98	0.02	0.4835	2.3%	0.3%
DH2 724.275 – 279 m	ORG-2693	12.0	0.02	0.196	0.001	336	4	1.22	0.03	0.5607	1.1%	0.4%
DH2 724.282 – 285 m	ORG-2707	19.2	0.06	0.230	0.001	482	4	1.62	0.02	0.5407	1.2%	0.5%
DH2 724.282 – 285 m dup.	ORG-2655	13.9	0.16	0.213	0.002	362	8	1.30	0.03	0.4503	1.9%	0.4%
DH2 724.294 – 298 m	ORG-2694	20.0	0.04	0.226	0.001	516	6	1.70	0.03	0.6221	0.7%	0.3%
DH2 724.306 – 310 m	ORG-2720	9.06	0.02	0.231	0.001	207	1	0.88	0.01	0.5068	2.3%	0.6%
DH2 724.315 – 319 m	ORG-2708	13.7	0.04	0.254	0.001	292	2	1.11	0.01	0.4895	1.7%	0.5%
DH2 724.315 – 319 m dup.	ORG-2709	13.6	0.05	0.253	0.001	293	3	1.11	0.02	0.5741	1.7%	0.5%
DH2 724.315 – 319 m trip.	ORG-2657	13.3	0.06	0.227	0.004	323	9	1.21	0.05	0.6130	1.9%	0.4%
DH2 724.324 – 328 m	ORG-2658	16.3	0.12	0.240	0.004	379	11	1.34	0.06	0.6430	1.6%	0.4%

Continued to Table A2

DH5R drill core												
Lardyfjellet Member												
DH5R 607.007 – 607.010 m	ORG-2672	19.2	0.03	0.328	0.004	327	8	1.34	0.05	0.6817	1.3%	0.3%
DH5R 607.022 – 607.027 m	ORG-2673	4.15	0.01	0.086	0.001	263	8	1.18	0.06	0.5788	7.6%	1.3%
DH5R 607.060 – 607.065 m	ORG-2662	24.2	0.04	0.399	0.003	340	4	1.37	0.02	0.6164	1.2%	0.4%
DH5R 607.096 – 607.100 m	ORG-2663	22.1	0.05	0.370	0.001	333	3	1.35	0.02	0.5732	1.3%	0.4%
DH5R 607.114 – 607.118 m	ORG-2664	19.2	0.03	0.319	0.002	336	5	1.36	0.03	0.6446	1.4%	0.5%
DH5R 607.143 – 607.147 m	ORG-2665	48.4	0.23	0.510	0.003	566	7	1.94	0.03	0.5672	0.6%	0.3%
DH5R 607.155 – 607.159 m	ORG-2670	50.5	0.07	0.518	0.003	583	5	1.98	0.03	0.6524	0.6%	0.2%
DH5R 607.166 – 607.171 m	ORG-2671	24.0	0.04	0.376	0.001	359	2	1.42	0.01	0.6000	1.0%	0.2%
DH5R 613.540 – 613.545 m	ORG-1571	23.5	0.09	0.427	0.002	304	3	1.26	0.02	0.5434	0.9%	0.2%
DH5R 613.555 – 613.565 m	ORG-1570	21.5	0.05	0.398	0.001	299	2	1.25	0.01	0.5865	1.0%	0.2%
DH5R 613.609 – 613.620 m	ORG-1870	23.3	0.19	0.450	0.001	285	4	1.21	0.01	0.3039	0.7%	0.1%
DH5R 613.625 – 613.629 m	ORG-2667	19.3	0.03	0.369	0.001	287	2	1.21	0.01	0.5887	1.5%	0.3%
DH5R 613.640 – 613.645 m	ORG-2756	22.7	0.03	0.433	0.002	288	2	1.22	0.01	0.6416	1.2%	0.3%
DH5R 613.653 – 613.657 m	ORG-2683	20.1	0.04	0.374	0.002	297	3	1.25	0.02	0.6280	1.1%	0.2%
DH5R 613.660 – 613.664 m	ORG-2691	20.4	0.03	0.398	0.005	282	7	1.21	0.04	0.6582	0.8%	0.2%
DH5R 613.667 – 613.674 m	ORG-1569	40.0	0.09	0.536	0.002	426	4	1.55	0.02	0.5974	0.5%	0.1%
DH5R 613.674 – 613.678 m	ORG-2668	18.7	0.03	0.345	0.003	300	4	1.25	0.03	0.6604	1.5%	0.3%
DH5R 613.687 – 613.690 m	ORG-2669	20.0	0.03	0.372	0.001	296	2	1.24	0.01	0.6160	1.4%	0.3%
DH5R 613.695 – 613.705 m	ORG-1568	47.1	0.10	0.726	0.004	363	4	1.36	0.02	0.6330	0.5%	0.1%
DH5R 613.705 – 613.708 m	ORG-2757	22.3	0.04	0.415	0.002	295	3	1.24	0.02	0.6349	1.1%	0.3%
DH5R 613.719 – 613.728m	ORG-1871	27.5	0.21	0.460	0.001	334	4	1.33	0.01	0.2636	0.6%	0.1%
DH5R 613.729 – 613.733 m	ORG-2692	18.6	0.06	0.389	0.006	261	8	1.16	0.05	0.6629	1.1%	0.3%
DH5R 613.737 – 613.742 m	ORG-2684	18.6	0.04	0.413	0.001	244	1	1.11	0.01	0.5488	1.1%	0.2%
DH5R 613.745 – 613.755 m	ORG-1567	28.6	0.26	0.500	0.002	318	5	1.29	0.02	0.3550	0.7%	0.1%
DH5R 613.750 – 613.755 m	ORG-2759	28.6	0.05	0.498	0.003	319	3	1.29	0.02	0.6692	0.7%	0.2%
DH5R 613.763 – 613.767 m	ORG-2685	20.2	0.06	0.416	0.003	266	4	1.16	0.03	0.6202	1.1%	0.2%
DH5R 613.78 m	ORG-1566	23.4	0.07	0.494	0.001	259	2	1.14	0.01	0.4884	0.9%	0.1%
Oppdalen Member												
DH5R 658.012 – 658.016 m	ORG-1549	3.68	0.01	0.207	0.001	91	1	0.64	0.01	0.5102	3.2%	0.3%
DH5R 658.054 – 658.059 m	ORG-1550	5.26	0.01	0.219	0.001	125	1	0.73	0.01	0.6287	2.3%	0.3%
DH5R 658.085 – 658.090 m	ORG-2704	7.79	0.02	0.182	0.001	230	2	1.01	0.02	0.6038	1.5%	0.3%
DH5R 658.105 – 658.110 m	ORG-1551	9.05	0.02	0.227	0.002	212	3	0.95	0.02	0.6325	1.3%	0.3%
DH5R 658.150 – 658.160 m	ORG-1552	7.48	0.01	0.208	0.002	191	4	0.90	0.03	0.6290	1.6%	0.3%
DH5R 658.163 – 658.170 m	ORG-2705	4.32	0.01	0.192	0.001	117	2	0.71	0.02	0.5417	3.2%	0.3%
DH5R 658.185 – 658.190 m	ORG-2710	11.8	0.04	0.240	0.001	268	2	1.11	0.01	0.4956	1.1%	0.3%

[$] Re-Os isotopic results were not used for isochron.

dup. and trip. denote duplicate and triplicate for the sample.

Table A3 TOC, trace elements, and C, N, O, and S stable isotope results

DH2 drill core

Slottsmøya Member	TOC (wt.%)	Al	Ca	Fe	K	Mg	Na	S	Ti	Ba	Cr	Cu	Li	Mn	Ni	P	Sr	V	Zn	Zr	Ag	As	Be	Bi	Cd	Co
unit -->	wt %	wt %	wt %	wt %	wt %	wt %	wt %	wt %	ppm	ppm	ppm	ppm	ppm	ppm	%	ppm	ppm	ppm	ppm	ppm	ppm	ppm	ppm	ppm	ppm	ppm
detection limt	0.01	0.01	0.01	0.01	0.0	0.0	0	0	1.00	1.00	0.20	0.5	1	0.5	0.001	0.2	0.2	1	0.2	1	0.05	0.1	0.1	0.02	0.01	0.1
Dh2 497.153 - 157 m	2.22	8.48	0.51	4.23	3.09	1.18	0.51	2.68	0.482	56	106	53.8	126	111	108	0.075	133	122	112	120	0.58	14.5	2.6	0.32	0.2	9.2
Dh2 497.170 - 173 m	2.08	8.66	0.53	3.77	3.2	1.17	0.52	1.95	0.481	70	104	42.5	130	113	83.4	0.074	140	124	169	122	0.54	10.4	2.6	0.3	0.4	8
Dh2 497.180 - 185 m	2.74	9.06	0.56	4.49	2.98	1.17	0.55	2.58	0.442	65	169	60.7	134	163	75.2	0.078	130	129	117	127	0.68	15.1	2.5	0.31	0.3	10.1
Dh2 497.192 - 195 m	2.94	8.33	0.56	3.4	2.99	1.11	0.54	1.66	0.463	84	181	44.5	139	115	82.9	0.092	131	123	128	118	0.61	10.8	2.4	0.33	0.4	8.1
Dh2 497.200 - 205 m	2.95	8.83	0.59	4.97	2.88	1.17	0.52	3.28	0.438	46	167	61.8	134	115	81.5	0.094	130	126	143	123	0.81	18.1	2.4	0.3	0.4	11
Dh2 497.215 - 220 m	3.49	9	0.64	3.61	3.23	1.2	0.57	1.63	0.465	131	173	51.6	145	110	65.2	0.111	140	131	153	129	0.99	10.2	2.5	0.3	0.4	8.9
Dh2 497.228 - 233 m	3.38	8.44	0.68	4.2	2.18	1.14	0.5	2.49	0.452	62	182	51.1	141	104	115	0.146	148	122	163	121	0.94	13.8	2.4	0.31	0.4	9.4
Dh2 497.235 - 240 m	3.16	9.11	0.8	4.25	3.24	1.21	0.57	2.22	0.455	94	181	55.5	146	123	76.5	0.168	161	133	165	133	1.03	15.5	2.7	0.32	0.4	9.9
Dh2 497.247 - 252 m	3.36	8.9	0.72	3.65	3.35	1.21	0.58	1.61	0.453	113	169	49.1	142	110	68.7	0.133	150	132	169	129	0.95	12.2	2.4	0.29	0.5	9.3
Dh2 497.260 - 265 m	2.87	9.1	0.61	3.48	3.29	1.2	0.57	1.51	0.463	80	186	50.1	134	106	63	0.099	142	129	163	126	0.69	10.4	2.6	0.28	0.3	9.1
Dh2 497.283 - 287 m	2.75	7.89	0.56	3.96	2.7	1.09	0.52	2.44	0.439	56	186	67.8	124	110	127	0.076	135	115	154	120	0.69	13.8	2.4	0.32	0.3	9
Dh2 497.290 - 295 m	2.61	9.01	0.58	3.8	2.26	1.2	0.56	1.96	0.449	69	176	48.4	128	110	62.7	0.072	130	125	147	124	0.59	13.4	2.8	0.3	0.2	8.8
Lardyfjellet Member																										
DH2 660.820 - 830 m	6.11	6.38	0.76	2.31	1.63	0.92	0.38	1.75	0.455	135	104	47.7	80.6	128	57.2	0.073	132	163	243	75	1.98	13.4	2.1	0.2	1.8	5.9
DH2 660.850 - 860 m	8.4	6.72	0.59	2.57	1.62	0.87	0.34	2.18	0.502	61	122	62.7	79.5	116	71.7	0.063	129	187	166	91	2.34	19.3	2.5	0.27	1.2	6.9
DH2 660.880 - 890 m	6.92	6.96	0.59	2.43	2.58	0.89	0.37	1.91	0.507	68	118	56.2	76.7	106	55.3	0.068	123	192	122	81	1.27	16.3	2.4	0.28	0.7	6.8
DH2 660.925 – 933 m	8.19	6.9	0.7	2.35	2.6	0.8	0.3	1.98	0.492	137	135	67.3	48.7	111	67.3	0.081	135	170	227	136	2.1	15.1	1.8	0.3	1.5	7.8
DH2 660.953 – 960 m	8.17	6.89	0.57	2.93	1.95	0.86	0.33	2.58	0.487	57	120	66.8	78.7	118	71.1	0.071	128	198	122	81	2.57	46.8	2.7	0.27	0.8	7.5
DH2 660.965 – 970 m	7.73	7.2	0.7	2.5	2.1	0.9	0.3	2.18	0.513	93	141	58.4	50.9	118	65.5	0.079	134	174	139	142	1.8	16.7	2	0.3	0.8	8.1
DH2 660.982 – 990 m	10.7	6.75	0.54	2.65	2.54	0.82	0.32	2.42	0.469	68	132	81.8	81.3	99	90.7	0.06	132	207	523	87	3.89	29.2	2.5	0.27	5.7	6.9
DH2 661.010 – 661.01	8.26	7.02	0.53	2.35	2.67	0.81	0.35	1.88	0.498	85	132	66.3	83.1	115	70.7	0.071	126	212	151	79	3.08	18.3	2.7	0.29	1	7
DH2 670.005 - 008 m	6.44	8.68	0.55	2.26	3.03	1.03	0.46	1.59	0.514	132	182	40	62	115	112	0.046	201	193	156	114	1.2	11.8	2.5	0.25	1.1	9
DH2 670.015 - 018 m	5.89	8.51	0.66	2.75	3.16	1.05	0.46	2.05	0.492	105	206	37	60	147	152	0.047	190	182	143	109	1	13.8	2.4	0.23	0.9	9
DH2 670.032 - 035 m	7.47	8.99	0.51	2.45	3.44	1	0.45	1.78	0.539	148	139	47	65	119	110	0.049	198	215	148	119	1.5	12.9	2.7	0.27	0.9	9
DH2 670.043 - 047 m	4.37	8.27	0.44	2.52	3.43	0.91	0.44	2	0.544	89	133	54	64	104	142	0.046	198	212	277	117	1.8	15.3	2.8	0.28	2.1	10
DH2 670.056 - 060 m	7.06	8.41	0.55	2.43	3.35	1.01	0.47	1.85	0.542	87	152	52	65	122	140	0.05	205	205	133	118	1.4	13.3	2.6	0.26	0.8	9
DH2 670.070 - 075 m	7.09	8.75	0.54	2.62	3.5	1.05	0.47	2.01	0.554	63	155	47	66	125	151	0.053	224	216	152	121	1.1	14.4	2.9	0.27	0.8	9
DH2 670.085 - 089 m	7.05	9.02	0.54	2.93	3.46	1.06	0.45	2.37	0.547	58	176	47	66	114	190	0.049	218	213	137	116	1.4	17.8	2.9	0.28	0.8	10
Dh2 673.005 - 010 m	7.59	7.29	1.21	2.13	2.26	0.83	0.4	1.91	0.393	90	135	48.1	63.1	91	85.5	0.246	175	274	145	18	1.86	16.5	2.9	0.23	2.6	6.7
Dh2 673.031 - 036 m	3.47	3.75	9.1	3.5	1.37	2.11	0.31	2.89	0.117	84	79	47.3	38.7	298	292	2.18	768	175	2290	8	1.71	29.8	3.4	0.2	19.9	11.8
Dh2 673.070 - 074 m	5.9	5.57	4.35	2.61	1.71	1.35	0.32	2.14	0.131	118	109	52.1	43.9	174	171	0.895	463	225	242	4	1.77	19.6	3.2	0.21	3.2	7.7
Dh2 673.087 - 090 m	10.3	7.4	1.02	2.36	2.78	0.84	0.37	2.22	0.422	67	148	64.6	58.8	124	115	0.151	172	299	382	127	2.52	20.2	2.9	0.27	7	7.9
Dh2 673.108 - 113 m	8.67	7.75	0.78	2.53	2.96	0.81	0.42	2.4	0.436	55	143	88.1	64.3	96	93.2	0.103	148	304	185	127	2.35	22.9	2.8	0.26	2.4	8.5
Dh2 673.136 - 141 m	7.74	6.81	0.84	3.08	2.52	0.78	0.43	3.11	0.402	35	129	59.5	63.1	75	95.9	0.104	136	277	379	128	2.52	21.3	2.4	0.24	6.3	7.1
Dh2 673.157 - 162 m	7.55	6.67	1.11	3.42	2.34	0.73	0.42	3.72	0.36	118	121	55.3	63.8	87	104	0.213	185	257	407	114	2.94	22.1	2.4	0.2	6.5	7
Dh2 674.080 - 090 m	8.37	5.91	1.94	2.36	2.11	1.3	0.38	2.16	0.408	99	108	56.7	58.8	163	84.5	0.203	197	271	482	70	2.81	20.2	2.2	0.21	6.8	6
Dh2 674.093 - 098 m	7.28	6.64	1.78	1.86	2.09	1.11	0.38	1.46	0.376	87	148	42.5	55.8	119	105	0.221	209	259	88.7	28	1.89	12.5	2.5	0.25	1.1	6
Dh2 674.105 - 110 m	9.95	5.67	1.59	2.06	1.84	1.08	0.34	2.09	0.426	83	113	71.1	54	149	88	0.188	167	275	363	66	3.87	18.5	2.2	0.24	5.3	5.8
Dh2 674.115 - 120 m	11.4	6.99	1.24	2.08	2.24	1.04	0.37	1.9	0.455	98	147	83.3	61	121	103	0.168	169	336	561	45	4.41	17.2	2.6	0.27	9	6.5
Dh2 674.130 - 133 m	9.04	7.11	1.37	1.84	2.5	1.03	0.36	1.38	0.411	118	150	48.7	57.1	147	70.5	0.128	197	286	107	119	2.47	13.2	2.9	0.25	1.7	6.3
Dh2 674.140 - 144 m	7.59	7.32	0.89	2.28	2.75	0.82	0.41	2.08	0.431	68	151	47.6	60.5	79	69.3	0.15	153	282	72.7	121	2.47	16.3	2.9	0.25	0.9	6.8
Dh2 674.145 - 150 m	9.45	6.76	0.74	2.24	2.35	0.78	0.37	2.32	0.479	66	124	69.5	63.8	112	93.3	0.141	147	303	246	74	3.28	19.6	2.8	0.26	3	6.7
Dh2 674.156 - 160 m	9.15	7.17	0.64	1.83	2.71	0.75	0.38	1.62	0.439	58	168	50.2	63.7	70	83.4	0.109	147	300	180	125	2.4	14.4	2.8	0.26	2.7	7.1
Dh2 674.166 - 170 m	8.68	8.3	0.67	2.06	3.02	0.89	0.44	1.62	0.441	58	195	64.8	62.5	119	97.5	0.094	131	337	147	128	2.4	19.4	2.6	0.26	1.9	7.9
Dh2 674.175 - 180 m	11.6	6.13	1	2.34	1.54	0.87	0.36	2.34	0.473	89	128	77.6	63.7	128	99.2	0.159	179	310	457	74	4	29.6	2.8	0.28	6.6	6.3
Dh2 680.295 - 300 m	7.83	7.39	0.95	1.74	2.08	0.81	0.38	1.27	0.441	208	121	37.6	65.2	107	58.7	0.201	240	141	114	28	0.99	5.9	2.5	0.23	0.9	5.8
Dh2 680.303 - 310 m	7.76	6.58	0.87	3.46	2.15	0.79	0.38	3.53	0.435	31	112	40	56	110	94	0.207	312	139	744	61	1	9.1	2.1	0.2	3.8	6
Dh2 680.315 - 320 m	6.54	7.7	0.63	2.78	2.81	0.86	0.38	2.55	0.448	51	116	44.6	68.6	75	81.2	0.081	169	154	195	121	1.31	17	2.7	0.28	2.4	8.6
Dh2 680.324 - 328 m	6.56	9.17	0.76	2.46	3.93	1.12	0.46	1.99	0.542	81	98	48	66	109	77	0.082	195	175	177	112	1.3	14.8	2.9	0.29	1.7	10
Dh2 680.335 - 340 m	6.91	8.28	0.65	1.91	3.06	0.94	0.4	1.39	0.469	101	115	43.2	70.1	86	64.1	0.066	185	160	226	122	1.16	8.9	2.8	0.29	3	8.2
Dh2 680.345 - 349 m	6.3	8.36	0.61	1.83	3.06	0.93	0.42	1.22	0.478	120	119	42.7	70.8	100	63.3	0.057	176	159	191	122	1.18	7.1	2.9	0.27	2.4	8.2
Dh2 680.357 - 362 m	6.36	7.96	0.55	1.81	3.08	0.87	0.39	1.39	0.505	101	108	40.5	67.8	85	57.5	0.055	175	152	200	120	1.16	7	2.7	0.3	2.8	8.1
Dh2 680.373 - 376 m	7.41	8.1	0.42	2.22	3.29	0.83	0.38	1.79	0.488	69	124	51.1	71.1	79	80.1	0.048	179	163	317	123	1.51	11.1	2.7	0.31	4.6	9.4
Dh2 680.389 - 393 m	8.94	8.07	0.37	2.03	3.16	0.78	0.35	1.66	0.495	69	119	46.8	73.9	72	71.1	0.047	180	166	243	128	1.32	11.1	3	0.32	3.4	8.8
Dh2 680.410 - 415 m	8.74	7.48	0.4	1.72	2.96	0.76	0.38	1.3	0.485	152	116	42.4	71.1	80	59.7	0.045	168	156	187	125	1.17	6.8	2.6	0.29	2.5	7.3
Dh2 680.427 - 431 m	8.03	7.06	0.35	1.69	2.37	0.7	0.37	1.27	0.455	131	115	40.8	63.8	79	57	0.046	159	139	182	133	1.03	6.8	2.3	0.26	2.2	6.5
Dh2 680.446 - 451 m	9.7	7.27	0.32	1.91	2.81	0.71	0.36	1.58	0.465	92	119	41.4	69.3	75	56.1	0.052	202	155	111	142	1.19	9.8	2.6	0.29	0.9	6.6
Oppdalen Member																										
Dh2 724.243 - 247 m	0.753	8.42	0.2	3.4	2.61	0.71	0.36	2.18	0.52	92	47	28.9	114	79	66.6	0.037	151	141	97.9	163	0.49	26.4	2.5	0.37	0.1	9.3
Dh2 724.255 - 258 m	0.737	8.14	0.19	2.44	2.26	0.67	0.36	1.05	0.522	238	47	23.6	110	74	42	0.042	147	131	133	173	0.29	15.7	2.2	0.34	0.2	10.9
Dh2 724.263 - 267 m	0.773	8.42	0.19	3.34	2.68	0.74	0.36	2	0.543	92	45	22	115	79	51.9	0.04	146	140	89.9	180	0.3	33.1	2.5	0.37	0.1	16.6
Dh2 724.275 - 279 m	0.86	8.01	0.18	2.21	2.35	0.71	0.34	0.72	0.517	472	67	23.2	113	71	36	0.038	144	135	101	171	0.32	9.7	2.4	0.38	< 0.01	7.9
Dh2 724.282 - 285 m	0.843	7.92	0.2	2.17	2.25	0.7	0.35	0.65	0.526	488	70	25.3	110	71	33.5	0.04	154	133	112	185	0.28	19.1	2.3	0.39	0.2	11.1
Dh2 724.294 - 298 m	0.937	8.05	0.21	2.15	2.2	0.7	0.34	0.64	0.536	461	88	21.8	111	71	36.8	0.044	145	133	132	171	0.25	16.2	2.2	0.37	0.2	9.5
Dh2 724.306 - 310 m	0.928	7.34	0.19	2.11	2.22	0.68	0.33	0.7	0.478	452	69	32.4	107	77	33.7	0.037	142	127	88	170	0.26	16.2	2.2	0.36	< 0.01	9.8
Dh2 724.315 - 319 m	0.905	7.74	0.18	2.14	2.27	0.69	0.34	0.69	0.545	477	77	24.4	111	69	34.2	0.04	154	133	110	184	0.26	24.7	2.3	0.37	0.1	12.1
Dh2 724.324 - 328 m	0.963	9.34	0.24	2.23	2.01	0.69	0.35	0.68	0.537	450	67	36.8	111	136	37.6	0.041	151	136	103	183	0.28	19.1	2.3	0.7	0.2	11.6

Continued to Table A3

Cs	Ga	Hf	Hg	Mo	Nb	Pb	Rb	Sb	Sc	Se	Sn	Th	Tl	U	Y	Ta	W	Re	Os	La	Ce	Pr	Nd
ppm	ppm	ppm	ppb	ppm	ppm	ppm	ppm	ppm	ppm	ppm	ppm	ppm	ppm	ppm	ppm	ppm	ppm	ppb	ppb	ppm	ppm	ppm	ppm
0.05	0.1	0.1	1	0.05	0.1	0.5	0.2	0.1	1	0.1	1	0.1	0.05	0.1	0.05	0.1	0.1	0.01	0.001	0.1	0.1	0.1	0.1
10.7	23	3.6	182	6.51	17.9	20	148	1.2	17	5	3	10.8	0.93	4.7	24.7	1.1	1.6	21.93	0.343	32.8	73.1	8.2	33.3
11.1	23.9	3.7	159	5.62	18.6	18.3	149	1.2	17	5.2	2	11.3	0.77	4.4	24.5	1.1	1.6	11.10	0.292	32.8	70.4	8.2	32.8
9.96	23	3.5	138	5.97	18.6	21.1	136	1.3	16	7.5	3	10	0.85	4.6	26.9	1.1	2	12.45	0.214	35.2	72.6	8.7	33.8
10.2	22.5	3.6	152	4.4	17.8	19.4	137	1.1	16	5.3	2	10.6	0.76	4.2	28.2	0.6	1.6	19.33	0.399	35.4	74.5	8.9	36.3
9.51	22.3	3.3	172	6.77	19.1	21.8	134	1.3	16	9.7	2	8.9	0.89	4.2	30.5	1	1.4	8.77	0.202	34.9	71.4	8.7	35.7
10.1	23.1	3.4	135	3.26	19.7	19.4	144	1	18	7.6	2	11.7	0.78	4.5	32.2	1.1	1.5	15.65	0.238	38.3	76.6	9.4	37.6
10.1	22.3	3.6	199	4.45	18.9	20.4	115	1.2	18	7.9	2	10.3	0.82	4.8	38.8	1.2	1.6	19.11	0.425	39.1	84.9	10.4	42.7
10.5	23.6	3.6	153	4.07	17.9	19.5	146	1.1	19	7.9	2	11.3	0.83	5.1	45.1	0.3	1.6	11.71	0.221	43.3	92.3	11.7	46.9
10.2	23.1	3.6	125	3.09	20.5	17.6	144	1	18	6.4	2	11.9	0.74	4.5	36.9	1.1	1.6	11.45	0.221	39.6	83.6	10.5	41.4
10.5	23.4	3.6	121	2.84	20.3	16.7	147	1.1	17	5.4	2	11.6	0.73	4	30.7	1.2	1.6	10.00	0.213	35.1	72.2	9	36.2
9.8	21.7	3.5	176	4.19	17.8	18.8	132	1.2	16	6.4	2	10	0.76	3.9	25.8	1.1	1.4	17.33	0.392	31.3	66.6	8.2	32.5
10.3	22.5	3.6	140	2.84	19.3	18.2	117	1	16	5.3	2	10.6	0.72	3.7	25.3	1.1	1.5	7.83	0.179	32.6	66.4	8.2	30.1
6.2	14.3	3.2	116	4.65	9.8	14.4	66	1	14	6.5	3	10.4	0.77	4.8	26.2	0.7	1.1	22.60	0.297	31.3	53.6	7.9	31.3
7.17	16.8	3.5	157	5.6	11.2	18.3	63	1.2	14	8.3	3	9.6	0.92	4.8	25.9	0.8	1.2	30.17	0.401	31.5	53.7	7.7	30
7.87	17.2	3.3	160	3.77	11.3	18.4	86.2	1.2	14	7.1	3	10.5	0.69	4.2	26.3	0.8	1.3	18.18	0.302	32.3	53.2	7.6	29.2
6.95	13.3	3	145	4.9	11.6	16.8	96.3	1.3	14	7.7	3	9.5	0.8	3.8	24.6	0.8	0.9	33.05	0.416	34.8	57.7	6.6	31.6
7.61	16.6	3.3	202	5.6	11.3	18.4	75.3	1.4	14	8.9	3	9.4	0.85	4.9	27.6	0.8	1.2	26.13	0.402	33.3	55.5	8.2	31.3
7.2	14.1	3.1	157	4.6	12.2	19.1	85.3	1.3	15	7.3	3	9.5	0.7	3.8	24.7	0.8	1	24.67	0.362	36.7	59.6	6.5	31.5
7.14	17.1	3.4	166	6.45	10.6	17.5	84	1.6	13	11.8	3	9.3	1.54	4.6	26.4	0.7	1.2	39.13	0.551	31	51.3	8.1	32.2
8.03	18.2	3.3	150	5.27	11.3	18.6	87.2	1.3	13	8.2	3	8.7	0.84	3.7	27.8	0.8	1.3	30.81	0.420	32.9	51.7	8	31.4
8.01	19.3	3.5	157	5	13.3	13	124	1.2	13	6	3	11.5	0.69	5	34.7	0.8	1.6	17.48	0.329	39.1	67.8	9.3	35.8
7.28	18.2	3.3	173	7	13.4	13	118	1.4	13	6.6	2	11	0.67	4.8	34.2	0.8	1.6	15.36	0.322	37.5	67.7	9.4	35.6
8.98	21.7	3.6	159	5	14.9	12	138	1.5	14	7.6	3	12.1	0.87	5.2	36.6	0.9	1.7	21.11	0.377	41.2	72.4	9.9	38.2
8.98	21.8	3.5	182	5	15	16	139	1.5	13	8.8	3	11.6	1	5.1	35.6	0.9	1.8	28.80	0.458	41.1	73.3	9.9	38.9
8.72	20.5	3.6	180	6	15.4	13	139	1.4	13	8.1	3	12.3	0.78	5.1	36.4	0.9	1.8	19.40	0.368	41.5	75	10.3	39.3
9.28	21.8	3.7	178	6	16.2	14	145	1.4	14	7.8	3	13.2	0.8	5.7	38.4	1.1	1.8	19.13	0.370	44.1	79.4	11.4	43.7
8.85	21	3.5	199	7	15.7	14	139	1.5	14	8.2	3	12.7	0.87	5.6	35.3	1	1.7	22.75	0.397	42.3	74.9	10.7	40.7
7.46	16.9	0.2	178	11.6	8.8	16.5	96.7	2.3	14	13.9	2	8.8	1.83	6.9	55	0.1	1.3	44.75	0.485	39.4	69.5	10.1	41.3
3.18	10.7	0.3	254	23.9	0.9	14.5	55.9	3.6	23	37.2	1	11.1	10.6	33.2	274	< 0.1	0.5	76.64	0.517	151	206	34.8	146
5.72	13	0.1	205	14.5	0.2	15.2	79.2	1.2	19	19.9	1	9.5	5	15.1	143	< 0.1	0.5	61.86	0.534	87.7	125	21.3	91.6
7.64	19	3.4	168	14.2	12.3	18.3	113	3	14	17.5	2	9.3	2.43	6	38.3	0.8	1.3	61.21	0.730	35.2	61.8	8.9	35.2
8.25	19.2	3.5	190	11.7	12.9	20	119	3.1	13	19.4	2	11	1.59	5.8	30.9	0.9	1.5	42.23	0.610	33.4	63.8	8.6	35
7.13	17.2	3.4	201	13.7	11.9	18.3	105	2.4	12	19.5	2	9.2	2.34	5.9	33.2	0.8	1.3	36.63	0.533	30.7	58.2	8	32
6.32	15.9	3.1	221	15.4	10.5	17.3	95	2.9	13	21.2	2	12	2.46	9.3	56.8	0.7	1.2	42.39	0.536	42.3	81.9	12.6	54.2
6.19	13.9	2.9	141	11.2	9	14.8	77	2	15	10.6	3	11.1	1.66	10.2	49.8	0.7	1.2	42.36	0.491	44.9	67.9	11.2	45
6.9	15.8	0.3	152	8.03	9.1	15.3	88.3	1.9	14	10.5	2	8.8	0.88	8.2	56.5	0.1	1.3	26.49	0.445	42.5	69	9.7	41.7
5.85	13.7	2.6	151	11.6	8.9	15	64.2	2.1	15	11.3	3	9.3	1.61	9.2	42.6	0.7	1.1	46.55	0.600	38.7	58.1	9.7	38.5
7.44	16.9	0.9	141	10.9	9.4	16.8	80.5	2.1	15	12.8	3	11	1.84	9.8	45.8	0.5	1.3	55.51	0.698	42.2	63	10.6	42.9
7.77	17.2	3.3	147	7.07	11.3	15.9	104	1.8	13	10.5	2	8.2	1.04	5.7	38.7	0.8	1.4	30.96	0.517	34.1	58.3	7.9	33.1
8.02	17.6	3.5	175	7.95	12.3	18.3	113	2.3	13	14	2	8.6	0.82	5.3	41.1	0.9	1.4	29.71	0.438	34.1	59.8	8.3	33.3
7.67	15.4	3.1	167	9.08	10.3	18.3	84.8	1.9	14	12.6	3	10.3	1.2	7.4	37.9	0.7	1.3	48.94	0.590	39.4	62.6	10	40.1
8.51	18.9	3.6	169	7.56	12.4	18.1	113	2.2	13	12.2	2	9.1	1.16	5.1	34.4	0.8	1.4	44.15	0.570	32.6	58	7.6	32.3
8.34	19.7	3.4	174	8.45	13.3	19.2	119	2.1	12	14.1	3	9.2	1.1	5	32.2	0.5	1.4	34.45	0.515	34	61.2	7.5	28.7
7.19	15.8	3.1	167	9.46	10.2	17.1	57.2	2.1	15	13.7	3	11.4	1.32	15	42.6	0.7	1.2	55.50	0.732	40.8	68.4	11.8	49.3
7.77	18.4	0.2	128	4.05	9.8	15.7	95.4	1	15	6.3	2	10.7	0.69	8.8	78.2	0.2	1.3	31.62	0.361	53.2	89.7	13.5	56.9
5.96	15.9	0.9	121	8	7.9	10	89.2	0.9	13	8.1	2	10	1.04	10.3	78.6	0.6	1.2	50.16	0.395	54.7	92.3	15.4	61.9
9	20.9	3.3	159	7.16	13.5	21.7	119	1.5	13	10.3	2	8	1.25	5.5	37.9	0.8	1.5	65.97	0.478	36.5	65.2	8.3	34.1
9.15	21.3	3.5	138	8	15.1	15	138	1.1	14	7.4	3	12.1	0.94	6	34.3	1	1.7	41.52	0.397	40	70	9.3	34.6
9.97	22.6	3.5	112	6.87	13.8	20.9	128	1.2	14	9	3	11.8	1.36	6.1	29.9	0.9	1.5	46.37	0.426	37.8	71.1	9	34.8
9.69	22.4	3.5	97	6.07	14.1	20.3	128	1.1	14	8.5	3	10.9	1.03	5.3	28.3	0.5	1.5	38.23	0.382	37	67.5	8	31.3
9.56	21.5	3.4	110	6.49	13.9	21	133	1.2	14	8.6	3	10.9	1.07	5.5	26.8	0.9	1.5	35.53	0.370	35.4	66.6	8.2	32.2
10.2	23.1	3.4	133	9.81	14.3	24.8	141	1.5	13	11.8	3	11.1	1.66	5.7	27.1	0.9	1.6	47.38	0.478	36.8	69.5	8.5	32.9
10.3	22.9	3.6	135	7.73	14.3	23.6	133	1.4	14	10.8	3	10.3	1.3	5.8	27.5	1	1.6	49.38	0.471	35.5	68.3	8.9	34.2
9.5	20.8	3.5	122	5.55	13	20.5	124	1.1	13	9	3	10.6	0.84	5.5	25.5	0.9	1.4	47.45	0.443	35.7	65.7	8.3	32.5
8.67	18.6	3.8	110	4.98	12.6	18.2	106	1	13	7.6	2	9.4	0.87	5.5	27	0.8	1.5	39.90	0.386	35.5	64.8	8.7	33.1
9.39	20.4	3.9	154	4.57	13.3	20.9	124	1.1	13	8.3	2	9.5	0.72	6.4	32	0.9	1.5	45.99	0.441	39.1	76.9	11	44.4
10.9	20.6	4.8	231	7.4	15.6	20.8	135	0.5	15	1.4	3	9.5	1.14	3.5	23.9	1	1.8	6.78	0.231	32.9	79.4	8.5	33.1
9.79	19.2	5.2	115	1.44	14.4	23.2	120	0.6	15	1.4	3	11.8	0.75	3.6	23.6	1	1.6	6.65	0.201	33.3	78	8.3	32.7
10.4	20.3	5.2	137	1.55	15.9	30	136	0.7	15	1.8	3	9.4	0.86	3.7	24.7	1	1.7	10.58	0.236	34.4	81.9	8.8	33.7
9.85	17.7	5.2	99	1.41	14.6	18	120	0.5	15	0.8	3	11.9	0.83	3.6	22.9	1	1.7	11.98	0.196	34.4	81.7	8.5	34.2
9.53	18.5	5.5	60	0.83	14.7	20.8	115	0.5	15	1	3	12.7	0.87	3.7	24.3	0.9	1.7	19.24	0.230	36.4	84.4	8.8	34.3
9.21	17.7	5.1	70	1.51	14.2	18.8	109	0.5	15	0.8	3	12	0.82	3.6	23.9	0.9	1.8	20.04	0.226	34.8	82.3	8.4	34.6
9.18	17.3	4.8	81	1.05	13.1	18.6	117	0.5	14	1.2	2	11.3	0.75	3.6	23.8	0.9	1.6	9.06	0.231	35.2	82.2	8.9	34.2
9.62	17.7	5.5	60	0.84	15.3	20.5	119	0.6	14	0.9	3	12.5	0.75	3.7	24.7	1	1.7	13.66	0.254	36.1	84.1	8.9	35.1
9.66	19.5	5.4	65	1.04	13.4	22.9	107	0.6	15	1.2	3	12.6	0.73	3.8	25.3	0.9	1.8	16.29	0.240	38.8	88.1	9.3	35.8

Continued to Table A3

Sm	Eu	Gd	Tb	Dy	Ho	Er	Tm	Yb	Lu	$\delta^{13}C_{inorg}$	$\delta^{18}O$	$\delta^{13}C^{o}_{rg}$	N	$\delta^{15}N$	δ^{34S}
ppm	ppm	ppm	ppm	ppm	ppm	ppm	ppm	ppm	ppm						
0.1	0.05	0.1	0.1	0.1	0.1	0.1	0.1	0.1	0.1						
5.9	1.17	4.8	0.7	4.6	0.9	2.7	0.4	3.1	0.4	-10.6	-10.6	-29.7	0.2	4.1	-26.2
6	1.14	4.7	0.7	4.3	0.9	2.7	0.4	3	0.4	-10.2	-10.7	-29.7	0.2	3.9	-24.0
6.6	1.24	5.1	0.7	4.8	1	2.9	0.4	3.2	0.4	-10.7	-10.5	-29.8	0.2	4.0	-23.2
6.3	1.34	5.6	0.8	4.9	1	3	0.4	3.3	0.4	-10.1	-10.9	-29.9	0.2	4.2	-21.3
6.7	1.41	6.1	0.8	5.3	1.1	3.3	0.4	3.3	0.4	-10.6	-10.4	-29.8	0.2	4.3	-24.0
7	1.52	6.3	0.9	5.9	1.2	3.4	0.5	3.6	0.4	-10.4	-10.4	-29.9	0.2	4.2	-19.5
8.3	1.87	7.6	1.1	7	1.4	3.9	0.5	4.1	0.5	-10.4	-11.2	-29.9	0.2	4.2	-26.5
9.5	2.22	9.3	1.3	8.1	1.6	4.4	0.6	4.5	0.6	-10.6	-10.6	-29.9	0.2	4.3	-24.4
8.4	1.81	7.7	1	6.7	1.4	3.8	0.5	4	0.5	-10.5	-10.8	-29.8	0.2	4.2	-20.4
6.9	1.43	5.9	0.8	5.3	1.1	3.3	0.4	3.4	0.4	-10.2	-10.6	-29.7	0.2	4.1	-17.0
6.4	1.25	5.3	0.7	4.8	1	2.8	0.4	3.1	0.4	-10.1	-10.6	-29.7	0.2	4.0	-22.8
6.2	1.22	5	0.7	4.6	0.9	2.8	0.4	3	0.4	-10.1	-10.1	-29.6	0.2	4.1	-17.7
5.6	1.18	5.3	0.8	4.6	1	2.8	0.4	2.6	0.5	-9.4	-12.1	-26.0	0.2	4.5	-13.5
5.7	1.12	5	0.7	4.5	0.9	2.9	0.4	2.7	0.5						
5.5	1.09	4.8	0.7	4.4	0.8	2.8	0.4	2.7	0.5						
4	1.25	5	0.7	4.1	1	2.5	0.3	2.5	0.4						
5.9	1.15	5.2	0.8	4.7	0.9	3	0.5	2.9	0.5						
4	1.3	5.1	0.7	4.2	1	2.7	0.3	2.5	0.4	-9.6	-12.9	-26.1			-16.5
6	1.17	5.4	0.7	4.7	0.9	3	0.4	2.8	0.5						
5.8	1.16	5.5	0.8	4.9	1	3	0.4	2.7	0.5						
6.8	1.51	6.4	0.9	5.6	1.1	3.5	0.5	3.1	0.4	-11.4	-13.2	-25.9	0.3	4.1	-9.7
6.8	1.59	6.7	1	5.6	1.1	3.4	0.5	3.1	0.4	-11.4	-13.2	-25.9	0.2	4.3	-5.1
6.4	1.66	6.9	1	6.2	1.3	3.8	0.5	3.4	0.5	-11.2	-13.3	-26.0	0.3	4.1	-10.1
6.2	1.59	6.5	0.9	5.7	1.2	3.9	0.5	3.4	0.5	-11.0	-12.8	-26.0	0.3	4.1	-14.8
6.4	1.67	6.8	1	6	1.3	3.8	0.5	3.4	0.5	-11.3	-12.7	-25.8	0.3	4.2	-6.1
7.3	1.83	7.5	1.1	6.6	1.3	3.9	0.5	3.5	0.5	-11.1	-13.1	-25.9	0.3	4.2	-9.9
7.7	1.67	6.6	0.9	5.7	1.2	3.7	0.5	3.3	0.5	-11.3	-13.3	-25.8	0.3	3.6	-12.4
8.4	1.75	7.8	1.1	7.6	1.6	4.8	0.6	4.7	0.6	-12.2	-13.1	-25.9	0.3	4.3	-14.6
28.1	6.37	29.2	4.1	28.9	6.2	18.6	2.4	17.2	2.1	-11.9	-14.0	-26.1	0.2	4.5	-24.5
16.3	3.98	18.4	2.5	16.6	3.5	10.3	1.3	9.4	1.1	-13.0	-14.0	-26.0	0.2	4.2	-22.1
6.2	1.41	6.1	0.9	5.9	1.1	3.5	0.5	3.7	0.5	-12.6	-13.5	-25.9	0.4	4.2	-20.5
7	1.32	5.8	0.8	5.1	1	3.1	0.4	3.3	0.4	-12.3	-13.3	-25.9	0.3	4.4	-15.5
6.3	1.19	5.3	0.8	5.1	1	3.1	0.4	3.5	0.4	-11.9	-12.4	-26.0	0.3	4.6	-8.6
10.2	2.06	9.7	1.4	8.7	1.7	4.7	0.6	4.5	0.5	-12.1	-13.3	-26.1	0.3	4.4	-9.8
8.8	1.81	8.5	1.2	7.6	1.5	4.8	0.7	4.1	0.8	-13.6	-14.5	-26.4	0.3	4.9	-17.0
7.9	1.68	7.8	1.1	7.5	1.6	5	0.7	5.1	0.6	-13.5	-14.6	-26.2	0.3	4.3	-14.1
7.7	1.55	7.3	1	6.5	1.3	4.2	0.6	3.7	0.7						
8.4	1.68	8	1.2	7.1	1.5	4.5	0.7	4	0.7						
6.6	1.29	5.7	0.8	5.6	1.2	3.6	0.5	3.8	0.5	-13.2	-15.5	-26.2	0.4	4.3	-19.5
6	1.37	5.9	0.9	5.7	1.3	3.7	0.5	4	0.5	-12.2	-14.0	-26.1	0.3	4.1	-14.0
8.2	1.52	7	1	6.3	1.2	4	0.6	3.5	0.6	-11.8	-13.9	-26.2	0.3	4.8	-16.7
5.5	1.23	5.4	0.8	5.1	1.1	3.3	0.5	3.7	0.5	-11.8	-14.5	-26.1	0.4	4.2	-17.0
4.3	1.09	4.6	0.6	4.8	1	3.1	0.5	3.2	0.5	-11.5	-14.3	-26.0	0.4	4.1	-17.2
9.4	1.9	9	1.3	7.5	1.4	4.3	0.6	3.5	0.6						
12	2.64	11.7	1.7	11.1	2.3	6.5	0.8	5.8	0.7	-11.6	-12.6	-25.3	0.3	3.7	-18.5
12.1	3.12	13.9	1.9	12.1	2.4	7	0.8	4.9	0.7	-11.3	-13.8	-25.6	0.3	4.2	-12.6
6.6	1.33	5.8	0.8	5.7	1.2	3.7	0.5	3.8	0.5	-10.4	-12.3	-25.4	0.3	4.0	-30.8
6.3	1.45	5.8	0.8	5.3	1.1	3.7	0.5	3.4	0.5	-9.5	-12.0	-25.4	0.3	5.5	-28.5
5.8	1.2	5.2	0.7	5	1	3.1	0.4	3.5	0.4	-10.1	-12.0	-25.4	0.3	4.1	-26.1
5.8	1.12	4.5	0.7	4.3	0.9	2.8	0.4	3.3	0.4	-10.2	-11.6	-25.3	0.3	4.1	-25.0
5.5	1.07	4.6	0.6	4.4	0.9	2.8	0.4	3.2	0.4	-10.2	-12.0	-25.3	0.3	3.8	-24.5
5.9	1.08	4.8	0.7	4.4	0.9	3	0.4	3.3	0.4	-10.3	-12.0	-25.3	0.3	3.9	-26.3
6.5	1.13	4.7	0.7	4.7	0.9	2.9	0.4	3.3	0.4	-10.1	-12.9	-25.1	0.3	3.7	-27.4
5.3	1.05	4.6	0.7	4.4	0.9	2.7	0.4	3.1	0.4	-11.1	-14.1	-25.1	0.3	4.0	-23.9
5.6	1.14	4.9	0.7	4.6	1	3	0.4	3.2	0.4	-10.2	-11.8	-25.1	0.3	3.9	-21.3
7.8	1.47	6.6	0.9	5.7	1.1	3.3	0.4	3.5	0.4	-10.4	-12.6	-25.0	0.3	3.8	-25.6
4.9	1.13	5	0.7	4.7	1	2.8	0.4	3.1	0.4	-7.1	-10.2	-24.9	0.1	3.5	-42.1
5.6	1.18	4.9	0.7	4.8	0.9	2.7	0.4	3	0.4	-8.1	-9.9	-25.4	0.1	3.5	-39.4
6.2	1.16	5	0.7	5	1	2.9	0.4	3.2	0.4	-8.3	-10.7	-25.2	0.1	3.2	-38.5
6.1	1.15	4.9	0.7	4.4	0.9	2.7	0.4	3	0.4	-7.1	-10.7	-25.1	0.1	3.6	-35.6
7.1	1.18	5.1	0.8	4.8	1	2.8	0.4	3.2	0.4	-8.3	-11.3	-25.1	0.1	3.3	-41.5
6.8	1.22	5.3	0.7	4.6	1	2.7	0.4	3	0.4	-7.5	-11.9	-25.1	0.1	3.3	-40.9
6.7	1.2	5.5	0.8	4.9	0.9	2.8	0.4	3.1	0.4	-8.0	-10.7	-25.3	0.1	3.4	-41.3
6	1.21	5.5	0.8	4.9	0.9	2.9	0.4	3.3	0.4	-8.2	-10.4	-25.3	0.1	3.7	-40.8
6.1	1.22	5.2	0.8	4.9	1	2.9	0.4	3.3	0.4	-7.5	-10.4	-25.3	0.1	3.7	-41.4

Continued to Table A3

H5R drill core

tsmøya Men	TOC (wt.%)	Al	Ca	Fe	K	Mg	Na	S	Ti	Ba	Cr	Cu	Li	Mn	Ni	P	Sr	V	Zn	Zr
DH5R 489.	1.69	7.7	0.7	3.5	2.7	1.3	0.4	1.53	0.56	247	120	53.6	67.9	136	54.5	0.058	146	130	142	141
DH5R 489.	1.98	8.91	0.64	3.66	3.27	1.47	0.57	1.59	0.551	62	137	49.2	101	142	59.8	0.053	150	138	132	161
DH5R 489.	2	9.38	0.63	3.24	3.38	1.53	0.6	0.99	0.599	259	159	45.8	105	152	48.9	0.057	154	144	120	167
DH5R 489.	1.83	9.06	0.67	4	3.23	1.47	0.6	1.98	0.533	55	116	49.2	96.1	123	60.7	0.054	160	137	159	164
DH5R 489.	2.13	8.99	0.45	3.09	3.23	1.35	0.64	1.1	0.529	172	132	52.8	96.9	125	58.6	0.049	156	136	144	164
DH5R 491.	1.74	8.86	0.57	6.17	3.41	2	0.42	1.31	0.495	219	126	50	89	302	52	0.054	153	146	128	110
DH5R 491.	1.95	9.07	0.43	4.99	3.56	1.57	0.42	2.36	0.521	60	102	60	94	184	68	0.053	146	147	135	111
DH5R 491.	2.12	>10	0.38	4.3	3.78	1.63	0.47	2.01	0.542	67	218	59	99	147	65	0.05	147	150	143	115
DH5R 491.	2.12	>10	0.45	3.73	3.83	1.67	0.51	1.56	0.547	182	99	57	97	128	61	0.049	163	155	143	118
DH5R 491.	2.21	>10	0.48	3.39	3.54	1.56	0.51	1.04	0.545	298	134	48	93	142	52	0.05	177	160	134	128
DH5R 491.	2.31	>10	0.42	3.68	3.66	1.49	0.46	1.47	0.554	158	104	54	93	143	61	0.05	155	153	146	123
DH5R 491.	2.42	9.37	0.43	3.53	3.53	1.54	0.48	1.43	0.587	566	142	52	99	152	80	0.052	171	158	145	122
dalssåta Member																				
DH5R 542.	4.71	9.09	0.39	3.41	3.67	1.06	0.53	2.57	0.52	47	132	55.4	63.4	93	70.6	0.079	145	159	87.6	161
DH5R 542.	7.59	8.68	0.22	3.94	3.44	0.95	0.52	3.26	0.499	26	198	72	67.6	104	91.6	0.058	147	170	196	203
DH5R 542.	5.43	9.22	0.3	2.91	3.04	0.97	0.51	1.97	0.516	74	185	52.4	64.4	96	62.5	0.061	141	162	137	178
DH5R 542.	5.76	7.91	0.43	3.48	3.11	1.04	0.5	2.43	0.498	63	166	62.5	63.3	146	77.2	0.081	164	139	313	166
DH5R 542.	5.67	8.73	0.29	3.09	2.72	0.94	0.52	2.36	0.534	68	181	51.7	61.6	89	66.9	0.079	158	146	273	179
yfjellet Member																				
DH5R 599.	5.09	7.27	0.55	2.59	2.77	0.94	0.41	2.1	0.466	112	206	39	56	107	180	0.075	174	123	121	119
DH5R 599.	5.86	7.4	0.51	2.72	2.86	0.86	0.36	2.47	0.488	81	172	58	56	86	209	0.069	182	134	138	120
DH5R 599.	3.8	4.37	3.88	9.85	1.81	2.96	0.22	7.02	0.261	18	227	29	37	552	614	0.078	293	113	618	81
DH5R 599.	6.15	7.38	0.5	3.77	3.04	0.87	0.39	3.74	0.469	29	212	47	57	103	280	0.076	200	134	114	116
DH5R 599.	6.19	8.84	0.47	2.28	3.52	0.98	0.4	1.79	0.527	96	183	57	64	86	213	0.061	189	157	269	119
DH5R 599.	6.21	8.18	0.51	2.62	3.56	1.02	0.41	2.04	0.529	67	224	47	64	111	300	0.06	186	163	119	119
DH5R 599.	5.94	8.1	0.51	2.58	3.49	1.04	0.41	2.07	0.519	57	207	47	62	100	234	0.059	183	155	190	114
DH5R 600.	6.36	9.31	0.5	2.46	3.1	1.03	0.51	1.88	0.566	83	166	42.7	70	107	63.8	0.085	200	167	101	168
DH5R 600.	6.41	8.93	0.46	2.8	3.92	1	0.44	2.17	0.632	82	106	43	63	152	100	0.087	218	178	96	121
DH5R 600.	6.39	8.12	0.39	2.67	2.09	0.93	0.39	2.52	0.524	63	111	52.9	74	102	71.1	0.071	153	161	99	82
DH5R 600.	6.23	8.94	0.46	2.76	3.73	1.1	0.41	2.17	0.54	58	98	55	63	107	64	0.078	198	170	90	119
DH5R 600.	6.41	8.53	0.43	2.92	3.32	1.01	0.44	2.33	0.508	90	182	41	59	99	129	0.076	211	165	149	123
DH5R 600.	6.93	7.2	0.4	2.6	2.9	0.8	0.3	2.31	0.527	113	118	51.1	41.3	157	70.3	0.068	152	143	146	133
DH5R 600.	6.65	7.57	0.38	2.59	2.04	0.88	0.38	2.29	0.509	66	105	46.9	73.9	91	66.2	0.067	162	160	98.7	77
DH5R 600.	7.15	7.9	0.37	2.49	2.24	0.91	0.4	2.08	0.524	74	116	52.5	80.5	97	71.5	0.068	185	170	124	86
DH5R 607.	6.74	6.92	0.43	2.29	2.88	0.81	0.35	2.17	0.466	73	122	39.9	62.9	71	62.1	0.058	197	180	67.4	126
DH5R 607.	1.68	1.62	0.09	32.3	0.66	0.15	0.07	20	0.111	76	48	13.3	12.8	27	74.6	0.012	42.7	46	17.9	33
DH5R 607.	7.92	7	0.45	2.47	2.78	0.8	0.35	2.48	0.438	70	138	49.2	64.1	83	73.5	0.067	216	198	89.4	131
DH5R 607.	7.15	6.83	0.45	2.24	2.43	0.81	0.34	2.07	0.435	72	133	47.9	62.3	71	64.5	0.068	215	189	58.7	124
DH5R 607.	6.59	6.58	0.44	1.82	2.29	0.8	0.33	1.51	0.431	106	131	35	62.3	71	55.7	0.063	212	185	66.5	123
DH5R 607.	8.7	6.76	0.38	2.22	2.37	0.77	0.32	2.25	0.454	60	135	53.7	60.2	66	77.6	0.056	220	205	244	123
DH5R 607.	8.69	6.54	0.4	2.62	2.53	0.79	0.33	2.73	0.441	47	134	57.1	61.1	84	85.6	0.051	215	198	547	124
DH5R 607.	7.32	7.41	0.45	2.77	2.41	0.87	0.37	2.61	0.428	64	134	47.2	64.7	88	72.2	0.054	227	198	89.1	129
DH5R 613.	8.91	8.44	0.42	2.88	2.8	0.94	0.47	2.84	0.539	38	178	62.8	70.4	103	71	0.091	241	268	171	161
DH5R 613.	8.53	9.02	0.47	2.44	2.89	1.03	0.48	2.16	0.544	53	129	53.7	73.7	108	65.4	0.098	257	275	112	154
DH5R 613.	8.88	6.7	0.4	2.9	2.6	0.8	0.3	3.07	0.507	62	136	60.8	45.1	94	77.5	0.103	201	228	98	132
DH5R 613.	7.53	6.66	0.31	2.35	2.57	0.73	0.34	2.44	0.447	62	118	39.5	65.9	65	81.6	0.058	228	240	142	117
DH5R 613.	8.34	8.54	0.33	2.9	2.94	0.93	0.37	2.64	0.499	56	185	51	65	88	129	0.061	226	273	161	123
DH5R 613.	7.81	7.18	0.29	1.82	2.71	0.71	0.33	1.7	0.457	80	121	41.9	65.7	81	52.9	0.058	212	248	50.7	116
DH5R 613.	8.4	8.2	0.31	2.02	2.89	0.78	0.36	1.82	0.465	99	126	46.6	71	62	55.1	0.065	256	269	139	127
DH5R 613.	10.3	9.26	0.36	2.49	2.95	1.04	0.48	2.42	0.591	42	159	63.1	77.5	118	86.5	0.068	273	305	349	169
DH5R 613.	7.06	6.63	0.37	1.98	2.57	0.72	0.37	1.89	0.445	67	116	38.7	64.7	77	57.2	0.083	239	225	95.9	117
DH5R 613.	6.08	7.84	0.31	2.18	2.94	0.8	0.35	1.96	0.459	84	125	46.2	69.4	63	58.7	0.052	268	259	74.5	123
DH5R 613.	11.7	8.2	0.39	3.11	2.69	0.93	0.45	3.2	0.521	27	189	81.4	71.7	111	152	0.078	257	278	733	160
DH5R 613.	8.44	8.33	0.36	2.34	2.95	0.92	0.4	1.94	0.501	112	182	50	64	140	122	0.054	242	261	254	119
DH5R 613.	8.86	7.2	0.3	2	2.8	0.7	0.3	1.87	0.548	139	135	59	46.1	91	70.2	0.053	183	237	173	128
DH5R 613.	8.01	6.98	0.25	1.88	2.63	0.65	0.34	1.74	0.455	115	121	40.8	62.5	77	50.7	0.057	191	249	74.1	116
DH5R 613.	8.02	7.75	0.3	2.33	3.04	0.76	0.36	2.18	0.458	74	128	46.9	69.2	57	57.9	0.059	232	268	96.2	128
DH5R 613.	9.05	8.95	0.34	2.7	2.95	0.97	0.46	2.49	0.531	36	144	57.7	75	72	81.4	0.058	237	266	202	157
DH5R 613.	8.45	8.97	0.33	2.83	3.29	0.94	0.39	2.55	0.527	63	120	57	67	83	82	0.062	264	282	222	116
DH5R 613.	7.9	7.01	0.28	1.8	2.54	0.67	0.33	1.63	0.471	82	124	42.8	64.5	66	56.4	0.067	205	254	152	119
DH5R 613.	8.93	8.7	0.37	3.14	2.73	0.92	0.44	3.13	0.524	33	173	56.8	71	73	82	0.082	227	258	224	151
pdalen Member																				
DH5R 655.	1.18	7.41	0.25	2.15	2.46	0.76	0.4	0.71	0.531	355	178	21	64	125	337	0.042	131	112	84	144
DH5R 655.	1.16	7.17	0.25	2.39	2.47	0.74	0.41	0.92	0.507	188	122	24	63	115	217	0.04	147	110	71	142
DH5R 655.	1.11	6.82	0.25	2.02	2.28	0.72	0.36	0.62	0.509	446	168	21	62	104	154	0.04	117	106	82	135
DH5R 655.	1.12	6.6	0.32	2.19	2.52	0.69	0.37	0.71	0.49	238	179	22	60	114	262	0.038	121	105	94	151
DH5R 655.	1.07	6.73	0.34	2.3	2.24	0.73	0.36	0.77	0.49	352	209	22	60	129	363	0.038	118	102	125	153
DH5R 655.	1.2	6.66	0.26	2.36	2.34	0.7	0.37	0.86	0.51	434	223	22	62	120	225	0.04	133	104	95	169
DH5R 655.	1.15	6.95	0.31	2.3	2.51	0.7	0.39	0.66	0.503	443	229	22	62	134	354	0.04	134	105	83	159
DH5R 658.	1.37	>10	0.33	3.6	2.96	1.18	0.57	1.35	0.593	147	71.1	34.7	128	169	47.1	0.052	166	173	130	183
DH5R 658.	1.38	8.88	0.28	3.23	1.78	0.89	0.42	1.29	0.546	274	70	27.4	120	113	43.4	0.052	164	158	103	142
DH5R 658.	1.25	8.77	0.3	4.59	2.04	0.88	0.4	3	0.536	62	50	32.9	113	215	50.4	0.052	165	153	106	138
DH5R 658.	1.42	>10	0.33	4.48	3.16	1.17	0.57	2.3	0.573	53	79.8	38.2	126	208	53.9	0.05	145	168	123	179
DH5R 658.	1.18	8.75	0.27	2.81	1.5	0.86	0.4	0.8	0.55	445	61	24.1	112	109	30.7	0.051	172	148	119	141
DH5R 658.	1.19	>10	0.34	4.43	2.79	1.17	0.55	2.46	0.602	40	74	40.5	123	233	49.4	0.053	163	166	130	174
DH5R 658.	1.35	9.98	0.33	3.27	3.06	1.16	0.55	1.04	0.64	148	89	36.7	125	151	37.7	0.057	161	167	145	180
DH5R 658.	1.31	8.85	0.29	2.8	1.9	0.87	0.41	0.66	0.541	540	63	23.8	116	112	30.6	0.052	143	149	90.6	146
DH5R 658.	1.34	>10	0.34	4.41	3.14	1.16	0.56	2.32	0.595	46	85.6	37	126	197	55.2	0.054	166	159	150	179
DH5R 663.	0.4	5.98	0.27	1.74	2.19	0.49	0.35	0.4	0.433	364	179	15	41	92	189	0.037	110	72	56	131
DH5R 663.	0.469	6.41	0.28	2.64	2.2	0.51	0.33	1.68	0.423	111	192	20	41	92	333	0.037	121	75	62	117
DH5R 663.	0.485	6.31	0.21	1.56	2.29	0.44	0.35	0.39	0.408	451	199	14	42	77	234	0.034	143	62	53	110
DH5R 663.	0.481	5.67	0.21	1.5	2.18	0.46	0.34	0.34	0.401	321	172	14	42	83	419	0.035	69.7	62	54	108
DH5R 663.	0.523	5.8	0.23	1.63	2.15	0.42	0.33	0.47	0.459	377	208	19	42	77	350	0.035	104	80	53	122
DH5R 664.	0.449	5.88	0.22	1.57	2.12	0.4	0.35	0.45	0.442	430	175	14	40	78	326	0.035	165	77	54	137
DH5R 664.	0.454	5.8	0.21	1.56	2.21	0.39	0.33	0.41	0.43	365	223	14	39	85	281	0.035	100	74	51	143

Continued to Table A3

Ag	As	Be	Bi	Cd	Co	Cs	Ga	Hf	Hg	Mo	Nb	Pb	Rb	Sb	Sc	Se	Sn	Th	Tl	U
0.7	22.1	2.2	0.3	0.2	11.4	9.8	15	3.3	75	2.3	20.6	21.7	129	0.5	18	2.4	3	12.5	0.7	4.2
0.74	16.1	3.2	0.3	0.3	10.8	9.94	24.6	6.9	74	2.26	37.4	19.3	165	0.6	19	2.9	3	11.3	0.84	3.4
0.64	10.5	3.2	0.3	0.3	9.7	10.4	17.2	7.2	62	1.53	40.6	19.5	170	0.5	20	1.8	3	12.5	0.81	3.4
0.68	23.1	3.1	0.28	0.4	11.4	9.79	24.8	6.9	77	2.91	38.4	19.8	163	0.6	18	2.4	3	10.5	0.85	3.5
0.75	10.8	2.9	0.29	0.4	10.5	9.87	20	7	59	3.62	37.8	18.4	164	0.6	17	2.7	3	11.8	0.85	3.4
0.5	16.9	2.9	0.29	0.15	9	10.3	22	3.4	72	3	18.1	14	157	0.5	17	2.8	3	13.4	0.83	3.6
0.7	25.6	2.8	0.3	0.15	12	9.99	22.9	3.4	94	2	17.9	17	141	0.6	16	3.8	3	10.6	0.96	3.4
0.8	17.5	3	0.31	0.4	12	10.4	24.1	3.5	87	2	19	16	162	0.6	16	3.5	3	14.1	0.96	3.9
0.7	15	3	0.31	0.3	11	10.5	23.3	3.6	87	1	18.8	15	160	0.6	16	4	3	14.6	0.99	3.9
0.6	10.5	3	0.3	0.3	10	10.9	23.4	3.8	60	0.5	20.2	12	155	0.5	16	2.8	3	14.6	0.93	4
0.7	15.8	3	0.31	0.4	12	11.1	23.8	3.7	76	0.5	19.4	15	160	0.5	16	3.8	3	14.4	1	3.9
1.1	14.3	3.1	0.33	0.15	11	11.2	20.9	3.9	76	0.5	20.2	14	176	0.6	16	3.8	3	14.9	0.96	3.8
0.75	35.1	3.2	0.28	0.7	10.2	9.22	25	6.7	145	5.85	26.7	19.4	158	0.9	17	4.8	3	10.4	1.06	5
1.72	26.4	2.9	0.32	2.5	10.2	8.76	24	7.6	141	9.16	25.3	23.9	152	1	17	7.1	3	9.7	1.43	5.5
1.22	25	3.2	0.3	1.2	9	8.41	23	6.9	102	4.88	26	18.6	131	0.8	17	4.6	3	8.3	0.99	4.1
1.83	20.6	2.5	0.29	5.2	8.8	7.97	21.6	6.6	81	8.38	23.6	20.2	132	0.9	15	7.6	3	8.7	1.36	4.9
1.27	38.1	2.8	0.28	4.1	9.5	7.96	22.1	6.9	85	5.74	24.7	18.7	123	0.8	17	4.6	3	9.1	1.14	4.5
0.7	18	2.1	0.22	0.4	8	6.9	16	3.8	145	7	11.7	9	111	1.1	11	4.8	2	11	0.68	4.5
0.9	22.1	2.4	0.23	0.5	9	7.7	17	3.8	167	5	12.7	13	116	1.2	11	5.9	2	10.8	0.79	4.7
0.5	14.3	1.2	0.14	4.3	5	4.11	10.5	2.2	124	10	8	9	69	0.7	27	6.1	2	6.5	0.5	3.7
1.2	31.5	2.3	0.22	0.4	8	7.47	17	3.6	187	10	12.8	12	115	1.2	11	7.2	2	10.6	0.85	5.3
1.3	18.2	2.5	0.27	2.1	9	8.86	19.4	3.8	141	9	15.1	12	135	1.3	12	6.9	3	13.6	1.02	4.9
1.4	18.4	2.6	0.27	0.7	10	8.93	19.9	3.8	152	12	14.8	12	136	1.3	12	7.5	3	12.7	0.93	5
1.1	22.6	2.8	0.26	1.1	10	8.49	18.8	3.7	141	12	13.9	14	131	1.4	12	6.8	3	13.4	1.04	4.9
1.22	18.2	3.2	0.27	0.4	8.4	8.81	22.6	6.9	128	5.97	25.2	15.9	137	1.3	17	5.3	3	10.3	0.79	5.1
1.2	16.2	2.8	0.27	0.4	9	9.49	21.2	3.7	143	7	25.4	12	148	1.2	14	6.2	3	13.1	0.92	5.4
2	18.4	2.9	0.28	0.5	7.5	8.82	17.4	3.6	146	5.98	11.6	18.2	79.6	1.2	14	6.2	3	11	0.95	5.4
1.1	15.9	2.9	0.27	0.4	9	9.63	21	3.6	146	5	15.3	13	143	1.1	13	6	3	12.6	0.89	5
1	20.4	2.5	0.25	0.7	9	8.9	20.5	3.6	128	8	14.5	11	139	1.2	13	6.4	3	11.6	0.92	5.1
1.1	15.5	1.9	0.3	0.6	9.1	8.3	14.4	2.9	135	5.6	12.4	17.7	109	1.1	15	5.9	3	9.7	0.7	3.7
1.5	16.1	2.8	0.27	0.5	7	8.8	17	3.5	139	5.13	11.4	17.7	80.4	1	14	5.7	3	11.1	0.77	5.4
1.53	16.7	2.9	0.28	0.7	7.5	9.58	18.5	3.6	135	4.66	12	18.5	83.3	1	14	6.5	3	12.5	0.83	6
1.18	16.4	2.5	0.25	0.3	7.1	8.91	18.5	3.6	249	3.13	12.4	19.3	124	1.8	13	8.3	2	9.4	0.88	4.3
0.37	143	0.5	0.06	0.3	3	2.24	4.6	0.8	363	52.5	3.7	8.2	30.8	2.2	3	5.6	< 1	2.7	0.79	1.1
2.44	14.9	2.5	0.23	0.7	7.4	8.71	18.5	3.6	226	4.92	12.2	18.1	120	2.2	13	10.9	2	9.4	0.99	4.5
1.56	14.6	2.4	0.25	0.4	7	8.96	18.1	3.6	191	5.05	12.1	18.9	110	2	13	9.5	2	9.3	0.92	4.8
1.33	10.8	2.4	0.25	0.7	6.8	8.74	17.8	3.5	142	3.78	12.1	17.6	107	1.6	13	7.8	2	10.2	0.77	4.3
2.18	14.1	2.5	0.27	2.8	7.6	8.8	18.3	3.4	163	4.98	12	18.4	102	1.8	13	11.7	2	9.6	1.28	4.6
2.15	21.6	2.3	0.25	7.8	8.1	8.38	18.6	3.5	168	5.85	11.8	18.7	109	2.1	12	11.7	2	9.2	1.82	4.7
2.01	16.3	2.5	0.24	0.9	7.1	8.5	18.5	3.5	176	5.99	12.4	19	106	2	13	11.1	2	9.4	1.1	4.9
1.8	20	3.1	0.27	1.4	8.1	8.34	22.2	6.4	159	4.24	23.3	18.5	123	2	17	11	3	8.9	0.71	4.9
1.61	18.3	3.2	0.27	0.7	7.8	8.77	22.8	6.2	193	4.05	24.3	19	133	1.8	17	10	3	9.9	0.75	5.5
2	23.7	2.1	0.3	0.6	8.4	7.6	14.2	2.9	188	4.8	12.3	19.3	95.5	2	14	10.6	3	7.2	0.6	4
1.76	15.4	2.5	0.25	1	7	8.28	18.3	3.3	183	5.83	11.8	20.7	109	2.7	13	11.6	2	8.5	0.75	4.8
1.8	23.4	2.9	0.27	1	9	9.1	20.4	3.5	236	6	14	15	124	2	13	11.5	3	9.9	0.83	5.8
1.1	11.5	2.6	0.26	0.5	6.4	9.65	18.9	3.4	157	3.05	11.9	19.6	110	1.6	13	9.6	2	9.6	0.62	5.1
1.37	13.1	2.8	0.28	1	7.2	10	20.4	3.7	193	3.51	12.9	20.6	125	2	15	10.2	2	10.9	0.84	5.6
2.6	21.1	3.3	0.29	3.8	9	9.13	24.2	6.6	159	5.49	25	19	137	2.2	18	11	3	10.1	1.02	6
1.26	11.4	2.5	0.22	0.9	6.8	8.04	17.7	3.4	147	3.68	11.7	16.6	104	1.7	13	8.7	2	8.1	0.66	4.6
1.38	13.5	2.7	0.27	0.6	7.2	9.85	20.1	3.6	171	4.05	13.3	20.9	125	2	13	10.1	3	10.6	0.84	5.5
3.13	28.3	3.2	0.28	9.6	10.1	8.06	23.3	6.1	203	17.2	22.7	19.2	125	2.6	16	15	3	9	1.59	6.1
1.8	14.8	2.7	0.26	1.9	9	8.41	19.3	3.5	176	6	13.2	13	119	1.8	13	9.9	3	11.1	0.75	5.4
1.8	14.3	2.1	0.3	1.4	8.6	8.4	14.7	2.9	163	4.4	12.5	20.7	100	1.7	15	9.2	3	7.9	0.7	3.5
0.98	10.8	2.7	0.29	0.5	6.8	8.96	19.3	3.5	178	2.85	12.2	19.4	102	1.7	12	9.4	2	7.6	0.7	3.4
1.26	15.2	2.8	0.28	0.7	7.5	9.87	20.7	3.6	198	3.41	13.2	19.8	120	2	14	11	3	9.9	0.75	5.5
2.05	21.3	3.3	0.29	1.8	9.1	9.11	24.1	6.2	190	5.41	24.1	20.5	138	2.2	17	11.7	3	9.8	0.81	5.7
1.9	19.7	3	0.29	1.9	10	9.84	21.4	3.5	209	6	14.8	18	138	2	14	11.6	3	10.9	0.99	6.3
1.23	10.6	2.5	0.26	1.6	6.9	8.66	19.5	3.5	154	2.98	12.1	18	102	1.7	13	9.7	3	8.5	0.6	4.2
2.11	24.8	3.2	0.28	2.7	8.4	8.2	23	6.1	235	4.96	22.8	20.1	122	2.3	16	12.8	3	8.1	0.87	5
0.4	7.4	2	0.29	0.15	8	6.78	14.7	4.4	96	6	14.1	12	103	0.4	11	1.2	2	11.5	0.55	3
0.5	10	1.9	0.28	0.15	9	6.65	14.7	4.3	123	3	14.4	16	101	0.6	10	1.3	2	10.9	0.54	2.9
0.5	6	1.7	0.26	0.15	7	6.45	13	4.1	88	5	13.7	12	98.9	0.4	10	1.1	2	10.9	0.53	2.8
0.4	6.5	1.7	0.25	0.15	7	6.19	13.9	4.6	111	7	13.7	12	98	0.4	10	1.4	2	10.9	0.49	2.9
0.5	7.6	1.4	0.25	0.15	7	6.03	13.1	4.8	113	9	13.7	12	93.8	0.4	10	1.5	2	10.7	0.5	2.9
0.5	8.4	1.8	0.27	0.15	8	6.72	13.4	5	135	7	14.1	14	102	0.5	10	1.8	2	11.3	0.51	3
0.5	7.8	1.9	0.28	0.15	7	6.39	13.7	4.7	91	8	12.9	13	102	0.4	11	1.4	2	11.3	0.52	3
0.86	22.6	3.2	0.45	0.1	11	10.6	21.7	7.7	158	1.34	30.7	24.6	153	0.6	18	< 0.1	3	11.5	0.77	3.2
0.29	21.1	2.7	0.45	0.1	11	11.8	21.4	4.3	129	1.03	16.1	28.2	109	0.7	16	1.7	3	10.9	0.86	3.1
0.48	24.1	2.6	0.48	0.2	10.7	11	22.1	4.2	238	1.43	16.1	28	116	0.8	16	3.2	3	9.4	0.93	3.1
0.69	28.1	3	0.44	< 0.01	11.3	10.1	24.9	7.7	232	1.61	29.9	25.4	154	0.7	18	0.1	3	8.9	0.83	3.2
0.3	9.5	2.5	0.42	0.2	8.4	11	19.7	4.4	89	0.84	14.2	21.9	102	0.6	17	0.9	3	11.7	0.8	3.1
0.72	21.9	3.3	0.44	0.1	10.4	9.86	25.5	7.6	216	1.47	30.2	21.6	144	0.6	19	0.8	3	8.5	0.8	3.2
0.55	20.3	3.2	0.43	0.2	10.4	9.87	20.4	7.6	136	1.01	30	20.3	153	0.6	19	< 0.1	3	11.2	0.8	3.2
0.26	11	2.5	0.44	0.1	9.1	11.5	18.7	4.5	78	0.7	14.6	22	115	0.5	17	0.6	3	12.2	0.86	3.3
0.53	29.4	3.1	0.41	0.2	12.1	9.68	24.3	7.5	197	1.5	29.2	22.7	156	0.6	18	< 0.1	3	8.7	0.84	3.1
0.3	12.3	1.7	0.2	0.15	8	4.22	11.6	4.1	151	8	6.4	11	77.7	0.3	8	0.6	2	9.3	0.42	2.5
0.4	20.1	1.4	0.21	0.15	8	4.21	12.9	3.6	39	11	11	15	78	0.4	8	0.7	2	9	0.51	2.4
< 0.3	11.9	1.6	0.22	0.15	7	4.49	11.7	3.7	49	5	2	12	81.1	0.2	8	0.7	2	9.6	0.44	2.6
0.3	9.6	1.5	0.2	0.15	7	4.22	11.8	3.5	39	6	1.1	11	76.7	0.2	8	0.4	2	9.4	0.42	2.5
0.3	13.9	1.6	0.22	0.15	8	4.56	12.1	3.7	48	10	9.3	12	77	0.4	8	0.6	2	9.4	0.42	2.5
0.4	13.9	1.5	0.2	0.15	7	4.24	10.9	4.2	51	8	9.8	12	76.6	0.4	8	0.5	2	9.5	0.41	2.5
0.4	11.4	1.4	0.2	0.15	6	4.23	11	4.4	57	9	8.9	10	77.1	0.3	8	0.6	2	9.4	0.42	2.5

Continued to Table A3

Y	Ta	W	Re	Os	La	Ce	Pr	Nd	Sm	Eu	Gd	Tb	Dy	Ho	Er	Tm	Yb	Lu	$\delta^{13}C_{inorg}$	$\delta^{18}O$	$\delta^{13}C^{o}_{rg}$	N	$\delta^{15}N$	$\delta^{34}S$
20.5	1.1	1.1	48.98	0.307	42.1	78.7	7.6	36.1	4.4	1.3	5.1	0.7	3.8	0.9	2.3	0.3	2.3	0.4						
25.4	3.4	4.7	10.69	0.317	39	76.6	9.8	38.4	6.6	1.27	4.9	0.7	4.8	1	2.9	0.4	2.9	0.4						
26.2	3.7	2.4	6.36	0.281	41.2	78.2	10	39.3	6.9	1.29	5	0.8	5	1	2.9	0.4	3	0.4	-8.4	-8.9	-29.6	0.2	3.4	-18.4
26.6	3.5	2.5	11.13	0.306	39.2	77.5	10.1	39.6	7.2	1.35	5.3	0.8	5.1	1	2.9	0.4	2.9	0.4			-29.7	0.2	3.5	-28.2
25.2	3.3	2.2	9.94	0.318	39.8	76.2	9.8	38.2	6.8	1.24	4.8	0.7	4.7	0.9	2.8	0.4	2.9	0.4						
26.9	1	1.7	7.45	0.235	41.9	78.9	10.1	37.6	6.1	1.58	6.3	0.9	4.9	1	3.1	0.4	2.8	0.4	-11.4	-9.4	-29.1	0.2	5.1	-22.4
22.7	1.1	1.6	9.98	0.282	27.2	59.2	8	30.9	6	1.33	5.3	0.8	4.8	0.9	2.8	0.4	2.7	0.4	-9.1	-8.9	-29.6	0.2	4.9	-27.8
25.8	1.1	1.6	12.19	0.284	41.6	81.1	10.2	38.1	7	1.48	5.9	0.8	5	1	2.9	0.4	2.8	0.4	-8.6	-8.7	-29.6	0.2	4.5	-30.0
25.7	1.1	1.7	10.66	0.277	43.3	82	10.4	38.3	6.7	1.54	6.1	0.8	4.8	1	3.1	0.4	2.7	0.4	-8.2	-9.0	-29.4	0.2	4.3	-22.4
27.1	1.2	1.7	9.51	0.263	44.1	83.2	10.4	38.4	6.9	1.56	6.1	0.8	5.1	1	3.1	0.4	2.8	0.4	-8.1	-8.5	-29.5	0.2	3.8	-19.4
25.8	1.2	1.7	11.41	0.292	44.2	84.1	10.5	37.6	7.4	1.51	6	0.8	4.9	1	2.9	0.4	2.8	0.4	-8.1	-8.8	-29.4	0.2	3.7	-23.6
26.8	1.2	1.8	9.45	0.297	46	84.5	10.6	38.8	7.1	1.52	6	0.9	4.9	1.1	3	0.4	2.9	0.4	-8.1	-9.2	-29.5	0.2	3.7	-23.0
33.5	2.7	2.2	14.58	0.266	36.8	69.4	9.6	38.1	7.1	1.44	5.9	0.9	5.9	1.2	3.4	0.5	3.3	0.5	-7.2	-8.0	-26.9	0.2	3.5	-29.0
30.3	2.6	1.8	22.94	0.344	36.5	71.3	9.8	38.6	6.8	1.3	5.2	0.8	5.4	1.1	3.3	0.5	3.3	0.5						
26.4	2.6	2	16.76	0.257	33	58.6	8.4	33	5.9	1.17	4.6	0.7	4.6	0.9	2.8	0.4	2.8	0.4						
33.7	2.4	1.7	33.13	0.328	34.5	65.7	9.2	37.7	7.3	1.43	5.9	0.9	5.8	1.2	3.4	0.5	3.3	0.5			-27.0	0.3	3.4	-26.4
34.1	2.5	2	25.90	0.285	36.2	66.7	9.6	38.8	7.4	1.39	5.8	0.9	5.9	1.2	3.5	0.5	3.3	0.5						
29.8	0.7	1.4	20.02	0.322	35.7	64.7	8.7	32.8	5.6	1.33	6	0.8	5	1	3.2	0.4	2.8	0.4	-9.8	-10.9	-25.9	0.2	4.1	-17.3
28.8	0.8	1.5	24.78	0.367	37.3	67	9.2	34.4	5.6	1.34	6	0.8	4.9	1	3.1	0.4	2.8	0.4	-9.0	-10.6	-26.0	0.2	3.9	-17.7
26.6	0.5	1	11.28	0.268	26.3	51	7.4	29	5.8	1.38	6	0.8	4.7	0.9	2.7	0.4	2.4	0.3	-10.2	-13.0	-26.1	0.1	4.4	0.5
33	0.8	1.4	31.77	0.459	37.9	73.3	10.5	41.2	7.8	1.74	7.4	1	5.9	1.2	3.5	0.5	2.9	0.4	-8.5	-9.3	-26.0	0.2	3.9	-19.8
25.4	1	1.5	28.73	0.423	38.1	67.3	8.9	32.6	6	1.27	5.4	0.7	4.4	0.9	2.9	0.4	2.7	0.4	-9.0	-9.9	-26.0	0.2	4.0	-20.6
25.1	1	1.6	21.93	0.420	36.8	66.5	8.6	32.3	5.2	1.25	5.1	0.7	4.4	1	2.8	0.4	2.7	0.4	-9.4	-10.2	-25.9	0.2	4.2	-24.1
24	0.9	1.5	26.78	0.428	36	65.6	8.8	33.4	5.5	1.28	4.9	0.7	4.5	0.9	2.7	0.4	2.7	0.4	-9.5	-10.4	-25.9	0.2	3.9	-23.1
34.5	2.5	1.9	26.96	0.388	37.7	68.7	9.7	39	7.2	1.34	5.5	0.9	5.6	1.2	3.5	0.5	3.6	0.5						
33	1.4	1.6	23.28	0.384	38.5	72.1	10.6	37.8	6.1	1.63	6.7	1	5.7	1.2	3.4	0.5	3.2	0.5	-8.6	-9.5	-26.2	0.3	4.2	-19.5
26.7	0.9	1.4	24.13	0.385	35.9	63.6	8.9	34.7	6.4	1.27	5.5	0.8	5.1	1	3.2	0.5	3	0.6						
31.5	1	1.5	23.13	0.360	38.6	70.6	9.4	35.7	6.3	1.46	6.2	0.9	5.4	1.1	3.4	0.5	3.1	0.5	-7.9	-8.8	-26.2	0.2	4.0	-20.8
31.9	0.9	1.6	27.68	0.394	39.4	72.2	9.9	37.4	6.6	1.54	6.5	0.9	5.3	1.2	3.5	0.5	3	0.4	-9.0	-9.9	-26.2	0.3	4.5	-21.4
22.1	0.8	0.9	28.72	0.418	35.9	63.4	6.5	31.7	3.9	1.2	4.9	0.7	3.8	0.9	2.4	0.3	2.3	0.4						
26.9	0.8	1.2	25.63	0.391	35.7	63.8	9.2	35.4	6.7	1.3	5.7	0.8	5	1	3.1	0.5	2.9	0.5	-7.3	-10.1	-26.2	0.3	4.8	-22.4
30.5	0.8	1.2	30.63	0.452	41.4	75.6	10.8	41.8	8	1.54	6.7	0.9	5.8	1.1	3.4	0.5	3.1	0.5	-8.1	-9.5	-6.4	0.3	4.6	-21.8
30.5	0.8	2.3	19.21	0.328	33.1	62.6	8.1	31.8	5	1.09	4.8	0.7	4.9	1	3.2	0.4	3.5	0.5	-7.9	-9.6	-25.9	0.3	3.9	-6.0
8.2	0.2	0.4	4.15	0.086	8.2	15.6	2	7.8	1.5	0.26	1.2	0.2	1.2	0.3	0.8	0.1	0.9	0.1			-26.0	0.1	4.1	8.8
34.9	0.8	1.4	24.23	0.399	34.4	65.2	8.9	36.5	6.1	1.37	5.9	0.9	5.8	1.2	3.4	0.5	3.6	0.4	-7.7	-10.0	-25.9	0.3	3.9	0.6
35.4	0.8	1.3	22.07	0.370	33.4	63.7	9	36.8	6.2	1.41	6	0.9	5.9	1.2	3.6	0.5	3.7	0.4	-8.4	-10.3	-25.9	0.3	3.8	-0.3
31.2	0.8	1.4	19.19	0.319	35	63.6	8.7	34.1	6.6	1.25	5.5	0.8	5.4	1.1	3.2	0.4	3.5	0.4	-8.6	-10.2	-25.8	0.3	3.9	-1.5
29.4	0.8	1.3	48.43	0.510	32	59.7	8	32.2	5.4	1.11	4.8	0.7	4.9	1	3	0.4	3.3	0.4	-8.5	-10.6	-26.0	0.3	3.6	-15.1
28.3	0.8	1.5	50.51	0.518	30.1	58.2	7.8	30.4	6	1.1	4.7	0.7	4.8	1	2.9	0.4	3.3	0.4	-8.6	-10.7	-25.9	0.3	3.6	-19.0
32.2	0.8	1.5	23.98	0.376	33	62.8	8.5	33.8	6.3	1.22	5.4	0.8	5.5	1.1	3.3	0.4	3.5	0.5	-8.5	-9.8	-25.8	0.3	3.8	-6.2
37.3	2.3	1.9	23.47	0.427	35.2	61.4	9.4	37.4	7.1	1.35	5.8	0.9	6.1	1.2	3.7	0.5	3.5	0.5						
40.2	2.4	2	21.54	0.398	38	66.4	10	40.3	7.5	1.48	6.4	0.9	6.5	1.4	3.9	0.6	3.8	0.6						
29	0.7	1	23.34	0.450	33.9	57.4	7	35.3	4.7	1.5	6.3	0.9	4.8	1.1	2.9	0.3	2.5	0.4						
30	0.8	1.4	19.25	0.369	33.2	60.1	8.2	33.2	6.2	1.17	5.1	0.7	5	1	3.1	0.4	3.3	0.4	-9.6	-10.6	-25.7	0.3	4.2	-11.2
34.6	0.9	1.6	22.65	0.433	37.2	65.7	9.1	35.2	6.4	1.48	6.2	0.9	5.7	1.2	3.5	0.5	3.3	0.5	-9.0	-10.9	-25.9	0.3	3.9	-11.0
30.5	0.8	1.5	20.11	0.374	32.1	60.3	8.9	36.4	6.8	1.25	5.5	0.8	5.1	1.1	3.1	0.4	3.4	0.4	-9.0	-10.8	-25.7	0.3	3.9	-9.0
35.1	0.9	1.5	20.40	0.398	40.2	74.5	9.6	40.1	7	1.43	6.3	0.9	5.9	1.2	3.6	0.5	3.8	0.5	-8.6	-10.2	-25.7	0.3	4.0	-6.5
36	2.5	2	39.97	0.536	38.7	68.3	10.1	40.1	7.4	1.36	5.7	0.8	5.8	1.2	3.7	0.5	3.7	0.6	-8.8	-12.2	-25.8	0.4	4.0	-16.0
36.7	0.8	1.3	18.72	0.345	33	61.1	9.2	37.7	7.8	1.61	7	1	6.5	1.3	3.5	0.5	3.5	0.4	-10.0	-11.2	-25.7	0.3	4.1	-4.7
30.7	0.9	1.5	19.96	0.372	37.8	71.7	9.4	36.7	6.2	1.19	5.1	0.8	5.2	1.2	3.4	0.5	3.7	0.4	-9.5	-11.3	-25.7	0.3	4.2	-13.0
40.3	2.3	1.9	47.13	0.726	36.2	66.4	10.7	44	8.6	1.63	6.8	1	6.7	1.4	3.9	0.6	3.6	0.5						
31.1	0.8	2.8	22.25	0.415	38.4	65.6	9.3	34.9	5.9	1.36	5.8	0.8	5	1.1	3.4	0.5	3.1	0.5	-9.1	-11.5	-25.9	0.3	4.0	-6.9
20.7	0.7	1	27.52	0.460	34.1	52.6	6	28.5	3.3	1	4	0.6	3.2	0.8	2.2	0.3	2.2	0.4						
26.5	0.8	1.6	18.57	0.389	31.3	51.6	7.6	31.1	4.7	1.07	4.6	0.6	4.3	1	2.9	0.4	3	0.4	-8.9	-11.6	-25.6	0.3	4.3	-5.9
33.5	0.9	1.6	18.57	0.413	35.7	68.1	9	35.9	6.9	1.34	5.7	0.8	5.4	1.2	3.4	0.5	3.7	0.4	-8.9	-11.1	-25.7	0.3	4.3	-3.7
34.4	2.4	1.9	28.63	0.500	36.7	65.4	9.5	37.7	6.4	1.22	5.1	0.8	5.5	1.2	3.5	0.5	3.6	0.6	-7.6	-10.5	-26.0	0.3	4.3	-11.9
35.3	0.9	1.7	28.60	0.498	42.5	72	10.3	38.6	6.6	1.6	6.8	0.9	5.6	1.2	3.8	0.5	3.4	0.5	-8.2	-11.0	-25.9	0.3	3.9	-11.5
30.9	0.9	1.6	20.18	0.416	31.5	56.5	7.8	32.7	5.9	1.23	5.1	0.7	4.9	1	3.1	0.4	3.2	0.4	-9.2	-11.4	-25.7	0.3	4.4	-2.8
40.2	2.3	1.9	23.42	0.494	33.6	61.6	9.5	39.5	7.6	1.51	6.4	1	6.5	1.3	3.9	0.5	3.6	0.5	-9.2	-12.0	-25.9	0.3	4.3	-7.4
20.4	0.9	1.5	9.27	0.166	31.1	64.9	7.7	29.3	4.6	1.09	4.9	0.7	3.9	0.8	2.4	0.3	2.3	0.3	-11.3	-11.7	-24.9	0.1	3.9	-26.2
19.3	0.9	1.5	2.64	0.146	29.5	63.1	7.2	27.9	4.9	1.05	4.6	0.6	3.7	0.8	2.3	0.3	2.2	0.3	-11.4	-11.9	-24.8	0.1	3.6	-29.9
19.1	0.7	1.4	5.85	0.143	29.7	62.4	7.2	27.7	4.7	1.06	4.2	0.6	3.8	0.7	2.2	0.3	2.1	0.3	-11.3	-11.7	-24.9	0.1	3.8	-26.9
19.6	0.9	1.5	4.27	0.168	29.9	62.2	7.2	27.2	5	1.02	4.4	0.6	3.8	0.7	2.2	0.3	2.2	0.3	-11.7	-12.3	-24.9	0.1	4.1	-29.8
19.4	0.9	1.5	3.25	0.184	28.9	60.5	7	26.8	4.5	1.07	4.6	0.6	3.8	0.7	2.3	0.3	2.2	0.3	-11.5	-12.0	-24.9	0.1	3.9	-27.8
20.6	0.8	1.7	3.48	0.182	30.6	64.5	7.5	27.9	5.2	1.07	4.5	0.6	3.8	0.8	2.3	0.3	2.3	0.3	-11.3	-11.8	-24.7	0.1	3.9	-27.4
20.7	0.8	1.5	3.40	0.182	30.4	63.8	7.5	27.6	5.2	1.09	4.8	0.6	3.7	0.8	2.4	0.3	2.3	0.3	-11.2	-12.1	-24.9	0.1	4.5	-26.6
25.3	2.9	2.5	3.68	0.207	34	74.8	8.8	34.6	6.6	1.19	4.6	0.7	4.8	1	2.9	0.4	3	0.5						
22.5	1	1.9			31.5	75.3	7.9	32.4	6.5	1.2	5.1	0.7	4.6	0.9	2.7	0.4	3	0.3	-8.5	-9.9	-25.2	0.2	3.5	-35.3
23.3	1.1	1.9			29.6	75.4	7.9	32.9	6.2	1.19	5	0.7	4.7	0.9	2.7	0.4	3	0.4	-8.8	-10.2	-25.3	0.2	3.4	-36.1
24.5	2.9	2.3	5.26	0.219	30.4	70.7	8.3	32.9	6.1	1.15	4.3	0.7	4.6	0.9	2.8	0.4	2.9	0.4						
22.7	0.9	1.7	7.79	0.182	32.3	78	8	32.4	6.9	1.22	4.8	0.7	4.6	0.9	2.8	0.4	3	0.4	-8.8	-9.8	-25.3	0.2	3.4	-25.8
24.9	2.9	2.3	9.05	0.227	30.5	71.1	8.5	33.4	6.3	1.15	4.5	0.7	4.7	0.9	2.8	0.4	2.9	0.4	-9.3	-9.8	-25.3	0.2	3.3	-27.8
24.9	2.9	2.2	7.48	0.208	32.2	71.2	8.4	33.3	6.2	1.17	4.4	0.7	4.6	1	2.9	0.4	2.9	0.4						
23.9	0.8	1.9	4.32	0.192	34.1	80.1	8.4	35.1	6.4	1.26	5.5	0.8	4.7	0.9	2.8	0.4	3.2	0.4	-9.0	-10.2	-25.3	0.2	3.3	-28.2
25.1	2.8	2	11.83	0.240	30.4	69.6	8.3	33.4	6.3	1.13	4.6	0.7	4.7	1	2.8	0.4	3	0.4						
15	0.2	0.8	1.97	0.124	24.8	52.3	6.1	22.3	3.7	0.84	3.7	0.5	3	0.6	1.8	0.3	1.7	0.3	-9.9	-13.4	-25.8	0.1	4.2	-47.8
17.3	0.7	1.2	2.63	0.146	25	53.9	6.1	22.4	3.9	0.83	3.8	0.5	3.3	0.7	2	0.3	1.9	0.3	-10.0	-13.3	-25.7	0.1	3.8	-47.9
14.9	< 0.1	0.2	2.88	0.123	27.6	58.5	6.5	23.8	4.2	0.83	3.5	0.5	2.9	0.6	1.8	0.2	1.7	0.2	-9.4	-12.9	-25.6	0.1	4.0	-47.8
14.4	< 0.1	0.7	2.96	0.130	25.6	54.7	6.3	23.4	3.7	0.81	3.6	0.5	2.8	0.6	1.8	0.2	1.7	0.2	-10.4	-13.2	-26.0	0.1	4.2	-47.8
14.9	0.5	1.1	7.51	0.153	27.4	57.4	6.6	24.3	4.2	0.84	3.7	0.5	2.8	0.6	1.8	0.2	1.7	0.2	-10.4	-13.0	-26.2	0.1	4.5	-47.3
15.1	0.6	1.1	3.93	0.126	25.9	54.9	6.2	23.1	4.6	0.84	3.5	0.5	2.7	0.6	1.8	0.2	1.7	0.3	-10.9	-13.2	-26.4	0.1	4.2	-47.2
15.6	0.5	1.1	4.12	0.139	26	55.5	6.3	23.4	4.6	0.87	3.5	0.5	2.9	0.6	1.8	0.3	1.8	0.3	-11.0	-13.5	-26.3	0.1	3.5	-46.8

Table A4 New Hg contents in GRL and MNS shales by DMA with the previously published geochemical data from Georgiev et al. (2011) and Georgiev et al. (2012)

				Hg analysis			Rock-Eval pyrolysis				Major and trace element data																				
AIRIE Run #	Sample #	depth in outcrop or core (m)	unit -->	Hg 1 ppb	Hg 2 ppb	Avg. Hg ppb	TOC wt %	HI mg HC/g TOC [S2/TOC]	OI mg CO2/g TOC [S3/TOC]	unit -->	Al wt %	Ca wt %	Fe wt %	Mg wt %	S wt %	Cr ppm	Cu ppm	Mn ppm	Ni ppm	P ppm	Sr ppm	V ppm	Zn ppm	Cd ppm	Co ppm	Mo ppm	Rb ppm	Sc ppm	Th ppm	Re ppb	Os ppb
										detection limit	0.01	0.01	0.01	0.01	0.01	1	0.5	2	0.5	50	0.5	1	1	0.01	0.1	0.1	0.2	0.1	0.1		
East Greenland (GRL) Ravnefjeld Formation, outcrops samples, Triaselv area																															
	GRL-O1-a - Southeast side of Triaselv, Upper layers																														
ORG-210	GR08-SD9	0.00		106	109	108	2.41	157	43		1.46	3.62	3.48	1.17	0.5	40	32.2	520	57.6	320	113	44	232	1.86	17.6	26.8	39.6	6.4	7.9	24.95	0.3291
ORG-169	GR08-SD1	-1.20		94	97	95	3.03	202	22		1.3	5.15	2.97	1.15	1.06	42	30.3	454	58.7	350	159	62	304	4.24	13.5	35.6	35.2	5.8	7.7	283.33	0.8385
ORG-170	GR08-SD2	-1.40		104	107	105	3.04	180	35		1.3	5.21	3.04	1.12	0.78	40	31.9	514	65.8	400	156	64	270	3.77	16.8	45.3	34.8	6.5	7.7	109.60	0.6353
ORG-171	GR08-SD3	-1.60		112	114	113	3.00	201	36		1.46	4.03	3.31	1.24	0.5	43	36.7	447	69.1	400	127	72	302	4.08	19.2	40.2	38.5	6.6	8.6	95.15	0.6103
ORG-172	GR08-SD4	-1.80		98	102	100	2.57	153	43		1.5	4.11	3.46	1.29	0.81	43	33.9	428	68.5	400	134	77	314	3.64	18.2	41.3	39.9	6.8	7.9	115.75	0.6085
ORG-173	GR08-SD5	-2.80		88	94	91	2.87	201	33		1.48	5.19	3.28	1.31	0.89	41	34.9	399	81.5	490	147	78	303	3.76	14.6	31.8	37.5	6.5	7.1	156.19	0.8037
ORG-207	GR08-SD6	-3.10		85	88	86	2.50	194	37		1.5	5.07	3.36	1.35	1.12	41	33.3	400	72	460	143	77	292	3.65	16.6	34.1	36.9	6.2	7	148.84	0.6911
ORG-208	GR08-SD7	-3.30		88	94	91	2.51	168	41		1.5	5.07	3.36	1.35	1.12	41	33.3	400	72	460	143	77	292	3.65	16.6	34.1	36.9	6.2	7	145.88	0.5860
ORG-209	GR08-SD8	-3.60		131	134	132	6.04	276	31		1.27	5.01	3.17	1.16	1.65	45	38.8	368	101	440	151	130	414	5.99	18.3	75.3	32.2	6.1	7.9	328.23	1.4448
	GRL-O1-b -Southeast side of Triaselv, 10 meters lower in section																														
ORG-212	GR08-SD11	-13.60		34	36	35	1.71	225	36		0.53	2.02	1.55	0.47	0.6	20	15.2	258	40	220	75.9	20	368	2.65	10.9	13.2	14.9	3	3.1	40.10	0.2611
ORG-310	GR08-SD17	-14.80		58	59	58	4.05	164	42		1.36	1.3	3.53	1.1	0.61	45	36.5	314	68.3	430	63.3	54	158	1.8	19.1	24.2	40.6	6.1	8.7	59.55	0.6603
ORG-309	GR08-SD18	-14.85		60	62	61	3.93	166	47		1.27	2.12	3.26	1.02	0.55	51	34.5	332	67.2	410	86.6	51	157	1.95	17.6	22.5	37.5	5.9	8.3	48.33	0.6159
ORG-308	GR08-SD19	-14.90		52	55	53	3.49	156	53		1.25	1.86	3.22	1.02	0.61	49	30.5	316	69.3	400	70.5	51	220	1.89	18.3	23.1	38.3	6.1	7.8	46.72	0.5796
ORG-307	GR08-SD20	-14.95		25	27	26	1.49	195	44		0.68	10.8	1.81	0.65	0.51	23	16.4	566	30.9	310	177	29	110	2.28	9.4	12.3	20.1	4.9	4.2	29.76	0.2614
ORG-311	GR08-SD21	-15.02		45	43	44	2.15	142	47		1.28	2.25	3.24	1.02	0.56	35	29.3	381	53	350	68.5	47	201	1.85	18.8	21.5	40.5	6.4	8	30.34	0.3474
ORG-312	GR08-SD22	-15.07		45	49	47	2.22	156	44		1.28	1.8	3.29	1.03	0.64	37	30	372	61.7	340	60.3	46	163	1.58	19	23.5	39.6	5.9	7.7	43.36	0.3517
	GRL-O2-a - Triaselv, opposite (north) side of creek																														
ORG-400	GR08-SD23	0.00		84	90	87	3.19	185	41		1.41	4.36	3.38	0.91	1.01	57	33.1	555	65.8	310	145	49	705	4.13	18.9	27.5	39.7	6.5	7.7	71.31	0.4011
ORG-401	GR08-SD24	-0.07		74	80	77	2.94	159	55		1.61	4.69	3.74	1.02	0.32	40	33.5	540	58.8	300	154	50	976	3.09	18.2	23.6	37.3	6	7.1	33.59	0.3599
ORG-402	GR08-SD25	-0.17		79	83	81	2.34	182	34		1.22	5.1	2.95	0.82	0.89	35	27.5	560	53.8	270	170	38	689	3.84	17.1	18.6	33.9	5.8	6.4	80.53	0.3237
ORG-403	GR08-SD26	-0.22		76	80	78	2.55	218	21		1.24	4.75	2.94	0.83	1.3	35	28	581	55.6	330	149	37	513	3.75	19.7	21.8	35.8	6	7.1	122.79	0.3444
ORG-300	GR08-SD27	-5.22		36	39	38	3.19	146	67		0.82	3.8	2.47	0.48	0.36	26	37.9	253	58.2	330	156	39	1220	10.6	12.7	26.9	25.9	5.3	5.3	20.15	0.5463
ORG-301	GR08-SD28	-5.27		38	42	40	2.91	215	49		0.86	2.29	2.62	0.51	0.4	41	41.9	255	66.9	340	98.1	34	1450	17.3	12	22.9	26.3	5	5.5	14.56	0.4410
ORG-302	GR08-SD29	-5.67		29	30	30	2.90	152	59		0.55	2.5	1.73	0.32	0.37	75	27.4	328	81.5	240	56.6	22	773	8.02	9	13.5	17.6	3.4	3.7	11.10	0.3738
ORG-305	GR08-SD30	-5.72		24	25	25	1.85	219	42		0.6	3.9	1.72	0.38	0.47	33	23.9	444	47.7	260	80.6	23	648	8.82	8.3	15.9	20.4	3.8	4.1	118.18	0.2634
	GRL-O2-b - Triaselv, opposite (north) side of creek																														
ORG-285	GR08-SD31	-10.72		73	74	74	5.53	311	32		0.55	14.6	2.02	0.48	0.5	50	22.1	520	82.3	590	320	119	775	19.8	12.9	109	15.8	3.9	4	164.99	1.4297
ORG-286	GR08-SD32	-10.76		88	94	91	6.84	318	34		0.57	13.4	2.12	0.48	0.56	63	26.1	467	107	720	320	141	935	23.1	14.9	134	16.3	4	4.6	198.08	1.9534
ORG-287	GR08-SD33	-10.79		76	78	77	6.05	335	46		0.55	14.8	1.83	0.49	0.54	24	23.2	455	72.3	630	365	114	709	23.2	12.2	89.4	15	3.9	3.8	153.56	1.5164
ORG-288	GR08-SD34	-10.84		95	98	96	6.57	310	37		0.99	6.78	3.06	0.61	0.34	30	32.8	481	106	700	189	160	808	14.5	20.6	94.1	24.2	4.5	6.2	130.19	1.5809
ORG-289	GR08-SD35	-10.94		139	144	141	4.14	259	51		1.16	6.01	3.59	0.7	0.3	123	37.3	606	173	820	160	123	356	9.2	26.1	67.9	29.7	5.5	7.3	84.60	1.3532

Continued to Table A4

East Greenland (GRL) Ravnefjeld Formation, shallow drill-core GGU 303102, Triaselv area																												
	Upper Laminated Unit of the Ravnefjeld Fm.																											
ORG-454	4.562-4.572	127	135	131	2.29	171	46	1.8	7.14	3.76	1.54	2.16	51	32.4	622	72.4	330	161	66	254	2.96	23.5	23.3	38.8	11.2	6.4	79.34	0.3618
ORG-455	4.587-4.603	119	127	123	2.20	169	49	1.64	6.68	3.47	1.48	2.03	47	30.8	612	62.5	290	148	60	208	2.68	24.3	26.4	41	11.6	6.6	69.30	0.3435
ORG-456	4.626-4.633	134	143	138	2.33	179	41	1.72	7.14	3.71	1.54	2.2	45	34.1	677	67.4	340	158	64	212	2.79	26.9	27.2	41.4	11.7	6.7	72.84	0.4571
	Lower Laminated Unit of the Ravnefjeld Fm.																											
ORG-428	9.898-9.901	93	96	94	4.31	345	9	1.59	5.85	3.33	1.4	2.1	53	38	369	108	370	141	93	271	4.35	21.6	45.9	41.9	11.4	6.9	323.32	1.2344
ORG-429	9.916-9.925	103	113	108	3.83	333	13	1.66	5.57	3.53	1.38	2.28	55	38.4	381	100	350	133	95	255	3.99	25.8	56.4	46	12.9	7.3	246.21	0.9891
ORG-430	9.976-9.980	102	109	105	3.58	338	17	1.69	5.62	3.67	1.42	2.36	53	39.7	407	99.8	360	133	102	216	3.58	25.5	60.2	47.8	12.7	7.7	218.05	0.8871
ORG-431	10.064-10.072	92	99	93	3.61	333	17	1.69	6.43	3.49	1.42	2.19	53	37.9	385	94.3	370	156	91	346	5.31	23.6	47.8	44.8	11.9	6.9	226.77	0.9193
ORG-432	10.113-10.122	98	108	103	3.50	336	17	1.82	6.24	3.78	1.42	2.39	54	36.8	418	91.8	380	150	88	280	4.97	25.4	55.7	46.8	12.3	7.4	156.18	0.7321
ORG-452	10.122-10.135	95	102	98	3.18	323	14	1.74	7.48	3.52	1.33	2.24	49	31.7	424	79.4	370	187	83	217	3.21	20.6	43.3	43.1	10.6	5.9	146.70	0.6680
ORG-433	10.136-10.148	106	105	106	3.78	334	16	1.69	7.14	3.45	1.35	2.23	54	34.7	397	97.5	440	159	94	245	3.81	25.1	45.7	46.5	12.6	7.2	214.60	0.9227
ORG-453	10.158-10.164	112	122	117	3.27	338	18	1.65	6.57	3.42	1.3	2.23	48	34.3	405	88.2	400	145	88	368	5.81	24.6	45.3	42.6	11.7	6.5	210.01	0.8127
mid-Norwegian shelf (MNS) shallow drill-core IKU 6611/09-U-01																												
	Upper Laminated Interval 1 (UL1)																											
ORG-405	241.10-241.12	77	84	80	3.34	167	16	1.9	5.38	4.04	1.53	2.42	39	35.7	431	59.6	630	219	46	106	1.03	22.3	50.7	52.4	12.7	15.2	48.16	0.2450
ORG-475	241.12-241.14	81	92	86	3.52	178	20	1.77	5.8	4.11	1.52	2.85	42	37.7	420	76.6	640	224	52	158	1.77	22.6	48.5	46.2	13	14.9	133.41	0.5691
ORG-407	241.14-241.16	76	83	79	3.89	224	17	1.65	5.87	3.87	1.44	2.49	35	37.3	364	81.4	610	222	52	164	2.21	22.6	36.3	41.2	12.6	13.3	281.92	1.0308
ORG-476	241.16-241.17	89	96	93	2.91	134	26	1.92	6.11	3.88	1.44	2.21	37	29.4	423	48.6	710	247	54	78	0.85	21.5	34.1	56.8	13.2	15.5	28.27	0.1485
ORG-477	241.19-241.20	83	92	88	3.67	186	22	1.89	5.79	3.99	1.56	2.41	40	39	425	70.4	600	225	54	180	2.14	22.2	40.1	43.2	11.7	13.5	99.33	0.4808
ORG-478	241.92-241.94	60	62	61	3.09	161	25	1.97	5.43	4.12	1.5	2.68	40	35.1	367	71.2	690	222	60	124	1.6	22	31.5	50.5	11.8	14.9	156.44	0.5419
	Upper Laminated Interval 2 (UL2)																											
ORG-321	243.63-243.66	43	45	44	3.21	177	26	2.2	5.29	4.14	1.55	2.59	42	37.6	370	78.9	650	208	75	156	2.62	23.5	24.8	57.1	14.4	16	104.13	0.4318
ORG-322	243.66-243.68_vp Ia	49	51	50	3.12	164	26	2.08	4.96	4.38	1.53	2.93	41	34.5	388	68.4	610	196	69	141	2.13	24.5	38.7	55.8	13	14.6	84.95	0.3623
ORG-323	243.66-243.68_vp Ib	47	49	48	3.36	175	22	1.72	4.6	3.82	1.36	3.01	38	34.8	314	82.1	530	174	69	175	2.61	23.7	33.2	45.9	12.1	12.5	156.35	0.6001
ORG-324	243.68-243.71	49	53	51	2.93	148	20	2.06	5.14	4.48	1.56	3	37	35.4	349	72.9	540	200	66	132	2.62	25.2	33.9	51.5	13.4	14.1	170.85	0.5960
ORG-344	243.89-243.92	50	52	51	2.98	162	18	1.98	4.85	4.67	1.52	3.25	41	33.9	364	71.4	620	200	58	135	1.79	22.9	35.2	51.5	12.7	14.4	122.02	0.4535
ORG-345	243.92-243.94	41	44	43	2.75	157	20	1.87	5	3.92	1.43	2.6	40	32.9	334	69.5	570	196	53	120	1.54	22.2	34.9	48.6	13.9	14.2	109.33	0.4209
	Lower Laminated Interval (LL)																											
ORG-363	254.92-254.94	34	35	35	2.97	111	20	2.08	5.12	4.45	1.54	2.75	46	34.9	513	60.1	690	195	41	106	0.75	24.9	23.7	56.3	14.1	15.3	25.15	0.1736
ORG-364	254.94-254.96	33	33	33	3.14	114	18	2.16	5.21	4.69	1.51	2.9	46	33.3	510	54.5	730	205	43	97	0.52	22.9	18.6	58.6	14	16.3	15.82	0.1239
ORG-365	255.02-255.05	36	37	36	3.34	116	19	2.08	4.86	4.8	1.46	3.16	43	35	454	53.8	710	193	45	104	0.61	24.7	25.7	59.8	15.1	16.3	35.52	0.1754
ORG-366	255.06-255.08	34	35	34	3.10	129	19	2.1	4.47	4.43	1.53	2.69	46	36.6	452	62.5	620	178	43	112	0.69	25.5	29	57.1	14.7	15.2	48.66	0.2466
ORG-367	255.13-255.16	37	38	37	3.13	132	15	2	4.5	4.43	1.49	2.9	45	36.7	429	63	640	182	43	114	0.81	25.6	38.1	58.6	14.9	15.2	79.42	0.3438
ORG-368	255.18-255.20	37	38	38	3.31	142	16	2.09	4.48	4.47	1.54	2.79	43	35.3	426	64.1	630	182	45	116	0.82	25.4	32.7	57	14.6	15.4	55.97	0.2934
	Bottom Shale (BS)																											
ORG-384	279.35-279.37	20	20	20	0.62	*	*	2.64	6.57	4.13	1.86	0.23	50	38.1	493	57.4	750	272	49	97	0.17	20.4	0.2	51.9	13.6	9.8	3.10	0.1231
ORG-385	279.39-279.42_vp Ia	12	12	12	0.95	*	*	2.58	7.19	4.06	1.73	0.41	50	32.4	535	65.2	670	279	48	102	0.19	31.7	0.3	65.9	15.3	11.6	8.08	0.1388
ORG-450	279.39-279.42_vp Ib	10	no remnant	10	0.74	*	*	2.58	6.92	3.72	1.71	0.21	46	31.1	490	51.9	620	266	48	88	0.12	19.7	0.1	60.9	13.5	11.1	3.26	0.0852
ORG-386	279.42-279.45_vp I	15	16	15	0.55	*	*	2.73	6.34	4.17	1.86	0.20	51	43.1	481	60.9	620	264	50	95	0.13	21.5	0.2	57.6	13.5	10.7	2.93	0.0883
ORG-387	279.45-279.47	16	17	16	0.77	*	*	2.85	6.36	4.39	1.87	0.27	54	30.0	485	59.3	660	255	50	107	0.17	21.9	0.1	62.9	14.6	11.7	2.08	0.1012
ORG-451	279.50-279.53_vp Ib	17	no remnant	17	1.15	*	*	2.51	8.30	3.79	1.66	0.54	51	23.7	511	52.4	590	345	50	84	0.16	25.6	0.2	69.2	15.3	11.7	5.73	0.1573

*not measured